The Distribution Of Star-Forming Molecular Gas In Nearby Spiral Galaxies

by

Helena Faustino Vieira

A Thesis submitted to Cardiff University
for the degree of Doctor of Philosophy

September 2024

ABSTRACT

The question of whether star formation is directly affected by the large-scale dynamics within a galaxy, or merely dependent on the local conditions of the interstellar medium (ISM), is a matter of long-standing debate. This is hindered by the difficulty in simultaneously probing the small-scales associated with the star formation process, and the large-scales which might regulate the formation and evolution of molecular clouds, where stars form. This Thesis describes a newly developed imaging technique which utilises the dust extinction at optical wavelengths to produce high-resolution maps of the dust (and gas) of nearby galaxies. The dust attenuation is determined by comparing optical data to a reconstructed stellar light model at each pixel. Here, this technique is first applied to the spiral M51 as a proof-of-concept, followed by a wider sample of nearby disc galaxies.

This extinction imaging technique provides a foundation for an investigation into the distribution of the gas in nearby spiral galaxies at high resolution, with a particular focus on the impact of large-scale galactic environment. For that, an extensive catalogue of resolved clouds was extracted, enabling a statistical analysis of ISM properties. In this body of work, I find that there are clear changes in cloud populations between the centres and discs of galaxies, whilst differences between arm/inter-arm clouds are more subtle. Still, galactic environments within different galaxies do not always present the same physical conditions, and thus merely investigating cloud properties as a function of environment may result in loss of information on interesting galaxy-to-galaxy variations. Furthermore, the dust/gas images produced in this work have comparable resolution to JWST observations, enabling further studies into the correlation between, for example, the early, embedded phase of star formation and natal cloud properties.

PUBLICATIONS

FIRST AUTHOR

Faustino Vieira H., Duarte-Cabral A, Davis T. A., et al., 2023, *A high-resolution extinction mapping technique for face-on disc galaxies*, MNRAS, 524, 161

Faustino Vieira H., Duarte-Cabral A, Davis T. A., et al., 2024, *Molecular clouds in M51 from high-resolution extinction mapping*, MNRAS, 527, 3639.

Faustino Vieira H., Duarte-Cabral A, et al., *in prep*, *Cloud populations versus galactic environment in NGC 4689, NGC 628, NGC 1566 and NGC 4321.*

CO-AUTHOR

Gregg B., Calzetti D., Adamo A., et al., 2024, *Feedback in Emerging Extragalactic Star Clusters, FEAST: The Relation between 3.3 μm Polycyclic Aromatic Hydrocarbon Emission and Star Formation Rate Traced by Ionized Gas in NGC 628*, ApJ, 971, 115

Calzetti D., Adamo A., Linden S., et al., 2024, *JWST-FEAST: Feedback in Emerging extrAgalactic Star clusTers: Calibration of Star Formation Rates in the Mid-infrared with NGC 628*, ApJ, 971, 118

Pedrini A., Calzetti D., Adamo A., et al., 2024, *FEAST: Feedback in Emerging extragAlactic Star ClusTers: JWST Spots Polycyclic Aromatic Hydrocarbon Destruction in NGC 628 during the Emerging Phase of Star Formation*, ApJ, 971, 32

CONTENTS

List of Tables

List of Figures

ACKNOWLEDGEMENTS

"Space belongs to all of us."

MAE JEMISON

This work would not have been possible without the help, encouragement and heroic patience from my supervisory team. Ana Duarte Cabral has gone above and beyond as my supervisor, somehow always available for a meeting when I was desperately lost, and always with helpful advice and lighthearted banter. I would not have the confidence and resilience I have now as a scientist if it had not been for her. Ana is a fantastic researcher, and I am very honoured and proud to have been her student. Thank you for taking a chance on me. I also owe many thanks to Tim Davis, who always had little gems of wisdom[1] to hand out, my favourite of which being: "It's only Astrophysics, no one cares". He was always available for a quick chat about statistics or data reduction, which always saved me from spending many hours down a rabbit hole. Thank you both for the many hours of proof-reading, commenting, reference letter writing, encouragement and all-around support. I could not have asked for a better team.

Additionally, I thank my co-authors for their insightful comments and suggestions, and for the useful scientific discussions. I would particularly like to acknowledge Dario Colombo for his help with cloud extraction, Nicolas Peretto for his instrumental input in the early stages of developing the technique presented in this work, and Matthew Smith for running PPMAP for me so I would not have to. I also thank Miguel Querejeta, whose enthusiastic support and encyclopedic knowledge of M51 was greatly appreciated. The content of this Thesis was improved greatly from all of your contributions.

I acknowledge support from the Royal Society University Research Fellowship URF/R1/191609. The calculations performed here made use of the computing resources provided by the Royal

[1] Ha!

Society Research Grant RG150741.

This Thesis is based on observations made with the NASA/ESA Hubble Space Telescope, which is operated by the Association of Universities for Research in Astronomy, Inc. (Program 10452). DustPedia is a collaborative focused research project supported by the European Union under the Seventh Framework Programme (2007-2013) call (proposal no. 606847). The participating institutions are: Cardiff University, UK; National Observatory of Athens, Greece; Ghent University, Belgium; Université Paris Sud, France; National Institute for Astrophysics, Italy and CEA, France.

This research made use of `SCIMES`, a Python package to find relevant structures into dendrograms of molecular gas emission using the spectral clustering approach (Colombo et al., 2015). This work made use of `Astropy`[2]: a community-developed core Python package and an ecosystem of tools and resources for Astronomy (Astropy Collaboration et al., 2013, 2018, 2022), and `astrodendro`[3], a Python package to compute dendrograms of Astronomical data. The following Python libraries were instrumental to the data analysis performed in this work: `NumPy` (Harris et al., 2020), `Matplotlib` (Hunter, 2007), `SciPy` (Virtanen et al., 2020), and `seaborn` (Waskom, 2021).

[2]http://www.astropy.org
[3]http://www.dendrograms.org/

Para a minha família - não sei o que faria sem vocês.

Em memória da minha Avózinha,
Filomena de Ascensão Ornelas Vieira,
que muito me ensinou sobre paciência e resiliência.
Saudades e beijinhos.

DEDICATION

"E sentar-me um instante
Na beira da janela contra os astros" *

SOPHIA DE MELLO BREYNER ANDRESEN

I think I have always been ambitious, but never in little Lena's wildest dreams would she ever think she would end up being a professional Astronomer. This PhD has definitely been the most difficult, demanding and downright terrifying roller-coaster ride of my life. Of course, I wouldn't have been able to do this without the wonderful people that surrounded me during these 4 very hard years (which I will get to in a second), but I would like to state for the record that I am so incredibly proud of myself. I did it!

The environment at Cardiff has been nothing but welcoming, friendly, and filled with incredibly smart, funny and down-to-earth people. I've got to say I won't miss the single-pane windows, but I will miss the rest-frame breaks with the wildly off-tangent conversation topics, board game nights, pub Fridays, I-don't-want-to-work Mondays and of course, Cake Thursdays. Starting this PhD in 2020 was not fun, as you can well imagine, but it sure brought our PhD cohort together like nothing else[4]. Lottie, Carys (and honorary PhD student George), Andy, Jacob, Holly, Hidde, Hannah, Eva, Gethin, Luke, Patrick, Matt C., Matt L., Terri, Michael - I thoroughly enjoyed spending these last 4 years with everyone, and I hope we will cross paths again. Doing a PhD has given me a chance to travel around the world, and I will never forget the friendships I have made because of it. Kammy, Seamus, Ahmad (among many others), I'm glad to have met you.

I would like to particularly single out the surviving crew of the infamous office N/3.27: Andy, Jacob and, of course, Roger, our honorary member. Despite having to have two radiators pointed

* Translation: And sitting down for a moment / On the edge of the window against the stars
[4]Trauma bonding?

at me at all times in the winter, and some oozy ceiling architecture, I could not have asked for a better office. Playing cards every day with you guys brought me much joy, and was a much needed de-stresser. Of our official 160+ league games, plus many other unofficial ones with and without guests, I thoroughly enjoyed absolutely enraging Roger with my awe-inspiring ability to win all the time, watching Andy make some seriously dumb and yet incredibly funny decisions with his plays, and listening to Jacob say "sorry" approximately 15,678 times every game[5]. I also need to mention our after-work games of Carcassonne (with the addition of Luke), which were just as fun as they were infuriating. Without you guys, I could have probably written 4 more papers, 17 different observing proposals and a whole other thesis - but I wouldn't have had nearly as much fun.

I would also like to thank my academic twin, Eva, for always being a sympathetic ear and for making conferences some of the most outrageously fun moments of my life. Between ABBA conga lines, snorkeling in Vietnam, pool-side shots, the fanciest nightclub ever in Sweden, gossiping and Greek dancing, the infamous bus ride to Meteora, joining random pub quizzes in France, sharing hotel rooms and all-around getting way too drunk, I'm not sure we're good influences on each other, but we sure racked up some great stories. Perhaps my favourite memory of the last 4 years was running around Athens[6] after a conference with Eva, Kammy and Hannah, sitting down, watching the sunset, and getting serenaded some beautiful Greek song. I hope we can keep having more of these moments.

My lovely friends Carys and George who opened up their home to me so I wouldn't be homeless (twice!) - I don't deserve you or your fabulous gifts. Thank you both, as well as Hannah and Lottie, for always being down for a charity shop run, Twilight marathon, cute brunch get-together, pumpkin carving, afternoon tea, Shrek rave, nature hike, and for being the best friends someone could ask for. Lottie, I think one of the best decisions I made in my PhD was ask if you wanted to grab tea sometime. We supported each other through the hardships of a PhD, being technically homeless, and being women in Physics. I will forever treasure our book talks, adorable little Christmas meals, getting glammed up together, and coffee hang-outs. I am so thankful for our friendship which I am sure will last many, many more years.

[5]Not even getting shot with a nerf gun would stop him.
[6]Still can't believe I walked around in the Acropolis...

Last, but certainly not least, I would like to thank my family. Tenho, sem dúvida alguma, a melhor família do mundo inteiro. Obrigada por terem toda a fé em mim, e por nunca duvidarem do que eu sou capaz. Tal como qualquer família portuguesa, existe uma catrefada de Faustinos e Vieiras por aí, por isso vou agradecer assim: obrigada a todas as avós e avôs, tias e tios, primas e primos. A vida é mais colorida com vocês por perto. Quero falar, em particular, da minha avózinha Filomena. Passei muito da minha infância na casa da minha Avó, onde ela ensinou-me a cozinhar, a costurar e bordar, a ter paciência e orgulho no meu próprio trabalho. Tenho muitas saudades de si, Avózinha.

Sobretudo, tenho que agradecer aos meus pais, Paulo e Maribel, que muito sacrificaram por mim, mesmo quando eu não tinha maturidade suficiente para vos apreciar. Crescer como eu cresci foi uma alegria. Obrigado Pai, por me leres um livro todas as noites, e por continuares a alimentar o meu apetite por ler mesmo até agora. Obrigado por seres um brincalhão, e por estares sempre exatamente onde os teus filhos precisam de ti. Obrigado pelas paparocas deliciosas, e por fazeres sempre as vontadinhas da filhota. Obrigado, também, à minha Mãe, que sempre quis as melhores oportunidades para os seus filhos. Obrigado por me ensinares a ser uma pessoa responsável e capaz, e claro, por me ensinares a conseguir sempre os melhores descontos possíveis. Eu até pedia desculpa pela minha teimosia, mas quem sai aos seus não degenera, não é? Admiro-te muito, Mãe. Sinto-me muito afortunada por ser vossa filha; não podia ter pedido por melhores pais. Adoro-vos. Obrigada por tudo.

Não podia deixar de falar do meu irmãozinho, também. Rodrigo - seu pequenote grande - adoro-te muito. A maior alegria da minha vida é ser tua irmã, e tenho muita pena de só poder ver-te a crescer à distância. Estou muito orgulhosa, e de certeza que os pais também, do quão gentil, carinhoso, esperto e atentivo tu és. Obrigada por atenderes sempre os meus telefonemas a qualquer hora do dia, e por fazeres a minha vontade quando eu quero ver filmes ou simplesmente passar tempo juntos. Guigo, és e sempre serás o melhor presente que os pais alguma vez me deram.

Chapter 1

INTRODUCTION

"Scientists too seldom stress the enormity of our ignorance."

VERA RUBIN

1.1 BRIEF JOURNEY THROUGH THE HISTORY OF THE COSMOS

More than anything, what unites us humans is our innate sense of wonder and curiosity. Why do we exist? What is out there? What is our place in the Universe? This insatiable need to know naturally developed into one of the oldest disciplines of science: Astronomy. Derived from the Ancient Greek words *ástron* meaning stars and *nómos* meaning law, Astronomy sets out to study and understand the skies above us. Although tracking moon phases and cataloguing stars served a utilitarian purpose in timekeeping, navigation and farming, our ancestors could not help but imbue the cosmos with fantastical stories and myths. The Inuit believe the celestial sphere (*Qilak*) is the final home for souls of the departed. Ancient Egyptians thought that after death, the souls of their kings would ascend to the heavens and become the Morning Star[1]. The Ancient Greeks told stories of the nymph Callisto, follower of Artemis, who was transformed into a bear after a run-in with Zeus, and later elevated to the skies alongside her son Arcas, as the Ursa Major and Minor constellations.

Putting storytelling and myths aside, early Astronomers were also very interested in

[1]Which is not a star at all, but the planet Venus.

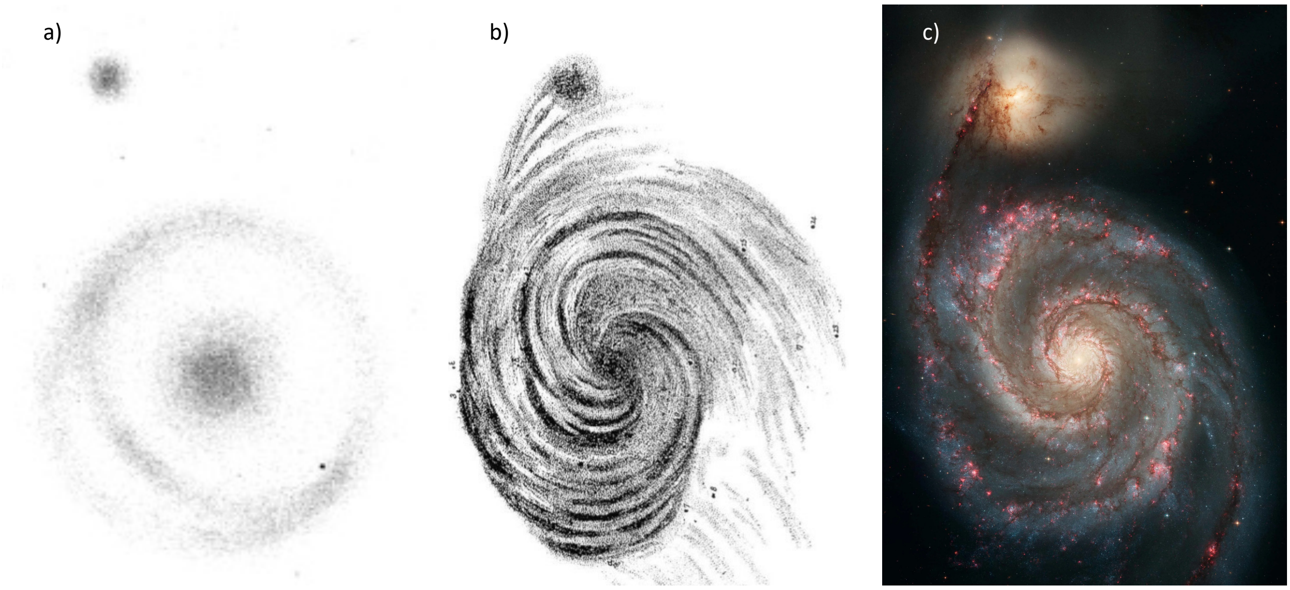

Figure 1.1 – ***a)*** Illustration of the M51 nebulae by William Herschel (Herschel, 1833). ***b)*** Sketch of M51 done by William Parsons in 1848, showcasing the spiral structure of the object (sourced from Steinicke, 2012). ***c)*** Composite image of M51 taken with the Hubble Space Telescope. Credit: S. Beckwith (STScI) Hubble Heritage Team, (STScI/AURA), ESA, NASA.

quantifying and cataloguing the skies above. Wanting to calculate the size of the known cosmos (at the time), the Ancient Greek mathematician Archimedes tried to estimate how many grains of sand the Universe could hold. To do so, he adopted the highly controversial heliocentric model, first proposed by Aristarchus of Samos, writing:

> *"His* [Aristarchus] *hypotheses are that the fixed stars and the sun remains unmoved, that the earth revolves about the sun in the circumference of a circle, the sun lying in the middle of the orbit".*
>
> *Heath & Aristarchus (1913)*

For the curious, Archimedes estimated that the Universe could not be any larger than a sphere 2 light years across, which held at most 10^{63} grains of sand of approximately 19 μm in size[2] (Heath & Archimedes, 1897). Our picture of the known cosmos remained rather fuzzy and confined to our Solar System, until one of the greatest inventions in the history of humankind: the telescope.

In 1750, Thomas Wright proposed that our Galaxy is composed of a flat layer of stars, and hypothesised that the faint cloudy spots in the skies (i.e. nebulae) could be other galaxies that are simply out of reach for the observational instruments of the time (Wright, 1750). A few years later, William Parsons was the first to resolve the spiral structure of the "faint nebula" M51,

[2] Of course making some oversimplified and frankly unsubstantiated assumptions, in true Astronomer fashion.

which we now know to be a grand-design spiral galaxy (Fig. 1.1, see Steinicke 2012). In fact, the existence of these faint "spiral nebulae" was a topic of major debate among astronomers, since it clashed with the anthropocentric view of the Universe at the time. It was not until 1912, with Henrietta Swan Leavitt's discovery of a new method to determine distances to objects using Cepheid variable stars (Leavitt & Pickering, 1912), that this debate could finally be put to rest. Using her technique, Edwin Hubble measured the distance to the Andromeda "nebula" to be 285 kpc, a distance far greater than any estimate of the size of our own Galaxy (Hubble, 1925). A logical conclusion then followed: the Milky Way is not alone in the Universe.

Since Hubble's discovery, our knowledge of the Universe has significantly expanded. Of course, we now know it is populated by a wealthy variety of galaxies with vastly different properties and morphology. We also know these are made up of stars, and the processes associated with their life-cycle are intrinsically tied to the evolution and growth of the host galaxy. Consequently, one of the keys to further our knowledge of the cosmos lies in understanding the relationship between stars, their birthplace (see Fig. 1.2), and the larger scale galactic context.

1.2 GALAXY FORMATION AND EVOLUTION

Observations of the cosmic microwave background (CMB) reveal that the very early, post-Big Bang Universe had very small density contrasts. This is of course in stark contrast with the present-day Universe, which we observe to be highly structured and complex, full of galaxies with wildly different characteristics. Attempting to reconcile these two states is at the forefront of cosmological studies of galaxy formation and evolution (e.g. Tacconi et al., 2020; Crain & van de Voort, 2023).

One such cosmological theory is the standard ΛCDM model, which describes a Universe composed of baryonic and dark[3] matter, as well as a theoretical dark energy, which is responsible for driving the accelerating expansion of the Universe (e.g. Planck Collaboration et al., 2016). The CMB is observed to have very small temperature fluctuations (order of $\sim 10^{-5}$), which are thought to be an imprint of the small density fluctuations in the early Universe during inflation (Guth, 1981). These fluctuations or perturbations eventually lead to matter over-densities, which over time accrete both dark and baryonic matter, forming the first galaxies. In a hierarchical assembly model, these first galaxies (and their dark matter haloes) eventually merge together to form larger galaxies (e.g. Wechsler & Tinker, 2018).

Numerous observations of galaxies across redshift have built a picture in which the rate of star formation peaked at redshift $z \approx 2$, steadily declining by a factor $10 - 15$ until the present-day Universe (e.g. Lilly et al., 1996; Madau & Dickinson, 2014). Although the literature is mostly in

[3]A form of matter that does not radiate (hence "dark"), and only interacts with other matter via gravity.

Figure 1.2 – The star cluster NGC 346 located in the Small Magellanic Cloud, as shown by the James Webb Space Telescope Near-Infrared Camera. Credit: NASA, ESA, CSA, O. C. Jones (UK ATC), G. De Marchi (ESTEC), M. Meixner (USRA), A. Pagan (STScI), N. Habel (USRA), L. Lenkić (USRA), L. E. U. Chu (NASA Ames).

good agreement on this, it is important to note that this result is not impervious to sample selection and completeness effects, as well as the exact methodology employed when deriving star formation rates and integrated stellar masses (Renzini & Peng, 2015). In fact, deriving a star formation history from a galaxy's integrated spectrum is not trivial, particularly at higher redshifts, as we cannot easily determine and disentangle the separate stellar populations that form the composite spectrum (e.g. Leja et al., 2017). This is made especially difficult given the degeneracy of some intrinsic galactic properties, which can have the same effect on a galaxy's spectrum. For example, older stellar populations, higher metallicity and dust attenuation can all redden the spectrum of a galaxy. In response, there has been a real push into improving stellar population synthesis models, which build on our knowledge of individual stellar spectra and stellar evolution (e.g. Conroy, 2013), to better fit and derive properties from galaxy spectra. Still, this knowledge is imperfect, and assumptions often have to be made, particularly when deriving a star formation rate from a galaxy's integrated light. One such assumption is the shape of the initial mass function (IMF), which describes how mass is distributed within a stellar population for a single star formation event, typically constrained with observations of very nearby Milky Way stellar populations. The IMF, among other things, dictates the ratio between hot, young stars which dominate a galaxy's light, and cooler, fainter stars which are the bulk of a galaxy's stellar mass (e.g. Gunawardhana et al., 2011; Jeřábková et al., 2018, and references therein). Typically, the IMF is assumed to be universal at all cosmic times and for all galaxies, which, if untrue, would have significant implications on the derived galactic properties across redshift (e.g. Madau & Dickinson, 2014).

Cutting-edge cosmological simulations provide an attractive method into testing theories of galaxy formation and evolution (for a review see Bertschinger, 1998; Naab & Ostriker, 2017; Crain & van de Voort, 2023), examples of which include `Illustris` (Genel et al., 2014), `EAGLE` (Crain et al., 2015), and `Auriga` (Grand et al., 2017). The sheer volume of these simulations forces the use of simplified "subgrid" models, despite increasing computational power and sophisticated modelling procedures. These subgrid models encompass the small-scale, unresolved physics that lead to certain large-scale, integrated effects. Namely, the processes behind the formation of stars, as well as the life-cycle of stars, and how the gas flows in and out of galaxies, are often implemented as subgrid models. This approach requires extreme caution, as just the implementation of different subgrid models can lead to different outcomes (e.g. Kim et al., 2014). For example, simply adopting a density threshold of ~ 0.1 cm^{-3} (Springel & Hernquist, 2003) above which star formation kickstarts, leads to very clumpy and unrealistic galactic discs (Somerville & Davé, 2015). It is thus important to calibrate these subgrid models with detailed and resolved observations of small-scale processes, therefore ensuring simulated galaxies closely resemble the characteristics of real, observed galaxies.

In conclusion, systematic observations of the gas and stars in galaxies in the local Universe are crucial in understanding how galaxies form and evolve throughout time, since they serve as constraints in cosmological models but can also help calibrate the assumptions made when interpreting higher-redshift observations.

1.3 THE INTERSTELLAR MEDIUM

Although the presence of molecular hydrogen (H_2) in outer space had already been theoretically predicted (e.g. Spitzer, 1949), it was not until 1970 that it was finally detected outside of the Solar System (Carruthers, 1970). Shortly after, Spitzer et al. (1974) observed H_2 in absorption towards nearby stars. Subsequent observations showed that the hydrogen molecule is ubiquitous in the interstellar medium (ISM; for a review see Spitzer & Jenkins, 1975). After the discovery of candidate protostars in the Orion Nebula (Becklin & Neugebauer, 1967; Kleinmann & Low, 1967), it was not long until astronomers recognised the strong relation between dense, H_2-rich clouds and star formation. It was quickly understood that since these molecular clouds seem to be the birthplaces of stars - and thus hold the initial conditions for star formation - it is very important to systematically catalogue and characterise their properties. This task is however made difficult by the physical attributes of the H_2 molecule itself, which prevent it from being easily observed in the conditions present within the cold, molecular ISM.

The H_2 molecule is composed of two hydrogen atoms which are linked by a covalent bond, in which electrons are shared between the two nuclei, making this molecule highly symmetric. Additionally, H_2 is a very light molecule, with a low moment of inertia and large rotational constant, which results in energy levels with wide spacing between them. Since H_2 is homonuclear, it has no permanent dipole moment, which arises when atoms have different electronegativity and thus there is an uneven distribution of charge. A dipole moment facilitates rotational transitions, given that by definition the molecule's centre of mass and centre of charge are not the same, making it easier for the molecule to rotate and subsequently radiate. Since H_2 is perfectly symmetric, these rotational dipole transitions are strongly forbidden, and instead we observe the quadrupole transitions ($\Delta J = \pm 2$, with J being the rotational quantum number; see Herzberg 1949), which have low transition probabilities. The first accessible transition of H_2 is therefore $J = 2 - 0$ for para-H_2 (nuclei have parallel spins), with an upper energy level of $E/k_B \approx 510\,\mathrm{K}$ above ground state, and the $J = 3 - 1$ transition for ortho-H_2 (antiparallel nuclear spin alignment), which corresponds to $E/k_B \approx 1015\,\mathrm{K}$ (Dabrowski, 1984). This means that, at the typical temperatures of molecular clouds ($T \lesssim 100\,\mathrm{K}$), H_2 is virtually invisible in emission. For a more in-depth review see Wakelam et al. (2017) and references therein.

1.3.1 CO as an observational tracer of the ISM

The ISM is not made up of just H_2. Heavier elements are fairly abundant (of the order $\sim 10^{-4}$ per hydrogen nucleon; Bolatto et al. 2013), particularly oxygen and carbon. Under moderate radiation field conditions and for solar metallicity, available carbon atoms will combine with oxygen to form carbon monoxide (CO)[4] in the ISM. Unlike H_2, CO is not symmetric, and thus does have a permanent dipole moment and the corresponding transitions. Its lowest rotational transition, $J = 1 - 0$ (hereafter CO(1-0)), sits at an energy level of only $E/k_B \approx 5.53\,\mathrm{K}$ above the ground state. Furthermore, because of the high abundance of CO, emitted photons are radiatively trapped (i.e. they are absorbed by nearby CO molecules before they can escape the region), which maintains the excitation of the $J = 1$ energy level, and so the CO(1-0) line becomes optically thick quickly. This all leads to bright lines that are easily detected and mapped at a wavelength of 2.6 mm for CO(1-0), which also coincides with a reasonably transparent atmospheric window, making it accessible to ground-based facilities. Furthermore, low-J transitions of the isotopes ^{13}CO and C^{18}O, as well as other low-J transitions of CO, are also sufficiently bright to be observed (e.g. Barnes et al., 2015; Rigby et al., 2016; Jiménez-Donaire et al., 2019; den Brok et al., 2022), which are optically thinner, and thus complement the information derived from ^{12}CO observations. Altogether, these factors have made CO a prime molecular tracer of the cold ISM, where star formation originates.

The first outer space detection of CO was in 1970, towards the Orion nebula (Wilson et al., 1970), and a short few years later, CO was already being detected outside of the Galaxy (Rickard et al., 1975; Solomon & de Zafra, 1975). Since then, there has been a real effort in studying the molecular ISM via observations of CO, with surveys of molecular clouds both in the Milky Way (e.g. Solomon et al., 1972; Scoville & Solomon, 1975, being among the first) and in other galaxies (Vogel et al., 1987; Wilson et al., 1988).

Since we are interested in CO as a tracer of H_2 (i.e. the cold molecular ISM), it is helpful to define a conversion factor between the two:

$$N_{\mathrm{mol}} = X_{\mathrm{CO}}\, W_{\mathrm{CO}}, \tag{1.1}$$

where N_{mol} is the molecular gas column density in cm^{-2}, X_{CO} is the CO-to-H_2 conversion factor in cm^{-2} (K km s^{-1})$^{-1}$, and W_{CO} is the observed integrated CO line intensity in K km s^{-1}. To instead derive molecular gas mass ($\mathrm{M_{mol}}$), we can write:

$$\mathrm{M_{mol}} = \alpha_{\mathrm{CO}}\, L_{\mathrm{CO}}, \tag{1.2}$$

[4] Unless otherwise stated, here CO always refers to ^{12}C^{16}O.

with M_{mol} in $M_\odot$, L_{CO} in $\mathrm{K\,km\,s^{-1}\,pc^2}$, and α_{CO} being another form of the CO-to-H_2 conversion factor in units of $M_\odot\,(\mathrm{K\,km\,s^{-1}\,pc^2})^{-1}$. This X_{CO} is, of course, an empirically derived factor. The "standard" value of X_{CO} that is often adopted, $X_{CO,MW} = 2 \times 10^{20}\ \mathrm{cm^{-2}\,(K\,km\,s^{-1})^{-1}}$, was determined in the disk of the Milky Way from various methods (for an in-depth review on this topic see Bolatto et al. 2013). However, many studies have found different X_{CO} values departing from this Milky Way standard, suggesting that there might be galaxy-to-galaxy variations, and even environmental variations within a galaxy (e.g. Guélin et al., 1995; Sandstrom et al., 2013; Gong et al., 2020).

The underlying cause of the observed variations of X_{CO} values is the fact that CO does not always perfectly trace H_2 (neglecting systematic errors). Firstly, given that CO(1-0) is optically thick, it will saturate after it reaches a certain column density, no longer tracing the remaining molecular gas (e.g. Lombardi et al., 2006). Furthermore, the CO(1-0) line intensity depends on the column but also the temperature of CO; therefore higher temperatures can lead to larger CO intensities for a given amount of H_2, and thus introduce variations in X_{CO} (e.g. Narayanan et al., 2012). Additionally, the CO molecule is easily photodissociated; therefore for CO to survive, it requires dust to provide a shielding layer from UV radiation. On the other hand, H_2 is a self-shielding molecule, meaning that within a region, the outer layer of H_2 protects the inner layers from dissociating UV photons by absorbing them and becoming optically thick. It follows that in low-metallicity environments, where there is less dust given the lower abundance of metals, the amount of CO decreases significantly (as it retreats deeper into the region), unlike H_2 whose column is roughly independent of metallicity. This naturally leads to much higher values of X_{CO} measured for lower-metallicity systems (see Bolatto et al., 2013, and references therein), to account for this "CO-dark" or "CO-faint" molecular gas (Planck Collaboration et al., 2011). Furthermore, in cold regions with high column, CO can freeze out onto dust grains and form ices (Bergin et al., 1995), again affecting the abundance of CO relative to H_2.

Still, under moderate radiation and for column densities above $1 - 3 \times 10^{21}\,\mathrm{cm^{-2}}$ (where most of the available carbon in the ISM is within CO, Visser et al. 2009), CO is an adequate tracer of the molecular ISM. Additionally, there has been a real effort to calibrate X_{CO} as a function of metallicity to more realistically trace H_2 (e.g. Wolfire et al., 2010; Sun et al., 2022). In conclusion, CO with its various low-J transitions, as well as its isotopes, remains a workhorse of ISM and star formation studies.

1.3.2 Dust as an observational tracer of the ISM

Many of the Aboriginal Nations in Australia told stories of an Emu in the sky (Fig. 1.3) – a "dark constellation" next to the Southern Cross. In the 18th century, William Herschel also

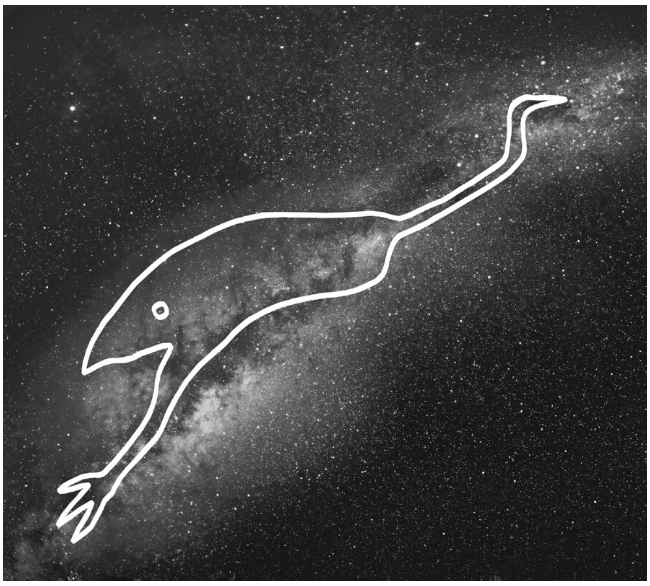

Figure 1.3 – The Australian Aboriginal "Emu in the Sky" or "Dark Emu" constellation, composed of dusty dark clouds against the glow of the Milky Way. Image credit: Noon & De Napoli (2022), sourced from thamesandhudson.com.au.

wrote about a "hole" or a dark patch in the sky towards the Scorpius constellation, where no stars were visible (Herschel, 1785). Edward Barnard noted the spatial correlation between these dark clouds and bright starry nebulae after creating the first comprehensive photographic catalogue of such objects (Barnard, 1927). The first clue as to what these dark nebulae might be came from Wilhelm Struve in 1847, after he found a decrease of stellar density with distance from the Sun, which could be explained by stellar light being absorbed by some interstellar material (i.e. dust, Struve 1847). Trumpler (1930) supplied the first concrete evidence of dust in the ISM, after noticing a discrepancy between different methods of determining distances to stars, which he attributed to selective extinction by dust particles. In the 1970's, with the advent of space telescopes, the first observations of the thermal emission of heated dust grains were made (e.g. Andriesse, 1978, see also Whittet, 2022 for a review). This all leads to the confirmation that these dark patches in the sky are not empty after all, but filled with dust grains and cold dense gas.

Interstellar dust is thought to originate in the ejecta of asymptotic giant branch stars and of core-collapse supernovae (for a summary see Galliano et al., 2018), and is now known to be a vital component of the ISM, even though it constitutes only $\simeq 0.1\%$ of the baryonic mass in galaxies (e.g. Bohlin et al., 1978). Depletion measurements of the ISM suggest that dust is mostly composed of heavy elements such as O, C, Mg, Si and Fe (e.g. Jenkins, 2009), of varying sizes (e.g. Mathis et al., 1977; Kim et al., 1994).

Dust particles play a critical role in ISM physics through their ability to scatter, absorb and

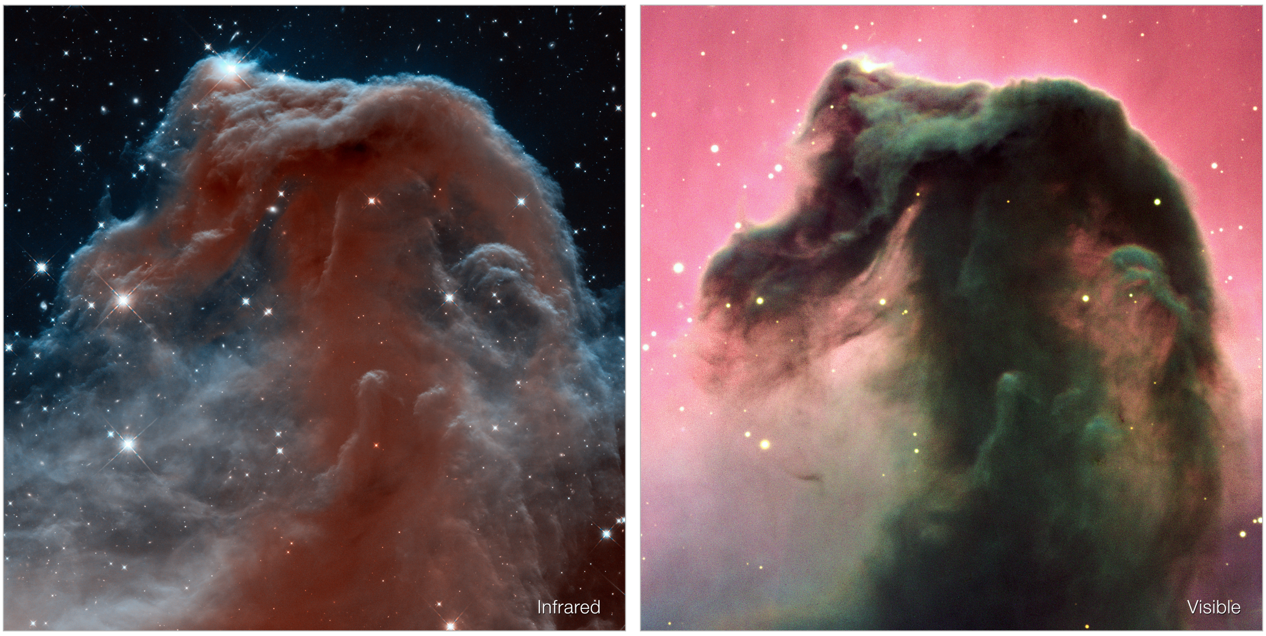

Figure 1.4 – The Horsehead Nebula as seen in the (near-)infrared (*left*) by the Hubble Space Telescope, and in the optical (*right*) by the Very Large Telescope. Credit: NASA, ESA, and the Hubble Heritage Team (AURA/STScI); ESO.

re-emit starlight. It is estimated that about half of the stellar light ever emitted in the Universe has been absorbed by dust (Puget et al., 1996). Dust is responsible for heating the gas in photodissociation regions via the photoelectic effect (Draine, 1978), and also for dissipating the energy generated when the very dense cores in molecular clouds undergo gravitational collapse prior to forming stars. Consequently, dust provides cooling and heating mechanisms in the ISM, which can be integral to the process of star formation. Finally, dust grains act as a catalyst in the formation of H_2 (e.g. van de Hulst, 1946; Hollenbach & Salpeter, 1971). Once H atoms attach themselves to dust grain surfaces, they undergo migration until they combine with other surface H atoms, releasing the excess binding energy of this reaction into the grain lattice, and the resulting H_2 molecule is ejected from the dust grain (e.g. Wakelam et al., 2017). Without interstellar dust, the formation of H_2 is not efficient enough to account for its observed gas-phase abundance.

Dust and gas are typically assumed to be well-mixed within the ISM (e.g. Knapp et al., 1973), and thus dust can be used as a gas tracer (e.g. Hildebrand, 1983; Eales et al., 2012) such that:

$$M_{\rm gas} = M_{\rm dust}/\delta_{\rm DGR}, \tag{1.3}$$

where $M_{\rm gas}$ is the total gas mass (i.e. atomic and molecular, $M_{\rm gas} = M_{\rm HI} + M_{\rm H_2}$), $M_{\rm dust}$ the dust mass, and $\delta_{\rm DGR}$ the dust-to-gas mass ratio. Under normal conditions (i.e. moderate interstellar radiation fields and solar metallicity), $\delta_{\rm DGR}$ is often assumed to be around 1% (e.g. Bohlin et al., 1978; Sandstrom et al., 2013). There are, however, some variations particularly towards environments with low metallicity (e.g. Smith et al., 2016; Giannetti et al., 2017; Aniano et al., 2020).

Dust grains absorb stellar light in the optical-UV part of the spectrum, and re-emit this radiation in the infrared (IR). Therefore, at different wavelength regimes, dust provides different insights into the structures of interstellar clouds, as is beautifully shown in Fig. 1.4. We can quantify the change of the light intensity (I_λ) of a given wavelength λ as it interacts with interstellar dust via the radiative transfer equation (e.g. Spitzer, 1998):

$$\frac{{\rm d}I_\lambda}{{\rm d}s}(s) = -\alpha_\lambda(s)\, I_\lambda(s) + j_\lambda(s), \tag{1.4}$$

assuming the photons are travelling along a linear path s. In this equation, $\alpha_\lambda(s)$ is the extinction coefficient[5] along the line-of-sight and $j_\lambda(s)$ is the emission coefficient. We can define a source function, $J_\lambda(s)$, as a measure of how the medium re-emits the radiation it absorbed, such that $J_\lambda(s) = j_\lambda(s)/\alpha_\lambda(s)$. Additionally, we can introduce the concept of optical depth, τ_λ, which is the integrated opacity along the path: ${\rm d}\tau_\lambda = \alpha_\lambda(s){\rm d}s$. These lead to a simplified version of Eq. 1.4:

$$\frac{{\rm d}I_\lambda}{{\rm d}\tau_\nu}(s) = -I_\lambda(s) + J_\lambda(s), \tag{1.5}$$

which has the general solution:

$$I_\lambda = I_\lambda(0)\, e^{-\tau_\lambda} + \int_0^{\tau_\lambda} e^{-(\tau_\lambda - \tau'_\lambda)}\, J_\lambda(\tau'_\lambda)\, {\rm d}\tau'_\lambda. \tag{1.6}$$

Here, $I_\lambda(0)$ represents the value of the intensity I_λ at the emitting source (i.e. where $s = 0$). Assuming that the source function does not depend on the optical depth, we can write that:

$$I_\lambda = I_\lambda(0)\, e^{-\tau_\lambda} + J_\lambda \left(1 - e^{-\tau_\lambda}\right). \tag{1.7}$$

Equation 1.7 states how the propagation of stellar radiation is affected by the emission, as well as the absorption and scattering (i.e. extinction) caused by dust grains in the ISM. The following sub-sections divide this equation into its emission and extinction components, and demonstrate how this can be used as an observational tracer of the cold molecular ISM.

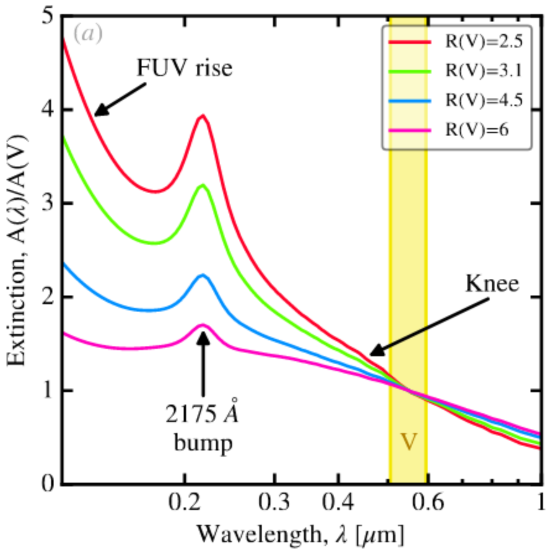

Figure 1.5 – Extinction curves for the Milky Way, for different visual-to-selective extinction ratios, $R(V)$, taken from Galliano (2022). The V-band (centred at $\sim 0.55\,\mu$m) is highlighted in yellow.

1.3.2.1 Dust in extinction

It is possible to extract the extinction-only component of the radiative transfer equation (Eq. 1.7), by assuming any emission is negligible:

$$I_\lambda \approx I_\lambda(0)\, e^{-\tau_\lambda}. \tag{1.8}$$

Effectively, Eq. 1.8 is implying that all of the observed light is being extincted, or in other words, that all the light has to travel through an absorbing/scattering dust screen that sits between the emitting source and the observer (i.e. a foreground screen, Holmberg 1958). Optical observations of edge-on galaxies, for example, show dark dust lanes within the galactic plane, showcasing that this foreground screen assumption is an oversimplification (see Calzetti, 2001, and references therein). An alternative method is outlined and discussed in Chapter 2. Nevertheless, we can see from Eq. 1.8 that the strength of the dust extinction is directly proportional to the dust optical depth (which is in turn proportional to the column density of dust), and independent of the temperature along the line-of-sight.

Early studies of dust were observations of its extinction effect on visible light, and thus often used the magnitude system[6]. For a given wavelength λ, the magnitude of a star, $m(\lambda)$, is:

$$m(\lambda) = -2.5 \log \left(\frac{F(\lambda)}{F_0(\lambda)} \right), \tag{1.9}$$

[5] Here the extinction coefficient is the sum of the absorption and scattering coefficients: $\alpha = \alpha_{\rm abs} + \alpha_{\rm sca}$.
[6] An Ancient Greek, naked-eye classification system, where larger magnitudes denote fainter stars.

where $F(\lambda)$ is the flux of the star, and $F_0(\lambda)$ is the reference flux of the photometric filter used (i.e. the calibration zero-point). The total extinction, $A(\lambda)$, can then be calculated by comparing the observed magnitude (or flux) of an object affected by extinction, against the intrinsic magnitude (or flux) of said object:

$$A(\lambda) = m_{obs}(\lambda) - m_{int}(\lambda) = -2.5 \log \left(\frac{F_{int}(\lambda)}{F_{obs}(\lambda)} \right). \tag{1.10}$$

This total extinction can be directly related to the dust optical depth through: $A(\lambda) = 1.086\, \tau_\lambda$.

Equation 1.10 then allows us to build what is called an "extinction curve", which measures the wavelength dependency of dust extinction (shown in Fig. 1.5). Originally, this was done via the pair method (Stecher, 1965), where you would compare observations of two stars of the same spectral type, one affected by extinction, one not. The differences in the stars' spectrum would then be extrapolated into an extinction curve. Knowing the spectral type of an observed star, you could instead compare its spectrum with a modelled spectral energy distribution (SED). This pair method is often also called colour-excess or stellar reddening (e.g. Kahre et al., 2018; Barrera-Ballesteros et al., 2020), and can be defined via:

$$E(\lambda - \lambda_0) = A(\lambda) - A(\lambda_0), \tag{1.11}$$

where $E(\lambda - \lambda_0)$ is the colour-excess between the observed colour of a star at a wavelength λ and its intrinsic colour at a reference λ_0. By definition, $E(\lambda - \lambda_0)$ is always positive since $\lambda_0 < \lambda$, and extinction always increases towards shorter wavelengths. However, these colour-based techniques suffer from some limitations, since they rely on resolving stars through obscuring dust as well as accurately identifying spectral types, which becomes increasingly difficult the poorer the spatial resolution (i.e. the further the distance). Still, by carefully studying extinction curves, it was found that in the visible light regime: $A(\lambda) \propto \lambda^{-1}$ (e.g. Stebbins et al., 1939). This implies the existence of "large" dust grains of sizes comparable to the wavelengths of visible light ($\sim 0.1\,\mu$m, e.g. Kim et al., 1994; Li, 2005; Whittet, 2022).

1.3.2.2 Dust in emission

Once dust grains absorb photons, they must release this energy to return to a steady state. van de Hulst (1946) predicted that this release of energy would be in the form of thermal emission. In fact, for the cold temperatures characteristic of molecular clouds (T $\sim 5 - 20$ K), dust emission is very bright at far-infrared (FIR) to submillimetre (submm) wavelengths. In this wavelength regime, the emission is dominated by the large dust grains ($\sim 0.1\,\mu$m) that are responsible for visible extinction, as shown in Fig. 1.6. These large grains are expected to be in

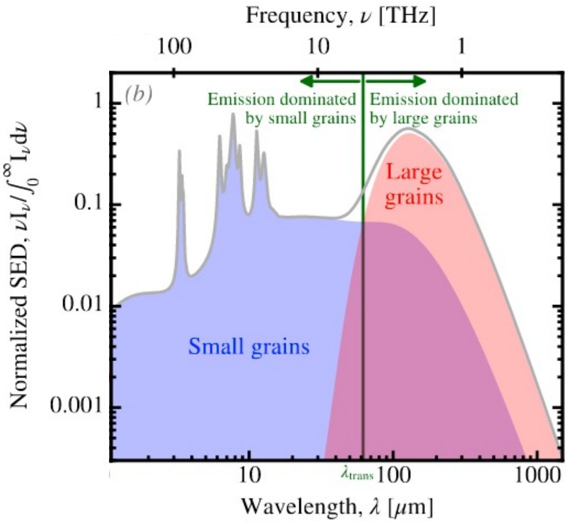

Figure 1.6 – Example spectral energy distribution (SED) of dust emission in the infrared-submillimetre wavelength regime, taken and slightly modified from Galliano (2022).

thermal equilibrium, since momentary (or stochastic) grain heating via single photon absorption should be negligible for these grain sizes (e.g. Whittet, 2022).

In the FIR part of the spectrum, we can also generally assume optically thin conditions, since the majority of the emitting dust grains have sizes much smaller than the FIR/submm wavelengths in question (e.g. Casey, 2012). Thus $\tau_\lambda \ll 1$ and $e^{-\tau_\lambda} \simeq 1 - \tau_\lambda$. Furthermore, in local thermal equilibrium conditions, the source function J_λ can be approximated to a blackbody, described by the Planck function:

$$B_\lambda(T) = \frac{2hc^2}{\lambda^5} \frac{1}{e^{hc/\lambda k_B T} - 1}, \tag{1.12}$$

where h is the Planck constant, c is the speed of light, k_B is the Boltzmann constant, and T is the temperature of the dust. With this information, we can write the emission-only component of Eq. 1.7, since extinction is negligible in this regime:

$$I_\lambda \approx B_\lambda(T)\, \tau_\lambda. \tag{1.13}$$

It is also possible to relate the dust optical depth to dust mass surface densities, $\Sigma_{\rm dust}$, through a dust mass absorption coefficient (Hildebrand, 1983), such that

$$\tau_\lambda = \kappa_\lambda \, \Sigma_{\rm dust}. \tag{1.14}$$

This absorption coefficient, κ_λ, can be described through a power-law:

$$\kappa_\lambda = \kappa_0 \left(\frac{\lambda_0}{\lambda}\right)^\beta, \tag{1.15}$$

where κ_0 is the dust mass absorption coefficient at some reference wavelength λ_0, and β is the dust emissivity spectral index. It is important to note that, despite the community's best efforts, κ_λ is far from being a constrained quantity, with estimates spanning orders of magnitude (Clark et al., 2019). This is because κ_λ is a quantity that tries to describe the dust population that causes the observed emissivity, and thus models with different combinations of grain sizes, chemical composition, morphology, etc., will give vastly different values of κ_λ. The β index controls the slope of the FIR curve at longer wavelengths (i.e. the Rayleigh-Jeans tail), and in the literature it often ranges between $1-2$ (Hildebrand, 1983), although recent work argues for a wider range, as well as potential environmental dependencies (e.g. Smith et al., 2012; Planck Collaboration et al., 2014).

Substituting Eq. 1.14 into Eq. 1.13 gives an expression which relates the observed intensity of a source to its dust temperature and mass surface density:

$$I_\lambda \approx B_\lambda(T)\, \kappa_\lambda\, \Sigma_{\rm dust}, \tag{1.16}$$

with I_λ and $B_\lambda(T)$ both in Jy units, κ_λ in $\mathrm{pc^2\, M_\odot^{-1}}$, and $\Sigma_{\rm dust}$ in $\mathrm{M_\odot pc^{-2}}$.

As is evident from Eq. 1.16, dust emission is dependent not only on the amount of dust along the line-of-sight, but also on the temperature of the dust, unlike dust extinction which is only affected by the column of dust. This temperature dependency complicates reliably retrieving dust masses from the observed radiation with simple, single-temperature modelling, since you may have temperature variations along the line-of-sight, and you may also have warmer dust (i.e. smaller grains) dominating the observed emission within the beam, leading to an underestimation of the dust mass (e.g. Stamatellos & Whitworth, 2003; Ysard et al., 2012).

1.4 MOLECULAR CLOUDS AND STAR FORMATION

Early observations of CO in the Galaxy (and in nearby galaxies) revealed spatially distinct structures in emission[7]. These were dubbed "molecular clouds" (MCs), with the term "giant molecular cloud" (GMC) being first used by Solomon & Edmunds (1980) for clouds with H_2 masses (converted from CO) higher than $10^5\,\mathrm{M_\odot}$, with typical densities of $n_H \sim 100\ \mathrm{cm^{-3}}$ and sizes of $\sim 50-100$ pc (Solomon et al., 1987). As was already mentioned, cross-correlations

[7]These structures and their boundaries are of course a product of resolution, sensitivity, and specific line tracer used, among other things.

between GMCs and signposts of star formation (e.g. young OB associations and H II regions[8]) revealed that star formation occurs within MCs (Blitz & Thaddeus, 1980). Since the cycle of baryonic matter in the Universe is intrinsically tied to the process of transforming gas into stars (e.g. McKee & Ostriker, 2007), and since stars form within MCs, it is thus imperative to understand the properties of clouds (i.e. mass, size, velocity dispersion, morphology), and how they may vary depending on the local galactic context.

1.4.1 Star formation: an inefficient process

The virial theorem describes a gravitationally bound system that is stable and in equilibrium:

$$2K + U = 0, \tag{1.17}$$

where K is the kinetic energy and U the gravitational potential energy. It naturally follows that a system will undergo collapse if the kinetic energy is not enough to balance out the self-binding potential energy, i.e. $2K < |U|$. A useful quantity is the virial parameter, $\alpha_{\rm vir}$, which is simply $\alpha_{\rm vir} = 2K/U$, and thus a cloud is gravitationally unstable if $\alpha_{\rm vir} < 1$. The potential energy of a uniform density sphere of gas can be written as:

$$U = -\frac{3}{5}\frac{GM^2}{R}, \tag{1.18}$$

with G being the gravitational constant, and M and R the mass and radius, respectively, of the system. The total kinetic energy of a system is given by:

$$K = \frac{3}{2}\frac{M}{\mu\, m_H} k_B T, \tag{1.19}$$

where μ is the mean molecular weight, and m_H the mass of a hydrogen atom. Equations 1.18 and 1.19 can therefore be used to write the condition under which systems such as MCs collapse (under no other influences):

$$\frac{3\, M k_B T}{\mu\, m_H} < \frac{3}{5}\frac{GM^2}{R}. \tag{1.20}$$

The radius of a cloud can be described through:

$$R = \left(\frac{3}{4}\frac{M}{\pi\,\rho_0}\right)^{1/3}, \tag{1.21}$$

where ρ_0 is the initial density of the cloud, assuming the cloud is a sphere of constant density.

[8]Young and massive stars release energetic photons which ionise the surrounding gas, creating H II regions.

Rearranging Eq. 1.20 for M, and substituting in Eq. 1.21, gives:

$$M_J \simeq \left(\frac{5\, k_B\, T}{G\, \mu\, m_H} \right)^{3/2} \left(\frac{3}{4\pi\, \rho_0} \right)^{1/2}. \tag{1.22}$$

This expression describes the *Jeans mass*, M_J: a cloud will be gravitationally unstable if $M > M_J$ (Jeans, 1902). In a similar manner, one can also determine the Jeans length, R_J:

$$R_J \simeq \left(\frac{15\, k_B\, T}{4\pi\, G\, \mu\, m_H\, \rho_0} \right)^{1/2}. \tag{1.23}$$

Although useful quantities, it is important to note that assuming a cloud collapses simply when it surpasses the Jeans mass or length is an oversimplication. Realistically, there are other elements in play, such as external pressure, magnetic fields, turbulence, rotation, and the fact that MCs are not perfect spheres of constant density.

In ideal conditions (i.e. under the influence of just self-gravity), a cloud would undergo a free-fall collapse. This would happen within a free-fall time, $t_{\rm ff}$:

$$t_{\rm ff} = \left(\frac{3\, \pi}{32\, G\, \rho_0} \right)^{1/2}. \tag{1.24}$$

As a cloud is collapsing, its density increases dramatically, becoming more opaque, which traps radiation within the cloud. This eventually leads to heating and an increase of thermal pressure, by which point a "protostar" forms (e.g. Larson, 2003). Most protostars seem to form in clusters (Lada & Lada, 2003), implying a more dynamical scenario in which individual dense regions within MCs fragment and collapse locally, rather than the whole cloud collapsing equally and generating one singular protostar (e.g. McKee & Ostriker, 2007; Ballesteros-Paredes et al., 2011).

One can describe the rate at which stars form within a free-fall time through:

$$\mathrm{SFR} = \epsilon_{\rm ff}\, \frac{M}{t_{\rm ff}}, \tag{1.25}$$

where SFR is the star formation rate, and $\epsilon_{\rm ff}$ is the efficiency of the star formation process per free-fall time (Krumholz & McKee, 2005). If a self-gravitating cloud is transforming all of its gas into stars within a $t_{\rm ff}$ (i.e. $\epsilon_{\rm ff} = 100\%$), then for a typical cloud with $M \sim 10^6$ M$_\odot$ collapsing under $t_{\rm ff} \sim 4$ Myr, we would expect a SFR of ~ 250 M$_\odot$ yr^{-1}. This is in clear contradiction with observed SFRs which are orders of magnitude lower, implying that $\epsilon_{\rm ff}$ is of the order of a few percent on cloud- and galactic-scales (Zuckerman & Evans, 1974; Krumholz & McKee, 2005, and references therein). However, on the smaller scales of dense clumps and cores within clouds, this efficiency can rise to $20 - 40\%$ (Alves et al., 2007; André et al., 2010; Könyves et al., 2015). There are several methods to measure SFRs, the most direct of which being the counting of young stellar objects of a certain age, which gets increasingly difficult the poorer the resolution of the observations. Other methods include measuring the far-ultraviolet (FUV) continuum emission, which is thought to be emitted from young and massive stars (10 – 100 Myr; e.g. Kennicutt 1998), or from emission line tracers such as Hα (∼656 nm), emitted from 3 – 10 Myr massive O- and B- type stars (e.g. Kennicutt & Evans, 2012). These approaches require constant calibration with stellar track models, extinction correction, and careful removal of non-star-forming contributions (e.g. heating from old stars; for a review see Calzetti, 2013).

One can also define a depletion time, $t_{\rm dep}$, as the time it takes for all the available fuel (i.e. molecular gas) to be consumed and transformed into stars, assuming a constant SFR (e.g. Young et al., 1986). This can be expressed as:

$$t_{\rm dep} = \frac{\Sigma_{\rm mol}}{\Sigma_{\rm SFR}}, \tag{1.26}$$

where $\Sigma_{\rm mol}$ is the molecular gas surface density, and $\Sigma_{\rm SFR}$ the SFR surface density. Observed SFRs (e.g. $\sim 3\,{\rm M_\odot yr^{-1}}$ in the Milky Way; McKee & Williams, 1997), imply long depletion times on galaxy-scales. In fact, the typical depletion time of molecular gas in nearby disc galaxies is $1-2$ Gyr (e.g. Wong & Blitz, 2002; Bigiel et al., 2011; Saintonge & Catinella, 2022). These are much larger timescales than the expected cloud lifetimes if they were freely collapsing under self-gravity (~ 4 Myr; e.g. Zuckerman & Evans, 1974).

Evidently, some other mechanism (or mechanisms) must be acting against the self-gravity of clouds, resulting in the observed inefficiency of the star formation process on cloud-scales, despite the available fuel. One of the main theories is that magnetic fields stabilise clouds, providing support against free-fall collapse (e.g. Mouschovias, 1976; Mouschovias & Spitzer, 1976). Ambipolar diffusion, a process which allows neutral particles within a cloud (i.e. H_2) to uncouple from the magnetic field, leads MCs to still be able to gradually collapse albeit at a much slower rate ($\gg t_{\rm ff}$, e.g. Zweibel, 2015; Machida et al., 2018). However, various observations of magnetic field strengths towards star-forming regions suggest that magnetic fields alone are not strong enough to prevent cloud collapse (e.g. Crutcher, 1999; Padoan et al., 2004; Crutcher et al., 2010).

The competing theory is that turbulence provides the necessary support against MC self-gravity (Stone et al., 1998; Mac Low, 1999; Klessen et al., 2000). The velocity dispersions of MCs in both the Milky Way and nearby galaxies have been observed to be highly supersonic ($1-10$ km s^{-1}, e.g. Engargiola et al., 2003; Rosolowsky & Blitz, 2005; Ballesteros-Paredes et al., 2011), which are much higher than what would be expected from just the thermal motions of molecules within MCs (~ 0.25 km s^{-1} for H_2 at T=15 K). Larson (1981) attributed these non-thermal motions to some internal turbulence which stabilises clouds against collapse (see also Krumholz & McKee, 2005, and references therein). However, supersonic turbulence is expected to disperse within a $t_{\rm ff}$, meaning that turbulence must be continuously replenished in clouds by either internal (stellar feedback, for a review see Chevance et al. 2020) or external (galactic dynamics) processes (e.g. McKee & Ostriker, 2007).

1.4.2 Are molecular clouds universal structures?

The influential work of Larson (1981) gave rise to what is now referred to as "Larson's relations", where scaling relationships between cloud properties were established based on Galactic CO data available at the time. Larson found a relation between cloud size and velocity dispersion (i.e. the size-linewidth relation), between linewidth and mass, and between cloud size and mass. Focusing on Larson's third empirical "law" - the mass-size relation[9] - where

$$\Sigma_{\rm mol} \propto R^{-0.1}, \tag{1.27}$$

with $\Sigma_{\rm mol}$ being the molecular gas surface density of a cloud, and R the size of said cloud. This is often also expressed as $M \propto R^{c_2}$, with $c_2 \approx 2$ (Lombardi et al., 2010). This relation essentially implies that MCs are universal structures, with uniform $\Sigma_{\rm mol}$. Although early observations seemed to validate this (e.g. Solomon et al., 1987; Heyer & Brunt, 2004; Bolatto et al., 2008; Lombardi et al., 2010), it has been put into question whether Larson's third relation is not simply a selection effect due to incompleteness of cloud samples (e.g. Kegel, 1989). Indeed, when re-examining Larson's relations, Heyer et al. (2009) found that poor sensitivity led to the cloud sample being biased towards the brightest objects, resulting in a limited range of observed surface densities (see also Scalo, 1990; Ballesteros-Paredes et al., 2011). Furthermore, numerical work has shown that this mass-size relation is a by-product of detection limits of the specific line tracer used (e.g. Vázquez-Semadeni et al., 1997; Ballesteros-Paredes & Mac Low, 2002).

If Larson's relations are valid, clouds should be turbulent, generally in virial equilibrium (i.e. gravitationally bound), and have uniform surface density (Larson, 1981; Solomon et al., 1987; Heyer & Brunt, 2004). Once investigations on these scaling relations extended towards other environments unlike the Milky Way disc (and Local Group systems), with much higher sensitivity, resolution and completeness (and with other tracers), these relations started to show significant variations (e.g. Oka et al., 2001; Rosolowsky & Blitz, 2005; Heyer et al., 2009; Colombo et al., 2014a; Henshaw et al., 2016; Traficante et al., 2018; Sun et al., 2020b; Rosolowsky et al., 2021). Additionally, Vázquez-Semadeni et al. (2007) showed that a gravitationally stable cloud and a cloud actively undergoing collapse could be observed to have identical virial parameters,

[9]Originally, this was expressed in terms of volume density, n, such that $n \propto R^{-1.1}$, and $\Sigma = n\,R$.

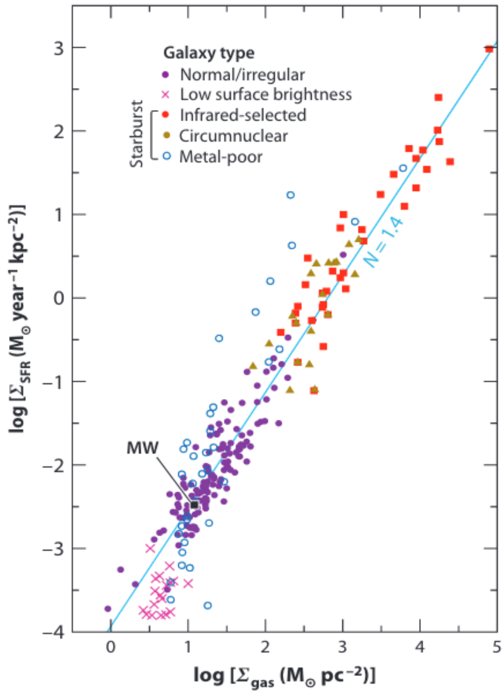

Figure 1.7 – The galaxy-scale Kennicutt-Schmidt law, relating the integrated star formation rate ($\Sigma_{\rm SFR}$) to the integrated gas surface density ($\Sigma_{\rm gas}$) for a sample of galaxies. A power-law with index $N = 1.4$ is shown as the blue line. Figure taken from Kennicutt & Evans (2012).

thus undermining the physical underpinnings of Larson's relations (i.e. that clouds are mostly in equilibrium). Consequently, Vázquez-Semadeni et al. (2009) argue that the formation of stars involves a more chaotic, dynamic collapse of clouds, in which dense clumps contract locally as the encompassing cloud is collapsing, generating the observed supersonic, non-thermal motions (see also Ballesteros-Paredes et al., 2011; Vázquez-Semadeni et al., 2019).

All of this highlights just how important systematic, high-resolution and high-sensitivity surveys of molecular clouds are to build our understanding of star formation. Over the years, there has been a multitude of such surveys both in our Galaxy and in other galaxies (e.g. Koda et al., 2009; Gratier et al., 2010; Hughes et al., 2013; Colombo et al., 2014a; Rosolowsky et al., 2021; Duarte-Cabral et al., 2021; Colombo et al., 2022; Choi et al., 2023; Koda et al., 2023), which have shown the diversity of molecular cloud properties across galaxies, as well as galactic environments. In fact, properties of clouds in the central environments of galaxies seem to show considerable differences from their counterparts in the disc (e.g. Querejeta et al., 2021; Liu et al., 2021), with some studies also finding different cloud properties between arm and inter-arm regions (e.g. Colombo et al., 2014a). Still, it is unclear whether these differences in cloud characteristics actually impact the star formation process happening within these clouds.

1.4.3 The Kennicutt-Schmidt relation

Another area of active research is the investigation of whether the star formation process is also directly affected by the large-scale galactic environment. One way of doing so, is by looking at the scatter in the relationship between the star formation fuel (i.e. molecular gas) and star formation itself in different regimes. The "Kennicutt-Schmidt" (KS) relation, first suggested by Schmidt (1959) and then further expanded by Kennicutt (1998), takes the form of

$$\Sigma_{\mathrm{SFR}} \propto \Sigma_{\mathrm{gas}}^{N}, \tag{1.28}$$

where the observed SFR surface density, Σ_{SFR}, is related to the observed total gas surface density, Σ_{gas} ($\Sigma_{\mathrm{gas}} = \Sigma_{\mathrm{H\,I}} + \Sigma_{\mathrm{H_2}}$), via a power-law of index N. Kennicutt (1998) found that for a sample of 97 galaxies, the globally integrated galactic values show a tight correlation with $N = 1.4 \pm 0.15$, as shown in Fig 1.7. Since then, it has been found that SFR is much more strongly correlated with molecular gas than with the total gas (e.g. Schruba et al., 2011). Additionally, studies have found a wide range of KS indices from sub-linear (e.g. Shetty et al., 2013), to linear (e.g. Bigiel et al., 2008; Rahman et al., 2012), to super-linear (e.g. Kennicutt et al., 2007; Liu et al., 2011; Kennicutt & Evans, 2012). There are theoretical expectations for the values N assumes. At the scale of individual MCs, if all the gas is collapsing and being converted into stars over a free-fall time, we would expect $N \approx 0.75$ (Krumholz & McKee, 2005). On the other hand, we would expect a super-linear index ($N \approx 1.5$) if molecular clouds only convert a roughly constant fraction of their total gas into stars within a free-fall time (e.g. Elmegreen, 1994).

The large range of N across observational studies could indeed imply that the star formation process occurs differently for different galaxies, but it also heavily suggests that the KS index is extremely sensitive to systematic errors or differences in methodology (e.g. Calzetti et al., 2012). As an example, the $N = 1.4$ slope found by Kennicutt (1998) was derived assuming a constant X_{CO} across the entire sample. Accounting for the likely metallicity-dependence of X_{CO} (see Section 1.3.1) can by itself result in different values of N (e.g. Narayanan et al., 2012). Another major factor that has not yet been mentioned, is the impact of spatial resolution in this empirical relation. Indeed, recent work has demonstrated that although the KS law holds at the kiloparsec and sub-kiloparsec scales (e.g. Bigiel et al., 2008; Saintonge et al., 2011; Leroy et al., 2013), it starts to break down at smaller resolved scales (e.g. Schruba et al., 2010; Feldmann et al., 2011; Pessa et al., 2021). In fact, once the spatial resolution of observations reaches cloud-scales, the observed scatter on $\Sigma_{\mathrm{SFR}} \propto \Sigma_{\mathrm{gas}}^{N}$ increases. This might be because when we start to resolve star-forming regions, there is an observed spatial offset between young stars (and the H II regions surrounding them) and the MCs where star formation occurs (e.g.

Schruba et al., 2010). Once (massive) stars are formed, stellar feedback processes such as intense radiation fields, stellar winds, and later on supernovae, disrupt and can even disperse their natal cloud, generating this spatial offset. These small-scale processes are averaged out in galaxy-scale studies, and thus the KS relation can still be observed in large scales. Altogether, this perfectly showcases the importance of resolution, and how we must be mindful of spatial scales when deriving conclusions.

1.4.4 Star formation and galactic environment

Several observational works have proposed that the local dynamical environment of MCs seems to affect the formation of stars (e.g. Meidt et al., 2013; Renaud et al., 2015; Pan & Kuno, 2017), by altering the initial conditions of star formation (i.e. the cold ISM). Specific environments within galaxies such as spiral arms have a higher concentration of young stars and thus higher observed SFRs (e.g. Vogel et al., 1988; Bigiel et al., 2008; Querejeta et al., 2021). The effect of spiral arms on the star formation process is of particular interest, since the majority of galaxies in the local Universe are observed to have some kind of spiral structure (e.g. Buta et al., 2015). Spiral arms are a natural consequence of the differential rotation[10] of disk galaxies (e.g. Binney & Tremaine, 2008). Due to this differential rotation, any disturbance in the disk can eventually wind up and create a spiral structure. Currently, there are two main theories describing the nature of spiral arms. In the quasi-stationary density wave theory (Lin & Shu, 1964), spiral arms are steady, long-lived structures that rotate with a single pattern speed (i.e. angular speed), and propagate throughout the disk much like ocean waves. The opposing theory is that spiral arms are transient features caused by encounters with companion satellites and/or seed disturbances that undergo swing amplification (e.g. Binney & Tremaine, 2008).

This increase in SFR towards spiral arms could be a sign of a direct influence in the efficiency of the star formation process. One scenario proposed by Fujimoto (1968) and Roberts (1969) proposes that star formation is triggered due to the development of shocks along the trailing edge of arms, which compress the gas and thus promote cloud gravitational collapse and the formation of stars. It could also be that MCs are better protected against shear within spiral arms, which would heavily disrupt or even destroy clouds and thus prevent stars from forming (e.g. Elmegreen, 1987; Dobbs et al., 2014).

However, higher SFRs do not inherently imply that the process of star formation itself is any more efficient towards a given region. Spiral arms, for example, do have higher SFRs, but they also naturally harbour more molecular gas. It could be that the underlying gravitational potential of spiral arms is simply acting to re-organise and gather gas together, with no direct

[10] Material takes less time to complete a full rotation towards the centre of the galaxy than at larger radii.

effect on the efficiency of star formation (e.g. Elmegreen & Elmegreen, 1986). In other words, the SFRs are higher purely because there is more fuel, not because the star formation process itself is more efficient towards those regions. It is often more informative to measure the SFR per unit gas mass, or "star formation efficiency" (SFE[11], Leroy et al. 2008):

$$\mathrm{SFE} = \frac{\Sigma_{\mathrm{SFR}}}{\Sigma_{\mathrm{gas}}} = \tau_{\mathrm{dep}}^{-1}. \tag{1.29}$$

If star formation is indeed triggered by spiral arms, then one would expect higher SFEs towards spiral arms relative to other galactic environments, which has indeed been observed in some cases (e.g. Lord & Young, 1990; Seigar & James, 2002; Silva-Villa & Larsen, 2012; Yu et al., 2021). However, there is also observational evidence of no significant increase of SFE towards spiral arms (e.g. Leroy et al., 2008; Foyle et al., 2010; Moore et al., 2012; Ragan et al., 2016; Kreckel et al., 2016; Querejeta et al., 2021, 2024). On the other hand, it could be that there are more mechanisms at play to counteract this potential triggering of star formation in arms or other dense regions. We expect an increase in cloud-cloud collisions in environments with high gas surface density, which can in fact momentarily boost star formation, but are also thought to increase the velocity dispersion of the gas, which could provide some additional turbulent support, preventing clouds from collapsing (e.g. Dobbs & Bonnell, 2007). Additionally, as was already mentioned, stellar feedback processes can act as a major disruptor by altering the chemical and physical structure of the surrounding ISM (e.g. Chevance et al., 2020). There is also shear, which is generated by the differential rotation of the gas in galactic discs, and it can lead to mass loss in MCs and even to full cloud dispersal (e.g. Dobbs & Pringle, 2013).

Altogether, understanding what mechanisms drive and regulate star formation is a complex, multi-faceted problem, which spans many physical scales. Disentangling the importance and role of each contributing factor is incredibly difficult, since these cloud- and galatic-scale processes are intrinsically connected, but hardly probed simultaneously. Still, significant progress is being made. On the theoretical side, we are shifting from the classical isolated, spherical molecular cloud models and assumptions, and increasing computational power is starting to allow modern simulations to resolve MCs without losing information on the galactic context, and the implementation of more sophisticated physics such as stellar feedback processes (e.g. Seifried et al., 2017; Treß et al., 2020; Jeffreson et al., 2020; Pettitt et al., 2020; Treß et al., 2021; Colman et al., 2022; Herrington et al., 2023; Ali et al., 2023). Huge strides have also been made in the observational field, with modern facilities like ALMA (Atacama Large Millimetre Array), VLT (Very Large Telescope), HST (Hubble Space Telescope) and JWST (James Webb Space

[11]Not to be confused with ϵ_{ff}, which is a fractional star formation efficiency (per free-fall time). This SFE is essentially a normalised SFR.

Telescope) - among other instruments - all being used to provide a higher resolution, higher sensitivity, multi-wavelength view of star formation across cosmic time (e.g. Schinnerer et al., 2013; Saintonge et al., 2017; Jiménez-Donaire et al., 2019; Rigby et al., 2021; Liu et al., 2021; Rosolowsky et al., 2021; Colombo et al., 2021; Lee et al., 2023; Messa et al., 2024; Pedrini et al., 2024; Calzetti et al., 2024).

Traditionally, the Galactic and extragalactic star formation communities are seen as virtually two completely separate fields. Within the Milky Way it is possible to resolve and study individual star-forming regions, and analyse how clouds fragment into clumps and pre-stellar cores. The trade-off is the loss of the larger-scale context, given the difficulty of precisely locating clouds and determining distances (e.g. Colombo et al., 2022), as well as potential issues with superposition (e.g. Ballesteros-Paredes et al., 2019). The extragalactic field does not suffer much from this issue, but is instead limited in terms of resolution and sensitivity given the larger distances involved, often working with integrated measurements. This limitation is of course diminishing given the advancement of instrumentation, and we are now in a position where Milky Way and extragalactic studies can together start to form a unified approach into understanding and breaking down the star formation cycle. The future looks even brighter, with facilities such as ELT (Extremely Large Telescope) and SKA (Square Kilometre Array) coming online within the next decade[12], and with other exciting telescopes being planned and designed like HWO[13] (Habitable Worlds Observatory) and AtLAST[14] (Atacama Large Aperture Submillimeter Telescope).

1.5 THESIS OUTLINE

This thesis presents an exploration into the distribution of the star-forming, molecular gas in a sample of nearby galaxies. I have developed a technique which exploits the high spatial resolution of archival HST optical data to build parsec-scale images of the dust (and gas) content of nearby disc galaxies via dust extinction. This poses a new and exciting high-resolution view into the initial conditions of star formation. The technique is tested and applied to the spiral galaxy M51 (also known as NGC 5194). Subsequently, clouds were extracted from the resulting high-resolution map, and I investigate for any trends of cloud properties with galactic context. Finally, this work is expanded to a wider sample of nearby galaxies which cover different morphological types. This thesis is outlined as follows:

- Chapter 2 introduces the extinction-based imaging technique, with its application to the nearby spiral M51 (NGC 5194). I discuss the advantages, as well as the downsides, of this

[12]Fingers crossed.
[13]https://habitableworldsobservatory.org/
[14]https://www.atlast.uio.no/

technique compared to other methods.

- In Chapter 3, I extract a cloud catalogue from the extinction-derived gas surface density map of M51, and calculate various cloud properties (e.g. mass, average surface density, aspect ratio, length, etc.). I search for trends with large-scale environments, as well as galactocentric radius. I discuss our results within the context of the literature for this galaxy.
- In Chapter 4, I expand the analysis performed in Chapter 3 to a larger sample of nearby disc galaxies. This sample is composed of disc galaxies ranging from flocculent (no discerning spiral arms), to spirals with and without bars.
- Chapter 5 holds a summary of the conclusions and key results of this thesis, as well as a future outlook.

Chapter 2

EXTINCTION-BASED IMAGING TECHNIQUE

"The role of the academic is to make everything less simple."

MARY BEARD

This Chapter is based on the work published in Faustino Vieira et al. (2023). All of the present content is my own original work and analysis. Ana Duarte-Cabral was involved with the concept and design of the technique outlined in this Chapter, and remaining co-author input came mainly in the form of scientific discussion and reviewing.

2.1 INTRODUCTION AND MOTIVATION

A key process in a galaxy's evolution is of course its ability to form stars. Star formation originates in the molecular phase of the ISM in galaxies (e.g. Young & Scoville, 1991). To better understand the initial conditions of star formation it is therefore important to study the molecular gas content in galaxies. By far, the most common method employed in molecular gas studies is CO emission observations (e.g. Koda et al., 2009; Schinnerer et al., 2013; Schuller et al., 2021; Leroy et al., 2021; Koda et al., 2023, see also Chapter 1). With the advancement of instrumentation, interferometric observations are now able to distinguish and resolve giant molecular clouds (GMCs) in nearby galaxies, catapulting us into an exciting era of star formation and ISM studies. Still, CO is not a perfect tracer; CO surveys are only sensitive to the "CO-bright" molecular gas since at low column densities CO is not abundant enough to self-shield (unlike H_2, the main component of the molecular ISM) and is rapidly photodissociated by the interstellar radiation field (see Section 1.3.1).

Another proxy for the invisible H_2 is interstellar dust (Section 1.3.2). Assuming that dust and gas are well-mixed, one can use measurements of dust emission or extinction to trace the gas content of a galaxy, since dust absorbs the stellar light in the visible-UV range and re-emits it at infrared (IR) to sub-millimetre (submm) wavelengths. This, of course, also assumes that the dust-to-gas mass ratio is constant and known. A constant dust-to-gas mass ratio of 0.01 is an often made assumption for the Milky Way and galaxies with similar metallicities (e.g. Hildebrand, 1983; Lada et al., 2007; Mentuch Cooper et al., 2012; De Looze et al., 2020), but might be underestimated in different density regimes such as the outskirts of galaxies (e.g. Smith et al., 2016). Dust extinction, in particular, is an attractive tracer for the molecular ISM, given that it is independent of dust grain temperature, unlike dust emission.

This Chapter presents a dust extinction technique that results in sub-arcsecond or parsec-scale dust (and by extension gas) surface density maps for entire galaxies. This method is adapted from dust extinction studies done for the Milky Way in the IR (Bacmann et al., 2000; Peretto & Fuller, 2009), where what is measured is not the extinction of individual stars. Instead, the attenuation is measured against a diffuse and smoothly varying background light. Fundamentally, the technique measures the attenuation of the local stellar background caused by dust on a pixel-by-pixel basis. In order to apply this technique to nearby galaxies, we use readily available, high resolution optical Hubble Space Telescope (HST) data to reconstruct the stellar background, and determine the column of dust (and gas) by comparing the observed intensity of each pixel against what the intensity would be if there were no dust to cause any extinction (i.e. the reconstructed stellar distribution). *Herschel* Space Observatory (Pilbratt et al., 2010) observations of dust emission are also used to calibrate the unknown contribution of foreground light in the line-of-sight. This novel technique allows us to map entire galaxies at sub-arcsecond resolution, practically an order of magnitude better than the typical resolution achieved by current interferometric observations of entire nearby galaxies (generally a few arcseconds). It is also not reliant on resolving individual stars and accurately measuring their colour, which is often a requirement of traditional extinction studies.

Here, the high-resolution extinction mapping technique is applied to the nearby spiral galaxy M51 (NGC 5194), chosen for its vast amount of multi-wavelength ancillary data and observational studies (e.g. La Vigne et al., 2006; Koda et al., 2009; Hughes et al., 2013; Schinnerer et al., 2010; Mentuch Cooper et al., 2012; Schinnerer et al., 2013; Messa et al., 2018), its relatively near distance (7.6 Mpc; Ciardullo et al. 2002), and its face-on inclination (22°; Colombo et al.

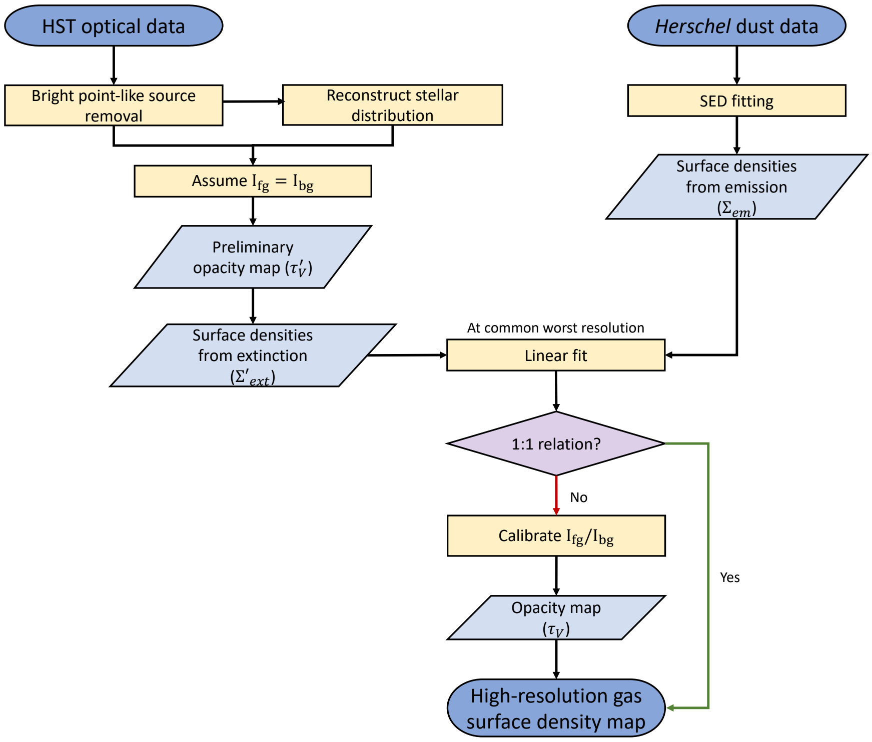

Figure 2.1 – Simplified flowchart of the high-resolution extinction mapping technique presented here (further details in Section 2.3).

2014b). The data used are described in Section 2.2, with the technique itself being detailed in Section 2.3. The resulting high-resolution, extinction-derived map of M51 is presented in Section 2.4, alongside a comparison with other dust mass and optical depth determinations, as well as with ^{12}CO (1-0) observations from the PdBI Arcsecond Whirpool Survey (PAWS; Schinnerer et al., 2013). A summary of this Chapter can be found in Section 2.5.

2.2 DATA

In this Chapter, I present a new high-resolution extinction mapping technique, and its application to M51 as a proof-of-concept. This Section presents the different datasets used. In particular, this technique measures dust extinction in the optical (using HST data) in order to build gas surface density maps. *Herschel* dust emission observations are used as a calibrator for the unknown foreground light contribution along the line-of-sight, and CO data from PAWS to compare the results.

2.2.1 Optical data

The F555W (V-band, centred at 0.536 μm) and the F435W (B-band, with pivot wavelength 0.433 μm) filters from the HST ACS (Advanced Camera for Surveys) Heritage, retrieved from the Hubble Legacy Archive[1] are used here to build extinction maps of M51 in the optical. Both the B- and the V-band have a pixel size of 0.049" and resolution 0.1" (Mutchler et al., 2005). An astrometric correction of 0.1" in the RA direction and −0.4" in the Dec. direction is applied to both the B-band and the V-band, as explained in Schinnerer et al. (2013) (see also Mutchler et al., 2005).

The V-band is chosen as the prime wavelength for the extinction mapping technique as it should achieve higher A_V (visual extinction) before reaching saturation compared to the B-band, therefore probing deeper into the structure of the clouds. The B-band is used for testing the applicability of the method on a different band.

As a proof-of-concept, this new technique is only applied to NGC 5194 (referred to here as simply M51). Its companion, NGC 5195, is therefore cut from the original HST observations since it is also known to have different metallicity and dust-to-gas mass ratio than NGC 5194 (e.g. Mentuch Cooper et al., 2012). Additionally, the outer edges of the HST observations are masked out using the reprojected *Herschel* data as a guide.

2.2.2 Infrared data

The high-resolution extinction mapping technique presented here allows us to map surface densities for nearby galaxies at an angular resolution close to the native resolution of HST. However, since we cannot make the simple assumption that all observed light is being attenuated by dust, *Herschel* dust emission observations are used to retrieve the corresponding total dust column densities at a lower resolution, to calibrate the contribution of foreground light along the line-of-sight. This is so that, statistically, the column densities obtained via dust emission and dust extinction measurements are consistent with each other.

At the IR-submm wavelengths where dust emission is brightest (Section 1.3.2.2), the spectral energy distribution (SED) of the galaxy is often modelled using a single-temperature modified blackbody (MBB) fit (details of which are outlined in Section 2.2.2.1). For this purpose, four bands from *Herschel* are used, retrieved from the *Herschel* Science Archive[2]. The bands are the 160 µm band from the PACS instrument (Photodetector Array Camera and Spectrometer; Poglitsch et al., 2010), and the 250 µm, 350 µm, and 500 µm bands from SPIRE (Spectral and Photometric Imaging Receiver; Griffin et al., 2010). The archival PACS and SPIRE data used here are the level 2.5 and level 3 data products, respectively (Davies et al., 2017). The pixel sizes for the 160 µm, 250 µm, 350 µm, and 500 µm bands are, respectively, 3.2", 6", 10" and 14", with the corresponding full width at half-maximum (FWHM) of ∼ 11.5", ∼ 18", ∼ 25" and

[1]https://hla.stsci.edu/
[2]http://archives.esac.esa.int/hsa/whsa/

~ 36". All SPIRE bands were converted from MJy/sr to Jy/pixel. The PACS 160µm data was chosen as the template pixel scale - remaining bands were therefore reprojected onto a 3.2"/pix grid. All bands were convolved to the angular resolution of the SPIRE 500 µm band (worst resolution), resulting in all four dust emission maps used here having a common FWHM of 36". The Gaussian kernels used in this operation were 34" (for the 160 µm), 31" (for the 250 µm) and 26" (for the 350 µm).

2.2.2.1 SED modelling

When approximating an object's SED to a blackbody, one is implicitly assuming that: (1) the dust emission is optically thin, (2) the galaxy's population of dust grains is homogeneous in size and composition, (3) the dust emission comes primarily from heated large dust grains that are at thermal equilibrium with the interstellar radiation field and thus share an average temperature along the line of sight (Section 1.3.2.2), and (4) the mass absorption coefficient, κ_λ can be described by a power-law (Eq. 1.15; Hildebrand, 1983). Despite all these assumptions, single-temperature MBB fits are commonly used, and can reliably retrieve estimates of dust properties for $\lambda \geq 100$ µm, where contributions from warmer dust are thought to be less important (Bianchi, 2013).

The pixel-by-pixel SED fitting performed here used non-linear least squares to estimate the dust temperatures ($T_{\rm dust}$) and dust emission surface densities ($\Sigma_{\rm em}$) in each pixel of M51. The reference absorption coefficient adopted was $\kappa_{250\mu\rm m} = 21.6$ cm^2 g^{-1} from Ossenkopf & Henning (1994, hereafter OH94), often used in Milky Way studies (e.g. Kauffmann et al., 2008; Schuller et al., 2009), which is valid for grains covered by a thick ice mantle that follow the classical Mathis, Rumpl, and Nordsieck (MRN) size distribution model (Mathis et al., 1977). A fixed dust emissivity spectral index of $\beta = 2$ was assumed - an appropriate assumption for metal-rich, late-type galaxies such as M51 (e.g. Boselli et al., 2012; Mentuch Cooper et al., 2012; Clark et al., 2016). The average values resulting from this SED fit are $T_{\rm dust} \simeq 21.7 \pm 3.64$ K and $\Sigma_{\rm em} \simeq 0.06 \pm 0.03$ M$_\odot$ pc^{-2}. For comparison purposes, the dust surface densities obtained using $\kappa_{250\mu m} = 3.98$ cm^2 g^{-1} from Mentuch Cooper et al. (2012) are about a factor 5.4 larger than the results here. Similarly, using $\kappa_{250\mu m} = 10$ cm^2 g^{-1} from Elia et al. (2013) (a Galactic study), the resulting dust surface densities are about a factor 2.2 larger.

2.2.3 Millimetre data

In this work, the extinction results are also compared to the column densities derived from the ^{12}CO(1-0) emission maps from PAWS (Schinnerer et al., 2013), retrieved from the PAWS website[3]. PAWS imaged the CO gas in the central 11×7 kpc region of M51 using both the Plateau de Bure Interferometer (PdBI) and the 30-metre single dish telescope from IRAM. The resulting combined datacubes (PdBI+30m) have a resolution of 1.16" $\times$ 0.97" (corresponding spatial resolution of $\sim 40\,\mathrm{pc}$), a pixel scale of 0.3"/pix, and a sensitivity of 0.4 K per 5 $\mathrm{km\,s^{-1}}$ channel (Colombo et al., 2014b).

2.3 HIGH-RESOLUTION EXTINCTION TECHNIQUE

Here, a new high-resolution extinction mapping technique is presented, which allows us to construct an all-galaxy dust surface density map at a resolution close to the native resolution of HST. In summary, this technique is similar to the techniques used in Galactic studies in the IR (e.g. Bacmann et al., 2000; Peretto & Fuller, 2009), which determine the amount of the local background radiation attenuated by the dust at each pixel. As such, this method only works if we can recover a reliable estimate of the local background radiation. This is only possible if the background radiation is smoothly varying - such that it can be reconstructed directly from the HST images using median filtering techniques. This is the case for the relatively diffuse stellar background traced by the B- and V-bands of HST, but it becomes less usable in the near-IR bands due to the increased detection of younger, embedded stars, which dominate in the dust regions studied here, consequently causing the stellar background to be less smooth.

The different steps involved in this technique (summarised in Fig. 2.1) are described in more detail in this section, namely the preparation of the images for the analysis (removing point-like sources), the reconstruction of the stellar background, computing the optical depth, and calibrating the results with lower-resolution surface density maps obtained from FIR dust emission observations from *Herschel*.

2.3.1 Removal of point-like sources

The first step in the method consists of removing bright point-like sources, which can produce artifacts in the final map. In particular, given that this technique estimates the attenuation caused by the dust against a smoothly varying background on a pixel-by-pixel basis, in regions where bright point-like sources appear in the foreground, any dust attenuation that might exist behind is completely hidden by the bright object. This effectively creates artificial "holes" of negative opacities in the background clouds. If these foreground stars are small enough (i.e. point sources of a size similar to the resolution of the HST image), it is possible to remove them from the map and refill those positions with an interpolated background, which will give an

[3] https://www2.mpia-hd.mpg.de/PAWS/; see also https://www.iram-institute.org/EN/content-page-240-7-158-240-0-0.html

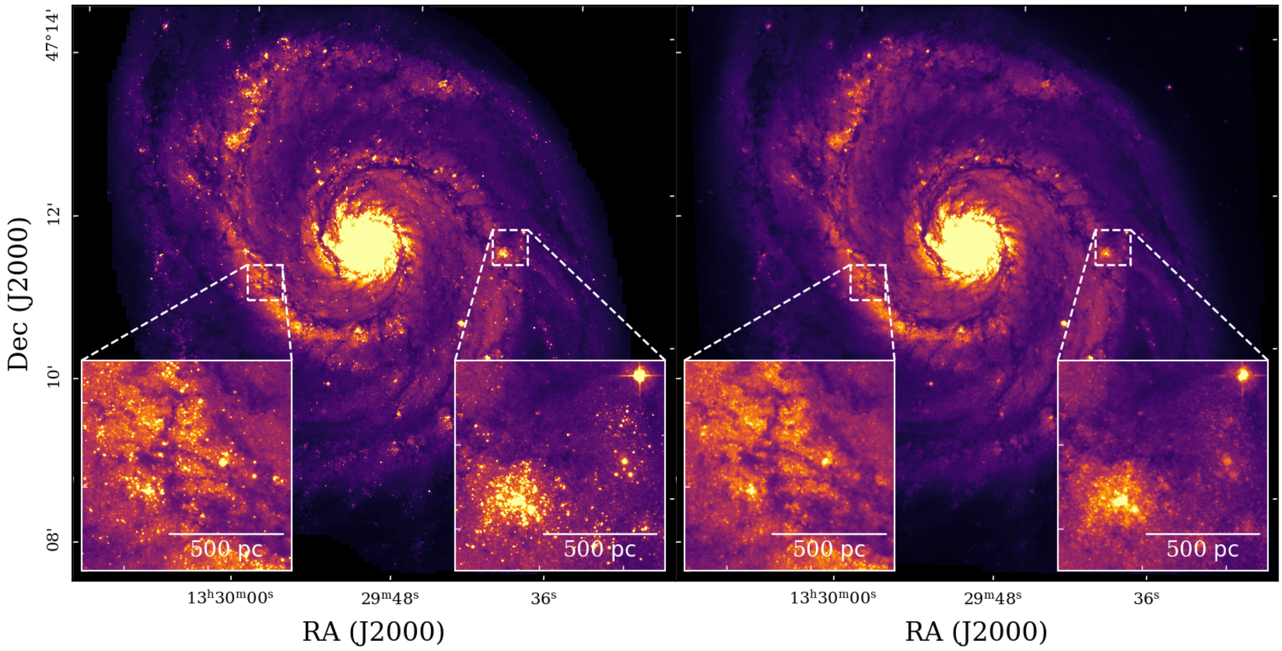

Figure 2.2 – *Left:* original HST V-band image of M51. *Right:* M51 after removal of bright point-like sources. At the bottom of both panels are the same two regions zoomed for better visualisation of the source-removal results. Given that star clusters are not point-like sources, they are not always removed from the image completely (as seen in the right panel).

estimate of the opacity of the clouds behind the bright sources. Additionally, a high density of bright point-like sources (such as a large cluster of stars) can skew the median filtering techniques (see Section 2.3.2), resulting in an overestimation of the average stellar distribution around those bright regions.

The simplest way to remove point sources from the original intensity would be to perform sigma-clipping and reject any pixels that are above a certain threshold. However, due to the wide dynamical range of intensities seen in the original HST map, this process is not straightforward. For example, if we use a relatively high value for the threshold (or if the median is skewed towards high values due to the really bright regions of the spiral arms or galactic centre), the sigma-clipping method will miss the fainter point-like sources clearly visible in the lower intensity regions such as the inter-arm. Conversely, if we use a lower value for the sigma-clipping, or the median, entire bright regions (like the galactic centre) are clipped off. To circumvent this, the sigma-clipping is performed on a map where background fluctuations are flattened, so that the sigma-clipping performs well across the entire map.

The `Background2D` function from `Photutils` (v1.0.1, Bradley et al., 2020) is used to compute a flattened background to subtract from the original HST image in order to facilitate the source removal. Essentially, the function splits the original map into a grid and estimates the median background of each square within the grid, ignoring all pixels that deviate more than 3 standard deviations (σ) in this calculation. The resulting grid is then transformed into the final, full-size estimated median background through bicubic spline interpolation. To capture the large background fluctuations, a grid of 7.35" $\times$ 7.35" boxes ($\sim 270 \times 270$ pc for M51) is defined, which is transformed into a full-size large-scale background map using a median filter with kernel size 0.245". Subtracting this large-scale background image from the original HST map does flatten the larger fluctuations of the original image, but many of the smaller variations are still included. Therefore, in an attempt to flatten the background as much as possible, a small-scale background is also estimated. This is done in a similar manner as the large-scale case, but with a smaller grid size of 0.15" $\times$ 0.15" ($\sim 5.50 \times 5.50$ pc for M51).

Removing both large- and small-scale backgrounds from the original HST V-band intensity leaves us with a map that includes only bright point-like sources surrounded by a relatively constant value. It is now possible to easily identify these point sources by creating a source mask using `make_source_mask` from `Photutils`. This source mask contains only sources that have at least three connected pixels that are all 3σ above the median of the map. In practice, this procedure eliminates (or attempts to) not only single point-like sources, but also clusters of stars, as well as saturated HST sources with diffraction spikes. Additionally, the bright pixels in the source mask are dilated with a 3×3 pixel square array to ensure that the whole bright source is clipped off rather than just the $> 3\sigma$ peaks.

After removing the bright point-like sources in the final source mask, they are filled with an interpolated background value, which is obtained by convolving the HST V-band image (ignoring the bright point-like sources) with a Gaussian kernel of ~ 0.3", which is roughly equal to the size of the empty regions. One final small convolution is applied to account for any boundaries that might have been created in the filling process or any other artefacts. This convolution has a kernel size of ~ 0.1" and it only slightly degrades the resolution of the source-removed image to 0.14", compared to the 0.1" native angular resolution of the HST data. The original HST V-band image and the respective source-removed image for M51 are shown in Fig. 2.2.

2.3.2 Reconstruction of stellar distribution

The next step in the method is the reconstruction of the total stellar distribution, which is meant to reproduce the stellar radiation field of the galaxy if there was no light being absorbed by the dust grains in the ISM. The stellar distribution, I_0, is reconstructed by applying a sizeable median filter to the source-removed image, I_λ (Section 2.3.1). In order to have a good approximation of the total stellar light, the kernel must be larger than the typical size of the absorbing structures (i.e. molecular clouds), so that the stellar light estimate is not sensitive to

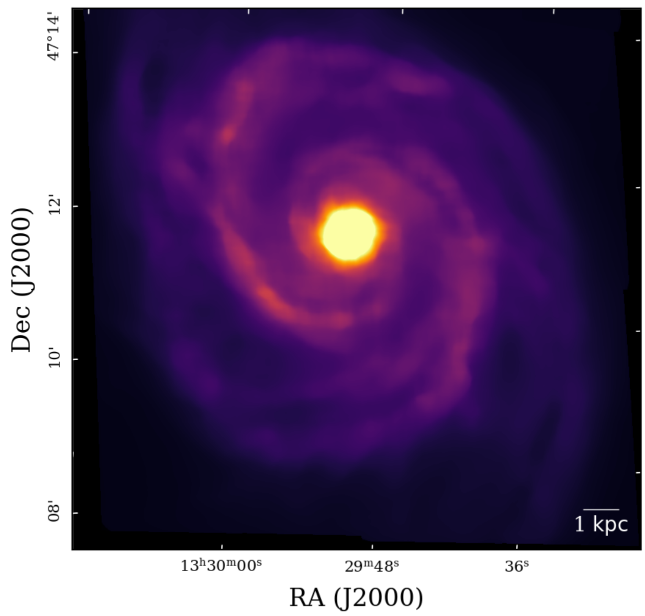

Figure 2.3 – Reconstructed stellar distribution of M51 for the V-band. Extinction features present in the original HST V-band image are eliminated, whilst the overall shape and features (such as the bright spiral arms) of the galaxy are preserved.

the absorbing medium, but not too big as to risk losing the intrinsic fluctuations of the stellar distribution due, for instance, to the spiral structure of the galaxy. The choice of the kernel is therefore crucial so as to not under- or over-estimate the stellar distribution, as that will result in under- and over-estimating the respective opacities. For M51, the kernel size chosen was $\sim$ 16" ($\sim$ 600pc) - a little under the size of the galactic nuclear bar (Colombo et al., 2014a). This scale is larger than the typical size of GMCs ($\sim$ 50 pc; Blitz 1993), but small enough to capture the changes due to spiral arms and the galactic centre. For M51, changing this kernel by a factor 2 either way - 300 pc or 1.2 kpc - changes the final calibrated opacities by a factor 1.1 and 0.97, respectively. The final reconstructed I_0 is shown in Fig 2.3.

2.3.3 Constructing a preliminary opacity map

Dust absorbs radiation in the optical. The simplest approach to describe how the observed light, I_λ, is being attenuated by dust is by assuming a flat foreground screen of dust, such that: $I_\lambda = I_0\ e^{-\tau_\lambda}$, where τ_λ is the optical depth of the dust (as explained in Section 1.3.2.1). In reality, dust is likely to be evenly mixed with the gas within a galaxy (see Calzetti, 2001, and references therein), and the use of a foreground dust screen often overestimates the total attenuation (e.g. Calzetti, 2001; Kessler et al., 2020). Here, a "sandwich" geometry model is adopted, where the dust sits in a layer close to the mid-plane of the galaxy (which is a fair assumption for face-on galaxies, such as M51), and no further assumptions are made on its

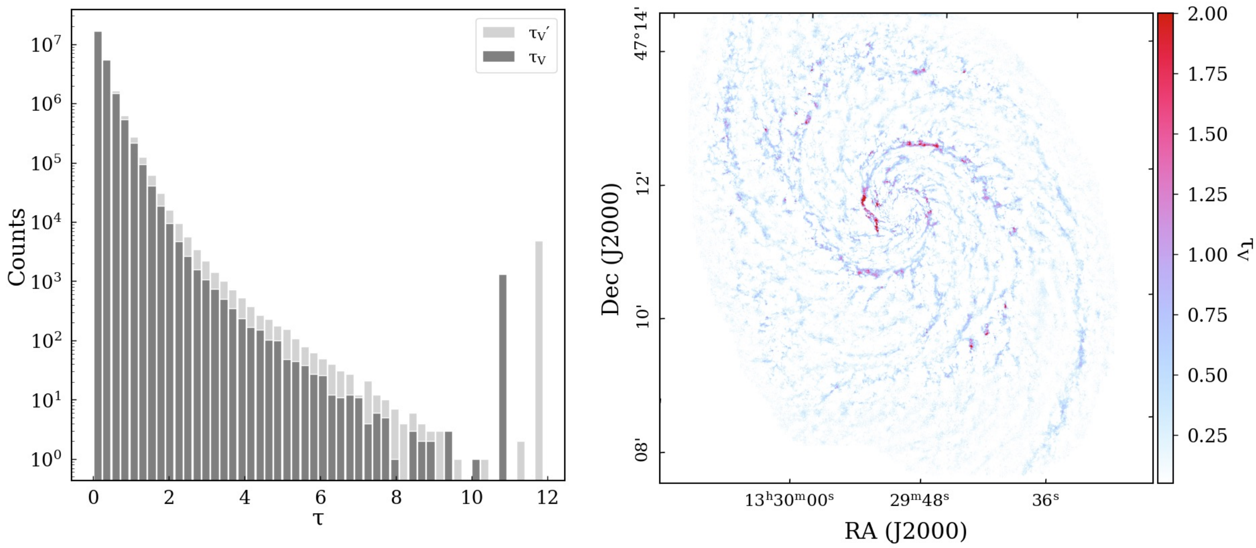

Figure 2.4 – *Left:* Histograms of first-guess optical depth, τ_V', (in light grey) and calibrated optical depth τ_V, (in dark grey). The isolated bins at the higher end of each dataset correspond to the saturated pixels of each map, set at 1% higher than the maximum optical depth value. *Right:* Spatial distribution of the optical depth of M51 resulting from the calibration process within the method (further details in Section 2.3.4). The calibrated optical depth, τ_V, is built with $b = 0.53$ and $f = 0.47$ as the background and foreground light fractions, respectively.

distribution as this is not necessary for the technique. This dust layer does not include any clumps (e.g. Tuffs et al., 2004). Considering this sandwich dust/stars geometry, the observed light can be described through:

$$I_\lambda = I_{\rm bg}\; e^{-\tau_\lambda} + I_{\rm fg}, \tag{2.1}$$

where I_λ (the point-like source removed-image, see Section 2.3.1) is the sum of the light that is free to travel in the line-of-sight without any obscuration (i.e. foreground intensity, $I_{\rm fg}$) and the light that has to travel through an absorbing medium to reach us (i.e. background intensity, $I_{\rm bg}$). The stellar distribution, I_0, can be related to the foreground and background intensities through $I_0 = I_{\rm fg} + I_{\rm bg}$. Additionally: $I_{\rm bg} = b\, I_0$, and $I_{\rm fg} = f\, I_0$, where b and f are the background and foreground fractions of the total light respectively, with $b + f = 1$. Equation 2.1 can be rearranged to give the spatial distribution of the optical depth or line-of-sight opacity:

$$\tau_\lambda = -\ln\left(\frac{I_\lambda - I_{\rm fg}}{I_{\rm bg}}\right). \tag{2.2}$$

To construct a preliminary opacity map for the V-band, τ_V', it was assumed that $I_{\rm bg}' = I_{\rm fg}'$, and therefore $b' = f' = 0.5$. Here, a prime superscript is adopted for the quantities referring to the first guess of background/foreground fractions. Physically, this would mean that the emitting light is split equally beneath and above the absorbing dust content of the galaxy. It is not expected that the background/foreground fraction would stray far from these values in face-on spirals (like M51), given that the gas scale height of a disc galaxy is typically smaller than that of the stars (e.g. Patra, 2019), and therefore we expect most of the obscuring dust to lie close to the galactic plane. Still, since clouds become optically thick relatively quickly in the optical, it would be possible to reach optical depths slightly offset from the exact mid-plane of the galaxy. It is also possible that the reconstructed stellar distribution is not an accurate representation of the true stellar distribution against which the clouds are absorbing (particularly where there are large patches of obscuring dust lanes that will skew the large median filters and underestimate the total stellar light), and therefore the background/foreground fractions might not lie exactly at 50%. Nonetheless, this initial background/foreground fraction assumption is not very important, as it will be calibrated at a later stage (described in Section 2.3.4). The distribution of the first-guess opacity map, τ'_V, is represented in Fig. 2.4 (left panel).

2.3.4 Constraining $I_{\rm fg}$ and $I_{\rm bg}$

It is impossible to constrain $I_{\rm bg}$ and $I_{\rm fg}$ with the optical data alone. However, dust emission observations in the IR-submm wavelength range can provide an independent measurement of the dust mass surface densities, albeit at lower resolution. Thus, a comparison is performed between the dust extinction maps and dust emission surface densities fitted from *Herschel* observations (Section 2.2.2) in order to calibrate the technique and automatically constrain the background/foreground fraction.

Before proceeding with this comparison, it is first needed to deal with the regions where the τ'_V estimates are not usable: negative optical depth pixels and "saturated" pixels. Pixels with negative τ'_V are masked to zero, since these would correspond to points where the observed intensity is brighter than the assumed background stellar distribution and therefore there is no measurable dust attenuation. In addition, in pixels where the observed intensity is lower than the assumed foreground emission, undefined values (NaNs) are obtained. These are dubbed "saturated" regions, and are filled with a fixed maximum value set at 1% higher than the peak value of τ'_V. Less than 0.01% of the pixels in the opacity map of M51 are saturated.

Remembering Eq. 1.14, the optical depth can be related to dust surface densities, $\Sigma_{\rm dust}$, through a dust mass absorption coefficient at the relevant wavelength, κ_λ. Since the dust extinction is being measured in the V-band, Eq. 1.14 becomes $\tau'_V = \kappa_V\,\Sigma'_{\rm ext}$, where τ'_V is the preliminary opacity, κ_V is the adopted dust absorption coefficient ($\kappa_V = 8.55 \times 10^3$ cm^2 g^{-1}, or equivalently $\kappa_V = 1.79$ pc^2 M$_\odot^{-1}$; Draine, 2003, hereafter D03), and $\Sigma'_{\rm ext}$ is the preliminary extinction-derived dust surface densities.

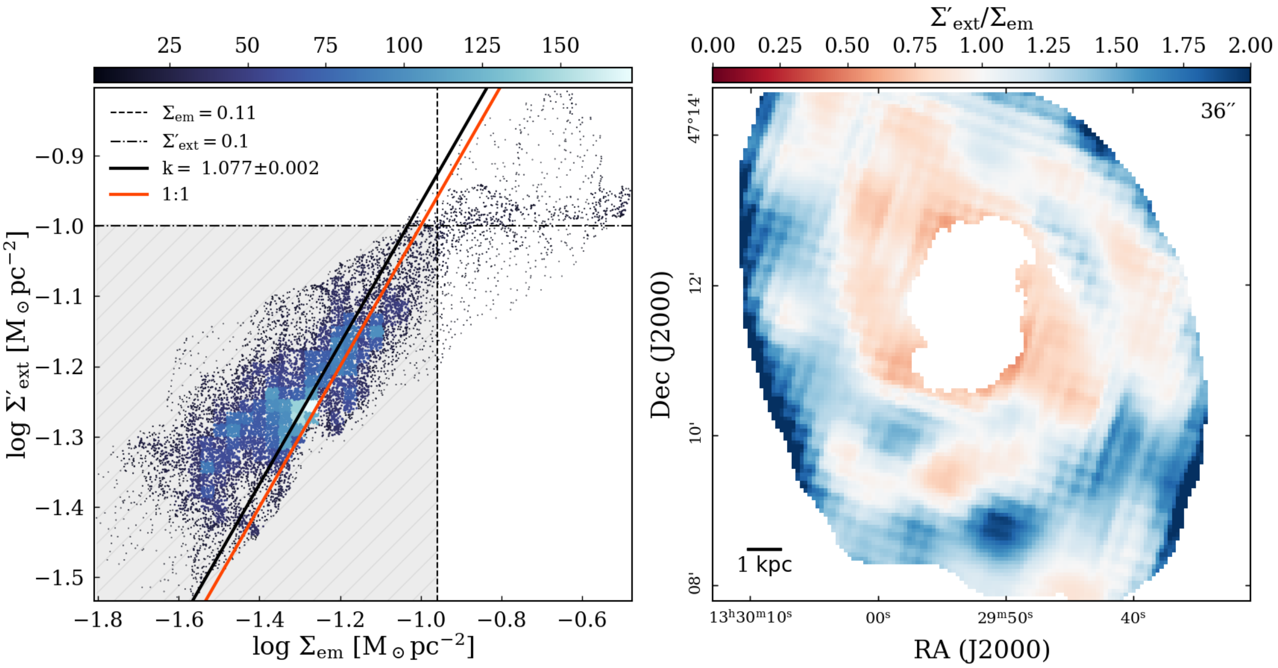

Figure 2.5 – *Left*: First-guess dust surface densities from the extinction technique, Σ'_{ext}, against the surface densities estimated from *Herschel* dust emission data, Σ_{em}. Both quantities are in logarithmic space. The blue scale represents the density of points. The significant scatter seen in the plot corresponds to regions where dust extinction and dust emission are not sensitive to the same column. A linear fit is performed where this scatter is minimal (grey shaded region in plot), shown as a solid black line. The desired 1:1 relation is plotted as a solid red line. *Right*: Ratio of the preliminary extinction dust surface densities, Σ'_{ext}, and the surface densities fitted from dust emission *Herschel* observations, Σ_{em}, done at the resolution and pixel scale of Σ_{em} (36" and 3.2"/pix, respectively). Only the points below $\Sigma'_{ext} = 0.1$ M$_\odot$ pc^{-2} and $\Sigma_{em} = 0.11$ M$_\odot$ pc^{-2} (i.e. grey-shaded region in left panel) are plotted, showing that the excluded points are exclusively in the centre of the galaxy.

The comparison between extinction and emission is done in the grid (3.2"/pix) and resolution (36") of the coarser dust emission column density map[4]. Consequently, the $\Sigma'_{\rm ext}$ is regridded and convolved accordingly. The left panel of Fig. 2.5 shows the relationship between the convolved, preliminary extinction surface densities from the method and the emission surface densities from *Herschel* (both at 36" resolution). It is clear from the figure that the relationship between the dust extinction and emission surface densities is not exactly linear, with a systematic flattening of $\Sigma'_{\rm ext}$ towards higher values of surface density (again, with the caveat that the data is oversampled). This is expected, as estimates of column density from dust extinction and emission do not always match exactly. In the densest regions with high surface densities, the dust becomes optically thick quickly at visible wavelengths, and so the surface densities derived from dust extinction will be a lower estimate of the column, while dust emission should still be sensitive to the full column. On the other hand, for the more diffuse regions with lower surface densities and for regions where the dust is being heated (such as the centre of M51, see Section 2.3.6), the ISM is warmer and thus the SED will start peaking at shorter wavelengths (and outside the wavelengths used for our SED fitting), causing the surface densities from the dust emission to be less accurate. In terms of spatial agreement between dust emission and dust attenuation, Thilker et al. (2023) recently analysed the spatial distribution of attenuation from the HST B-band against several wavelengths tracing dust emission from PHANGS-JWST (Lee et al., 2023). The authors found that in NGC 628, over 40% of sight lines contain both dust emission and extinction at 25 pc scales (increasing to 55% at 200 pc). Furthermore, the authors argue that this may be a lower estimate due to line-of-sight effects and difficulties in consistently extracting filamentary structures. It is difficult to retrieve any measurement of dust extinction wherever star clusters sit in front of the gas/dust, whereas dust emission can measure the full column. Still, this comparison between extinction and emission is performed at a spatial resolution of about 1 kpc, where any significant smaller scale variations should average out, and thus differences in column sensitivity between the two tracers should be predominant. These sensitivity differences are in fact what is seen in the right panel of Fig. 2.5, which shows the spatial distribution of the ratio between the two surface density maps, $\Sigma'_{\rm ext}/\Sigma_{\rm em}$. As expected, in regions of high density (i.e. spiral arms, mostly shown in red), $\Sigma'_{\rm ext} < \Sigma_{\rm em}$, and in more diffuse regions (shown in blue) $\Sigma'_{\rm ext} > \Sigma_{\rm em}$.

In order to calibrate the extinction surface densities with the emission ones so that the final calibrated extinction map is (statistically) consistent with the emission map, we start by analysing the relation between the first-guess of $\Sigma'_{\rm ext}$ and the reference $\Sigma_{\rm em}$ from the emission. In this comparison, the centre of M51 is ignored due to not only potential temperature effects (further explained in Section 2.3.6) but also saturation effects. Considering only the points where

[4]The pixel size was kept small to avoid pixelization, with the caveat that the data is now oversampled.

$\Sigma'_{\rm ext} < 0.1$ M$_\odot$ pc^{-2} and $\Sigma_{\rm em} < 0.11$ M$_\odot$ pc^{-2} (shaded region shown in left panel of Fig. 2.5), a linear regression is a reasonable approach within the scatter. A simple linear fit gives a slope of $k = 1.077 \pm 0.002$[5]. Changing the cutoff values by 30% changes the slopes of the linear fit only marginally: $k = 1.030 \pm 0.002$ for $\Sigma'_{\rm ext} < 0.13$ M$_\odot$ pc^{-2} and $\Sigma_{\rm em} < 0.14$ M$_\odot$ pc^{-2}, and $k = 1.14 \pm 0.003$ for $\Sigma'_{\rm ext} < 0.07$ M$_\odot$ pc^{-2} and $\Sigma_{\rm em} < 0.08$ M$_\odot$ pc^{-2}. The $k = 1.077 \pm 0.002$ fit is used to make a new decision on the background/foreground fraction, and thus calibrate the optical depths.

Neglecting non-linearity (i.e. where dust extinction and emission are not sensitive to the same column), the calibrated extinction surface densities, $\Sigma_{\rm ext}$, should equal $\Sigma_{\rm em}$. Knowing that the preliminary $\Sigma'_{\rm ext}$ relate to the emission surface densities through $\Sigma'_{\rm ext} = k\,\Sigma_{\rm em}$, with k being the aforementioned slope of the linear fit, then it is possible to write a relation between the first estimate and the calibrated estimate of extinction dust surface densities:

$$\Sigma_{\rm ext} = \frac{\Sigma'_{\rm ext}}{k}. \tag{2.3}$$

This relation (and consequently k) tells us by how much we should change the measured extinction surface densities such that they match the emission on a global scale (at lower resolution). Under the assumption that this global "fractional" change remains the same for the finer grid of the high-resolution map, it is possible to use this to re-calibrate the b and f fractions.

Combining Eq. 1.14 with Eq. 2.3, gives $\tau_V = \tau'_V/k$. Replacing Eq. 2.2 into the previous expression gives:

$$\frac{I_V - I_{\rm fg}}{I_{\rm bg}} = \left(\frac{I_V - I'_{\rm fg}}{I'_{\rm bg}}\right)^{1/k}, \tag{2.4}$$

which relates the new calibrated opacity (τ_V) to the preliminary opacity (τ'_V). Remembering that $I_{\rm bg} = b\,I_0$, and likewise $I_{\rm fg} = (1-b)\,I_0$, it is possible to rearrange Eq. 2.4 to give the new calibrated background distribution, b:

$$b = \frac{I_V - I_0}{I_0\left[\left(\frac{I_V - I'_{\rm fg}}{I'_{\rm bg}}\right)^{1/k} - 1\right]}, \tag{2.5}$$

where I_V is the source-removed intensity for the V-band (Section 2.3.1), I_0 is the reconstructed stellar distribution (Section 2.3.2), $I'_{\rm fg}$ and $I'_{\rm bg}$ are the first-guess foreground and background intensities with $f' = b' = 0.5$ (Section 2.3.3), and k is the slope of the linear fit between $\Sigma'_{\rm ext}$

[5]The error on the linear fit is given from the covariance, which is likely an underestimation given the observed scatter.

and Σ_{em}. Equation 2.5 gives, for each pixel in the high-resolution map, what the background fraction b (and consequently the foreground fraction since $f = 1 - b$) should be so that the surface densities derived from the dust attenuation technique correlate with the kpc-scale surface densities computed from dust emission at IR/submm wavelengths.

We choose to adopt a single value for the calibrated b and f, rather than use a pixel-by-pixel correction that would guarantee the convolved extinction surface densities match the *Herschel* dust emission surface densities exactly. As explained before, dust extinction and emission are not always sensitive to the same column. Furthermore, in regions where dust emission is particularly bright (i.e. in galaxy centres), dust temperatures and properties may be different than the rest of the galaxy, which will not be accounted for with the single-temperature and single-β SED fits. In order to not propagate these ambiguities into the dust extinction - which is independent of dust temperature - we prefer to adopt a statistical approach to estimate the typical b (and f) across the galaxy. This is further discussed in Section 2.3.6.

For M51, the medians of the calibrated background and foreground fraction are, respectively, $b = 0.53$ and $f = 0.47$, with a tight interquartile spread of $\mathrm{Q75} - \mathrm{Q25} = 0.01$. Note that this background/foreground calibration process gives similar results for different initial assumptions of b' and f' (e.g. starting with $b' = 0.6$, the background fraction is calibrated to $b = 0.51$, with $\mathrm{Q75} - \mathrm{Q25} = 0.01$).

To construct the new optical depth map for the V-band, τ_V, the calibrated b and f are simply plugged into Eq. 2.2, keeping the remaining maps (I_V and I_0) the same as before. The calibrated opacity map receives the same treatment described in Section 2.3.3: negative opacities are masked to zero, and saturated pixels are filled with a value corresponding to a 1% increase of the peak value of τ_V. The resulting τ_V distribution is shown in Fig. 2.4. We estimate that values of opacity within 30% of the maximum value of τ (i.e. opacities close to saturation, $\tau \gtrsim 7$) are more uncertain, and likely lower limits due to saturation effects, but a more detailed analysis of the uncertainties are shown in the following Section.

2.3.5 Uncertainties in the opacity estimates

Assuming a fixed specific opacity law, the uncertainty in the opacity estimates (and consequently in the extinction technique) will translate into relative errors for the dust/gas surface densities. In order to quantify the uncertainty in the opacities, σ_τ, the standard deviation obtained across 10^4 Monte Carlo realizations of τ are measured for each pixel. Equation 2.2 can be rearranged to showcase the dependence of τ in I_V, I_0, and b:

$$\tau = -\ln\left(\frac{I_V - (1-b)\,I_0}{b\,I_0}\right), \tag{2.6}$$

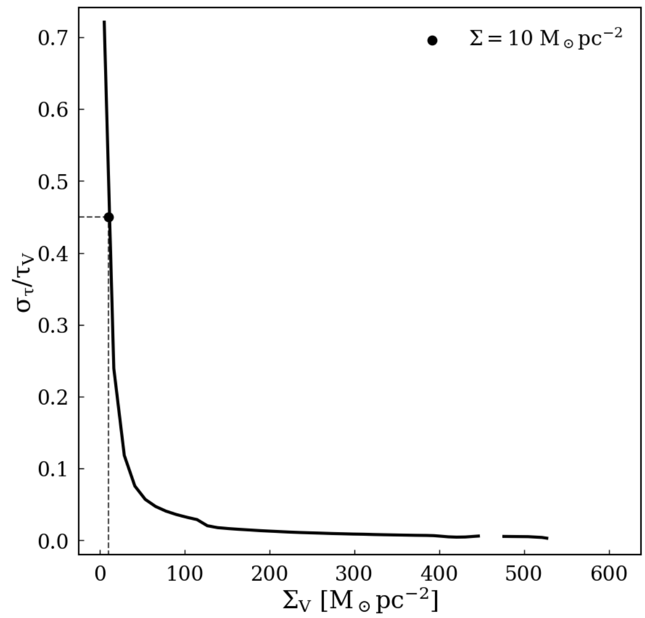

Figure 2.6 – Running median of the relative error on the opacities (σ_τ/τ_V) against the extinction gas surface densities, Σ_V. The often adopted molecular surface density threshold, $\Sigma > 10$ M$_\odot$ pc^{-2}, corresponds to a maximum relative uncertainty of 45% (highlighted in the figure by the solid black dot and dashed lines), although note that it decreases very rapidly to well below 30% uncertainty.

where I_V is the source-removed intensity, b the assumed background light fraction and I_0 the reconstructed stellar distribution. In the Monte Carlo simulations, these 3 parameters are allowed to vary within their respective standard deviations. The σ_{I_V} (i.e. the photometric noise) is estimated by measuring and averaging the standard deviation within low-emission regions of the source-removed map: $\sigma_{I_V} = 8.59 \times 10^{-3}$ e$^-$/s. Given that the stellar distribution is reconstructed by applying a median filter on the source-removed map, we can assume that the uncertainty in I_0, σ_{I_0}, will be related to the photometric noise through: $\sigma_{I_0} = 1.2533\, \sigma_{I_V} / \sqrt{\mathrm{MF}} = 5.94 \times 10^{-4}$ e$^-$/s, i.e. the standard error on the median, where MF is the median filter used in pixels (330 pix, see Section 2.3.2). The scatter on the estimate of b (Section 2.3.4) is taken as its uncertainty, resulting in $\sigma_b = 6.65 \times 10^{-3}$. The running median of the relative error in the opacities (i.e. σ_τ/τ) is shown in Fig. 2.6, as a function of the local gas surface density Σ_V. Above 10 M$_\odot$ pc^{-2} (the often quoted molecular threshold; e.g. Bigiel et al. 2008), the maximum relative uncertainty is 45%, rapidly dropping below 30% above 14 M$_\odot$ pc^{-2}.

Besides these relative uncertainties on the opacities, there is another key observational limitation to the method, which is the fact that the amount of extinction that can be effectively measured depends not only on the photometric noise, but also on the background level. Indeed we expect that the maximum opacity that can be measured will be lower for lower intensity backgrounds. Thus, we need to ensure that the measured surface densities are well below the maximum measurable limit.

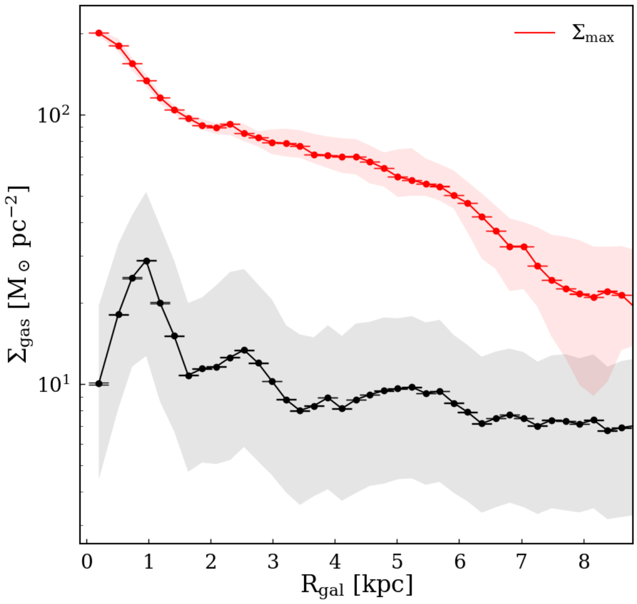

Figure 2.7 – Comparison between the running median of the gas surface densities, $\Sigma_{\rm gas}$ (in black), and the running median of the theoretical maximum value of surface density, $\Sigma_{\rm max}$, given the photometric uncertainties in the HST data (in red), as a function of galactocentric radius, $R_{\rm gal}$. The errorbars depict the standard error on the median, defined as $1.253\,\sigma/\sqrt{N}$ (N being the bin count and σ the standard deviation). The black and red shaded regions represent the interquartile ranges for $\Sigma_{\rm gas}$ and $\Sigma_{\rm max}$, respectively.

In order to verify this, we can determine the maximum opacity, $\tau_{\rm max}$, (and consequently surface density) that can be reliably measured with this extinction technique at each pixel. Remembering Eq. 2.2, the maximum value of τ is obtained when $I_V - I_{\rm fg}$ is at a minimum. If we impose that $I_V - I_{\rm fg} = 3\sigma_{I_V}$, i.e. if this minimum cannot be lower than 3 times the photometric error of the star-subtracted image, σ_{I_V}, then:

$$\tau_{\rm max} = -\ln\left(\frac{3\sigma_{I_V}}{I_{\rm bg}}\right), \tag{2.7}$$

where $I_{\rm bg}$ is the background fraction of the stellar distribution (with $b = 0.53$, see Section 2.3.4). The maximum surface density that can be measured, $\Sigma_{\rm max}$, is related to $\tau_{\rm max}$ by $\Sigma_{\rm max} = \tau_{\rm max}/\kappa_V$. Figure 2.7 shows the running median of $\Sigma_{\rm max}$ as a function of galactocentric radius for M51. It is clear from the figure that, on average, the extinction gas surface densities are below the theoretical maximum surface density.

2.3.6 Temperature effects in the centre of M51

When calibrating the dust extinction surface densities with dust emission, we opted to exclude the contribution from pixels with large $\Sigma_{\rm em}$ located at the centre of M51 (see Section 2.3.4

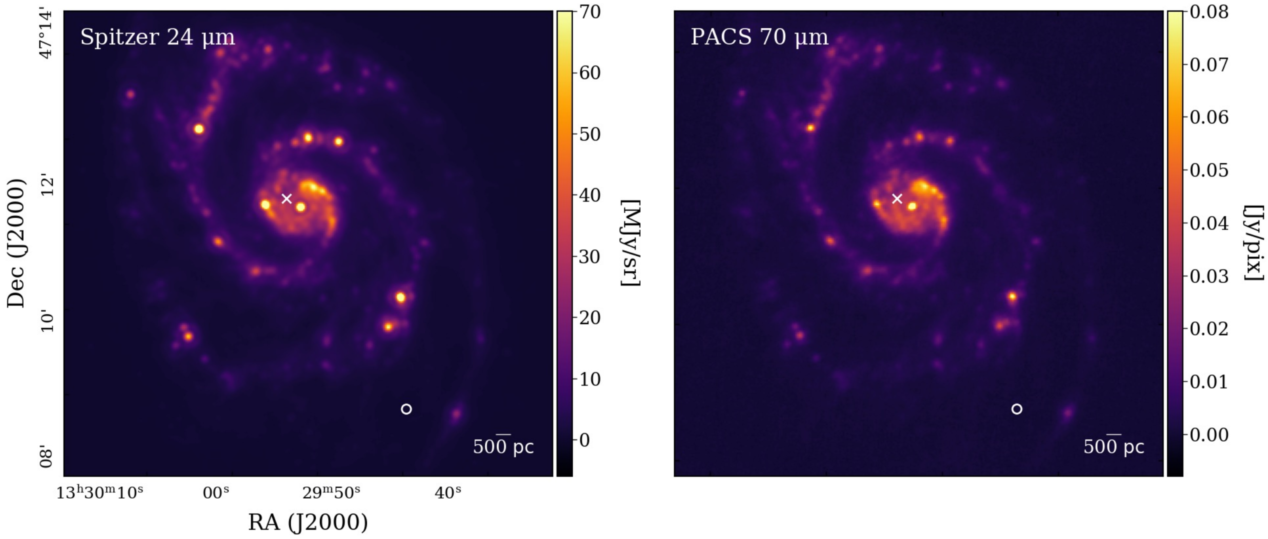

Figure 2.8 – Observations of M51 in 24 μm with *Spitzer* MIPS (*left*) and the 70 μm *Herschel* PACS (*right*). The centre of the galaxy hosts extended warm emission, likely due to heating from old stars (e.g. Schinnerer et al., 2013). The white cross and white circle depict two representative pixels from the centre and disc of the galaxy, respectively.

and Fig. 2.5), as those are the points at which the Σ_{em} and Σ_{ext} stop following a linear trend, potentially due to temperature effects (or different dust properties).

Unlike dust extinction, dust emission is heavily dependent on the dust temperature along the line-of-sight. As a simple single-temperature MBB model is employed to retrieve measurements of column density and temperature for *Herschel* dust emission observations, we intrinsically assume that dust properties do not vary significantly not only along the line-of-sight but also across M51. In the centre of M51 ($R_{\mathrm{gal}} \lesssim 2$ kpc), where a multitude of physical processes are in play, this assumption may not hold. In fact, Muñoz-Mateos et al. (2009) report an excess of dust luminosity in relation to the derived dust mass for the inner 2 kpc of the galaxy. From Fig. 2.8, we can see that in the centre of M51 the dust emission is dominated by extended emission in the MIPS 24 μm (Multiband Imaging Photometer for *Spitzer*, Rieke et al. 2004) and PACS 70 μm dust maps. An increase of 24 μm and 70 μm emission indicate an increase of dust temperatures, which is indeed what is reported by Mentuch Cooper et al. (2012) in M51's centre. This increase in luminosity (and consequently temperature) can be caused by heating from the prominent old stellar population observed at small galactocentric radii (e.g. Schinnerer et al., 2013; Nersesian et al., 2020, and references therein).

Our single-temperature SED fit from 160 μm onwards cannot accurately describe this diffuse warm emission in the centre. Figure 2.9 depicts an example of an SED curve of a pixel within the inner 2 kpc of M51 (highlighted by a white cross in Fig. 2.8). It is clear that with this wavelength coverage, we are not able to effectively capture the turnover in the SED towards

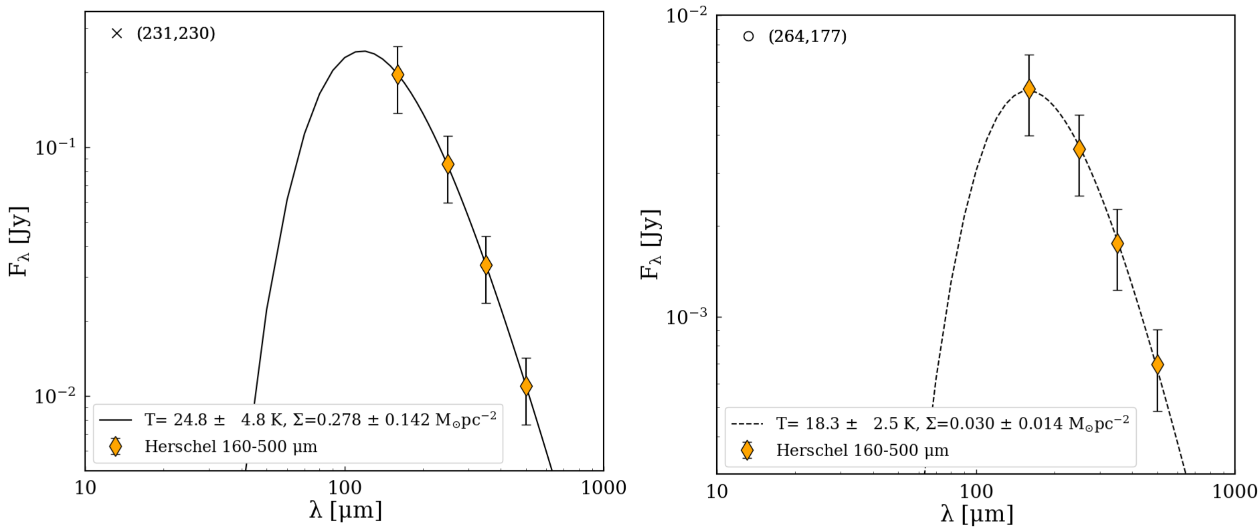

Figure 2.9 – Examples of fitted SED curves for a representative pixel within the centre of M51 (*left*), and for a pixel within the disc of the galaxy (*right*). In both plots, the upper left corner shows the coordinates of the chosen pixel, as well as the corresponding marker shown in Fig. 2.8. The orange diamonds represent the fitted *Herschel* data points, with the black errorbars displaying the uncertainty on the flux. For the central pixel shown in the top panel, the modified blackbody model fits a temperature of $T \simeq 25 \pm 5$ K and a dust surface density of $\Sigma \simeq 0.28 \pm 0.14$ $\mathrm{M_\odot\,pc^{-2}}$. For the disc pixel in the bottom panel: $T \simeq 18 \pm 2$ K and $\Sigma \simeq 0.03 \pm 0.01$ $\mathrm{M_\odot\,pc^{-2}}$.

shorter wavelengths, which is reflected on the larger uncertainties in the fitted temperatures and surface densities. The right panel of Fig. 2.9 shows instead the SED curve of a pixel within the disc (highlighted by a white circle in Fig. 2.8), where the SED turnover is better constrained. In order to capture the higher temperatures in the centre, we would require a more sophisticated SED model to fit *Spitzer* and *Herschel* emission together (rather than a simple blackbody curve), which is beyond the scope of this work. Since the goal was simply to retrieve a statistically reliable conversion between dust emission and dust extinction column densities, we opt for using the bulk of the disk of M51 where the simplified SED fitting is more reliable.

2.4 APPLICATION TO M51 AS A PROOF-OF-CONCEPT

Recalling Eq. 1.14, it is possible to convert the calibrated opacities, τ_V, into dust surface densities through a dust absorption coefficient, $\kappa_V = 1.786$ $\mathrm{pc^2\,M_\odot^{-1}}$ (D03). Additionally, assuming a dust-to-gas mass fraction of 0.01, and that the gas and dust are well-mixed, the dust surface densities are easily converted into their gas equivalent. The resulting gas surface density map, Σ_{gas}, will inherit the resolution and pixel scale of the optical depth map (0.14" and 0.049"/pix, respectively), which translates into a spatial resolution of ~ 5 pc for M51 at the adopted distance of 7.6 Mpc (Ciardullo et al., 2002). Fig. 2.10 showcases the final high-resolution

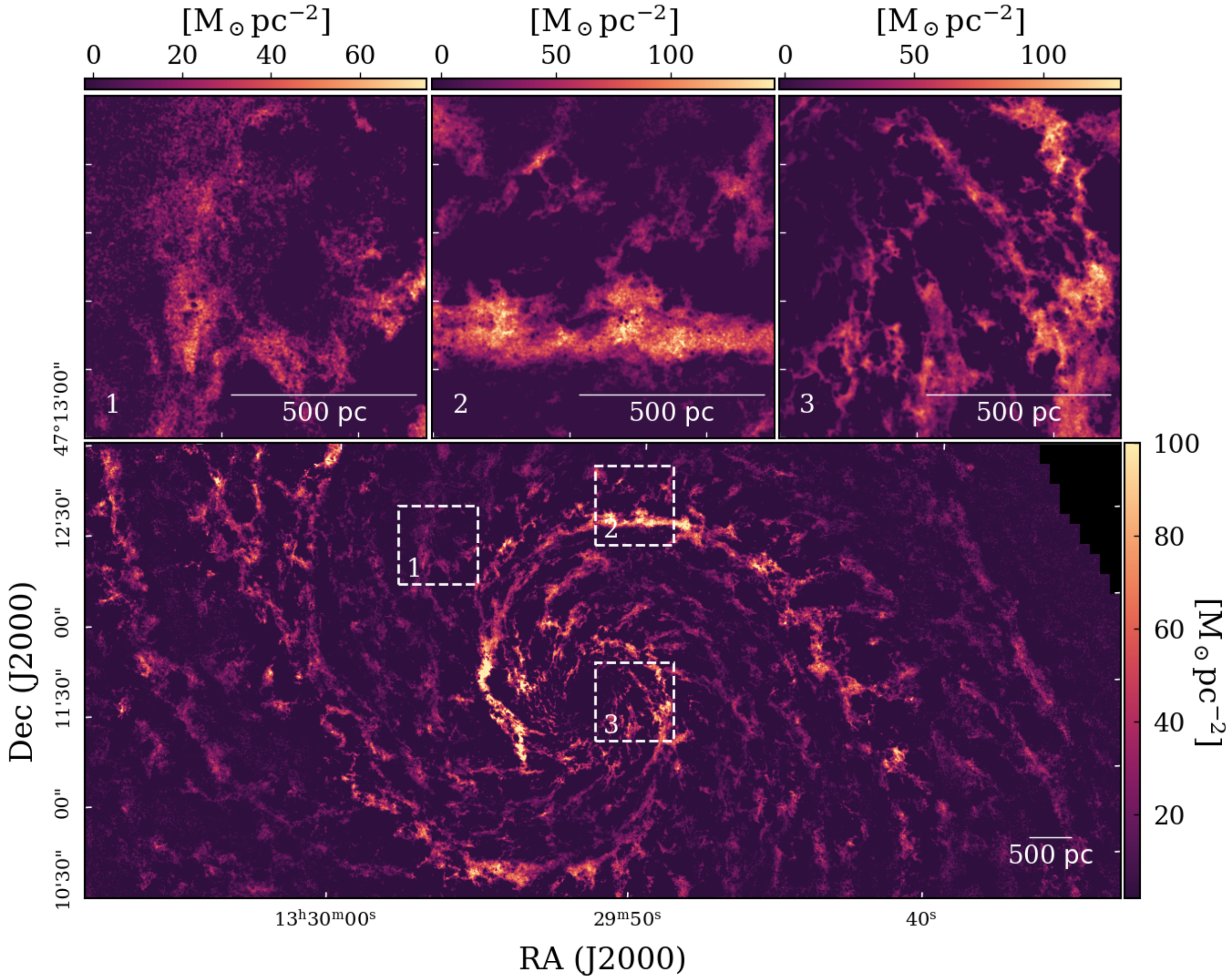

Figure 2.10 – Gas surface density map of a portion of M51 resulting from the high-resolution extinction-mapping technique (*bottom*), with zoom-ins of three example regions in the inter-arm (1), spiral arm (2) and centre (3), shown in the top row.

gas surface density distribution resulting from the extinction mapping technique for M51[6].

2.4.1 Impact of dust absorption coefficient

As previously stated, this extinction technique employs the D03 specific opacity for the V-band and the OH94 specific opacity at intermediate densities for the IR. Consequently, the calibrated gas surface densities will reflect these dust estimates. In order to calibrate the background/foreground split of stellar light in relation to the dust (Section 2.3.4), the technique requires that the opacity laws used in the two different wavelength regimes (i.e. visual and IR) be consistent with each other. Keeping κ_V from D03 and instead adopting $\kappa_{250\mu\mathrm{m}} = 3.98\ \mathrm{cm}^2\,\mathrm{g}^{-1}$ from Mentuch Cooper et al. (2012) to construct Σ_{em}, for example, would lead the calibration procedure to output a background fraction of just $b = 0.13$ (i.e. only the bottom 13% of the stellar light in M51 would be attenuated), and the calibrated optical depth would peak at values of roughly 14.3. Additionally, over a quarter of the final map would be saturated, preventing us from estimating an opacity value in a significant portion of M51.

Alternatively, one could fix the background/foreground light fraction and instead attempt to retrieve a new dust absorption coefficient in the optical that would match the $\kappa_{250\mu\mathrm{m}}$ from Mentuch Cooper et al. (2012) (or any other $\kappa_{250\mu\mathrm{m}}$). Remembering Eq. 1.14, the new specific opacity in the visual, κ_V^{new}, would simply be the ratio between τ_V (assuming a fixed $b = 0.53$ and $f = 0.47$) and the dust emission surface densities derived using $\kappa_{250\mu\mathrm{m}}$ from Mentuch Cooper et al. (2012), $\Sigma_{\mathrm{em}}^{\mathrm{new}}$. This results in a median $\kappa_V^{\mathrm{new}} = 0.345\ \mathrm{pc}^2\,\mathrm{M}_\odot^{-1}$, or $\kappa_V^{\mathrm{new}} = 1.65 \times 10^3\ \mathrm{cm}^2\,\mathrm{g}^{-1}$. Utilising this combination of absorption coefficients (i.e. $\kappa_{250\mu\mathrm{m}}$ from Mentuch Cooper et al. 2012 and the derived κ_V^{new}) results in a final gas surface density map with values a factor ~ 5 larger than the original map (with OH94), but otherwise retains the same structure (i.e. the maps are proportional to each other).

It is possible to write a scaling relationship between our calibrated extinction surface densities, Σ_{ext} (using OH94 and D03), and other dust absorption coefficients for the IR:

$$\Sigma_{\mathrm{ext}}^{\mathrm{new}} = \left(\frac{21.6\,\mathrm{cm}^2\mathrm{g}^{-1}}{\kappa^{\mathrm{new}}} \right) \Sigma_{\mathrm{ext}}, \tag{2.8}$$

where $\Sigma_{\mathrm{ext}}^{\mathrm{new}}$ is the extinction-derived gas surface density map resulting from calibrating to a different opacity law in the IR (κ^{new} at 250 µm). It is important to note that although this allows for the use of different dust absorption coefficients (and therefore different dust models), this scaling relationship is only true if the background/foreground fraction (b/f) is fixed at

[6]This map is publicly available at https://dx.doi.org/10.11570/23.0010, and also at the FFOGG (Following the Flow of Gas in Galaxies) project website (https://ffogg.github.io/ffogg.html).

$b = 0.53$ and $f = 0.47$. Since the relationship between b/f and the assumed opacity laws is not linear, it is not possible to calibrate for both b/f and κ_λ at the same time. In this work, we prefer to adopt an established value of κ_λ from the literature and calibrate for b/f instead.

As previously stated, adopting a different combination of specific opacity laws will only change the final gas surface density map by a scaling factor; the observed structural hierarchy, or environmental trends, will remain the same. As will be shown in the following sections, after correcting for the difference in dust recipes used (i.e. applying a scaling factor), the high-resolution extinction mapping technique is able to retrieve similar gas/dust surface density (and optical depth) values to estimates of other studies which apply various independent approaches.

2.4.2 Comparison with other dust studies

The dust extinction technique outlined in this Chapter is one of many ways of measuring the dust mass of galaxies (see e.g. Calzetti, 2001, and Section 1.3.2). One such method involves measuring the reddening of stellar light in order to retrieve colour-based extinction maps (e.g. Regan, 2000; Thompson et al., 2004; Kainulainen et al., 2007). For M51, Holwerda et al. (2007) constructed a colour map using near- to mid-IR bands, (I - L), and found an average optical depth of $\tau_{(I-L)} = 0.18 \pm 0.09$ within one of the areas imaged by WFPC2 aboard HST. For roughly the same region in our map (coverage differs due to the cropping of NGC 5195 here), we report a similar median optical depth ($\tau_V = 0.15 \pm 0.1$).

Colour-based extinction approaches often assume a simple foreground dust screen geometry and a single colour (and consequently age) for the stellar population, with the resulting dust masses being systematically lower than estimates from attenuation of ionised gas emission lines (e.g. Kreckel et al., 2013). An alternative method to measure the dust mass within a galaxy is to perform radiative transfer simulations. These high-resolution models can account for more complex dust/stars geometry, as well as different dust heating sources (e.g. young ionising stars, old stellar population, AGN). Nersesian et al. (2020) utilise a state-of-the-art 3D radiative transfer simulation, which includes the `THEMIS` dust model (Jones et al., 2013, 2017), and the `CIGALE` SED fitting routine (Noll et al., 2009; Boquien et al., 2019). They find that the M51 system holds a total dust mass of $M_{\rm dust} = 3.40\,(\pm0.65) \times 10^7$ M$_\odot$ for a dust absorption coefficient of $\kappa_{250\mu\rm m} = 6.40$ cm^{2}g^{-1} (adapted from the `THEMIS` model). Our high-resolution extinction technique retrieves a dust mass for M51 (i.e. just NGC 5194) of $M_{\rm dust} = 9.70 \times 10^6$ M$_\odot$. As discussed above (Section 2.4.1) and shown in Eq. 2.8, we can apply a scaling factor to our estimates of dust surface density to account for a different dust absorption coefficient assumed for the IR. Using the specific opacity from the `THEMIS` model would scale our surface densities by roughly a factor 3.4, resulting in a final dust mass of $M_{\rm dust} = 3.27 \times 10^7$ M$_\odot$, which is consistent with the dust mass range found by Nersesian et al. (2020)[7]. Using a similar radiative transfer simulation but with the Draine et al. (2007) dust recipe, De Looze et al. (2014) retrieve a dust mass of $M_{\rm dust} = 7.70 \times 10^7$ M$_\odot$ for M51. Again following Eq. 2.8, our estimate for the total dust mass would increase by roughly a factor 5 if we had adopted the Draine et al. (2007) absorption coefficient in the dust emission modelling (equivalent to $\kappa_{250\mu\rm m} = 3.98$ cm^2 g^{-1}, Mentuch Cooper et al. 2012), which is within a factor 0.7 of the mass value quoted by De Looze et al. (2014).

2.4.3 Comparison with CO

Molecular line observations of the CO(1-0) emission are one of the most commonly used tracers for the invisible, cold H_2 in the molecular ISM. Unlike H_2, at the cold temperatures characteristic of MCs, CO - the second most abundant molecule in the ISM - is still easily excited. Despite this, CO emission is not always sensitive to the total gas column within a cloud, as was already addressed in Section 1.3.1. Additionally a CO-to-H_2 conversion factor is often used to retrieve the molecular column densities of MCs using CO observations (Eq. 1.1). $X_{\rm CO}$ is an empirically derived value, and is known to have a large uncertainty associated to it (e.g. Lada et al., 2007; Bolatto et al., 2013; Barnes et al., 2018). The most commonly adopted value of $X_{\rm CO}$ is the Galactic $X_{\rm CO} = 2 \times 10^{20}$ cm^{-2} (K km s^{-1})$^{-1}$, obtained through observations of MCs in the Milky Way disc (Strong & Mattox, 1996; Dame et al., 2001). However, many studies suggest that $X_{\rm CO}$ varies significantly from galaxy to galaxy, and even within different environments of the same galaxy (e.g. Pineda et al., 2008; Sandstrom et al., 2013).

In the PAWS field-of-view (FoV, shown in Fig. 2.11), Colombo et al. (2014a) quote 84 M$_\odot$ pc^{-2} as the median gas mass surface density value, derived assuming the Galactic $X_{\rm CO}$. If we estimate the median in the same region that PAWS imaged (and at the same angular resolution and pixel grid), but using the extinction surface densities instead, we obtain a much lower value ($\sim$ 7 M$_\odot$ pc^{-2}). This median value is calculated considering only surface densities within the PAWS FoV above 5σ, where σ, the average standard deviation in low-emission areas, is 0.44 M$_\odot$ pc^{-2}. Dust extinction traces the total gas, whilst CO traces only the molecular gas; calculating the same median only in regions more likely to be molecular (i.e. $\Sigma > 10$ M$_\odot$ pc^{-2}) gives a value of roughly $\sim$ 20 M$_\odot$ pc^{-2}. Both of the medians we report within the PAWS FoV are much smaller (between a factor 4 to 12 smaller) than the PAWS gas surface density median computed using the Galactic $X_{\rm CO}$, even when only considering pixels above a molecular surface density threshold.

Guélin et al. (1995) find that their dust-derived molecular masses are about a factor 4 smaller than masses computed from CO$(1-0)$ emission using the Galactic $X_{\rm CO}$, suggesting

[7]Although we caution that in the `THEMIS` model, a $\beta = 1.79$ is assumed rather than $\beta = 2.0$.

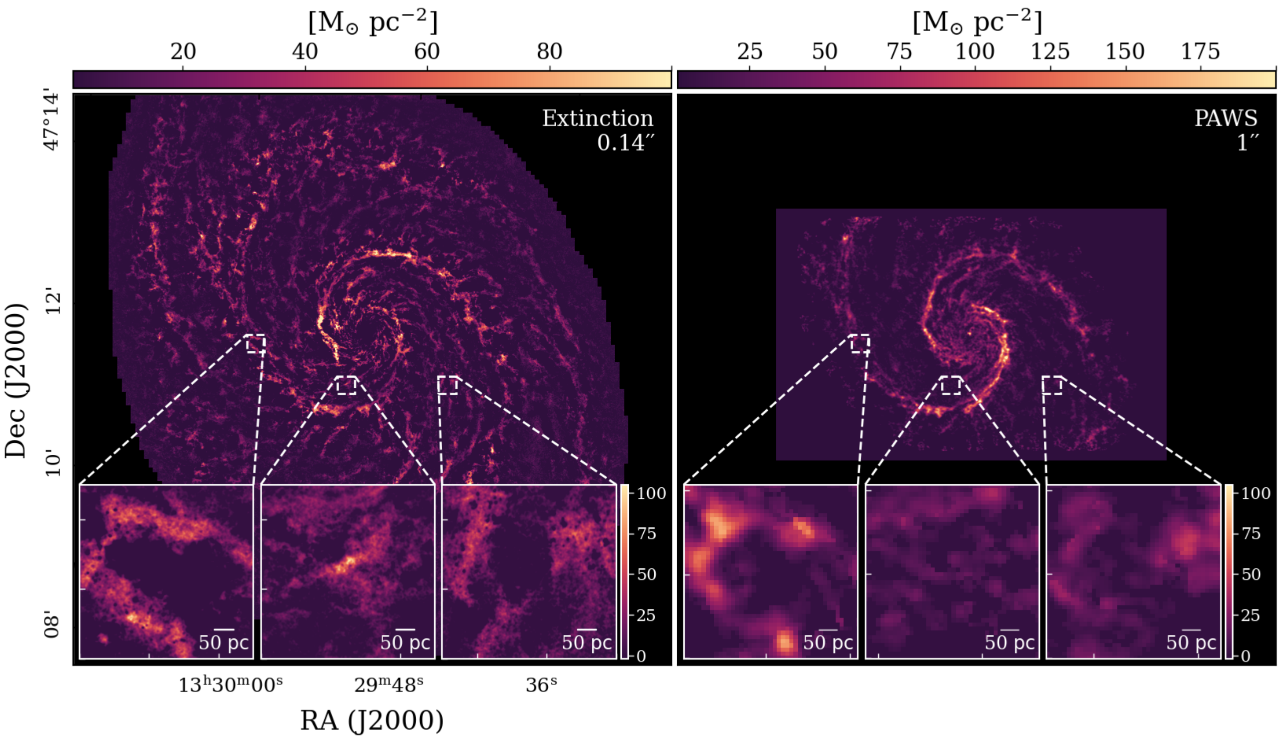

Figure 2.11 – Gas surface density maps, $\Sigma_{\rm gas}$, from the dust extinction method (*left*) compared to the gas surface densities obtained from converting the PAWS ^{12}CO(1-0) integrated intensity with $X_{\rm CO} = 3.14 \times 10^{19}$ cm^{-2} (K km s^{-1})$^{-1}$ (*right*). Zoom-ins of 3 example regions are shown at the bottom of both panels for better visualisation of the spatial resolution achieved by the two different methods (all shown in the same colour scale).

that the CO-to-H_2 conversion factor in M51 might be lower than the Galactic value. Bell et al. (2007) found $X_{\rm CO} = 2.5 \times 10^{19}$ cm^{-2} (K km s^{-1})$^{-1}$ in the centre of M51 through comparison of observed emission line intensity ratios and predictions from photon-dominated region (PDR) chemical models (see also Bell et al., 2006). Using large velocity gradient (LVG) modelling of several transitions of ^{12}CO and ^{13}CO, as well as neutral carbon, Israel et al. (2006) calculated $X_{\rm CO} = 1\,(\pm 0.5) \times 10^{20}$ cm^{-2} (K km s^{-1})$^{-1}$ for the centre of M51. On the other hand, several studies reiterate that the standard Galactic $X_{\rm CO}$ should be applicable in M51 (e.g. Schinnerer et al., 2010; Leroy et al., 2017), given its nearly constant solar metallicity (e.g. Croxall et al., 2015).

In order to make the extinction method's results comparable to the CO results from PAWS, instead of assuming an ad-hoc value such as the Galactic $X_{\rm CO}$, we re-derive the $X_{\rm CO}$ by comparing the PAWS $W_{\rm CO}$ map directly to the surface densities computed from the *Herschel* data (Section 2.2.2.1), as this is also what is used to calibrate the extinction column densities. It is possible to convert the dust emission surface densities into molecular gas column densities, N(H_2), through:

$$\mathrm{N(H_2)} = \frac{\Sigma_{\rm em,gas}}{\mu\, \mathrm{m}_H}, \tag{2.9}$$

where $\Sigma_{\rm em,gas}$ is the gas surface densities from *Herschel* (converted from dust, $\Sigma_{\rm em}$, assuming a dust-to-gas mass ratio of 1%), m_H is the mass of a hydrogen atom, and μ the mean molecular weight. Here, a mean molecular weight of $\mu = 2.8$ is adopted (Kauffmann et al., 2008)[8]. The PAWS $W_{\rm CO}$ map is regridded and convolved to the pixel grid (3.2"/pix) and resolution (36") of the *Herschel* column densities. The distribution of the *Herschel* N(H_2) against the convolved PAWS $W_{\rm CO}$ is depicted in Fig. 2.12. The resulting $X_{\rm CO}$ is almost a factor 7 smaller than the Galactic standard: the median is $X_{\rm CO} \simeq 3.14 \times 10^{19}$ cm^{-2} (K km s^{-1})$^{-1}$, with lower and upper quartiles of $X_{\rm CO} \simeq 2.84 \times 10^{19}$ cm^{-2} (K km s^{-1})$^{-1}$ and $X_{\rm CO} \simeq 3.52 \times 10^{19}$ cm^{-2} (K km s^{-1})$^{-1}$, respectively. This derived $X_{\rm CO}$ is within the range of lower $X_{\rm CO}$ values reported for M51 in the literature. It is important to note that this $X_{\rm CO}$ value is solely intended for the purposes of cross-calibration between this work's results and the PAWS CO data, and is certainly a lower limit since the contribution from HI gas was not accounted for.

As previously discussed in Section 2.4.1, the determination of an $X_{\rm CO}$ value for M51 will also be heavily influenced by the assumed dust models (see also Sandstrom et al., 2013; Roman-Duval et al., 2014), as are our final gas surface density estimates. Following Eq. 2.8, it is possible to combine Eq. 1.1 and Eq. 2.9 to give a scaling relation between our determined $X_{\rm CO}$ value and

[8]Already accounting for a contribution from helium of 27%.

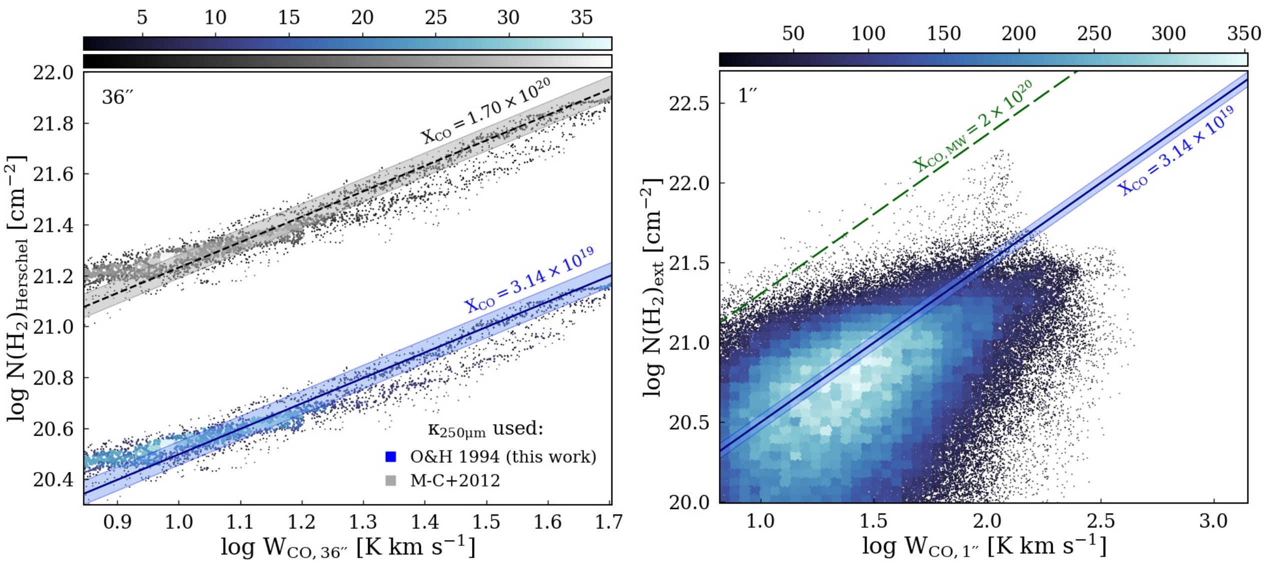

Figure 2.12 – *Left:* H_2 column densities from the *Herschel* dust emission data, $N(H_2)_{Herschel}$, against the integrated line intensity of ^{12}CO(1-0) from PAWS, $W_{CO,36"}$, at the resolution of the dust emission data (36"). The different colours represent the resulting dust emission column densities from adopting two different dust absorption coefficients: the OH94 specific opacity in blue (used in this work), and the Mentuch Cooper et al. (2012) specific opacity in grey (see Section 2.4.1). *Right:* H_2 column densities resulting from our extinction technique, $N(H_2)_{ext}$, also against the integrated line intensity of ^{12}CO(1-0) from PAWS, at the resolution of PAWS ($W_{CO,1"}$). In both panels: the solid blue line represents the value of X_{CO} retrieved assuming the OH94 (O&H 1994) dust absorption coefficient in the IR (see text for details) with the blue-shaded region being the interquartile spread on said X_{CO} at the *Herschel* resolution. The blue (and grey) scale in both plots represents the density of points. In the left panel, the dashed black line represents the resulting X_{CO} when assuming $\kappa_{250\mu m}$ from Mentuch Cooper et al. 2012 (M-C+2012). In the right panel, the green dashed line depicts the standard Galactic $X_{CO,MW}$.

the adopted absorption coefficient for the IR:

$$X_{\rm CO}^{\rm new} = 3.14 \times 10^{19} \left(\frac{21.6\,{\rm cm^2 g^{-1}}}{\kappa^{\rm new}} \right), \tag{2.10}$$

where $X_{\rm CO}^{\rm new}$ is the CO-to-H_2 conversion factor obtained when assuming a given dust absorption coefficient, $\kappa^{\rm new}$, at 250 µm. In particular, taking $\kappa^{\rm new} = 3.98$ cm^2 g^{-1} from Mentuch Cooper et al. (2012), retrieves a value of $X_{\rm CO}$ within a factor 0.5 from the standard Galactic value (shown in left panel of Fig. 2.12).

The main goal in determining a CO-to-H_2 conversion factor is to make the surface densities from PAWS comparable to our results. In fact, if we compare the PAWS $W_{\rm CO}$ with the extinction column densities at the PAWS resolution (right panel of Fig. 2.12), we can see that the $X_{\rm CO} \simeq 3.14 \times 10^{19}$ cm^{-2} (K km s^{-1})$^{-1}$ derived from the comparison with *Herschel* dust emission at kpc-scales works reasonably well at the higher resolution. It is also clear from this figure that adopting the Galactic $X_{\rm CO}$ would overestimate the molecular masses from CO, producing the discrepancy of statistics previously mentioned. Applying the new $X_{\rm CO}$ to the $W_{\rm CO}$ from PAWS gives a median mass surface density of ~ 18 M$_\odot$ pc^{-2} for M51, which is now consistent with the median values we report for the same region at the PAWS resolution. This calculation is only performed in regions with significant CO detections[9], and where our gas surface densities are above 5σ ($\sigma = 0.44$ M$_\odot$ pc^{-2}, as previously mentioned).

Comparing the spatial distributions of the gas surface densities from PAWS with those from the extinction method, there seems to be no substantial change in the surface density medians for the spiral arms between the re-scaled PAWS surface densities and our surface densities at the same resolution (~ 21 M$_\odot$ pc^{-2} and ~ 22 M$_\odot$ pc^{-2}, respectively). There is, however, a difference between the PAWS inter-arm surface density median and our value, with ~ 12 M$_\odot$ pc^{-2} and ~ 17 M$_\odot$ pc^{-2}, respectively. This discrepancy may be due to the enhanced presence of CO-dark gas towards the inter-arm, where CO does not trace the full column of gas due to the lack of shielding, whereas dust extinction is still sensitive.

The median from the re-scaled PAWS surface densities for the centre of M51 is 37 M$_\odot$ pc^{-2}, higher than the median we report for the same area (23 M$_\odot$ pc^{-2}). In the centre of M51, most of the gas is CO-bright, whilst dust extinction is limited to lower estimates of column due to saturation effects, and failures in the removal of bright sources. On the other hand, the centre of M51 is known to host different conditions than the disc (e.g. Mentuch Cooper et al., 2012; Schinnerer et al., 2013; Nersesian et al., 2020). In particular, the dust in that region is hotter due to considerable heating caused by the dominant old stellar population. Therefore, CO-based

[9]The PAWS ^{12}CO(1-0) map is already masked to only contain high-fidelity CO detections.

measurements are likely to be less accurate due to temperature effects. Furthermore, applying a single value of $X_{\rm CO}$ for the centre and the disc is probably not a fair assumption under these conditions (see Sodroski et al., 1995; Bolatto et al., 2013; Gong et al., 2020).

2.4.4 Comparison with HST B-band

The B-band emission is more heavily attenuated by the interstellar dust grains than the V-band, such that we reach saturation with lower dust columns. Consequently, the surface densities of the denser regions of M51 will be less accurately determined with the B-band than with the V-band, and thus we preferably use the V-band for this method. Nonetheless, the technique will still work for the B-band.

We adopt a dust mass absorption coefficient for the B-band of $\kappa_B = 1.19 \times 10^4$ cm^2 g^{-1} ($\kappa_B = 2.49$ pc^2 M$_\odot^{-1}$) from D03. Assuming an initial guess of $b' = f' = 0.5$, the technique corrects the background and foreground fractions of the B-band to $b = 0.52$ and $f = 0.48$, respectively. The ratio between the calibrated maps of τ_V and τ_B has a median of ~ 0.73, which is in agreement with the ratio of the respective specific opacity laws ($\kappa_V/\kappa_B \sim 0.72$). The resulting surface densities, Σ_B, are similar to the final V-band surface densities, with a median $\Sigma_{{\rm gas},V}/\Sigma_B \sim 1.04$, highlighting the fact that the V-band can reach higher surface densities, but that within the uncertainties, both bands perform equally well across the galaxy.

2.5 CONCLUSIONS

This Chapter presents a new dust extinction-based technique that allows the retrieval of high-resolution gas surface density maps for entire galaxies. The method is based on similar work done for our Galaxy in the IR, and consists of determining the dust attenuation pixel by pixel in the optical, through comparison with a reconstructed, smoothly varying stellar background. This method was applied to M51 as a test case, and the final gas surface density map has a resolution of 0.14" (or ~ 5 pc at the adopted distance), which is a factor ~ 7 better physical resolution than the currently highest resolution CO dataset for M51 (PAWS, Schinnerer et al., 2013).

The surface density estimates from extinction are compared to several independent dust- and CO-based approaches, and we find that our map correlates well with lower-resolution dust (and also gas) maps of M51. In particular, we find similar trends of surface density across large-scale environment as those seen in PAWS (Colombo et al., 2014a). Any disparities in gas/dust surface density estimates between our map and other studies arise primarily from the different dust opacity laws used. If the a priori assumptions of dust model are the same, our technique retrieves values of column consistent with independent studies.

A CO-to-H_2 conversion factor almost a factor 7 lower than the standard Galactic $X_{\rm CO}$ is retrieved[10]. Using the specific opacity law at intermediate surface densities from OH94 results in a conversion factor $X_{\rm CO} = 3.1\,(\pm 0.3) \times 10^{19}$ cm^{-2} (K km s^{-1})$^{-1}$, assuming a constant dust-to-gas ratio of 1%. It is also important to note that the constancy of the dust-to-gas ratio, which is assumed in this work, is in itself very uncertain and likely heavily contributing towards the small $X_{\rm CO}$ measured here. We find that the choice of absorption coefficient in the modelling of dust emission (i.e. adopting different dust compositions and therefore emissivity) has a significant influence in the determination of $X_{\rm CO}$. Using a lower dust absorption coefficient instead will result in much higher dust masses, which in turn returns a higher $X_{\rm CO}$ value. In fact, with the absorption coefficient from Draine et al. (2007), we obtain a value similar to the Galactic $X_{\rm CO}$ ($X_{\rm CO} = 1.7\,(\pm 0.2) \times 10^{20}\,{\rm cm}^{-2}$ (K km s^{-1})$^{-1}$).

In summary, the strength of this extinction technique lies in the high spatial resolution of the resulting map (almost an order of magnitude higher than previous studies), obtained from readily available optical data. Furthermore, we are able to probe the lower surface density regime composed of atomic and/or CO-dark molecular gas, thus providing new tools to study the ISM and its morphology in both its atomic and molecular forms. Our extinction technique is also applicable to the full disc of galaxies, providing a wider coverage which greatly enhances number statistics and completeness.

[10]Does not include contributions from HI.

Chapter 3

MOLECULAR CLOUDS IN M51

"When curiosity turns to serious matters,
it's called research"

MARIE VON EBNER-ESCHENBACH

This Chapter is based on the work published in Faustino Vieira et al. (2024). All of the present content is my own original work and analysis. Co-author input came mainly in the form of scientific discussion and reviewing, unless explicitly stated.

3.1 INTRODUCTION

Stars form in the cold and dense molecular phase of the ISM in galaxies. The mechanism (or mechanisms) that trigger and regulate star formation in galaxies is still not well understood. In particular, it is not clear if the galactic environment has a direct impact on the galaxy's ability to form stars, or serves just to re-organise and gather star-forming fuel (i.e. molecular gas; see also Section 1.4.4). Additionally, even if star formation is not directly enhanced by the galactic environment, the large-scale dynamics may still play a critical role in regulating and disrupting star formation across galaxies.

The molecular ISM of a galaxy is often divided by astronomers into discrete structures (i.e. molecular clouds), in order to better understand the initial conditions of star formation. It is possible to investigate the link (or lack of) between the small, cloud-scale physics and the overarching galactic dynamics by analysing any systematic differences between clouds situated within different large-scale environments (i.e. spiral arms, inter-arm, bars). In other words, by comparing the different cloud populations within galaxies (as well as across different galaxies), we can begin to understand if a galaxy's morphology and dynamics have a direct impact in its ability to form stars.

These complex dynamics are of course expected to have a significant effect on the ISM of a galaxy, and it is important to understand the connotations this will have with star formation. Following their study of GMCs in M51, Koda et al. (2009) propose an evolutionary picture: the spiral arm potential well encourages the molecular gas to consolidate into massive giant associations, which are then stretched apart and fragmented into smaller, lower-mass, elongated structures as they exit the spiral arms and encounter intense shear (see also La Vigne et al., 2006). This picture is supported by several other observational and numerical studies that report an abundance of filamentary objects in the inter-arms (e.g. Ragan et al., 2014; Duarte-Cabral & Dobbs, 2016, 2017), and high-mass objects in the spiral arms (e.g. Dobbs et al., 2011; Miyamoto et al., 2014; Colombo et al., 2014a). It is important to note the effect of resolution in these findings however, since lower resolution can blend structures into massive associations, notably in crowded regions like the spiral arms. In another study of M51, Meidt et al. (2015) found that both shear driven by galactic dynamics and stellar feedback can be responsible for disrupting clouds, and consequently suppressing star formation. More recently, Chevance et al. (2022) argue that early (pre-supernovae) stellar feedback mechanisms are the main driver of cloud disruption in galaxies. Determining which is the dominant process in star formation regulation (shear or stellar feedback), and where in galaxies this occurs, is crucial to better understand cloud lifecycles and lifetimes, and their role in star formation and in galaxy evolution. With the dust extinction technique presented in Chapter 2, we are able to break up large cloud associations and resolve cloud structure with a lot more detail, and thus observe the impact of these disruption mechanisms on individual clouds.

This Chapter holds an examination of the properties of extinction-derived clouds in search of systematic differences between large-scale environments, which could suggest a direct link between cloud-scale physics and galactic environment. Presently, there is no attempt to pinpoint the exact driver of different characteristics in cloud populations (i.e. driven by shear or stellar feedback), but the resulting spatially resolved cloud catalogue does allow for such an exercise. Section 3.2 describes the extraction of clouds from the extinction-derived map of M51. The properties of this extensive cloud sample are analysed across large-scale galactic environment (Section 3.3), as well as with galactocentric distance (Section 3.4). A summary of the findings can be found in Section 3.5.

3.2 CLOUD POPULATION FROM HIGH-RESOLUTION EXTINCTION METHOD

The gaseous content of galaxies is a multiphase continuum, and therefore "clouds" are not naturally occurring structures. Still, dividing the ISM into discrete clouds is a well-established technique that allows us to analyse the conditions of a galaxy's ISM in a statistical manner. In order to study how the properties of M51's ISM vary as a function of the galaxy's large-scale dynamics and galactocentric distance, we must first extract clouds from our extinction-derived surface density map (Σ). In Chapter 2, a novel technique was presented which retrieves measurements of dust extinction along each line-of-sight for entire disc galaxies at parsec-scales, using archival HST optical data (in F555W or V-band). The application of this extinction technique to M51 resulted in a gas surface density map of the galaxy at a spatial resolution of ~ 5 pc (0.14"), with which we are able to study spatially resolved cloud populations across the galaxy. Here, an inclination of 22° (Tully, 1974; Colombo et al., 2014b), a position angle of 173° (Colombo et al., 2014b), and a distance of 7.6 Mpc (Ciardullo et al., 2002) are adopted for M51.

3.2.1 `SCIMES` cloud decomposition

The gas surface densities derived from the technique outlined in Chapter 2 are decomposed into discrete clouds using the `SCIMES` clustering algorithm (v.0.3.2)[1], initially described in Colombo et al. (2015). The updated version of `SCIMES` used here is detailed in Colombo et al. (2019). `SCIMES` works on the dendrogram tree of the input image - building the dendrogram from the gas surface density map is therefore the first step in the cloud extraction process.

A dendrogram (Rosolowsky et al., 2008) is comprised of three types of hierarchical structures: *trunks* or "ancestors", which are the lowermost structures in the hierarchy of the input map from which all other structures in the dendrogram stem from; *branches* which are the intermediate structures within the tree (i.e. structures that both have a parent and at least one child structure associated to them); and *leaves*, the structures at the very top of the hierarchy with no child structures associated to them. This study makes use of the `ASTRODENDRO`[2] implementation package to compute a dendrogram. `ASTRODENDRO` requires three initial inputs: `min_value` (the minimum threshold below which no value is considered when building the dendrogram), `min_delta` (the minimum difference between two peaks for the dendrogram to consider them as two separate, independent structures), and `min_npix` (minimum number of pixels a structure must have to be considered an independent structure). To obtain the full dendrogram of our surface density map, we choose `min_value`$= 2\ \mathrm{M_\odot\,pc^{-2}}$, `min_delta`$= 9\ \mathrm{M_\odot\,pc^{-2}}$, and

[1] https://github.com/Astroua/SCIMES/
[2] http://www.dendrograms.org/

min_npix = 27 pix as our parameters. A min_value slightly above 0 is chosen to help segment the most diffuse material into trunks of a manageable size (if taking min_value = 0 $M_\odot\,pc^{-2}$, the larger trunks would span almost the entire map). Tests were conducted in several small regions of M51 to check the effect of this lower threshold - no significant differences were observed on the final SCIMES extraction (except on the exact position of the boundaries of the most diffuse clouds), since most clouds are segmented above this threshold. This choice of minimum value dismisses only 4.4% of the total number of pixels in our map, which hold only 0.1% of the total mass. To ensure that all structures within the dendrogram are spatially resolved, min_npix is set to be roughly equal to the number of pixels equivalent to 3 resolution elements (~ 9 pixels per resolution element). Tests were performed with different values of min_delta, from $3\times$ the min_value (i.e. 6 $M_\odot\,pc^{-2}$) to $6\times$ the min_value (i.e. 12 $M_\odot\,pc^{-2}$), in various small regions of the map, finding no significant difference in the final selection of structures, suggesting that the SCIMES segmentation outputs are not strongly impacted by the choice of dendrogram input parameters (Colombo et al., 2015).

Using the dendrogram as a guide, SCIMES uses graph theory to perform spectral clustering and find regions with similar properties in emission (or in our case, in surface density) (Colombo et al., 2015). In practice, SCIMES creates a graph that connects all leaves of the dendrogram (even those that do not have the same parent trunk) to build an affinity matrix that quantifies the relationship strength between the leaves. This process becomes extremely computationally (and memory) intensive when applied to large maps such as ours. To make cloud extraction more manageable, splitting the map into smaller sections is necessary. The most common way of doing this is to apply straight cuts to the data, which then requires dealing with clouds that touch those sharp edges separately (as e.g. Colombo et al., 2019; Duarte-Cabral et al., 2021). Here, a different approach is adopted, and "organic" masks are defined using the trunk structures from the dendrogram, since these structures are at the bottom of the hierarchy and encompass all other structures present in the data. From the full dendrogram, 29752 trunks in total were retrieved. Ancestors that have just one child structure and ancestors that have no children structures (i.e. isolated leaves) cannot be clustered and therefore bypass the need to run the SCIMES clustering algorithm on them - they can directly be considered clouds. The masks of the remaining ancestor structures (3406) are then retrieved and sorted into 4 horizontal strips of 0.03° (~ 2 arcmin), according to the Declination of their centroid position. This allows us to create 4 non-overlapping sub-fields of the gas surface density map that, alongside the dendrogram, can be fed to SCIMES.

For the cloud extraction with SCIMES, we opt to use the "radius" criterion for the clustering, with a user-defined scaling parameter of 90 pc (about two times the typical Milky Way GMC size, e.g. Blitz 1993), to aid SCIMES on the identification of structures of a few tens of parsecs

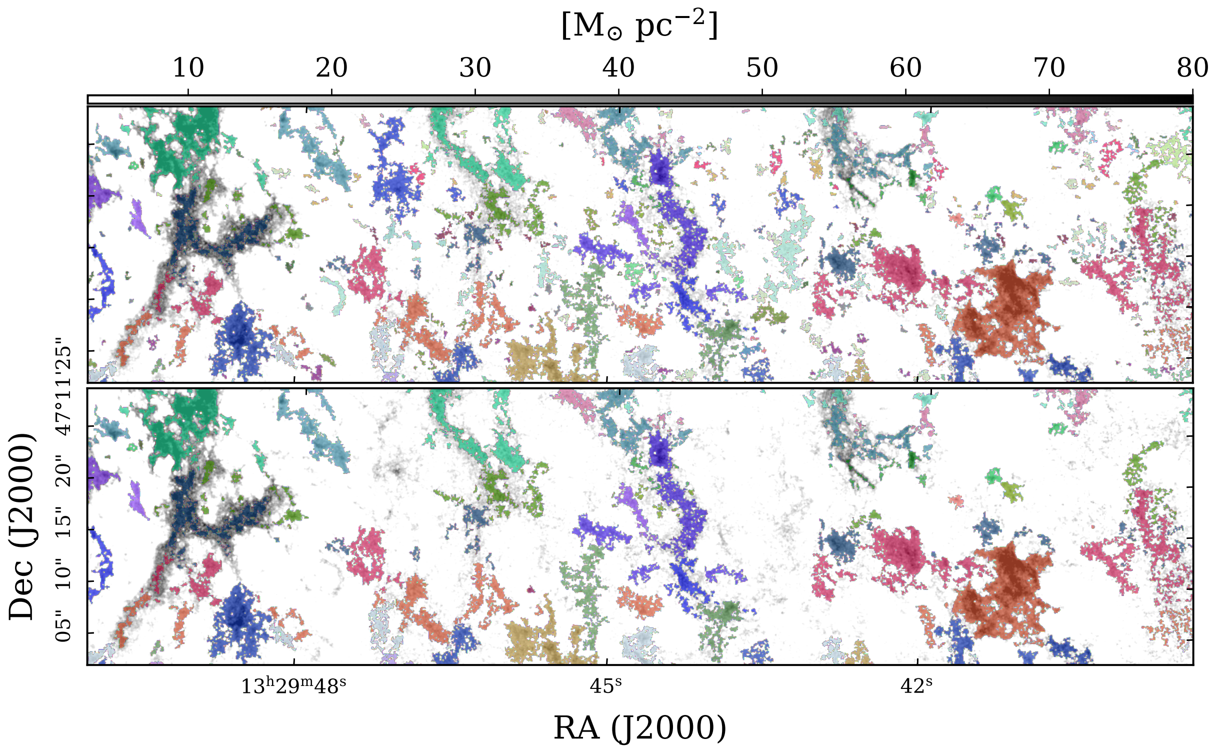

Figure 3.1 – Example of the cloud extraction performed with `SCIMES`, where the cloud masks are overlaid with different, random colours in transparency, and the gas surface density is in the background greyscale. For the same region, the top panel shows the full `SCIMES` extraction (i.e. full cluster sample), and the bottom panel shows the sub-sample of molecular clouds as per the science cut (see Section 3.2.2 for details).

equally across the 4 fields and make the cloud extraction more robust. If left to decide the scaling parameter on its own, `SCIMES` works out the number of clusters to assign based on the contrast of the affinity matrices by default. As such, any given structure can change the way the dendrogram leaves are clustered depending on the dynamic range of the dataset. The dynamic range present within structures in the complex inner parts of M51 will be very different from the range present in the more diffuse outer parts. Therefore, in regions that span more hierarchical levels, the `SCIMES` extraction could potentially differ from the more "flat" regions (i.e. outskirts) without defining a common scaling parameter, making the clustering non-comparable between regions. The `SCIMES` segmentation recovered a total of 25291 clusters across the 4 sub-fields. Including the smaller ancestors that were directly put aside from the original dendrogram, our full sample has 51633 clouds. We produce a catalogue with the properties of the full cloud sample as well as the cloud assignment map for M51 which are made available at `https://dx.doi.org/10.11570/23.0030`. The cloud properties held in the catalogue are detailed in Section 3.2.3.

3.2.2 Sub-sample of molecular clouds

Stars are known to form in the coldest and densest (i.e. molecular) phase of the ISM. To establish any link between star formation and galactic dynamics it is, therefore, necessary to focus on the structures encompassed in the star-forming molecular gas. The cloud catalogue of this work makes no distinction between atomic and molecular clouds since dust traces the total gas and no restrictions were imposed on the cloud extraction itself. To retrieve a molecular sub-sample, we can impose a surface density threshold from which we expect the ISM to be dominantly molecular. Consequently, we consider only the clouds with average surface density above 10 $M_\odot\,pc^{-2}$ (e.g. Bigiel et al., 2008; Saintonge & Catinella, 2022) as molecular clouds. To make sure the molecular clouds are well-resolved, we also impose that its footprint area be larger than 3 beams ($\sim$ 28 pix, or an area A of roughly 90 pc^2). Finally, this technique works out the dust attenuation through comparison with a reconstructed, smoothed stellar background. Therefore, structures that are picked up in regions with a faint background are not likely to be as well-defined as clouds in areas where the stellar background is more robust. We adopt a robust background threshold of $I_0 = 0.09$ e$^-$/s (justification of this choice in the following Section 3.2.3). Each of these criteria has a corresponding flag in the full cluster catalogue: *Molecular_ cut*, *Size_ cut*, and *Robust_ bg* (see Table 3.1). The resulting sub-sample of molecular clouds (which I will refer to as *science sample* from here on) contains 13258 molecular clouds, which are correspondingly flagged in the full cluster catalogue with *Molecular_ cut*=1, *Size_ cut*=1, and *Robust_ bg*=1. The bottom panel of Fig. 3.1 shows the molecular clouds retrieved for a small section of M51 versus the full sample of clouds for the same region (top panel).

3.2.3 Cluster properties and catalogue

This Section provides a description of the derived properties for all the clusters extracted in this work. Table 3.1 specifies the aforementioned cluster properties as shown in the released catalogue[3].

3.2.3.1 Coordinates

The right ascension and declination of each cloud's centroid (*RA_ deg* and *Dec_ deg*, respectively) was estimated by ASTRODENDRO when building the full dendrogram of the extinction-derived map of M51. The galactocentric distance, *R_ gal*, is estimated between the centroid position of each cloud and the centre of the galaxy. The galaxy's centre position is determined from the PAWS environmental mask. *R_ gal* already takes into account M51's position angle and inclination (173° and 22°, respectively, from Colombo et al., 2014b).

[3] https://dx.doi.org/10.11570/23.0030

Catalogue	Variable	Description
ID		Unique ID number of cloud
RA (J2000)		Right ascension of cloud in *hh mm ss.ss* format
Dec (J2000)		Declination of cloud in *dd mm ss.ss* format
RA_ deg		Right ascension of cloud (degrees)
Dec_ deg		Declination of cloud (degrees)
R_ gal	$\mathrm{R_{gal}}$	Distance of cloud centre to the galactic centre (kpc)
Sigma_ tot		Total sum of the gas mass surface density of every pixel in the cloud (10^3 $\mathrm{M_\odot\,pc^{-2}}$)
Sigma_ avg	Σ_{MC}	Average gas mass surface density of cloud ($\mathrm{M_\odot\,pc^{-2}}$)
Sigma_ peak		Peak gas surface density of cloud ($\mathrm{M_\odot\,pc^{-2}}$)
Area_ ellipse		Area of the ellipse defined by the second moments of the cloud ($\mathrm{pc^2}$)
Area_ exact	A	Exact area of cloud ($\mathrm{pc^2}$)
R_ eq	R_{eq}	Equivalent radius estimated using the cloud's exact area (pc)
Mass	M	Mass of cloud ($\mathrm{M_\odot}$)
Major_ axis_ a	a	Semi-major axis (pc)
Minor_ axis_ b	b	Semi-minor axis (pc)
AR_ ab	$\mathrm{AR_{a/b}}$	Aspect ratio between semi-major and semi-minor axis
PA		Position angle of cloud major axis, measured counter-clockwise from $+x$ axis (degrees)
Length_ MA	L_{MA}	Length of the geometrical medial axis (pc)
Width_ MA	W_{MA}	Width of the geometrical medial axis (pc)
AR_ MA	$\mathrm{AR_{MA}}$	Aspect ratio between the medial axis length and width
Sat_ pix_ area		Portion of cloud's exact area that feature saturated/uncertain pixels (%)
Rel_ err	σ_τ/τ_V	Relative uncertainty on the cloud's opacity (and thus surface density/mass) from the dust extinction technique alone
Env		Tag identifying the environment of the cloud (NB=nuclear bar, MR=molecular ring, SA=spiral arms, IA=inter-arms)
Robust_ bg		Tag identifying clouds detected in robust stellar backgrounds (1=robust, 0=faint)
Molecular_ cut		Tag identifying predominantly molecular clouds, i.e. $\Sigma_{\mathrm{avg}} >$ 10 $\mathrm{M_\odot\,pc^{-2}}$ (1=molecular, 0=atomic)
Size_ cut		Tag identifying clouds that pass the size criteria, i.e. $A >$ 3 resolution elements (1=yes, 0=no)

Table 3.1 – Description of the contents of the molecular cloud catalogue obtained from applying the high-resolution extinction-mapping technique to M51. The second column shows what the relevant quantities are referred as in this Chapter.

3.2.3.2 *Geometrical properties*

From the full dendrogram, ASTRODENDRO also computes the area of the ellipse encompassing each cloud (*Area_ ellipse*), the exact footprint area of a cloud (*Area_ exact*), the semi-major and semi-minor axis of a cloud (*Major_ axis_ a* and *Minor_ axis_ b*, respectively), and the cloud's position angle (*PA*, measured counter-clockwise in degrees from the $+x$ axis in pixel coordinates). Using the exact footprint area of each cloud, its equivalent radius, *R_ eq*, is calculated assuming that the cloud is a circle such that $R_{\mathrm{eq}} = \sqrt{A/\pi}$, where A is the exact area of the cloud.

Determining the aspect ratio of a cloud gives a basic estimate of the cloud's morphology: MCs with aspect ratio close to unity are likely circular, and MCs with high aspect ratio are likely elongated. The first aspect ratio considered here is the intensity-weighted moment aspect ratio, *AR_ ab*, defined as the ratio between a cloud's semi-major axis (*Major_ axis_ a*) and semi-minor axis (*Minor_ axis_ b*). The other aspect ratio metric used here is the medial axis aspect ratio, *AR_ MA*. The medial axis is the longest running spine of a cloud's mask that is also the furthest away from the external edges of the cloud (all holes within a cloud are filled before the calculation). It is not weighted by intensity, and is a purely geometrical approach. The medial axis is found by extracting the "skeleton" of the cloud (i.e. reducing the cloud to its filamentary structure). $\mathrm{AR}_{\mathrm{MA}}$ is then set as the ratio between the medial axis length, L_{MA}, and the medial axis width, W_{MA}, such that: $\mathrm{AR}_{\mathrm{MA}} = L_{\mathrm{MA}}/W_{\mathrm{MA}}$. L_{MA} is simply the length of the determined medial axis, and W_{MA} is twice the average distance from the medial axis to the cloud's external edge. The process of retrieving the medial axis fails when a cloud is too small (not enough pixels to erode away until only the skeleton remains); *AR_ MA* is set to 1 for these cases. We do not attempt to retrieve filamentary structures for "fluffy", diffuse clouds - i.e. clouds that do not pass the robust background cut (further explained in following paragraphs) - in order to economise computational time; *AR_ MA* is set 0 for these.

3.2.3.3 *Masses and surface densities*

The total "flux" of a cloud (i.e. the sum of each pixel's gas mass surface density within a cloud, *Sigma_ tot*) is computed by ASTRODENDRO using the bijection paradigm (see Rosolowsky et al. 2008). The average surface density of each cloud, *Sigma_ avg*, is then estimated by taking the total sum of surface densities within the cloud (*Sigma_ tot*) and dividing it by the cloud's footprint area (*Area_ exact*). Similarly, the peak surface density for each entry in the catalogue, *Sigma_ peak*, is simply the highest surface density observed within a cloud. The mass of the cloud, *Mass*, is then estimated as $M = \Sigma_{\mathrm{avg}}\, A$ (i.e. average surface density of cloud multiplied by its area).

In Chapter 2 (Section 2.3.5), I quantified the uncertainty of our opacity estimates through

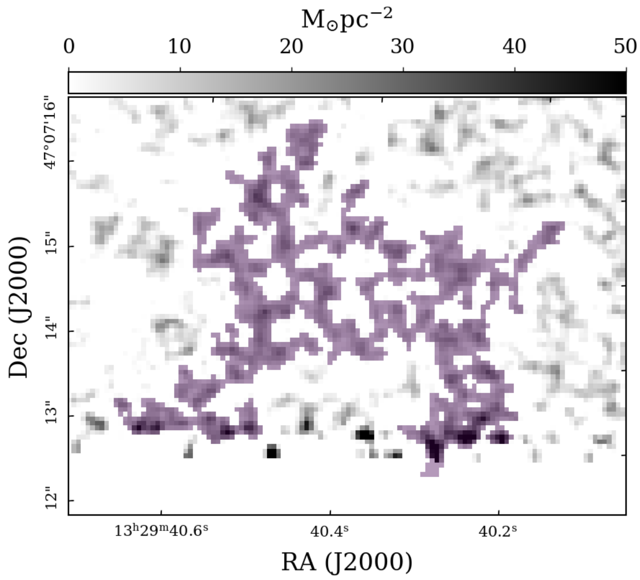

Figure 3.2 – Footprint mask of a cloud in the sample (ID: 3, in purple) that satisfies the size and molecular criteria (i.e. *Size_ cut*=1 and *Molecular_ cut*=1), but is not set against a sufficiently robust stellar distribution (i.e. *Robust_ cut*=0). The gas surface density map is in the background greyscale.

10^4 Monte Carlo realizations for each pixel in the gas surface density map of M51. The science sub-sample, which holds only clouds with average surface density above 10 $M_{\odot}\,pc^{-2}$, has a maximum relative uncertainty of 45%. Above 14 $M_{\odot}\,pc^{-2}$ (the median cloud surface density across the molecular sub-sample, see Table 3.2), the maximum relative error drops below 30%. It is also possible to obtain the relative uncertainty of masses and surface densities for each cloud in the catalogue. We compute the ratio between the total absolute error of the cloud (i.e. sum of the Monte Carlo mass/surface density uncertainties of each pixel inside the cloud in quadrature) and the total mass/surface density of the cloud. Each cloud's relative error on the mass and surface density is listed in the catalogue under *Rel_ err*. In Section 2.3.5, I also determined the maximum surface density we are able to measure reliably given photometric noise, which has little impact in the cloud catalogue. In fact, out of the 13258 clouds that constitute the molecular sub-sample, only 27 clouds have more than 30% of their area containing pixels where the surface density exceeds the maximum measurable surface density.

3.2.3.4 Additional tags

In this analysis, only a subset of the full sample is considered, where we are more certain the clouds are real and dominantly molecular. As described in Section 3.2.2, we consider only clouds that have a footprint area bigger than 3 resolution elements (flagged with *Size_ cut*=1), are above the molecular surface density threshold, $\Sigma > 10\ M_{\odot}\,pc^{-2}$ (*Molecular_ cut*=1), and are

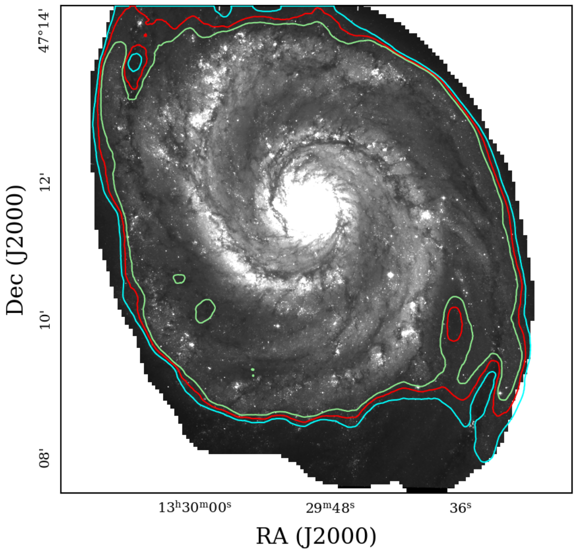

Figure 3.3 – Original HST V-band image of M51. The overlaid contours correspond to 0.08, 0.09 and 0.1 e^-/s levels (green, red, and blue respectively) in the stellar distribution map of M51 (Section 2.3.2).

against a robust stellar background (*Robust_ bg*=1). The last flag is necessary because the technique retrieves extinction features through comparison with a modelled stellar distribution. Consequently, in regions where the stellar distribution is faint, the structures seen in extinction might not be real and are instead artefacts of the choice of background. The cloud shown in Fig. 3.2 (ID: 3) is an example of such a structure. Although its average surface density is above the molecular threshold ($\Sigma_{\rm avg} \sim 10.9$ M$_\odot$ pc^{-2}) and its size is above 3 resolution elements ($A \sim 6.4 \times 10^3$ pc^2), it is not likely to be a real molecular cloud. In fact, almost 41% of the pixels within this object have a measured surface density above the maximum surface density that can be reliably measured (as explained in Section 2.3.5). This cloud borders the edge of M51 where there are not many stars that allow us to retrieve a reliable estimate of the stellar distribution (I_0), which is instrumental for the extinction technique (see Chapter 2 for details). We therefore apply a robust I_0 cut to rule out these diffuse structures. Figure 3.3 shows the original HST V-band image with a choice of I_0 contours overlaid. Taking too large of a cut (e.g. $I_0 = 0.1$ e$^-$/s, shown in green) rules out faint regions within the galaxy itself (which may be real), not just in the outskirts. Taking too little of a cut (e.g. $I_0 = 0.08$ e$^-$/s, shown in blue) will not sufficiently exclude all faint locations. The adopted I_0 threshold ($I_0 = 0.09$ e$^-$/s, shown in red) seems like an adequate choice of cut where most of the galaxy is still considered and the regions without much stellar light are dismissed.

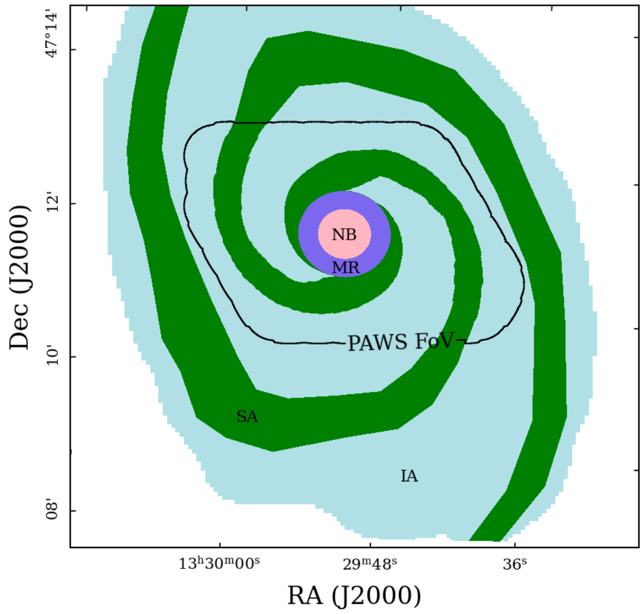

Figure 3.4 – Environmental mask of M51 with the nuclear bar (NB) in pink, molecular ring (MR) in purple, spiral arms (SA) in green, and inter-arm regions (IA) in light blue. The PAWS FoV (field-of-view) is depicted as a black line contour.

3.3 TRENDS WITH LARGE-SCALE ENVIRONMENT

It is unclear if star formation is more efficient in particular regions of galaxies, such as well-defined spiral arms, or if the higher rates of star formation seen towards certain regions are simply a natural consequence of material crowding. If star formation is dependent on the environment, then one could expect the cloud populations of those regions to have systematic differences in their characteristics. Some studies report some dissimilarities between their spiral arms and inter-arm populations (e.g. Koda et al., 2009; Colombo et al., 2014a; Pettitt et al., 2020), whilst other detect no significant differences in the global properties of the cloud population (e.g. Duarte-Cabral & Dobbs, 2016; Treß et al., 2021). The high resolution of our extinction map of M51 (~ 5 pc) provides a unique opportunity to perform an in-depth statistical characterisation of MCs across different dynamical environments.

In order to analyse the environmental dependency of MC properties across the entire disc of M51, we must first construct a mask with the different large-scale environments. The inter-bar and nuclear bar of M51 (NB) are approximated to a circle with galactocentric radius[4] $R_{gal} < 0.85$ kpc, and the molecular ring (MR) to a ring spanning $0.85 < R_{gal} < 1.3$ kpc (Colombo et al., 2014a). The M51 environmental masks (Colombo et al., 2014a, see their Fig. 2) from the PdBI Arcsecond Whirlpool Survey (PAWS; Pety et al., 2013; Schinnerer et al., 2013) of the

[4]The galactocentric radius, R_{gal}, is the deprojected distance to the galactic centre, accounting for the inclination and position angle of M51 (see Section 3.2.3).

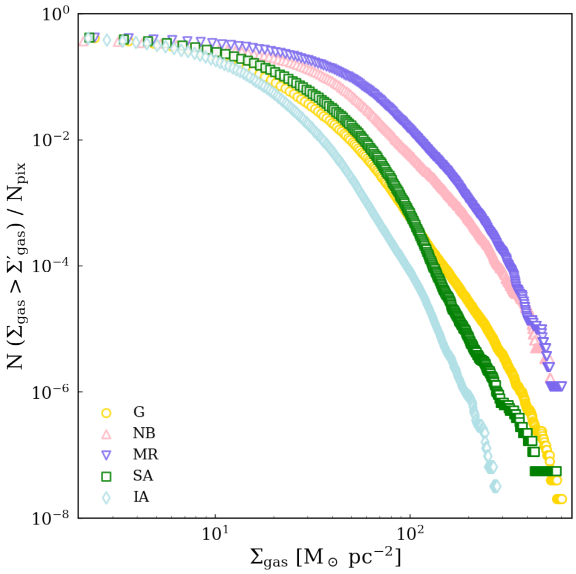

Figure 3.5 – Cumulative distributions of the gas mass surface densities from the full map of M51, Σ_{gas}. The different colours represent the different environments: full galaxy (G) in yellow, nuclear bar (NB) in pink, molecular ring (MR) in purple, spiral arms (SA) in green, and inter-arms (IA) in blue. The y-axis, $N(\Sigma_{gas} > \Sigma'_{gas})$, is the fraction of pixels with surface density greater than a given value. All distributions are normalised by the number of pixels of the relevant environment, N_{pix}. Saturated pixels, i.e. pixels whose column we are not able to retrieve since their observed intensity is lower than the assumed foreground emission, are not considered in this plot.

inner 5 kpc of the spiral arms (SA) and inter-arm (IA) are used, and expanded for the full disc. This is done by using the extinction surface densities (convolved with a $\sim 16''$ median filter) as a guide to continue the spiral arms from the end of the PAWS mask until the edges of the HST map of M51. Given that these masks were done mostly manually, they should not be taken as a strict or accurate definition of the spiral arm positions, instead, they serve as a means to provide all-galaxy statistical estimates. The resulting M51 environmental masks are shown in Fig. 3.4.

3.3.1 Surface density probability density functions

Using the $^{12}CO(2\text{-}1)$ observations from the PHANGS-ALMA survey (Leroy et al., 2021), Sun et al. (2020b) and Querejeta et al. (2021) both report higher gas surface densities towards the centre of galaxies, with a more pronounced increase for barred galaxies. This was attributed to gas inflows driven by bars. Using the higher-resolution surface density map of M51, I investigate these sorts of trends in M51.

Figure 3.5 showcases the reverse cumulative distribution, or probability density function (PDF), of the gas mass surface densities for each environment (normalised by the number of pixels in each environmental mask). Visually, it is clear from the figure that the centre of M51 (NB + MR) hosts overall higher surface densities than the other regions, with the

Env.	Env. tag	$\Sigma_{\rm gas}$	A	$N_{\rm MC}$	$n_{\rm MC}$	$R_{\rm eq}$	log M	$\Sigma_{\rm MC}$	$\rm AR_{a/b}$	$\rm AR_{MA}$	$L_{\rm MA}$
		$\rm M_\odot\,pc^{-2}$	$\rm kpc^2$		$\rm kpc^{-2}$	pc	$\rm M_\odot$	$\rm M_\odot\,pc^{-2}$			pc
(1)	(2)	(3)	(4)	(5)	(6)	(7)	(8)	(9)	(10)	(11)	(12)
Global	G	$8.62^{16.0}_{3.95}$	163.5	13258	81	$8.82^{13.7}_{6.76}$	$3.60^{4.00}_{3.34}$	$14.5^{19.7}_{11.7}$	$1.85^{2.35}_{1.49}$	$3.16^{4.77}_{2.34}$	$28.9^{50.6}_{19.9}$
Nuclear bar	NB	$20.2^{36.9}_{8.86}$	1.95	207	106	$10.9^{21.8}_{7.72}$	$3.93^{4.45}_{3.57}$	$21.0^{30.3}_{14.0}$	$2.05^{2.66}_{1.62}$	$3.32^{5.53}_{2.37}$	$36.1^{82.1}_{23.5}$
Molecular ring	MR	$23.6^{45.1}_{10.2}$	2.6	314	120	$9.47^{15.5}_{6.7}$	$3.87^{4.31}_{3.58}$	$25.8^{39.8}_{16.6}$	$1.93^{2.50}_{1.51}$	$2.75^{4.18}_{2.0}$	$28.9^{52.4}_{18.1}$
Spiral arms	SA	$10.8^{20.3}_{4.85}$	58	6042	104	$8.82^{14.0}_{6.76}$	$3.64^{4.05}_{3.37}$	$15.6^{22.1}_{12.2}$	$1.84^{2.34}_{1.50}$	$3.16^{4.7}_{2.3}$	$28.9^{50.6}_{19.9}$
Inter-arm	IA	$7.53^{13.4}_{3.51}$	101	6695	66	$8.76^{13.3}_{6.68}$	$3.55^{3.93}_{3.31}$	$13.5^{17.3}_{11.4}$	$1.85^{2.34}_{1.49}$	$3.18^{4.87}_{2.36}$	$28.9^{48.7}_{19.9}$

Table 3.2 – Properties of the different environments and of the molecular clouds within each environment of M51. (1) Large-scale environment. (2) Environment abbreviations/tags. (3) Gas mass surface density of the environment, $\Sigma_{\rm gas}$. (4) Area of environment, A. (5) Number of MCs per environment, $N_{\rm MC}$. (6) Number density of MCs per environment, $n_{\rm MC}$. (7) Equivalent radius, $R_{\rm eq}$. (8) Mass, log M. (9) Average gas mass surface density of MCs within the environment, $\Sigma_{\rm MC}$. (10) Ratio between major and minor axis of the MCs, $\rm AR_{a/b}$. (11) Medial axis aspect ratio, $\rm AR_{MA}$. (12) Length of the medial axis, $L_{\rm MA}$. For columns (3) and (7) - (12), the median of the relevant distribution is written, with the lower quartile (Q25) as the subscript, and the upper quartile (Q75) as the superscript.

molecular ring in particular being the densest environment of M51, consistent with the results reported by the PHANGS-ALMA survey (as well as PAWS). In fact, the median of the surface density distribution ($\Sigma_{\rm gas}$, listed in Table 3.2) for the molecular ring is over twice as large as the spiral arms value, and over 3 times the inter-arm value. The molecular ring is effectively a dynamical gas transport barrier where material can accumulate easily, and produce the high densities observed (e.g. Querejeta et al., 2016). When compared to the MR, the nuclear bar $\Sigma_{\rm gas}$ distribution displays a lack of intermediate to high surface densities (80-150 $\rm M_\odot\,pc^{-2}$), hinting at some disruptive mechanism that is absent from the molecular ring (likely streaming motions/shear driven by the bar's potential). The $\Sigma_{\rm gas}$ distribution in the inter-arms shows a steady decline past the 10 $\rm M_\odot\,pc^{-2}$ molecular threshold, consistent with a diffuse region from which we would expect more atomic gas. In comparison, the spiral arms contain a much larger amount of low to intermediate surface densities (10-80 $\rm M_\odot\,pc^{-2}$), although with a steeper decline towards high surface densities.

3.3.2 Molecular cloud properties

Since MCs are not isolated and perfectly spheroidal structures, the complex dynamics of their surroundings are expected to be reflected on the shape and size of the clouds. If there are systematic variations of cloud morphology (as well as mass) between large-scale environments, this could shine a light on the dynamics at play and their impact on the formation and evolution of clouds.

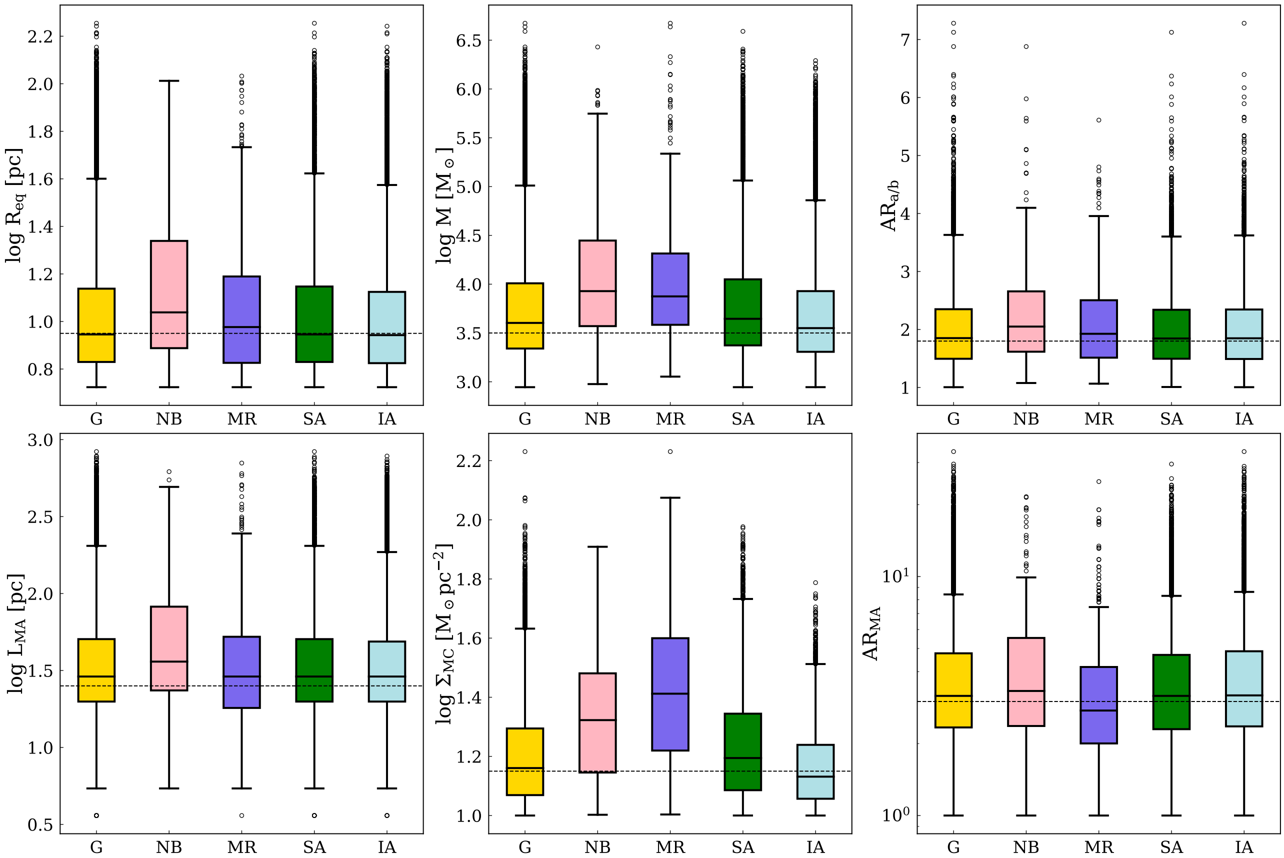

Figure 3.6 – Boxplot representation of properties of the MCs in the science sample for the different large-scale environments of M51 (full galaxy in yellow, nuclear bar in pink, molecular ring in purple, spiral arms in green, and inter-arm in blue): equivalent radius R_{eq} (*top left*), mass M (*top middle*), major/minor axis ratio $\mathrm{AR}_{\mathrm{a/b}}$ (*top right*), medial axis length L_{MA} (*bottom left*), average surface density of MCs Σ_{MC} (*bottom middle*), and medial axis aspect ratio $\mathrm{AR}_{\mathrm{MA}}$ (*bottom right*). The coloured box illustrates the interquartile spread of the distribution (i.e. from 25$^{\mathrm{th}}$ to 75$^{\mathrm{th}}$ percentile), with the solid black line within the box being the median. Circles represent the outliers of the distributions. Dashed lines are reference lines set at arbitrary values for better visualisation.

The various cloud properties analysed in this work are listed in Table 3.2, with some of them also illustrated in Fig. 3.6. Visually, the central region of M51 shows systematic differences from the MCs in the disc, with most of the analysed properties presenting higher median values in the centre. This suggests that M51's centre has a substantial impact in the formation and evolution of all of its clouds (also noted by Querejeta et al., 2021). In particular, MCs located in the molecular ring tend to be denser, whilst in the nuclear bar they seem more elongated (but equally massive). On the other hand, the spiral arm and inter-arm cloud populations do not show significant differences in their statistics, with the exception of the average cloud surface densities and mass, where the SA median is slightly higher. In their simulation of a M51 analogue, Treß et al. (2021) find similar trends in cloud properties; i.e. the central clouds show significantly different characteristics from the disc, whilst the SA and IA cloud populations seem very similar in their properties. The following sub-sections delve into this further.

3.3.2.1 Mass and surface density

As can be seen in Table 3.2, our molecular clouds have a median mass of roughly 4×10^3 $M_\odot$ and a radius of about 9 pc. These are smaller clouds (in both size and mass) than those from the numerical work of Treß et al. (2021), with a median mass and radius of 2×10^4 $M_\odot$ and 16 pc, respectively. Treß et al. (2021) (see also Treß et al., 2020) retrieved MCs from a simulated, interacting M51-like galaxy with time-dependent ISM chemistry, supernova feedback and sink particles for star formation. These cloud mass and radius values could be due to the model's resolution limitations in the lower column density regime (see Fig. 3 of Treß et al., 2020), coupled with the specific prescription for the supernovae feedback, which naturally leads to a lower amount of MCs with smaller masses and radii in low column regions such as the inter-arm. Nevertheless, we see similar trends in cloud properties between environments and the same range in cloud mass values (extending up to about $10^{6.5}$ $M_\odot$) as Treß et al. (2021). Our clouds are also much smaller on average than the PAWS clouds (Colombo et al., 2014a), where the median mass and radius are 7.6×10^5 $M_\odot$ and 48 pc, respectively. It is clear that comparing cloud masses between different studies is not the most informative, as masses (and sizes) are heavily dependent on each study's definition of a molecular cloud and its boundaries, as well as resolution limits which might lead to beam smearing in crowded regions, and undetections. In fact, given its 1" resolution ($\sim$ 40 pc), the completeness limit of the PAWS catalogue, 3.6×10^5 $M_\odot$, is already much higher than our median cloud mass. Similarly, the resolution limitations imply a minimum effective radius of 20 pc for the PAWS GMCs, which is already over a factor 2 larger than our typical cloud radius ($\sim$ 9 pc), meaning the average cloud in our catalogue might go undetected in PAWS or appear unresolved within a beam area. Therefore, care is needed when working with different cloud catalogues, especially when comparing absolute values.

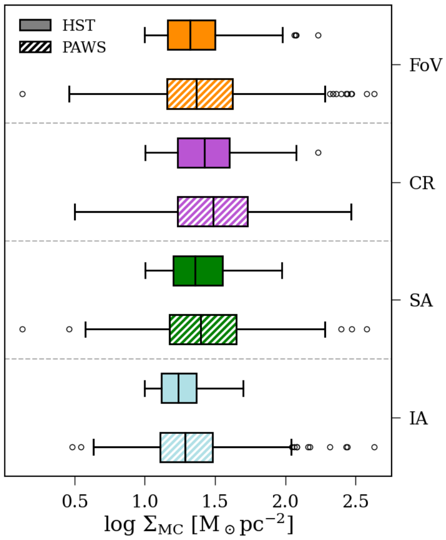

Figure 3.7 – Boxplot representation of average cloud surface densities, $\Sigma_{\rm MC}$, for the cross-matching subsets of the extinction-derived HST clouds (solid) and PAWS GMCs (hatched). The different large-scale environments are represented with the following colour-scheme from top to bottom: PAWS FoV in orange, central region (CR, encompasses nuclear bar and molecular ring) in violet, spiral arms in green, and inter-arm regions in blue. The coloured box illustrates the interquartile spread of the distribution (i.e. from 25$^{\rm th}$ to 75$^{\rm th}$ percentile), with the solid black line within the box being the median. Circles represent the outliers of the distributions.

Figure 3.7 presents a comparison of average cloud surface densities for the cross-matches between the PAWS GMCs and the extinction-derived HST MCs. By definition, average cloud surface densities already account for cloud size (i.e. $\Sigma_{\rm MC} = {\rm M}/A$), which reduces the effect of different resolutions between studies, although not entirely as will be addressed later. We perform this cross-matching to ensure that we are only comparing clouds that roughly exist in the same space, so that the comparison is as fair as possible. The footprint masks of the PAWS GMCs were deprojected into 2D masks and regridded to the HST native grid (0.049"/pix). We find that 1296 of the total 1507 PAWS GMCs have a spatial match with HST clouds, meaning our catalogue successfully matches with 86% of the PAWS catalogue. The remaining 211 unmatched PAWS GMCs are likely associated with clusters, which prevent any measurement of extinction in the relevant region (as detailed in Chapter 2). Out of the 4843 HST MCs in the PAWS FoV (highlighted in Fig. 3.4), only 35% (1700) match with at least one GMC in PAWS. This significant fraction of unmatched HST clouds is again a reflection of the differences in column sensitivity and resolution of the two catalogues: the unmatched HST clouds typically have lower average surface density ($\sim$ 15.1 $M_\odot$ pc^{-2}) thus likely associated with CO-dark molecular gas, and are also too small ($\sim$ 8.5 pc) to be resolved by PAWS. In addition to cross-matching, the average surface densities of PAWS clouds are also re-calculated with a scaled CO-to-H_2 conversion factor. Colombo et al. (2014a) employ the standard Galactic CO-to-H_2 conversion factor,

$X_{\rm CO} = 2 \times 10^{20}$ cm^{-2} (K km s^{-1})$^{-1}$, when deriving their cloud masses (and surface densities) from CO luminosity. In Section 2.4.3, it was discussed that the determination of $X_{\rm CO}$ is heavily influenced by the assumed dust model, and that assuming the Galactic $X_{\rm CO}$ overestimates the PAWS surface densities by roughly a factor 7 relative to this work's estimates. Adopting the scaled value of $X_{\rm CO} = 3.1\,(\pm 0.3) \times 10^{19}$ cm^{-2} (K km s^{-1})$^{-1}$ removes this discrepancy and makes the two studies comparable. Once all these steps are taken to ensure the comparison of cloud properties between our catalogue and the one from PAWS is as fair as possible, the median cloud surface densities (as well as observed trends between environments) are virtually identical for both catalogues (shown in Fig. 3.7). Still, from the figure, one can see that the observed range of cloud surface density values for the PAWS GMCs are consistently larger than the HST range. Again, this is likely linked to resolution: in crowded areas, a larger beam might blend multiple clouds in the same line-of-sight resulting in larger surface densities, whilst smaller and more isolated clouds might get smeared within the beam, resulting in a "dilution" of the observed flux in a larger area (i.e. lower surface density).

3.3.2.2 Elongation

In order to evaluate the elongation of clouds, two different methods of measuring aspect ratio are employed. The first is a moments-based aspect ratio, $\mathrm{AR_{a/b}}$, and the second metric is purely geometrical, based on the medial axis of the cloud, $\mathrm{AR_{MA}}$. For further details, refer to Section 3.2.3. Both aspect ratio metrics suggest the same trends between the spiral arms and inter-arm regions in that, although the values are higher overall for $\mathrm{AR_{MA}}$, both environments seem to have equally elongated clouds, as shown in Fig. 3.6 and Table 3.2. It is possible that any disparities between these two populations are only seen in the most extreme clouds (i.e. tails of the distributions) rather than the bulk of the population, which will be further examined in Section 3.3.4. Both $\mathrm{AR_{MA}}$ and $\mathrm{AR_{a/b}}$ suggest that MCs in the nuclear bar are more elongated than anywhere else in the galaxy. Due to their non-axisymmetric nature, bars are known to drive gas inflows and produce intense shear (e.g. Meidt et al., 2013; Querejeta et al., 2016), likely stretching clouds apart (i.e. providing higher aspect ratios). The picture is more unclear when considering the molecular ring population; the overall trend with the remaining large-scale environments is different for the two metrics: for $\mathrm{AR_{a/b}}$, the MR clouds have the second highest median, but for $\mathrm{AR_{MA}}$, the same clouds have the lowest median. The difference in trends between the two aspect ratio metrics employed here is not wholly unexpected. In a recent morphology study of the SEDIGISM clouds (Duarte-Cabral et al., 2021), Neralwar et al. (2022) note that measures of aspect ratio vary quite significantly depending on the methodology adopted. Using an aspect ratio as a proxy for cloud elongation is not straightforward, as it depends on the specific morphology of the clouds, and should therefore be used with care, as is

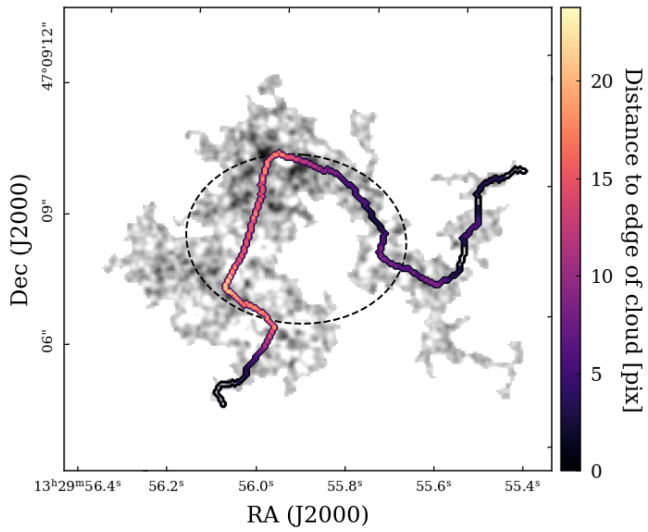

Figure 3.8 – Example molecular cloud in the sample (ID: 4620) for which the aspect ratio from the medial axis and from the moments differ significantly. The dashed black ellipse represents the moments of the structure from which the moment aspect ratio, $\mathrm{AR}_{\mathrm{a/b}}$, is derived. The coloured line represents the medial axis of the cloud, where each pixel is colour-coded with the corresponding distance to the edge of the cloud. The background grey scale illustrates the surface densities computed from the extinction technique within the cloud's mask as defined by `SCIMES`. For this particular cloud, $\mathrm{AR}_{\mathrm{a/b}} = 1.3$ whilst $\mathrm{AR}_{\mathrm{MA}} = 15.1$.

addressed in the following paragraph.

In a simplistic view, an aspect ratio would allow us to distinguish between "circular" clouds and "filamentary" clouds. As mentioned above, it is possible to estimate the aspect ratio of a cloud via an intensity-weighted ($\mathrm{AR}_{\mathrm{a/b}}$) or a purely geometrical approach ($\mathrm{AR}_{\mathrm{MA}}$). However, both of these metrics have issues when the morphology of a cloud becomes more complex, and also seem to behave differently between themselves. For example, for the cloud depicted in Fig. 3.8, the moments approach retrieves an $\mathrm{AR}_{\mathrm{a/b}}$ of 1.3, suggesting a fairly circular cloud, even though it is clear from the figure that this is not the case. On the other hand, the medial axis aspect ratio $\mathrm{AR}_{\mathrm{MA}}$ has a value of 15.1, suggesting that this cloud is highly filamentary in nature. Upon visual inspection, this MC is perhaps somewhere in between, and better classified as a "ring-like" cloud rather than a true filamentary structure. Thus while the aspect ratio can be used as a first glance at overall trends, any conclusions need to be carefully considered, as a more robust classification is needed in order to differentiate between real elongated, filamentary structures, and ring-like clouds (or other complex morphologies). It is beyond the scope of this Chapter to address this discrepancy between aspect ratios, but a more detailed cloud morphology study using Rotated J-plots, or RJ-plots (Clarke et al., 2022, based on the automated morphological classification technique J-plots developed by Jaffa et al. 2018) is employed in Chapter 4.

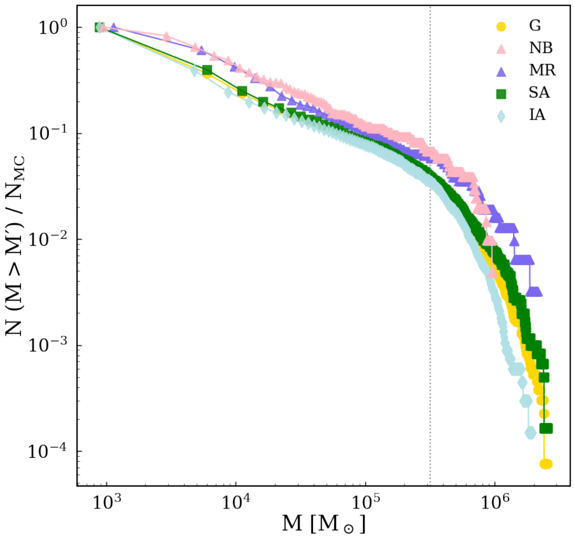

Figure 3.9 – Cumulative mass distributions for the different environments in M51 (full galaxy in yellow, nuclear bar in pink, molecular ring in purple, spiral arms in green, and inter-arm in blue). The distributions are normalised by the number of clouds of each environment, N_{MC} (listed in Table 3.2). Clouds with saturated pixels/uncertain opacities are not included.

3.3.3 Cloud cumulative mass distributions

As highlighted in the previous Section, although there are clear differences in the masses of MCs between the centre and the disc of M51, the medians of the distributions alone are not the most informative, particularly when analysing any potential differences between the IA and SA clouds. Therefore, an analysis of how cloud masses are distributed within each large-scale environment is performed, via cumulative mass distributions. Clouds that include saturated pixels were excluded when building the cloud mass spectra, since these clouds have more uncertain masses (see Section 2.3.4). Figure 3.9 shows the mass spectra for the MCs in the science sample for the different M51 environments, normalised by the number of clouds in each environment. From the figure, it is possible to see that the central regions of M51 (NB and MR) have the highest concentration of high-mass clouds (M$\gtrsim 10^{5.5}$ M$_\odot$), followed by the spiral arms. There's also a sharp decline in high-mass objects for the IA - the clouds in this region seem to have predominantly low to intermediate masses. These findings agree with what was found, albeit at a lower resolution, by Colombo et al. (2014a) in their GMC study of M51 using PAWS CO data, and more recently by Rosolowsky et al. (2021) in their study of GMCs across PHANGS spiral galaxies. The trends seen in the MC mass spectra follow the same trends as what was seen for the pixel-by-pixel surface density distributions (Fig. 3.5), and thus the cloud segmentation process used in this study is unlikely to be the cause of the cloud mass distributions seen here.

The cumulative mass distribution can be fit with a simple power-law of the shape: $N = (M/M_0)^{\gamma+1}$,

Full galaxy			
Env.	γ	M_0	N_0
		10^6 $M_\odot$	
G	-2.43 $\pm$ 0.01	2.21 $\pm$ 0.02	35.7 $\pm$ 1.04
NB	-1.01 $\pm$ 0.02	1.20 $\pm$ 0.01	...
MR	-1.28 $\pm$ 0.01	2.18 $\pm$ 0.02	24.5 $\pm$ 1.65
SA	-2.19 $\pm$ 0.01	2.42 $\pm$ 0.02	23.7 $\pm$ 0.57
IA	-2.61 $\pm$ 0.01	1.64 $\pm$ 0.01	18.99 $\pm$ 0.68
PAWS FoV			
G	-2.13 $\pm$ 0.01	2.16 $\pm$ 0.01	32.2 $\pm$ 0.86
SA	-1.77 $\pm$ 0.01	2.22 $\pm$ 0.02	25.4 $\pm$ 1
IA	-2.38 $\pm$ 0.01	1.81 $\pm$ 0.01	12.7 $\pm$ 0.38

Table 3.3 – Parameters from truncated power-law fits (γ, M_0 and N_0) for the full galaxy (top section) and for the PAWS FoV (bottom section). The errors quoted are the standard deviations of the fits. The N_0 estimate for the nuclear bar is omitted from this table as it does not have any physical meaning. The γ estimate for this region is nearly -1, the point for which Eq. 3.1 is no longer valid, and consequently determining N_0 becomes impossible.

where N is the number of clouds with mass M that is larger than the reference mass M_0, and γ the index of the power-law. However, given the steepening of the mass distributions seen at higher masses, it is often better to use a truncated power-law of the form:

$$N = N_0 \left[\left(\frac{M}{M_0} \right)^{\gamma+1} - 1 \right], \tag{3.1}$$

with M_0 being the maximum mass of the distribution, and N_0 the number of clouds corresponding to the truncation mass, $M_t = 2^{1/(\gamma+1)M_0}$ (i.e. the point at which the mass distribution stops following a simple power-law). The index of the truncated power-law informs us on how the mass is distributed: in massive cloud structures for $\gamma > -2$, and in smaller clouds for $\gamma < -2$. For the spiral arms and inter-arm regions, we fit the mass spectra with Eq. 3.1 for masses greater than $10^{5.5}$ $M_\odot$, which is the point from which the distributions seem to have a shape similar to a truncated power-law. A lower mass threshold of 10^5 $M_\odot$ is adopted for the nuclear bar and molecular ring due to the reduced number of clouds with masses higher than $10^{5.5}$ $M_\odot$. The resulting parameters from the fits are listed in Table 3.3, and the fits themselves (both simple and truncated) are shown in Fig. 3.10.

The global cumulative mass distribution of all the MCs is very steep, with a fitted index

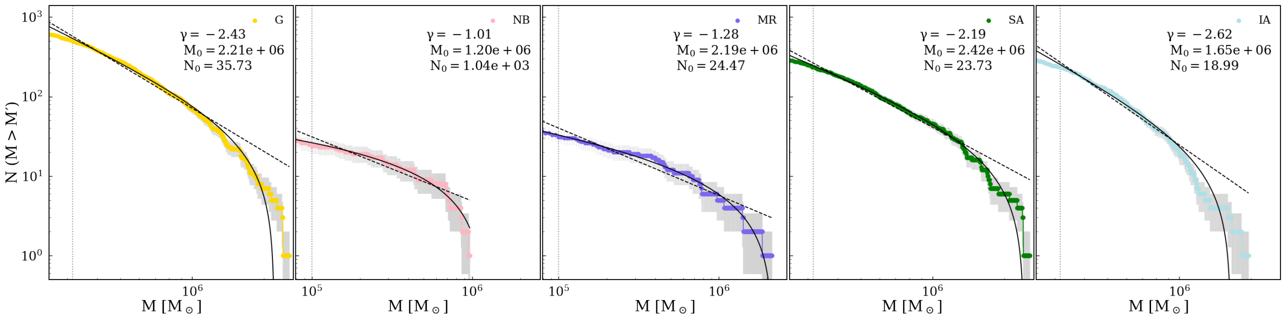

Figure 3.10 – Cumulative mass distributions for the MCs in the science sample for the different large-scale environments (from left to right: global in yellow, nuclear bar in pink, molecular ring in purple, spiral arms in green, and inter-arms in blue), normalised by the area of each environment. Dotted grey lines depict the fiducial mass starting from which the fits were performed ($10^{5.5}$ $M_\odot$ for G, SA, IA, and 10^5 $M_\odot$ for NB, MR). Dashed black lines represent the simple power-law fits performed, and solid black lines the truncated power-law fits. The environment label, as well as the spectral index γ, the maximum mass M_0 and N_0 for the truncated fits, are shown in the top right. The errorbars in light grey are the Poisson errors on the counts ($\sqrt{N}$). Clouds with saturated pixels are not included in these distributions.

of $\gamma < -2$, which indicates that our M51 clouds are preferentially low-mass objects. We can again see in Fig. 3.10 that the cloud population in the centre of M51 (NB + MR) has different characteristics from the disc (SA + IA), with very different slopes of the truncated fits. Both the nuclear bar and molecular ring present $\gamma > -2$, whilst the spiral arms and inter-arms fits have $\gamma < -2$, suggesting that clouds in the disc are typically low-mass, whilst MCs in the centre have larger masses, in line with the results from Section 3.3.2.

Although the nuclear bar truncated fit has the shallowest slope (indicative of preference towards high-mass objects), the distribution itself does not extend to high mass values (highest mass $\sim 9 \times 10^5$ $M_\odot$), suggesting that cloud growth is being hindered and/or that massive clouds are being destroyed in this region. This is likely a result of the complex dynamics and intense shear caused by the bar, although Colombo et al. (2014a) argue that the enhanced interstellar radiation field in M51's bulge could also have an effect. On the other hand, the molecular ring also has a low γ index but its distribution reaches higher mass values ($\sim 2 \times 10^6$ $M_\odot$), consistent with an environment that promotes cloud agglomeration.

The IA cumulative mass distribution presents the steepest slope out of all the considered environments, indicating that the inter-arm regions host predominantly lower mass MCs. Furthermore, the IA distribution reaches smaller mass values relative to the spiral arms cumulative mass distribution, even though the two distributions are very similar in the low-to-intermediate mass range ($< 10^{5.5}$ $M_\odot$, see Fig. 3.9). It seems that high-mass objects in the inter-arm either have difficulty forming or are destroyed quickly after formation. On the other hand, the spiral arms distribution reaches the highest mass among all considered environments

($\sim 2.6 \times 10^6$ M$_\odot$), even though its slope is relatively steep. The SA then appear to have favourable conditions for clouds to grow more massive even though most of its population seem to be low-mass objects. From their simulations of an interacting galaxy, Pettitt et al. (2020) also observe a steeper slope in their IA cumulative cloud mass distribution relative to the SA slope, with SA clouds reaching higher masses. Additionally, the fitted index of their whole cloud population, $\gamma = -2.39$, is very close to the value find here ($\gamma = -2.43$).

Interestingly, the fitted parameters (γ, M_0, and N_0) change quite significantly when fitting the mass cumulative distributions of only the MCs inside the PAWS FoV (i.e. clouds at smaller galactocentric radii, $\mathrm{R_{gal}} \lesssim 5$ kpc), as can be seen from the bottom section of Table 3.3. Overall, MCs seem to be more massive inside the PAWS FoV than when considering the full galaxy, hinting at a radial trend in cloud mass (which will be analysed in more depth in Section 3.4). Notably, the slope of the truncated fit for the inner spiral arms is much shallower than for the full arms, with $\gamma > -2$, whilst the index for the inner inter-arms is still $\gamma < -2$.

3.3.4 Extreme clouds

As evidenced by Section 3.3.2 and Section 3.3.3, although the bulk properties of a galaxy's different cloud populations may be fairly similar, differences arise when analysing the tails of the distributions (see also Duarte-Cabral & Dobbs, 2016; Duarte-Cabral et al., 2021). If "extreme" clouds (i.e. the clouds at the tail of the relevant distribution) are enhanced in certain large-scale galactic environments, then this points at physical processes that directly facilitate the formation of specific types of clouds in specific regions of the galaxy, which could then have a direct impact on star formation. Figure 3.11 showcases the spatial distributions of the top 100 most extreme clouds[5] for the different cloud properties considered: mass, average surface density, aspect ratio, and signatures of high-mass star formation. Table 3.4 holds the expected cloud fractions according to the global distribution of MCs across M51 (i.e. number of clouds in an environment divided by the total number of clouds), as well as the fractions reported for the tails of some of the analysed distributions (i.e. number of extreme clouds in an environment divided by size of extreme sub-sample, $N = 100$). If the environment has no direct role in dictating the existence of such extreme clouds, one would expect the fractions for the extreme clouds to simply reflect the global cloud fractions.

To determine if the distribution of these extreme clouds is significant, a Pearson χ^2 statistical analysis is conducted, which compares the observed distribution of a sample against a theoretical distribution, and searches for similarities in frequencies. The χ^2 value is given by the below

[5] Given the sample size (13258), this roughly corresponds to the top 1% of the distribution.

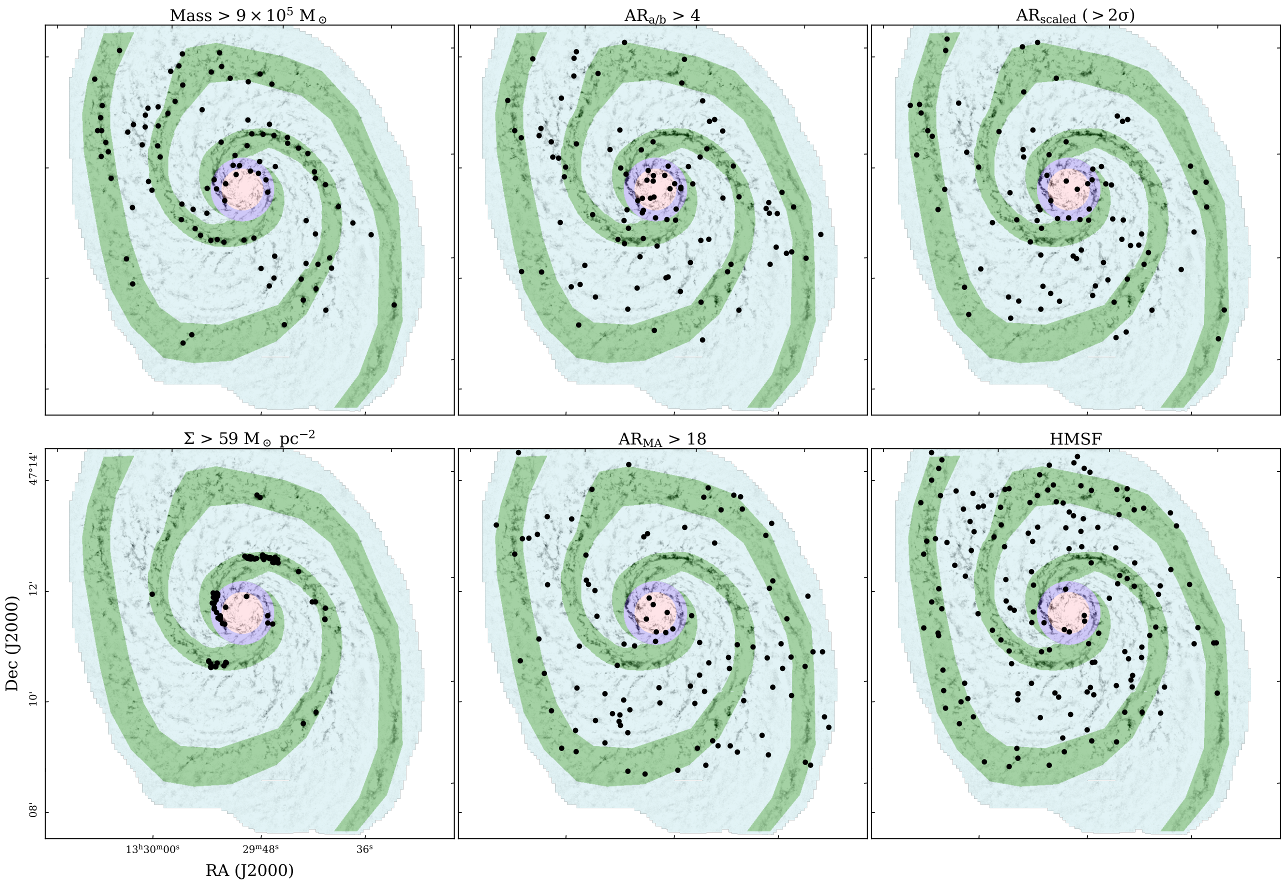

Figure 3.11 – Distribution of the most extreme clouds in the science sample in terms of their mass M (*top left*), major/minor axis ratio $\mathrm{AR}_{\mathrm{a/b}}$ (*top middle*), rescaled and standardised aspect ratio (above 2σ, *top right*), average surface density Σ_{MC} (*bottom left*), medial axis aspect ratio $\mathrm{AR}_{\mathrm{MA}}$ (*bottom middle*), and potential high-mass star formation (i.e. MCs with an associated 8 μm source, *bottom right*). Where relevant, at the top of each panel is the corresponding lower bound of the relevant property for the clouds shown.

Env. (1)	f (2)	f_M (3)	f_Σ (4)	$f_{\mathrm{AR_{MA}}}$ (5)	$f_{\mathrm{AR_{a/b}}}$ (6)	$f_{\mathrm{AR_{scaled}}}$ (7)	f_{HMSF} (8)	$f_{L_{\mathrm{MA}}}$ (9)	f_{A} (10)
NB	0.02	0.03	0.02	0.05	0.1	0.03	0.02	0.02	0
MR	0.02	0.08	0.22	0.03	0.08	0.08	0.05	0.03	0.01
SA	0.45	0.58	0.75	0.30	0.35	0.41	0.51	0.32	0.47
IA	0.51	0.31	0.01	0.62	0.47	0.48	0.42	0.63	0.52
χ^2		25.6	230	15.7	61.7	14.1^+	23.1^*	7.43	2.44
$\mathrm{p_{rnd}}$		0.0004	$<10^{-5}$	0.0036	$<10^{-5}$	0.007^+	0.0001^*	0.06	0.48

$^+$ estimated with $N = 88$ clouds.

* estimated with $N = 460$ clouds.

Table 3.4 – Extreme cloud fractions across galactic environments. (1) Environment tag: nuclear bar (NB), molecular ring (MR), spiral arms (SA), inter-arm (IA). (2) Fraction of clouds of each environment (N_{env}) with respect to the total number of clouds in the science sample (N_{MC}), f ($f = N_{\mathrm{env}}/N_{\mathrm{MC}}$). (3) Fraction of most massive clouds, f_M. (4) Fraction of clouds with the highest surface density, f_Σ. (5) Fraction of most elongated clouds according to the medial axis aspect ratio, $f_{\mathrm{AR_{MA}}}$. (6) Fraction of most elongated clouds according to the moment aspect ratio, $f_{\mathrm{AR_{a/b}}}$. (7) Fraction of most elongated clouds ($> 2\sigma$) according to both metrics of aspect ratio scaled and standardised, $f_{\mathrm{AR_{scaled}}}$. (8) Fraction of high-mass star forming clouds which have an associated 8 µm source (including both exact and closest match) from Elmegreen & Elmegreen (2019), f_{HMSF}. (9) Fraction of longest clouds according to their medial axis length, $f_{L_{\mathrm{MA}}}$. (10) Fraction of largest clouds in terms of their footprint area, f_A. The bottom portion of the table shows the results from the investigation into the significance of the statistical difference in the distribution of these extreme clouds compared to the global science sample. The χ^2 values listed are relative to each distribution of extreme clouds and the distribution of the full science sample. $\mathrm{p_{rnd}}$ represents the probability or likelihood of obtaining the listed χ^2 values from a pure random draw of $N = 100$ clouds ($N = 88$ and $N = 460$ for the $\mathrm{AR_{scaled}}$ and HMSF sub-samples, respectively) from the science sample.

expression:

$$\chi^2 = \sum_{i=1}^{n} \frac{(O_i - E_i)^2}{E_i}, \tag{3.2}$$

where n is the number of environments considered (i.e. NB, MR, SA and IA), O_i is the number of observed counts in environment i (i.e. number of clouds), and E_i is the number of expected counts within environment i for a sample of size N, such that $E_i = f_i\, N$, with f_i representing the probability of a cloud belonging to environment i (i.e. the fraction of the science sample situated in each environment, listed in Table 3.4). Here, the science sample is used as the theoretical distribution, and the χ^2 statistics between the top 100 extreme clouds and the theoretical distribution are calculated. To test if the derived χ^2 values are statistically significant, we determine the likelihood (p_{rnd}) of obtaining the calculated χ^2 values from a random draw of $N = 100$ clouds from the science sample (without replacement). To do so, 100 000 random draws of $N = 100$ clouds were performed, and the χ^2 value was determined for each draw against the expected distribution (i.e. the science sample). A cumulative distribution of the 100 000 derived χ^2 values was built to illustrate the likelihood of obtaining a certain χ^2 value from pure random sampling, as shown in Fig. 3.12. By comparing the χ^2 values of the extreme sub-samples to the values resulting from random sampling, we are able to determine how likely is the retrieval of the observed extreme cloud distribution from a random sampling of the global population, and therefore judge whether any observed differences are statistically significant. In cases where the likelihood is low, the large-scale environment may have a direct role in promoting those specific types of extreme clouds. The exact values resulting from the χ^2 statistics for the extreme clouds should not necessarily be taken at face value, and should serve instead as a means to compare between the different sub-sets of extreme clouds.

From this analysis, we can see that properties like the footprint area (A), the medial axis length (L_{MA}), and aspect ratio have the highest p_{rnd} values, suggesting that these properties mimic the general distribution, while others like surface density have much lower p_{rnd} (Table 3.4). In the following sections, I explore these trends in more detail, looking at extreme clouds in terms of their mass/surface density in Section 3.3.4.1, elongation in Section 3.3.4.2, and high-mass star formation in Section 3.3.4.3, putting the results in context with trends observed in the literature.

3.3.4.1 Most massive/highest surface density

Some observational studies of M51 have suggested that the spiral arms are the preferred location of the most massive MCs (e.g. Koda et al., 2009; Miyamoto et al., 2014; Colombo et al., 2014a) - a natural consequence of spiral arms hosting more material, which increases the frequency of cloud-cloud collisions leading to the formation of high-mass objects (e.g. Dobbs, 2008). In the

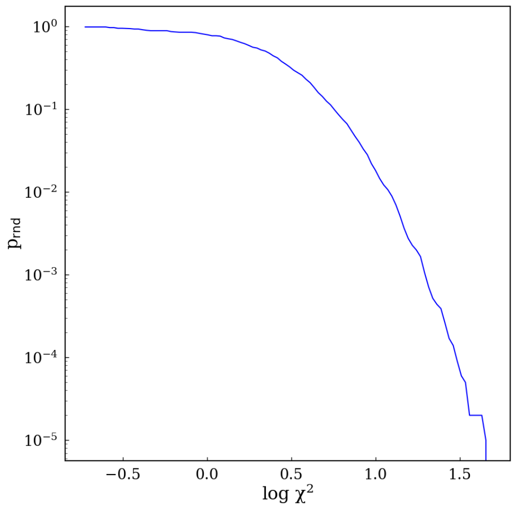

Figure 3.12 – Cumulative distribution of the derived χ^2 values for 100 000 random draws of $N = 100$ clouds from the molecular sub-sample. Effectively, the y-axis represents the probability, p_{rnd}, of obtaining a given value of χ^2 from a pure random draw.

previous Section, it was already highlighted that spiral arms seem able to form higher mass MCs than the inter-arm regions, despite having similar distributions in the low-to-intermediate mass range. It follows that when isolating the most massive clouds in the science sub-sample, the spiral arms boast a much higher number of these high-mass MCs than the inter-arms - a trend that does not follow the overall distribution of MCs across M51 and is therefore likely to be significant. Furthermore, a significant percentage of these extremely massive clouds reside in the molecular ring (a factor 4 more than what would be expected from statistics), a region also known to harbour an accumulation of material. The lack of high-mass MCs in the nuclear bar and inter-arm may be due to complex dynamics and shear, and was already seen and addressed in Section 3.3.3.

When looking at the bottom left panel of Fig. 3.11, it is clear that the densest MCs in the science sample prefer the spiral arms (an increase of roughly 63% relative to the cloud fraction expected from the overall statistics). Additionally, these extremely dense clouds are heavily concentrated towards the inner regions of M51, again hinting at some strong radial trends (further analysed in Section 3.4). Moreover, there is an increase of extremely dense clouds in the molecular ring relative to the expected statistics. From the figure, these dense MR clouds mostly correspond to the beginning of the spiral arms of M51 within the ring. The densest clouds seem to mostly be located in crowded areas where intense shear is likely absent.

For the most massive and highest surface density clouds, the calculated χ^2 values are 25.6 and 230, respectively, with corresponding likelihoods p_{rnd} of 4×10^{-4} and $< 10^{-5}$. Both extreme sub-samples are therefore unlikely to be randomly drawn from the science sample, especially the highest surface density clouds. It is important to note that although a small amount of these extreme clouds have masses/surface densities that we do not necessarily trust due to saturation effects or observational limits (see Section 2.3.5), the trends reported here remain the same when removing these more uncertain clouds from the analysis.

3.3.4.2 Most elongated

In their numerical study of GMCs of a two-armed spiral galaxy, Duarte-Cabral & Dobbs (2016) found that although the median properties of the inter-arm and spiral arm populations are similar in terms of aspect ratio, the most elongated MCs in their sample belong almost exclusively to the inter-arm. This could be suggestive of intense shear stretching massive MCs as they exit the spiral arms into the inter-arm (e.g. Koda et al., 2009), but could also be due to disruption driven by stellar feedback (e.g. Meidt et al., 2015).

From Section 3.3.2, it was seen that there are no significant differences in cloud elongation between the IA and SA populations when looking at the medians of either metric of aspect ratio. When looking at the top 100 most elongated MCs according to their $\mathrm{AR_{MA}}$ instead, the majority of highly elongated clouds are located in the inter-arm. However, using $\mathrm{AR_{a/b}}$ instead gives no significant increase of highly filamentary structures in the inter-arm regions. This discrepancy between the two metrics might be due to filamentary clouds that have a "curved" nature (e.g. ring-like), which would have a large $\mathrm{AR_{MA}}$ but a low $\mathrm{AR_{a/b}}$ (already discussed in Section 3.3.2.2). Clouds such as these might be potential "bubbles" which are driven by stellar feedback (e.g. Watkins et al., 2023; Barnes et al., 2023). Both metrics report higher fractions of extremely elongated clouds in the nuclear bar than expected from statistics alone (factor 2.5 increase for $\mathrm{AR_{MA}}$ and 5 for $\mathrm{AR_{a/b}}$), reflective of the complex dynamical processes and intense shear seen towards that region. The molecular ring presents the most drastic difference between the two metrics (as was already pointed out in Section 3.3.2), with the moment aspect ratio metric reporting a significant increase of extremely elongated clouds whilst the medial axis aspect ratio sees no increase at all. We derive a χ^2 value of 15.7 and $\mathrm{p_{rnd}} = 0.004$ for the extreme $\mathrm{AR_{MA}}$ sub-sample, and $\chi^2 = 61.7$ and $\mathrm{p_{rnd}} < 10^{-5}$ for $\mathrm{AR_{a/b}}$. The statistics suggest that these extreme sub-samples deviate from the theoretical distribution, however this seems to be driven predominantly by the nuclear bar of M51, where both metrics agree on a surplus of extremely elongated clouds.

The discrepancies between $\mathrm{AR_{a/b}}$ and $\mathrm{AR_{MA}}$ and in particular, their different behaviour with different cloud morphologies make it hard to draw any definite conclusions. In an attempt to isolate the truly elongated clouds, we instead retrieve the most elongated MCs from both metrics combined. To do so, both distributions are first standardised to make them comparable.

The AR_{MA} and $AR_{a/b}$ distributions are both scaled to have a standard deviation of 1 and a mean of 0. Looking at the clouds with aspect ratio above 3σ in both rescaled distributions returns just 23 MCs - 9% in NB, 9% in MR, 30% in SA and 52% in IA. If the threshold is relaxed down to 2σ, 88 MCs are considered and the percentages become 3% in NB, 8% in MR, 41% in SA, and 48% in IA, as shown in Table 3.4. In either case, there is no significant increase of highly elongated MCs towards the inter-arm, but the amount of extremely elongated clouds in the nuclear bar remains statistically significant. The molecular ring population still hosts a significant fraction of these extremely elongated clouds relative to the expected distribution. The MR is a region known to have low shear (e.g. Meidt et al., 2013; Querejeta et al., 2016), so it could be that stellar feedback is the mechanism responsible for disrupting the MCs in this environment, although a more detailed cloud classification and analysis is needed to draw any definite conclusions. The distribution of the AR_{scaled} sub-sample has a χ^2 value of 15.3 and a likelihood p_{rnd} of 0.005. We also do not observe any trend of cloud size (either through equivalent radius or medial axis length) across the large-scale environments.

3.3.4.3 High-mass star forming

The highest mass and densest MCs in this sample are preferentially located in the spiral arms (and also the molecular ring), as shown in Section 3.3.4.1. However, whether this enhancement of massive/dense clouds is then reflected on a different type of star formation happening in those clouds is still unclear. For instance, if high-mass star formation (HMSF) requires a cloud reaching higher masses or densities, then environments with a surplus of massive/dense MCs will also have a higher frequency of clouds hosting HMSF compared to the statistical distribution of clouds in general. In particular, if HMSF sites are enhanced in spiral arms then it may mean that star formation is directly enhanced or triggered from the passage of the spiral density wave (e.g. Roberts, 1969; Lord & Young, 1990), rather than just a byproduct of orbit crowding in spiral arms (e.g. Elmegreen & Elmegreen, 1986; Foyle et al., 2010; Urquhart et al., 2021).

The HMSF potential for this sample of clouds is thus investigated, through the use of the empirical relation derived by Kauffmann & Pillai (2010), which defines a surface density threshold above which clouds are potential hosts for HMSF. The original HMSF threshold in Kauffmann & Pillai (2010), $M[\mathrm{M}_\odot] = 870\,(R[\mathrm{pc}])^{1.33}$, was determined with the opacity law $\kappa_\lambda = 12.1\,(\lambda/250\,\mu\mathrm{m})^{1.75}\ \mathrm{cm^2\,g^{-1}}$. In turn, the adopted opacity law in this work is $\kappa_\lambda = 21.6\,(\lambda/250\,\mu\mathrm{m})^{2}\ \mathrm{cm^2\,g^{-1}}$ from OH94; consequently the HMSF threshold is scaled down to $M[\mathrm{M}_\odot] = 487\,(R[\mathrm{pc}])^{1.33}$. The difference in dust mass from using either the OH94 specific opacity with a dust emissivity index of $\beta = 2$ or the opacity employed by Kauffmann & Pillai (2010) with $\beta = 1.75$ is only around 20%, a small difference given the uncertainties on the masses themselves.

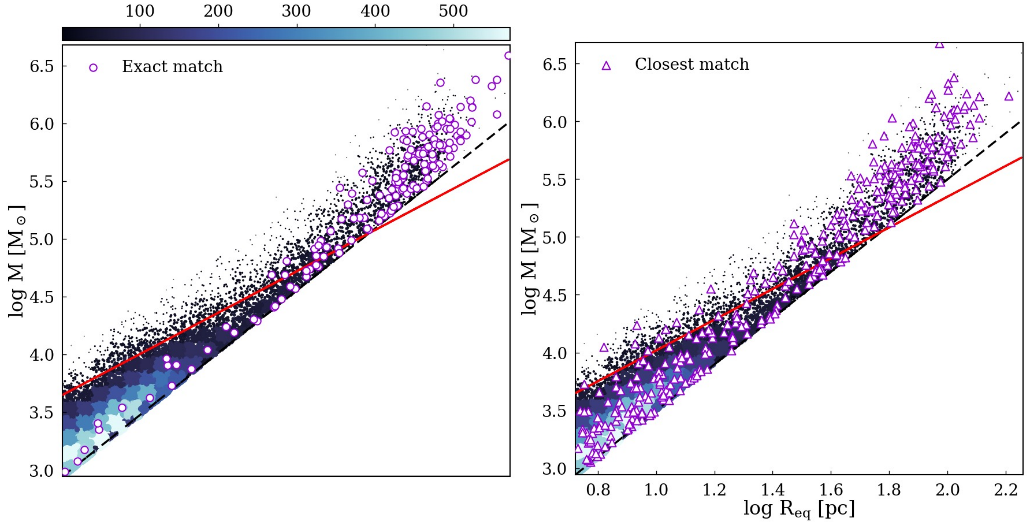

Figure 3.13 – Mass-size relation for the science sample. On both panels, the blue scale indicates the density of points and the dashed black line the $\Sigma = 10\ \mathrm{M_\odot\,pc^{-2}}$ cut applied to obtain the high-fidelity sample. The continuous red line represents the empirical threshold for HMSF from Kauffmann & Pillai (2010). This threshold has been scaled from the original (given the different opacity laws used) to $M = 487\,R^{1.33}$, where the mass is in $\mathrm{M_\odot}$ and the radius in pc. The violet circles on the left panel represent the clouds with an exact match to an 8 μm core from Elmegreen & Elmegreen (2019) (indicative of HMSF), whilst the violet triangles in the right panel depict the closest cloud match to a given source.

Figure 3.13 displays the mass-size distribution of the clouds in the sample, with the solid red line representing the aforementioned HMSF threshold scaled to the adopted absorption coefficient. Around 15% of the science sample sits above the HMSF threshold (2022 out of 13258 MCs). Of these 2022 MCs, 3% belong to the nuclear bar, 6% to the molecular ring, 53% to the spiral arms, and the remaining 38% to the inter-arm. The molecular ring and spiral arm fractions resulting from adopting this single threshold for HMSF are significantly higher than what would be expected from the overall distribution (2% and 45%, respectively, see f in Table 3.4). This indeed suggests that MCs in the molecular ring and spiral arms could be more prone to potentially host HMSF.

In Fig. 3.13, known 8 μm sources in M51 from Elmegreen & Elmegreen (2019) are also highlighted, which are thought to trace the embedded and young stellar population of the galaxy. These 8 μm cores have a typical diameter of 3” (barely above the 2.4” FWHM resolution of the *Spitzer* data), which corresponds to a physical size of about 110 pc for M51. Given the distances involved as well as the physical sizes of these sources (much larger than our typical cloud), it is likely that these are tracing unresolved sites of clustered HMSF. As such, these 8 μm sources are used as HMSF signposts to determine the validity of an empirical surface density threshold. Using the catalogued central position of each 8 μm source from Elmegreen & Elmegreen (2019), circular masks are created for each individual source with a 3” diameter.

Cross-matching the source masks with the footprint masks of our MCs gives 509 matches. Over 100 sources are dismissed in this step: some fall outside the bounds of our map (the original catalogue includes NGC 5195), others are encompassed in diffuse clouds that are not considered in the molecular sub-sample, and others are not embedded anymore (i.e. young clusters already showing in the visible) leading us to not be able to measure any visual extinction in that region. Out of these 509 sources, 169 match with only 1 MC, whilst the remaining 340 match with multiple clouds. In order to perform an environmental analysis, we choose to only keep the match with the closest cloud (i.e. shortest distance between centroid of source and centroid of cloud). The left panel of Fig. 3.13 illustrates the exact source-cloud matches, whilst the right panel depicts the closest matches in the multiple clouds cases.

The cross-matching performed here results in 509 8 μm sources from Elmegreen & Elmegreen (2019) matching with 460 of our clouds (49 MCs have multiple associated sources, whilst the rest have unique, one-to-one matches). Out of these 460 MCs with an associated HMSF signpost, 279 are above the empirical HMSF line, whilst 181 are below. Adopting such a surface density threshold would cause us to miss roughly 40% of true positives (i.e. MCs with an associated 8 μm core yet are below the HSMF line). It is important to note that due to this proximity-based source-cloud matching, some clouds may not be the true hosts of the 8 μm source, which will affect this fraction of missed true positives. Furthermore, while 8 μm can trace young clusters, it is not quite able to trace the younger and much more embedded young stellar objects present in the densest parts of MCs (i.e. tracers of "on-going" SF), and therefore the sample of HMSF signposts used here is by no means complete.

Although there is a concentration of potential HMSF signposts towards the upper right corner of both panels of Fig. 3.13 (i.e. towards higher-mass objects), there is still a significant amount of low-density and low-mass MCs that are HMSF candidates. In fact, of the highest surface density and highest mass clouds analysed in Section 3.3.4.1, only 11 and 43, respectively, have an associated 8 μm source. Additionally, there seems to be an increase of clouds linked to HMSF signposts towards the molecular ring and the spiral arms, as shown in Table 3.4 (see also Fig. 3.11), with a χ^2 and p_{rnd} values of 23.1 and 10^{-4}, respectively. This surplus towards the MR and SA was also noted when applying the Kauffmann & Pillai (2010) HMSF threshold. Despite this, from this analysis alone it is not possible to distinguish between a higher star formation rate in more crowded regions (MR and SA, given the increase of 8 μm sources) and an actual enhancement of star formation efficiency (i.e. the environment itself has a direct impact on the star formation process, rather than just gathering star-forming material). Even though the HMSF signpost sample used here is not complete, it does already hint at a complex interplay of effects leading towards HMSF rather than a simple density/mass threshold from which all clouds can start forming massive stars. It is also worth noting that the HMSF threshold proposed by

Kauffmann & Pillai (2010) was originally derived for infrared dark clouds, which are very high column density objects. Our data is much more sensitive to the lower end of column density, and therefore applying this threshold may not be particularly relevant or useful. This analysis will benefit from higher resolution near/mid-IR observations (e.g. from JWST) that are able to probe a younger, highly embedded stellar population.

3.4 TRENDS WITH GALACTOCENTRIC RADIUS

In the previous Sections, I have looked at whether galactic environments have a direct impact on the characteristics of their cloud population, and found that the large-scale dynamics do shape cloud characteristics. Non-axisymmetries in the gravitational potential (i.e. spiral arms, nuclear bars) cause the gas in a galaxy to continuously flow not just between large-scale environments, but also radially. Naturally, we would expect the distribution of the ISM to be heavily influenced by these flows. Schuster et al. (2007), for example, find a factor 20 decrease of molecular mass surface densities from the centre to the outskirts of M51 ($R_{gal} \sim 12$ kpc). More recently, Treß et al. (2021) also identify a trend of decreasing cloud masses towards larger galactocentric radii in their simulated MC population of an M51-like galaxy. We thus make use of our high-resolution dataset to analyse the distribution of several cloud properties as a function of galactocentric radius.

3.4.1 Radial profiles

Figure 3.14 shows the radial profiles of cloud properties, where M51 has been divided into 39 concentric bins of width 225 pc, with the exception of the first and last bin, which span 400 and ∼440 pc, respectively, given the lack of clouds seen at those radii. From the middle panels of the figure, it is confirmed that there is a general declining trend with galactocentric distance for both cloud mass and cloud average surface density, although the decline is less pronounced past $R_{gal} = 4$ kpc. The sudden spike in cloud masses at around $R_{gal} = 8$ kpc seems to be mostly due to a large group of MCs concentrated towards the end of the spiral arm leading up to NGC 5195. There is no obvious radial trend of cloud size either through equivalent radius or medial axis length (leftmost panels of Fig. 3.14), except in the first few bins corresponding to the nuclear bar, where clouds seem to be longer. Both metrics of aspect ratio (rightmost panels of Fig. 3.14) remain fairly constant at all radii, apart from a slight increase for the first radial bins again corresponding to the nuclear bar.

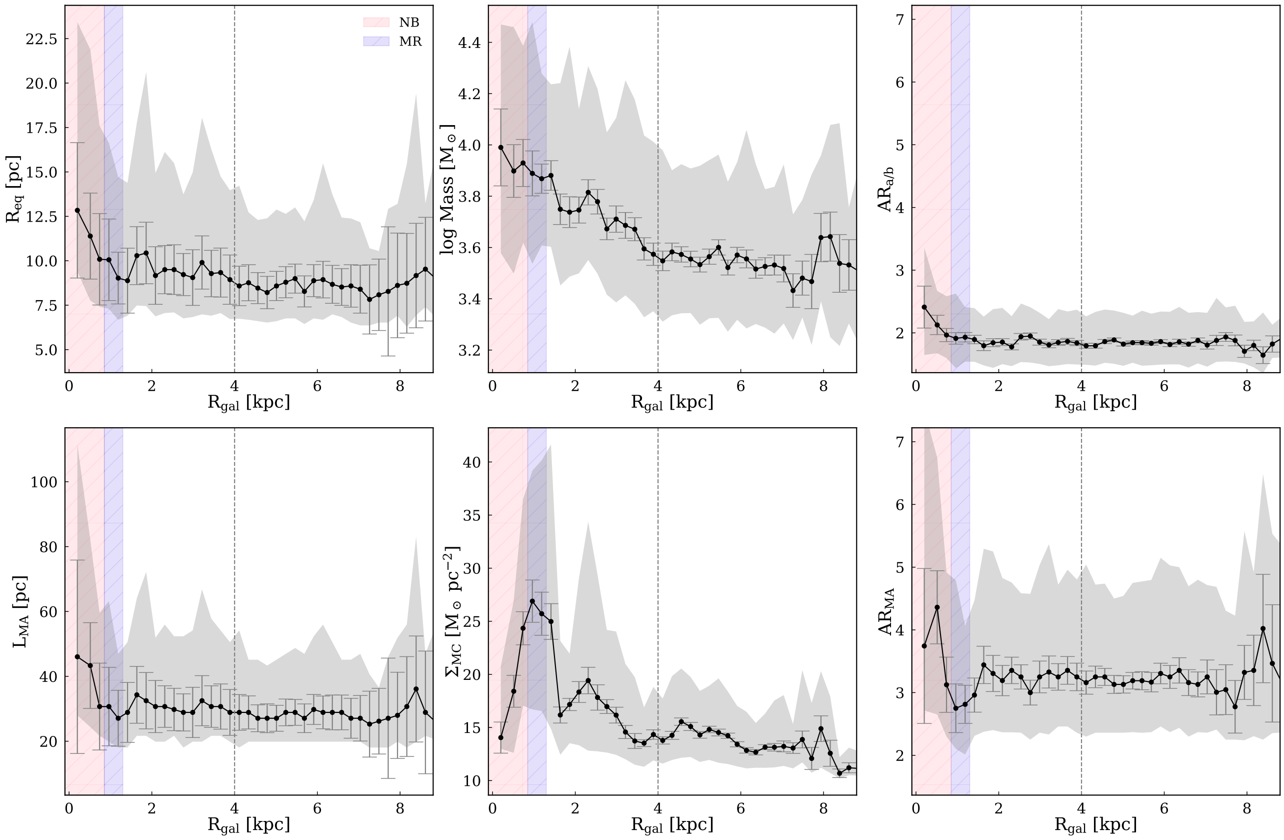

Figure 3.14 – Cloud properties as a function of galactocentric distance, $\mathrm{R_{gal}}$: equivalent radius R_{eq} (*top left*), mass M (*top middle*), major/minor axis ratio $\mathrm{AR_{a/b}}$ (*top right*), medial axis length L_{MA} (*bottom left*), average surface density Σ_{MC} (*bottom middle*), and medial axis aspect ratio $\mathrm{AR_{MA}}$ (*bottom right*). For all panels, the running median of each respective property is portrayed by filled black circles and the solid black line connecting them. The grey-shaded region represents the corresponding interquartile range of the distribution. The grey error bars depict the standard error on the median ($1.253\,\sigma/\sqrt{N}$, where N is the bin count), which show the uncertainty associated with the bin count and the dispersion of the sample median to the full population one. The vertical dashed line is placed at $\mathrm{R_{gal}} = 4$ kpc.

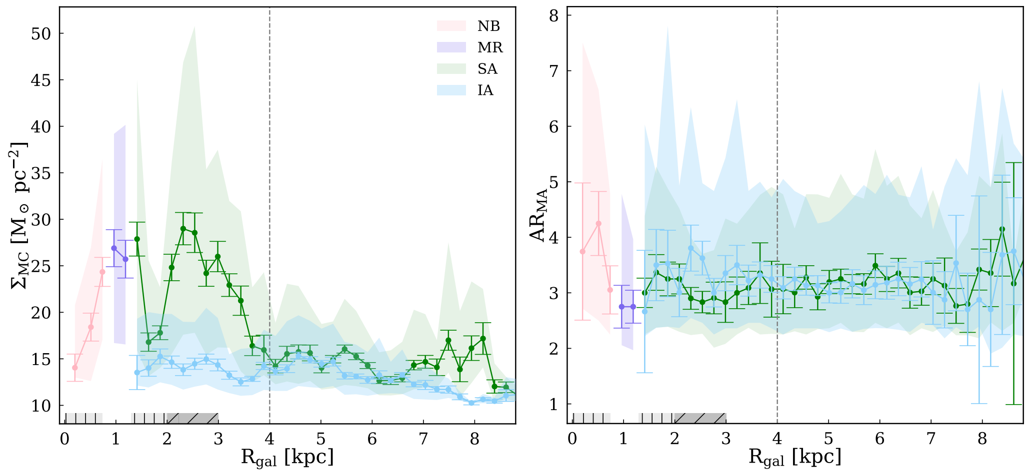

Figure 3.15 – Average cloud surface density, Σ_{MC} (*left*), and medial axis aspect ratio, AR_{MA} (*right*) across galactocentric distance for the different dynamical environments of M51: nuclear bar (NB in pink), molecular ring (MR in purple), spiral arms (SA in green) and inter-arm (IA in light blue). The coloured circles and lines represent the running median of the relevant property. The shaded regions are the corresponding interquartile range of the distributions. The coloured errorbars illustrate the respective standard error on the median ($1.253\sigma/\sqrt{N}$). The vertical dashed line is placed at $R_{gal} = 4$ kpc. The light grey shaded region with vertical hatches adjacent to the x-axis represents known regions of little to no star formation in M51 (e.g. Schinnerer et al., 2013). The darker grey shaded region with diagonal hatches represents a region with intense star formation (e.g. Meidt et al., 2013).

3.4.2 Radial profiles per large-scale environment

Simple 1D radial profiles average different environments together; looking instead at the same radial bins but within each environment separately will highlight any interesting signatures that might otherwise get washed out by the mixing with other environments. Figure 3.15 illustrates the average cloud surface density and medial axis aspect ratio for the separate galactic environments of M51 with R_{gal}. The remaining properties from Fig. 3.14 do not show significant changes, apart from cloud mass which has a similar trend to Σ_{MC}.

The Σ_{MC} radial profiles of the separate large-scale environments have very distinct features (shown in the left panel of Fig. 3.15). As can be seen from the figure, towards the inner galaxy there is a sudden drop of Σ_{MC} at $\sim$1.7 kpc in the spiral arms[6], and it coincides with a known region of little to no star formation (e.g. Meidt et al., 2013; Querejeta et al., 2019). In their kinematic study of M51 using PAWS data, Colombo et al. (2014b) find inflowing non-circular motions driven by the start of the spiral arms between $1.3 < R_{gal} < 2$ kpc, coinciding with this observed dip in Σ_{MC} for the spiral arms. Additionally, Henry et al. (2003) find a deviation from a pure spiral pattern caused by two dominant arms ($m = 2$ mode) for $1 < R_{gal} < 2.2$ kpc

[6] This drop is also present when building a radial profile of each pixel's surface density within the mask of the spiral arms, and thus is not a consequence of the cloud selection.

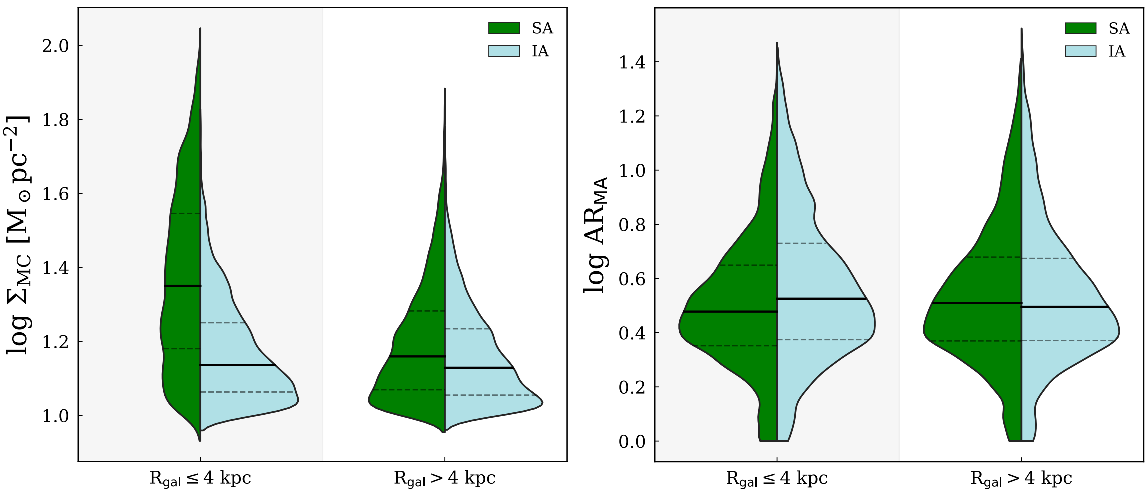

Figure 3.16 – Violin plots showing the contrast between average cloud surface density (Σ_{MC}, *left*) and medial axis aspect ratio (AR_{MA}, *right*) of MCs in the spiral arms (SA in green) and in the inter-arm (IA in blue). For both panels, the cloud populations of each environment are shown for the inner galaxy on the left (shaded region, $R_{gal} \leq 4$ kpc) and for the outer galaxy on the right ($R_{gal} > 4$ kpc). For all violin plots the solid black line represents the median of the distribution, whilst the dashed black lines indicate the upper and lower quartile (as seen from top to bottom).

(also seen by Colombo et al., 2014b), which could increase the non-circular motions of the gas, depleting the available reservoir at those radii and lowering the observed densities. Once approaching the molecular ring, cloud surface densities in the spiral arms seem to rise again, likely from gas being stalled against the MR dynamical barrier. There is also little to no star formation detected for the inner ~ 750 pc of M51, where peculiar motions driven by the bar are dominant and heavily disrupt and disperse the gas (e.g. Colombo et al., 2014b).

As shown in the top panel of Fig. 3.15, the distribution of Σ_{MC} for the inter-arm regions is fairly constant across radial distance, meaning that the declining trend seen for the global profile is indeed driven by the bar and spiral arms of M51. Additionally, the tentative flattening of cloud densities past $R_{gal} \sim 4$ kpc witnessed in Fig. 3.14 is much more pronounced when looking at the spiral arms, and the phenomena causing it does not seem to affect the inter-arm. To further investigate this shift in behaviour, Figure 3.16 highlights the differences in properties of the cloud populations in the inner ($R_{gal} < 4$ kpc) and outer ($R_{gal} > 4$ kpc) galaxy, for both the spiral arms and the inter-arm regions. As was already seen in the radial profiles, it is clear that MCs in the inner spiral arms are much denser than IA clouds at the same small radii, whilst the average density of both populations is similar at larger R_{gal} (see left panel of Fig. 3.16). The same trend is seen for cloud mass, although less pronounced. The most elongated clouds in the inner galaxy seem to develop in the inter-arm (since the upper part of the inner IA violin plot is more populated, shown in right panel of Fig. 3.16), whilst at larger radii the SA and IA distributions are virtually identical.

The clue to this behaviour may lie in the nature of the spiral arms of M51. If M51 was composed of a single quasi-stationary density-wave with a fixed pattern speed, we would expect to see enhanced surface densities/masses throughout the entire spiral arms (relative to the inter-arm regions), since the gas would be harboured and compressed in the strong gravitational potential well generated by the density wave (for a review see Binney & Tremaine, 1987, 2008). This behaviour is indeed similar to what we see in the top panel of Fig. 3.15 for $R_{gal} < 4$ kpc, but not so much for the outskirts of the galaxy. For a density-wave type of pattern, one would also expect to observe newborn stars within the spiral arms and increasingly older stars as you move along in azimuth (i.e. a stellar age gradient), which again is observed in M51 by some studies (e.g. Abdeen et al., 2022), but not by others (e.g. Schinnerer et al., 2017; Shabani et al., 2018). In fact, several studies, both numerical and observational, argue against a fixed pattern speed in M51, and thus against a single density-wave type of pattern (e.g. Tully, 1974; Elmegreen et al., 1989; Meidt et al., 2008; Dobbs et al., 2010). Instead, the spiral structure of M51 seems to have a more transient nature, which evolves dynamically with time as a function of the tidal interaction with its companion NGC 5195 (e.g. Toomre & Toomre, 1972; Elmegreen et al., 1989; Dobbs et al., 2010).

The top panel of Fig. 3.15 suggests that the gas in the spiral arms of M51 has two distinct behaviours. In the inner galaxy ($R_{gal} < 4$ kpc), the spiral arms boast much higher average cloud surface densities relative to the inter-arm regions, similar to the expected behaviour driven by a density-wave type of pattern which promotes a higher frequency of massive SA clouds. On the other hand, in the outer galaxy ($R_{gal} > 4$ kpc), cloud surface densities are very similar for both SA and IA. This change in behaviour occurs at around the same radii for which Querejeta et al. (2016) and Zhang & Buta (2012) identify as the co-rotation radius of the spiral pattern with the gas (at 3.8 kpc and 4.1 kpc, respectively). Given that there is substantial evidence that M51 does not have a single pattern speed, the notion of co-rotation becomes more complex; still it is clear that there is a sharp change in behaviour at this radius. It seems that, even though the spiral pattern is not rotating at a fixed speed in the inner galaxy, the gas is still rotating faster than the spiral arms, meaning that the gas feels the compression due to the passage through the spiral arm as it would on a density-wave type of pattern. As mentioned above, at large galactocentric radii the SA cloud surface densities become more comparable to the inter-arm values, suggesting that past $R_{gal} = 4$ kpc the spiral pattern and the gas are nearly co-moving. In other words, the outer spiral arms appear to be generated by local gravitational instabilities and behave more like material arms rather than a density-wave (see also Miyamoto et al., 2014; Colombo et al., 2014b), which is likely due to the influence of the tidal interaction. The outer spiral arms in M51 are therefore unable to drive the same density enhancement seen in the inner arms (e.g. Dobbs, 2008), since it seems that at large R_{gal} the gas does not have enough time to cross the bottom of the spiral potential well given both the larger gas crossing times between arms in the outskirts of the galaxy, and the fact that the outer spiral arms seem to evolve at a much quicker rate relative to the inner spiral arms (e.g. Dobbs et al., 2010). Additionally, due to the seemingly weaker gravitational potential, the outer arms are less protected against shear thus resulting in their "fractured" appearance (as can be seen from the environmental mask in Fig. 3.4). In the shear-dominated inter-arm regions, we would not expect the gas to be much affected by the tidal interaction. We thus hypothesise that the sharp change in behaviour for the spiral arms at $R_{gal} = 4$ kpc is due to the dynamics of the interaction of M51 with its companion.

Additionally, in M51 star formation seems to occur mostly on the convex side of the spiral arms at $2 < R_{gal} < 3$ kpc (e.g. Meidt et al., 2013), where we also find a peak in the average cloud surface density. The surrounding areas, namely within the inter-arm region, are likely to be affected by the feedback from these star formation events, potentially leading to cloud disruption, which could result in higher aspect ratios. For this region, there is a clear difference in the SA and IA medial aspect ratio profiles shown in the bottom panel of Fig. 3.15, where MCs in the inter-arm have higher aspect ratios than their counterparts in the SA. This could be consistent with stellar feedback disrupting the IA MCs, but could also be attributed to the strong shearing motions at this radii splitting clouds apart (e.g. Dobbs & Pringle, 2013; Miyamoto et al., 2014). Furthermore, the shaded areas in the bottom panel of Fig. 3.15, which represent the interquartile range of cloud aspect ratios, seem to have different peaks depending on galactocentric radii. In the outer galaxy, clouds with high aspect ratios appear to be evenly distributed between SA and IA, but this is not the case at smaller galactocentric radii. For $R_{gal} < 4$ kpc, the majority of the highly elongated clouds seem to reside in the inter-arm, meaning that at these radii the inter-arm regions could be more prone to develop the most elongated structures within the sample. This finding agrees well with the previously presented framework (and with the work of Duarte-Cabral & Dobbs, 2016): in the inner galaxy where the pattern resembles a density-wave, the stronger spiral potential will protect clouds from intense shear within the arms but not in the inter-arm regions, leading to a higher frequency of fragmented/stretched clouds in the IA. This also explains why we do not find a surplus of extremely elongated IA clouds in Section 3.3.4.2, since the extremely elongated sub-sample is taken from the entire sample, effectively losing any effect the different spiral patterns may have on the clouds at different galactocentric radii. To draw any firm conclusions, a more rigorous analysis in quantifying the shear and feedback in these regions is needed, as well as a more robust classification of truly filamentary clouds (as previously discussed in Section 3.3.2).

3.5 CONCLUSIONS

This Chapter presents an exploration of the properties of clouds extracted from the high-resolution gas surface density map of M51 (Chapter 2), and how they might be affected by large-scale galactic environments as well as galactocentric radius (and the combination of the two). The findings can be summarised as follows:

- Molecular clouds residing in the centre of M51 show distinct differences from the disc population. Average cloud sizes, masses, surface densities, and aspect ratios (mostly within the nuclear bar) are higher in the inner few kiloparsecs of M51 than in the disc.
- The gas in M51 is preferentially organised into low-mass clouds in the disc and high-mass clouds in the centre. Additionally, the spiral arms and molecular ring host the highest concentration of high-mass clouds, whilst the inter-arm and nuclear bar distributions show a sharper decline towards higher masses.
- No obvious enhancement of extremely large clouds (in both area and length) was found towards any large-scale environment. On the other hand, there is a surplus of extremely elongated clouds in the nuclear bar region of M51. Additionally, the most massive and highest surface density clouds in the science sample show a clear preference for the molecular ring and spiral arms, suggesting that these environments host beneficial conditions for cloud growth.
- It was found that assuming a surface density-mass threshold as an indicator of the ability of a given cloud to form stars is very likely to be an oversimplified approach that does not capture the complicated juxtaposition of effects in play.
- Although the average surface densities of the inter-arm molecular cloud population remain constant with galactocentric radius, the spiral arm clouds show a different behaviour at small and large radii. For $R_{gal} < 4\,kpc$, there is a clear contrast between cloud surface densities of the inter-arm and spiral arms, whilst at larger radii they have similar radial profiles. Additionally, at small R_{gal}, the most elongated (i.e. highest aspect ratio) clouds seem to mostly belong to the inter-arms.

Non-axisymmetric features (i.e. stellar bar, spiral arms) in M51 exert a substantial influence on how the gas is organised across the galaxy. There is a clear difference in characteristics between the cloud populations of the centre and the disc of M51. Peculiar motions driven by the nuclear bar heavily disrupt the clouds in that region, preventing and/or destroying higher mass objects and stretching out clouds, reflecting into high aspect ratios. Similarly, shearing motions (driven by the differential rotation of the gas) seem to have a similar effect in the inter-arm, albeit the observed characteristics of the inter-arm clouds could also be caused by stellar feedback. A more reliable quantification of cloud morphology is needed in order to distinguish the linearly elongated clouds driven by shear from the more distorted/ring-like clouds potentially associated with feedback regions. Nonetheless, in environments where shear is low (i.e. molecular ring and spiral arms), gas is allowed to accumulate resulting in the development of higher mass/density clouds.

Additionally, it was found that the tidal interaction between M51 and its companion has a strong influence on the cloud population of the spiral arms, but a minimal effect (if any) in the inter-arm clouds. At small radii, the spiral pattern resembles a density-wave type of pattern, where the strong spiral potential piles material up, and drives cloud masses up. Consequently, clouds in the inner spiral arms show enhanced surface densities/masses relative to their counterparts in the inter-arm regions. At large radii, the spiral arms appear to be driven by local gravitational instabilities, which affects both the gas and the stars similarly. Consequently, the outer spiral arms are not as able to promote cloud growth, resulting in the similarities seen between the inter-arm and spiral arm molecular cloud populations at those radii.

The work presented in this Chapter demonstrates the power of larger number statistics on resolved cloud populations, as well as wider coverage across entire galaxies, in unravelling the potential effects of the environment on the formation and evolution of clouds. The spatially resolved information obtained from the extinction-derived gas surface densities (Chapter 2) allows for cloud-scale studies to be conducted across not only various galactic environments, but also across different galaxy types (Chapter 4). Such exercises are fruitful in developing our understanding of star formation as a galactic-driven process, and learn which mechanisms hinder or enhance the formation of stars (and where this occurs), which naturally has repercussions in the evolution of galaxies.

Chapter 4

CLOUD POPULATIONS VERSUS GALACTIC ENVIRONMENT

"I am a person who believes in asking questions."

CHIMAMANDA NGOZI ADICHIE

4.1 INTRODUCTION

Galaxies in the local Universe come in all shapes and sizes. It is estimated that two out of three galaxies have a spiral structure (e.g. Willett et al., 2013; Buta et al., 2015), and that $\sim 30-60\%$ display stellar bars in their centre (e.g. de Vaucouleurs et al., 1991; Sheth et al., 2008; Masters et al., 2011). It is important to investigate the impact these morphological features have on the ISM and subsequently on star formation, since these structures are key drivers of secular evolution in galaxies (for a review, see Kormendy & Kennicutt, 2004). For example, spiral arms are notorious for accumulating gas, leading to higher star formation rates (whether this is natural consequence of more material or a "triggering" effect has not yet been determined; e.g. Foyle et al. 2010; Querejeta et al. 2024), whilst bars are very efficient at pulling gas inwards, potentially enhancing star formation in the centres of galaxies (e.g. Sheth et al., 2005).

This Chapter describes the application of the extinction imaging technique outlined in Chapter 2 to a wider sample of nearby galaxies of different morphology types. Section 4.2 describes the galaxy sample and data products used in this endeavor. Section 4.3 outlines the improvements implemented to the high-resolution extinction technique. A brief description of the extraction of resolved cloud catalogues and the derived cloud properties is held in Section 4.4. In Section 4.5, I explore any trends between a given cloud property and its host galaxy, either in terms of large-scale environment or galactocentric radius. Section 4.6 investigates correlations between large-scale environments and cloud characteristics at a common, homogeneous resolution across the sample. Section 4.7 describes some of the additional planned analysis for this sample of galaxies. A summary of the findings can be found in Section 4.8.

4.2 DATA

In this Chapter, the extinction technique outlined in Chapter 2 (see also Faustino Vieira et al., 2023) is applied to NGC 4689, NGC 628, NGC 1566, and NGC 4321. This technique allows the imaging of the dust (and gas) content in galaxies at high spatial resolution by measuring dust extinction in the optical. It also uses dust emission observations in the far-infrared (FIR) as a benchmark for the dust mass estimates. In this Chapter, the obtained dust (and gas) surface density maps have 0.11" angular resolution, ranging from $\sim 5-9$ pc in physical resolution at the respective distances of the galaxies in the sample. The properties of these nearby disc galaxies are summarised in Table 4.1. These specific galaxies were selected because of their nearly face-on inclinations (which facilitates the application of the extinction technique), the wealth of multi-wavelength data available for these targets, and for their morphology type. Given that the goal of this work is to investigate variations of the ISM as a function of environment, we aimed for a varied morphological sample, selecting barred galaxies (NGC 1566 and NGC 4321), a non-barred spiral (NGC 628) and a flocculent galaxy (NGC 4689).

4.2.1 Optical data

For all galaxies, the F555W filter (V-band, centred at 536 nm) from the HST Wide Field Camera 3 (WFC3) was used to build the extinction-derived surface density maps. The optical data for NGC 1566 is taken from the HST LEGUS (Legacy ExtraGalactic Ultraviolet Survey, Calzetti et al. 2015) program (ID13364), whilst the products for NGC 628[1], NGC 4321 and NGC 4689 are from the PHANGS-HST (Physics at High Angular Resolution in Nearby Galaxies, Lee et al. 2022) program (ID15654). The pixel scale across the sample is ~ 0.04", corresponding to an angular resolution of 0.08".

[1]A small offset in intensity of 0.046 e^-/s was found between the PHANGS-HST V-band for this galaxy and the earlier dataset towards the same target from LEGUS. The PHANGS-HST data was scaled up by the offset, to make the data products consistent with each other.

Galaxy	ϕ^{a} (deg)	i^{a} (deg)	D (Mpc)	Morph. Type	l_{ext} (pc)	M_{ext}^{dust} (10^6 $M_{\odot}$)
(1)	(2)	(3)	(4)	(5)	(6)	(7)
NGC 4689	164.1	38.7	15.0 ($\pm$2.25)[b]	SA(rs)bc	8.0	3.26 ($\pm$0.08)
NGC 628	20.7	8.9	9.84 ($\pm$0.63)[c]	SA(s)c	5.2	2.95 ($\pm$0.3)
NGC 1566	214.7	29.6	17.69 ($\pm$2)[d]	SAB(s)bc	9.4	10.8 ($\pm$0.09)
NGC 4321	156.2	38.5	15.21 ($\pm$0.49)[e]	SAB(s)bc	8.1	11.5 ($\pm$0.3)

Table 4.1 – Summary table of galaxy properties and observational parameters. (1) Galaxy name. (2) Position angle of galaxy. (3) Inclination of galaxy. (4) Distance to galaxy. (5) Morphological type of the galaxy, from the NASA Extragalactic Database, based on de Vaucouleurs et al. (1991). (6) Physical linear resolution of extinction-derived gas surface density map of the galaxy. (7) Total dust mass retrieved from extinction-derived surface density map, with the associated uncertainty (see Section 4.3).
References: [a] Lang et al. (2020). [b] Kourkchi et al. (2020). [c] Jacobs et al. (2009). [d] Kourkchi & Tully (2017). [e] Freedman et al. (2001).

4.2.2 Far-infrared data

The high-resolution dust extinction imaging technique outlined in Chapter 2 utilises FIR dust emission observations to ensure the mass estimates from dust extinction are consistent with those from dust emission. The FIR images used here were observed with the *Herschel* Space Observatory (Pilbratt et al., 2010), using both the PACS (Poglitsch et al., 2010) and SPIRE (Griffin et al., 2010) instruments. All of the targets have observations in the SPIRE bands (250, 350, and 500 μm) and all three PACS bands (70, 100, 160 μm), with the exception of NGC 4689 which was not observed at 70 μm. The FIR images used in this work have been processed with the pipeline (Clark et al., 2018) developed for the DustPedia database (Davies et al., 2017). The modelling of the FIR SED to recover dust properties for each galaxy is described in Section 4.3.2.

4.3 IMPROVEMENTS ON HIGH-RESOLUTION EXTINCTION TECHNIQUE

This Section outlines the improvements that have been implemented to the extinction technique (Chapter 2) after the publication of Faustino Vieira et al. (2023), as well as the updated uncertainty estimation. As a quick summary, this HST extinction technique compares, on a pixel-by-pixel basis, the observed optical light of a galaxy to a reconstructed stellar light model, which mimics what the galaxy would look like with no dust extinction. Additionally, there is a calibration step which adjusts the assumed dust/stars geometry so that the extinction dust masses match those from FIR emission. As in Chapter 2, a constant dust-to-gas mass ratio of 0.01 is adopted, as well as a gas mass absorption coefficient of $\kappa = 1.79$ pc^{2}M$_\odot^{-1}$ (or $\kappa = 8.55 \times 10^3$ cm^{2}g^{-1}) for the V-band (Draine, 2003).

4.3.1 Stellar light reconstruction

The extinction-based imaging technique estimates dust attenuation by comparing the observed optical light to a smooth, reconstructed stellar distribution. In Chapter 2 (and Chapter 3), this stellar distribution (I_0) is built by applying a carefully chosen median filter to the HST optical image (after the removal of bright point-like sources). Although careful tests were performed and the final opacity/surface density maps do not change much when varying the chosen median filter by a factor 2, the choice of a kernel to build I_0 still remained a human choice.

In this work, some changes were implemented such that the choice of kernel minimally impacts the final map, making the technique more robust. In particular, we wanted to improve the estimate of stellar light in highly extinct areas, since large and really prominent dark dust lanes may "contaminate" neighbouring regions when applying a large median filter, resulting in artificially lower values of I_0 next to dust lanes. To prevent this, we implemented a masking of extinction regions prior to the reconstruction of the final stellar distribution, so that the dust lanes may be interpolated over without any bleeding. This was done by obtaining an initial optical depth map (Eq. 2.2) generated with a rough initial guess of I_0 (estimated from the source-removed image using a first-guess median filter, ~ 8" for NGC 1566), and assuming a foreground/background fraction of 0.5. This allows us to retrieve all pixels where the resulting optical depth is above 0 (i.e. where extinction is occurring). These pixels are masked from the source-removed HST V-band image (I), and a piecewise linear interpolation is performed to essentially remove the dust lanes from the original I map, thus avoiding contamination when applying median filters (panel b of Fig. 4.1).

The next step in the method is to create a rough model of the stellar light of each galaxy, using the interpolated source-removed I map. Here, we choose to use a double-component median filter (rather than a single kernel as in Chapter 2), to better retrieve the intensity of the very centre of galaxies, which is more bulge-like. As can be seen from Fig. 4.1, as well as Fig. 4.2, if a single, larger median filter kernel (e.g. ~ 8", corresponding to 200 pixels; MF200) is adopted for NGC 1566 for example, a reasonable estimate for the disc of the galaxy is retrieved, but this severely underestimates the intensity in the centre of the galaxy (panel d1 of Fig. 4.1). When the intensity is greatly underestimated, it can lead to the loss of existing extinction features, as is exemplified in Fig. 4.3. We do not, however, want to adopt a smaller kernel everywhere in the galaxy, as this would not allow to smooth over the larger dust lanes seen in spiral arms, for instance. As such, a double-component approach is adopted, where a smaller

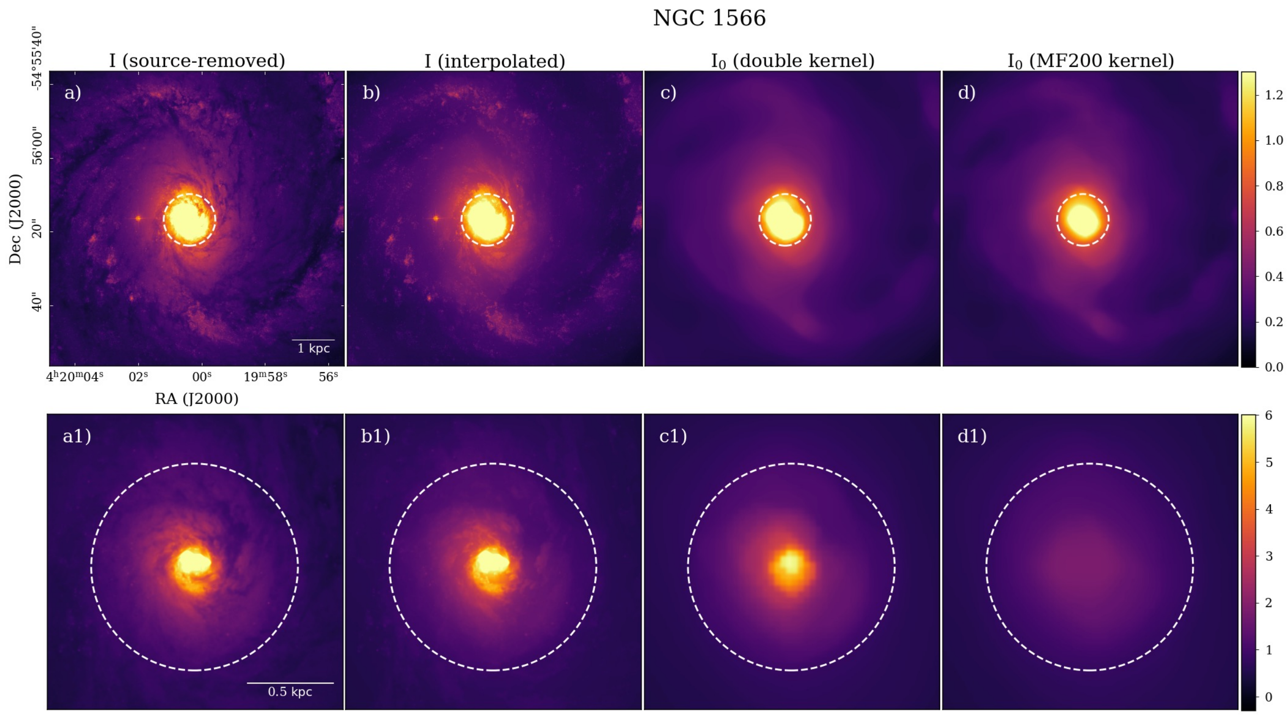

Figure 4.1 – Zoom-in of the central/bar region of NGC 1566 across different steps in the extinction mapping technique (top row). **a)** HST V-band observations, I (with bright, point-like sources removed). **b)** I after linear interpolation of extinction features (as explained in text). **c)** Reconstructed stellar light map, I_0, with two median filters. **d)** I_0 with a single median filter (MF200, $\sim$ 8"). In the bottom row are the same panels further zoomed-in, and with an adjusted colour scale that better illustrates the differences in the centre. Across all panels, the white circle represents the turnover at which we switch from a smaller kernel in the centre to a larger median filter for the disc (see Fig. 4.2).

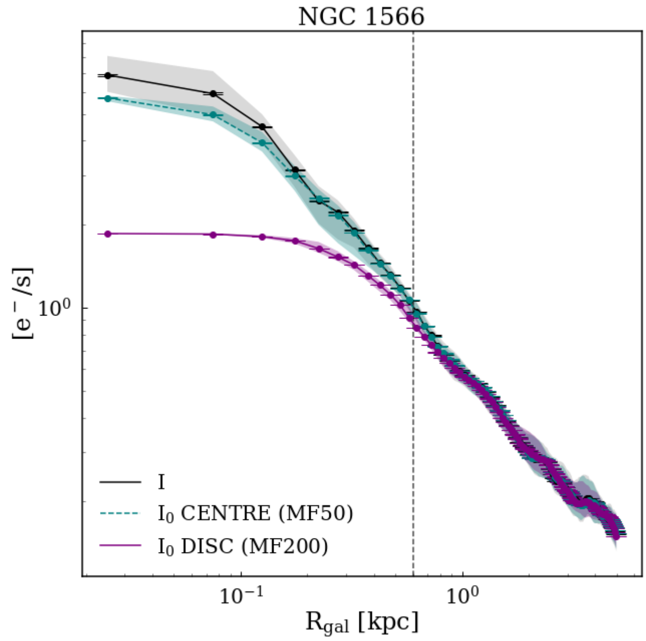

Figure 4.2 – Radial running median profiles for NGC 1566 of the source-removed HST V-band intensity (I, in black), the stellar light model for the centre with a 50 pix ($\sim$ 2") median filter, I_0 (in teal), and the disc I_0 with a median filter of 200 pix or $\sim$ 8" (in purple). The radial bins have a width of 50 pc. The shaded region for each profile depicts the respective interquartile range. The errorbars represent the standard error on the median given the bin count, N ($1.253\sigma\sqrt{N}$). The vertical dashed line represents the galactocentric radius at which the larger median filter approximates the I profile.

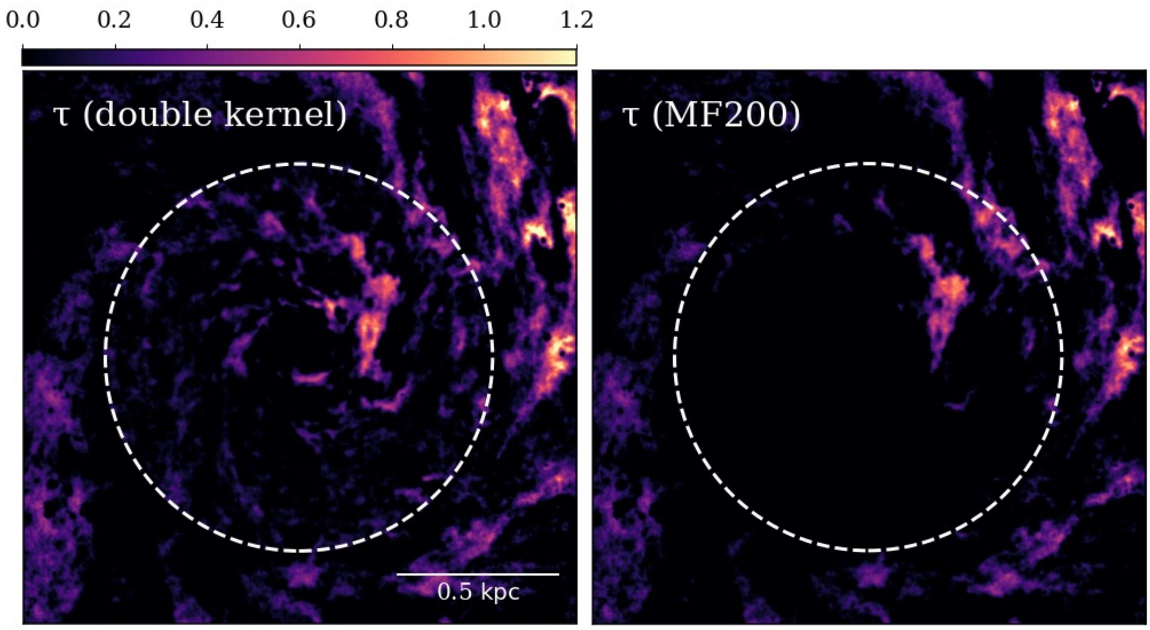

Figure 4.3 – Zoom-in of the central/bar region of NGC 1566 in the optical depth (τ, Eq. 2.2) maps for an interpolated, double-kernel stellar light model (*left*), and for a single large median filter I_0 (MF200, *right*). Across both panels, the white circle represents the turnover at which we switch from a smaller kernel in the centre to a larger median filter for the disc (see Fig. 4.2).

kernel is chosen for the centre and a larger kernel for the disc. The turnover from the centre to the disc kernel is selected from the radial profile of the maps (shown in Fig. 4.2), as the point from which the larger disc kernel starts reliably tracing the source-removed V-band profile. As a final step, the transition from the centre to the disc is smoothed with a small Gaussian convolution (FWHM $\sim$ 20 pix). Figure 4.1 showcases what this double-component I_0 map looks like against the original HST V-band image (treated to remove point-like sources) as well as the single-component I_0 distribution.

For the centres of the galaxies in the present sample, the median filters are kept in the 50–100 pix range ($\sim$ 2" − 4" or $\sim$ 150 − 290 pc), as we found this range more faithfully reproduced the radial profile of the original HST intensity (as exemplified in Fig. 4.2), whilst still smoothing over most existing extinction features (shown in Fig. 4.1). Likewise, we found that median filters between 200–300 pix ($\sim$ 8" − 12" or $\sim$ 570 − 720 pc) were reasonable approximations of the stellar light in the discs of our galaxies. Varying the chosen median filters by a factor 2, changes the resulting opacity map (prior to calibration) by only 20%.

4.3.2 FIR SED modelling: PPMAP

In Chapter 2, to derive dust masses in the FIR, a simple modified blackbody SED modelling was performed on the *Herschel* data. Here, PPMAP (Point Process Mapping; Marsh et al., 2015) is used to create higher resolution dust images of each galaxy in the sample (Matthew W. L. Smith, *priv. comm.*). PPMAP is a Bayesian procedure which fits multi-wavelength data with blackbodies, for a set grid of temperatures. In summary, PPMAP generates a map with increased noise and subsequently decreases this noise in a stepwise approach until it reaches the uncertainty of the input data. With each step, PPMAP minimises the reduced ^{2} between the observed and model values at each pixel, until it finds the optimal solution for both dust temperature and mass at each pixel (for more details see Marsh et al., 2015). Unlike traditional SED modelling, PPMAP takes the relevant instrument's point-spread function (PSF) into account, and therefore does not require the images to be degraded to a common resolution. This allows PPMAP to provide high-resolution dust maps, which are approximately limited by the highest resolution image provided ($\sim$ 5" from the 70 μm, except for NGC 4689 where it is $\sim$ 7" from the 100 μm). To run PPMAP, a dust emissivity index (β) of 1.8[2] was assumed (Planck Collaboration et al., 2011), and a dust mass absorption coefficient of $\kappa = 21.6$ cm^{2}g^{-1} at 250 μm (from Ossenkopf & Henning, 1994, hereafter OH94). For the PPMAP fits, initially 13 values of temperature were used, logarithmically spaced between 10 − 80 K. However, in the very lowest and highest temperature bins no significant dust column was found. Since including

[2]In Chapter 2, a β of 2 was used, rather than the $\beta = 1.8$ used here. The difference in dust mass resulting from these different β values is just $\sim$ 20%.

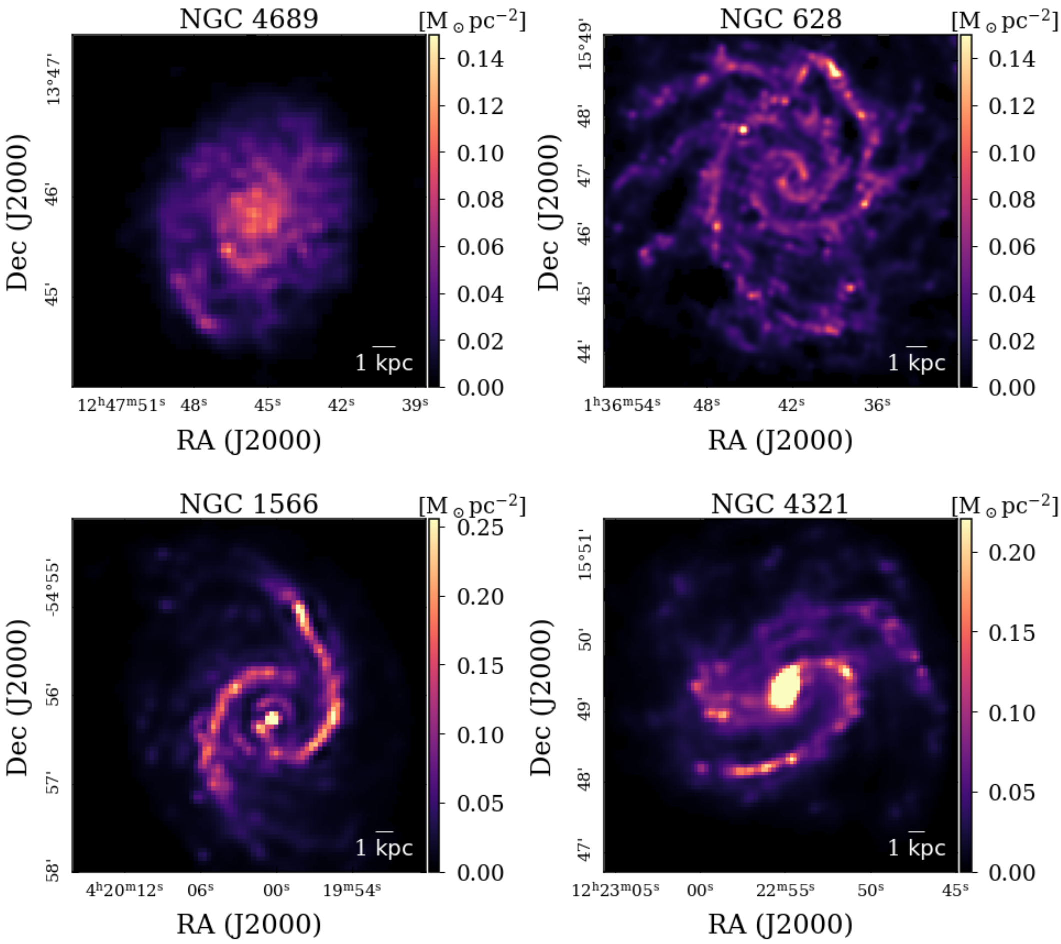

Figure 4.4 – Dust surface density maps resulting from the PPMAP fitting of FIR dust emission observations for NGC 4689, NGC 628, NGC 1566 and NGC 4321 (Matthew W. L. Smith, *priv. comm.*).

these temperature bins also created large uncertainties (most likely due to limited wavelength coverage), these temperature slices were removed and a restriction was placed to only consider temperatures between 16.8 – 40 K (or 16.8 – 67 K for NGC 628[3]). The final dust emission surface density map for each galaxy (Matthew W. L. Smith, *priv. comm.*) was created with the results from the PPMAP fits (i.e. summing the column through each temperature slice), and only the pixels whose values are greater than 3σ are used[4] (shown in Fig. 4.4). Similarly, the temperature maps for each galaxy are an average across all temperature slices, weighted by the measured dust surface density at each bin (Fig. 4.5).

[3]For this galaxy, there were some significant contributions from hot dust detected.

[4]The standard deviation σ is modelled by PPMAP, considering the photometric noise of each input image.

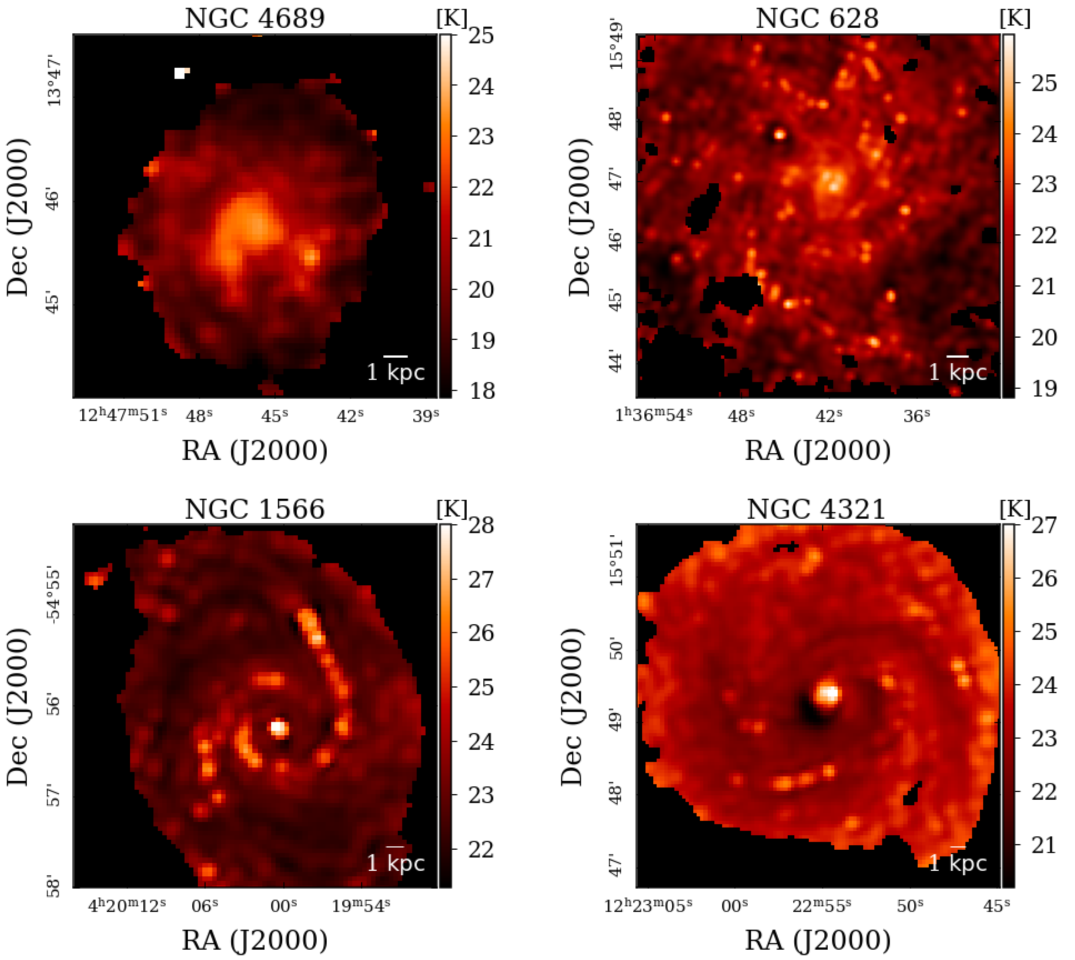

Figure 4.5 – Dust temperature maps resulting from the PPMAP fitting of FIR dust emission observations for NGC 4689, NGC 628, NGC 1566 and NGC 4321 (Matthew W. L. Smith, *priv. comm.*).

Galaxy	log σ_I	log $\sigma_{f/b}$	log $\sigma^*_{I_0}$
NGC 4689	-2.28	-2.71	-2.122 (-2.125)
NGC 628	-2.18	-1.5	-2.025 (-2.026)
NGC 1566	-1.94	-2.68	-1.791 (-1.792)
NGC 4321	-1.89	-2.07	-1.737 (-1.739)

* Values shown for centre (disc), given the different median filters.

Table 4.2 – The uncertainties (in log-form) of the quantities used to estimate the relative error of the final opacity (and surface density) map for each galaxy, on a pixel-by-pixel basis. σ_I is the photometric noise of the V-band image, after point-like source removal. $\sigma_{f/b}$ is the uncertainty on the calibration with dust emission (see text). σ_{I_0} is the uncertainty on the reconstructed stellar light map.

4.3.3 Monte Carlo uncertainties

To measure the uncertainty in this work's opacity estimates (τ), Monte Carlo realizations are performed for each pixel in the maps. As was already adressed in Section 2.3.5, τ will depend on the photometric noise of the HST V-band image, σ_I, the associated error when constructing the stellar light models, σ_{I_0}, and the uncertainty on the calibration with FIR dust emission observations, which is taken to be the scatter on the foreground/background fraction resulting from said calibration, $\sigma_{f/b}$.

Since the methodology on the stellar light modelling was changed from that of Chapter 2 (as explained in the section above), the calculation of σ_{I_0} is also updated accordingly. Before, with a single median filter, the uncertainty was computed through the standard error on the median, $\sigma_{\mathrm{MF}} = 1.2533\, \sigma_I \sqrt{\mathrm{MF}}$, where MF is the respective median filter in pixels. Here, this calculation is performed for the two median filters used, and additionally, the uncertainty on the linear interpolation used when building these maps is also calculated. Considering that the uncertainty in a linear interpolation (σ_{int}) can be approximated by propagating the uncertainties between 2 points[5], then

$$\sigma_{\mathrm{int}} = \sqrt{\sigma_I^2 + \sigma_I^2} \sim \sqrt{2}\, \sigma_I, \tag{4.1}$$

assuming that all points in the map have uncertainty equal to the photometric noise. Finally, the error on the double-component I_0 map can be estimated by propagating σ_{MF} and σ_{int}, such that

$$\sigma_{I_0} = \sqrt{\sigma_{\mathrm{MF}}^2 + \sigma_{\mathrm{int}}^2}. \tag{4.2}$$

The remaining uncertainties (σ_I and $\sigma_{f/b}$) are estimated with the same methodology as that described in Section 2.3.5. Table 4.2 holds the different uncertainties that are used when

[5]This is the approach for a linear interpolation in a 1D case, which serves to give a conservative estimate.

performing the 10^4 pixel-by-pixel Monte Carlo simulations for each galaxy. These can be propagated to give the uncertainty on the total dust mass retrieved for each galaxy in the sample (shown in Table 4.1, see also Section 2.3.5). It is important to note that these uncertainties do not take into account the uncertainty in the assumed distance to a galaxy, dust mass absorption coefficient, or any other systematic errors.

4.3.4 Total dust mass estimates

This Section provides a comparison of the total dust mass estimates from the literature for the present sample of galaxies, to the estimates retrieved from the application of the extinction technique.

Nersesian et al. (2019) performed FIR modified blackbody (MBB) modelling of DustPedia[6] galaxies, obtaining a dust mass of $2.9\,(\pm 1.3) \times 10^7$ $M_\odot$ for NGC 628, with $\kappa = 6.40$ cm^{2}g^{-1} at 250µm (i.e. the `THEMIS` dust model, Jones et al., 2013). As discussed in Section 2.4.1, when comparing dust mass values it is important to correct for the different dust model assumptions first, which can be done by applying a factor that accounts for the difference in assumed κ. Adjusting the Nersesian et al. (2019) dust mass to our adopted opacity law from OH94, gives $8.6\,(\pm 3.9) \times 10^6$ $M_\odot$, which is a factor ~ 3 larger than our value. We note however, that this particular MBB fit was performed on only 3 points making the resulting fitted values less certain, and that the field-of-view (FoV) of the HST observations are smaller than the data used by Nersesian et al. (2019). Also for NGC 628, Aniano et al. (2012) performed spectral modelling using the Draine & Li (2007) dust model ($\sim \kappa = 3.98$ cm^{2}g^{-1}, e.g. Mentuch Cooper et al. 2012), obtaining $2.9\,(\pm 0.4) \times 10^7$ $M_\odot$. Adjusted for the OH94 model, this dust mass becomes $5.3\,(\pm 0.7) \times 10^6$ $M_\odot$, which is within a factor 2 of our result for a more limited FoV.

The dust mass values for NGC 1566 in the literature range from $4.3\,(\pm 0.6) \times 10^6$ $M_\odot$ (from the DustPedia MBB fits with `THEMIS`) and 1.6×10^8 $M_\odot$ (from the near-IR to FIR spectral modelling done in Wiebe et al., 2009, using $\kappa = 3.05$ cm^{2}g^{-1} at 250 µm). Adjusted to OH94, this mass range becomes $1.3\,(\pm 0.2) \times 10^6$ $M_\odot - 2.3 \times 10^7$ $M_\odot$, where our value of 1.1×10^7 $M_\odot$ fits comfortably.

The extinction-based mass estimate of NGC 4321 is also slightly lower than the literature, given the smaller FoV of the HST V-band observations compared to *Herschel*. The OH94-adjusted dust mass from the DustPedia MBB fit is $1.5\,(\pm 0.2) \times 10^7$ $M_\odot$ (originally $5.1\,(\pm 0.5) \times 10^7$ $M_\odot$ with `THEMIS`), compared to the extinction-derived $1.2\,(\pm 0.03) \times 10^7$ $M_\odot$.

Finally, for the flocculent NGC 4689, Nersesian et al. (2019) performed both a `THEMIS`

[6] http://dustpedia.astro.noa.gr/MBB

MBB fit and a spectral fit using `CIGALE` (Noll et al., 2009), based on the Draine & Li (2007) dust model. The respective masses found were $9.0\,(\pm 1.1) \times 10^6$ M$_\odot$ and $2.2\,(\pm 0.2) \times 10^7$ M$_\odot$. Adjusting both to the OH94 opacity law gives a mass range between $2.7\,(\pm 0.3) \times 10^6$ M$_\odot$ and $4.1\,(\pm 0.03) \times 10^6$ M$_\odot$, which is consistent with our value of $3.26\,(\pm 0.08) \times 10^6$ M$_\odot$.

4.4 CLOUD POPULATIONS FROM EXTINCTION MAPS

Figure 4.6 showcases the gas mass surface density maps for the 4 galaxies in the sample, with the environment masks from Querejeta et al. (2021) overlaid as white contours. Throughout this work, these masks are used to investigate systematic trends in the cloud populations. They are composed of 3 major environments: the centre (+ bar, where relevant), C(+B); the spiral arms, SA; and the inter-arm regions, IA. NGC 4689, being a flocculent galaxy, has no well-defined spiral arms, and so we simply denote the entire disc, D.

With the goal of statistically studying the variations of ISM properties as a function of large-scale environment, the extinction-derived gas maps are segmented into clouds. This is achieved with the use of the `ASTRODENDRO`[7] package with which the dendrogram of the gas surface density maps is constructed, and the spectral clustering algorithm `SCIMES`[8] (Colombo et al., 2015, 2019). This approach to the cloud extraction is similar to the one employed in Chapter 3.

The parameters required for the construction of the dendrogram are the minimum threshold for segmentation (`min_value`), the minimum difference in emission for two structures to be considered independent (`min_delta`), and the minimum area a structure must be (`min_npix`). For all galaxies, we adopted `min_value` $= 5$ M$_\odot$ pc^{-2} and `min_delta` $= 5$ M$_\odot$ pc^{-2} to ensure the extraction is consistent across the sample. A wide parameter space was explored, and there was minimal difference in the resulting clouds (see also Colombo et al., 2015). The `min_npix` was set to the number of pixels which correspond to 3 resolution elements (~ 27 pix), to ensure all identified structures are well-resolved. The major difference in the cloud extraction performed here versus that performed in Chapter 3, is the use of the "luminosity" as well as the "radius" criterion to aid the `SCIMES` clustering. Furthermore, a user-defined scaling parameter of 100 pc was employed for the "radius" criterion, which helps the algorithm identify structures in an equal manner across different galaxies, which will have different dynamical ranges.

The `SCIMES` segmentation resulted in a total of ~ 97000 clusters recovered across the galaxy sample, which encompass on average $\sim 70\%$ of the total mass in the maps. Since this cloud catalogue is based on extinction-derived maps, both atomic and molecular clouds are included,

[7] https://dendrograms.readthedocs.io/en/stable/
[8] https://github.com/Astroua/SCIMES/

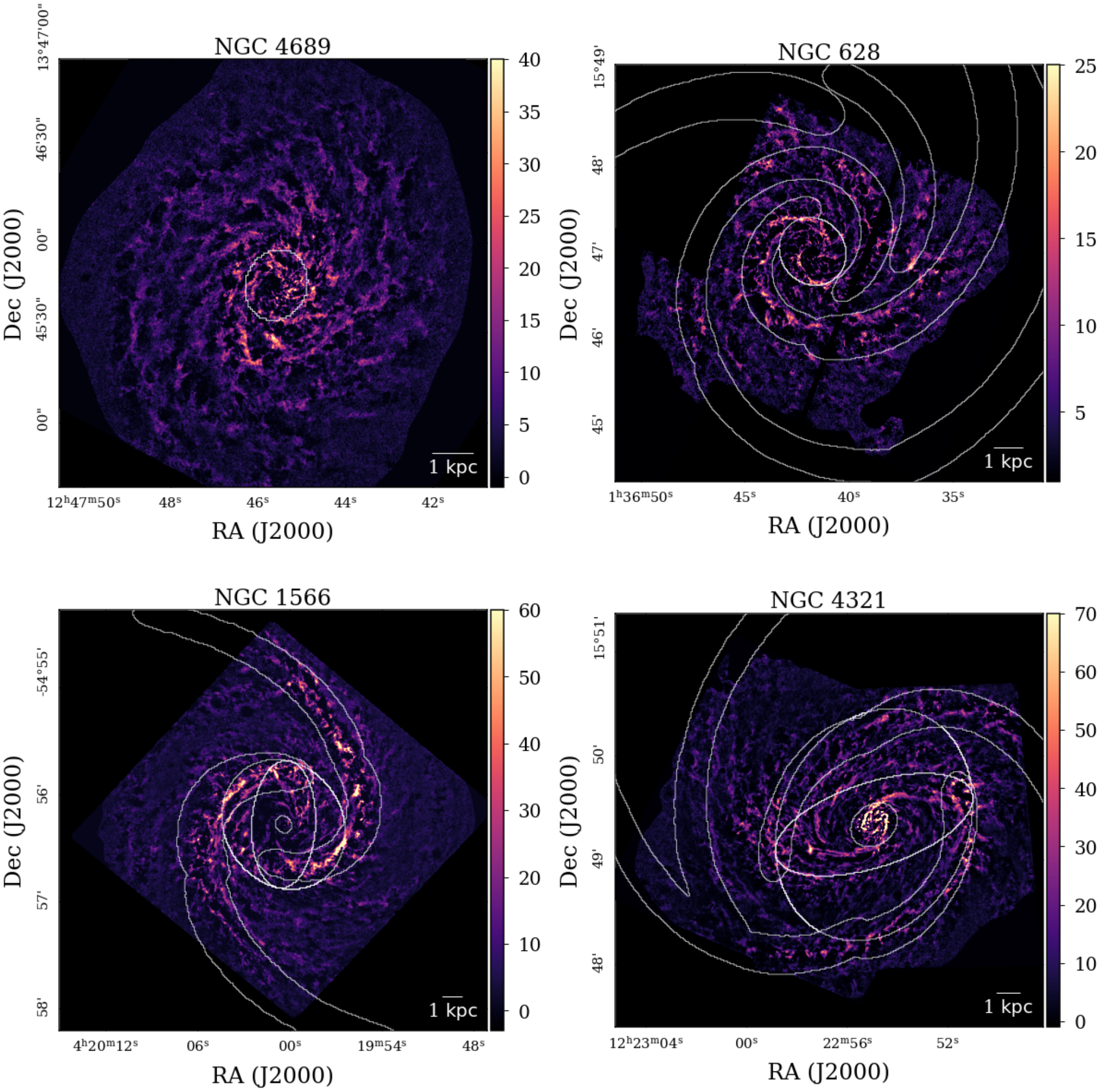

Figure 4.6 – Gas mass surface density maps of the galaxies in the sample (NGC 4689, NGC 628, NGC 1566, and NGC 4321). The white contours correspond to the environments present in the masks from Querejeta et al. (2021), which are used here. The colourbars have $M_{\odot}\,pc^{-2}$ units.

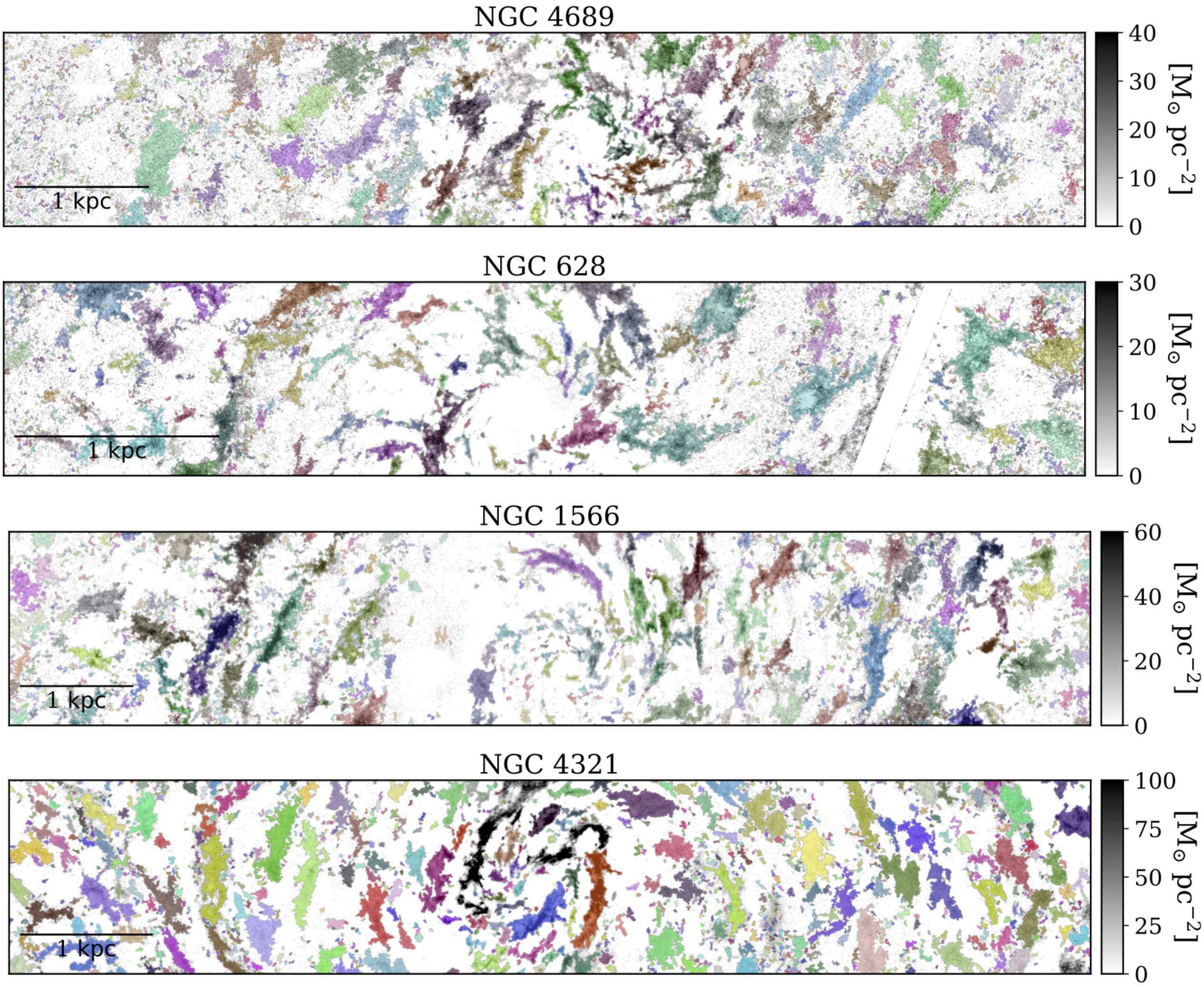

Figure 4.7 – Clouds (in random colours) from the native resolution catalogue for an example region of NGC 4689, NGC 628, NGC 1566 and NGC 4321 (from top to bottom). The gas surface densities are the background greyscale for each galaxy.

given that dust traces the total gas (not just molecular). In order to build a science subsample of clouds for the analysis performed in this Chapter (i.e. the science subsample), a number of further selection criteria were applied to ensure the clouds have robust properties.

The relative uncertainty of each cloud in the sample is estimated through Monte Carlo simulations (Section 4.2). In the science sample, we keep only clouds with a relative uncertainty $< 30\%$, which are subsequently flagged in the catalogue with *Rel_ err_ cut*=1. Furthermore, the maximum measurable limit, $\tau_{\rm max}$, is also measured at each pixel across all the maps. This quantity is dictated by the photometric noise of the original HST V-band images, and so, remembering Eq. 2.2, we impose that this maximum measurable limit is when $I - I_{\rm fg} = 3\,\sigma_I$ (σ_I being the photometric noise). This is because the maximum value of τ corresponds to the term $I - I_{\rm fg}$ being at a minimum. We determine the fraction of pixels within each cloud where the optical depth estimate surpasses $\tau_{\rm max}$, which would reflect higher uncertainty in surface density/mass estimates for that cloud. The science subsample holds only clouds whose fraction of pixels where $\tau > \tau_{\rm max}$, relative to the total number of pixels within the cloud, is less than 30%. These clouds are flagged in the catalogue with *Tau_max_cut*=1. It is important to note that for NGC 4321, we diverge slightly from this decision, since a considerable amount of clouds in one of the segments of the bar do not pass this *Tau_max_cut*. The estimate of a single background/foreground value for the entire galactic disc (see Section 2.3.4) is likely failing for this portion of the large bar, since we do not account for bar inclinations, and so the dust might not be at the same scale height across the bar. Accounting for this in our calibration process is not straightforward and requires more sophisticated modelling of the stellar light in bars, which is beyond the current scope of this work. In an effort to minimise the loss of statistics for bar environments, which is essential to the analysis of impact of environments performed in this Chapter, these bar clouds are still included, but are attributed an additional flag in the NGC 4321 catalogue (*Uncertain_mass_tag*=1), alerting that the mass estimates for these clouds are more uncertain. There are 220 of these clouds, constituting 7% of clouds in those environments. All observed trends with cloud properties in this work remain the same with or without these more uncertain clouds in NGC 4321.

Furthermore, two size cuts are employed to ensure clouds are well-resolved: one based on each galaxy's native resolution, and one based on a homogenised or common resolution for the full sample. Clouds that have a size larger than 3 resolution elements, with the resolution element being that of the data for the relevant galaxy, pass the native size cut (*Native_size_cut*=1). For the purpose of comparing cloud populations between galaxies, we take the resolution of NGC 1566, the furthest galaxy in the sample, as the common resolution. As such, for the remaining clouds in the sample, the tag *Size_cut*=1 is applied to clouds that have a size equivalent to 3 resolution elements for NGC 1566 (~ 303 pc^2). There are some issues with this latter common resolution size cut, which are addressed in full in Section 4.6.2. Finally, any clusters that directly touch the image's edge (or inner mosaic edge in the case of NGC 628) are also ruled out. The science subsample for the native resolution holds $\sim 77,000$ clouds across the sample of galaxies (see Fig. 4.7), whilst the homogenised subsample is currently composed of $\sim 50,000$ clouds.

4.4.1 Cloud properties

The ISM is not impervious to the large-scale physical processes undergoing in its host galaxy. Evidence of this could be in any observed systematic variations in cloud properties within different galactic environments, as well as between different types of galaxies. Therefore, in this

Catalogue Column	Description
ID	Unique ID number of cloud
RA_deg	Right ascension of cloud (degrees)
Dec_deg	Declination of cloud (degrees)
RA_pix	Right ascension of cloud (pixel coordinates)
Dec_pix	Declination of cloud (pixel coordinates)
R_gal	Distance of cloud centre to the galactic centre (kpc)
Sigma_tot	Total sum of the gas mass surface density of every pixel in the cloud ($\mathrm{M_\odot\ pc^{-2}}$)
Sigma_avg	Average gas mass surface density of cloud ($\mathrm{M_\odot\ pc^{-2}}$)
Sigma_peak	Peak gas surface density of cloud ($\mathrm{M_\odot\ pc^{-2}}$)
Area_ellipse	Area of the ellipse defined by the second moments of the cloud ($\mathrm{pc^2}$)
Area_exact	Exact area of cloud ($\mathrm{pc^2}$)
R_eq	Equivalent radius estimated using the cloud's exact area (i.e. $R_{\mathrm{eq}} = \sqrt{A/\pi}$; pc)
Mass	Mass of cloud ($\mathrm{M_\odot}$)
Major_axis_a	Semi-major axis (pc)
Minor_axis_b	Semi-minor axis (pc)
AR_ab	Aspect ratio between semi-major and semi-minor axis
PA	Position angle of cloud major axis, measured counter-clockwise from $+x$ axis (degrees)
Length_MA	Length of the geometrical medial axis (pc)
Width_MA	Width of the geometrical medial axis (pc)
AR_MA	Aspect ratio between the medial axis length and width
RJ1	Rotated J-value, $\mathrm{R_1}$
RJ2	Rotated J-value, $\mathrm{R_2}$
RJ_class	Rotated J-value cloud morphology classification. (1=circular-like, 2=ring-like, 3=centrally overdense filament-like, 4=centrally underdense filament-like)
Rel_err	Relative uncertainty on the cloud's opacity (and thus surface density/mass) from the dust extinction technique alone
Env	Tag identifying the environment of the cloud, as per Querejeta et al. (2021). (Centre+Bar=1,2,3. Spiral arms=5,6. Inter-arm=4,7,10)
Native_size_cut	Tag identifying clouds that are well-resolved in the native resolution of the respective galaxy, i.e. $A > 3$ resolution elements (1=yes, 0=no)
Size_cut	Tag identifying clouds that are (1=yes, 0=no)
Not_edge_cut	Tag identifying clouds that do not touch the edge of the map (1=not edge, 0=edge)
Rel_err_cut	Tag identifying clouds that pass the relative uncertainty $< 30\%$ criteria (1=yes, 0=no)
Tau_max_cut	Tag identifying clouds that have less than 30% of their pixels with $\tau > \tau_{\mathrm{max}}$ (1=yes, 0=no)
*Uncertain_mass_tag**	Tag identifying clouds with *Tau_max_cut*=0, but we choose to keep in the science sample (1=yes, 0=no)

* Only for the NGC 4321 catalogue.

Table 4.3 – Description of the cloud catalogues for NGC 4689, NGC 628, NGC 1566, and NGC 4321, obtained in this work.

work, I analyse any trends between cloud properties and their galactic context. All the derived cloud properties included in the catalogue are listed and described in Table 4.3.

The average gas mass surface density of each cloud ($\Sigma_{\rm avg}$) is estimated from the total "flux" (i.e. total gas mass surface density) computed by `ASTRODENDRO` for the structure, divided by the footprint area of the cloud. The cloud mass (M) is then given by its $\Sigma_{\rm avg}$ multiplied by its physical area (A in pc^2). Finally, to get an estimate of each cloud's length and elongation, the medial axis of each cloud is retrieved. The medial axis is the longest running spine of a cloud, i.e. the longest continuous line that is the furthest away from the edges of the cloud. Utilising the medial axis is a purely geometrical approach which is more faithful to the actual size and shape of a resolved cloud. The medial axis length ($L_{\rm MA}$) is computed, as well as the medial axis aspect ratio (AR$_{\rm MA}$), which is $L_{\rm MA}$ divided by the width of the cloud (i.e. the average distance from the medial axis to the cloud edges). When this aspect ratio is close to unity, the cloud tends to be circular.

In addition, to categorise clouds in terms of their morphology, the automated technique RJ-plots (Jaffa et al., 2018; Clarke et al., 2022) is employed. This is a way to quantitatively characterise a cloud's morphology by comparing its principal moments of inertia to those of a circle of equal area and weight[9]. RJ-plots automatically categorise clouds into four classifications: circular (RJ=1), ring-like (RJ=2), elongated and centrally overdense (RJ=3), elongated and centrally underdense (RJ=4).

4.5 CLOUD TRENDS WITHIN HOST GALAXY

In this Section, I explore any trends of cloud properties as a function of galactic environment and galactocentric distance for each galaxy in the sample, at their native resolution (see Table 4.4). To construct running radial medians, all galaxies were divided into concentric radial bins of width 250 pc. The exceptions are the first and last bins, which are increased to ∼500 pc to account for the lower number of clouds at those radii. These galactocentric radii already account for the inclination and position angle of each galaxy (listed in Table 4.1).

4.5.1 Cloud mass and surface density

From the cumulative $\Sigma_{\rm avg}$ distributions shown in Fig. 4.8, it is evident that the surface densities of clouds in the central regions are distributed differently than other environments within the respective galaxy, with the exception of NGC 1566 where the centre and spiral arm clouds show somewhat similar distributions. This is further exemplified in Fig. 4.9, which also

[9]Weight here is the integral of each pixel's weighting (see Clarke et al., 2022).

Env.	$N_{\rm clouds}$	M ($10^3\,{\rm M}_\odot$)	$\Sigma_{\rm avg}$ (${\rm M}_\odot\,{\rm pc}^{-2}$)	$L_{\rm MA}$ (pc)	${\rm AR}_{\rm MA}$
(1)	(2)	(3)	(4)	(5)	(6)
		NGC 4689			
C	141	$6.0^{21.2}_{3.4}$	$11.8^{15.3}_{9.5}$	14^{26}_{10}	$3.0^{4.24}_{2.25}$
D	13,212	$3.2^{5.2}_{2.3}$	$8.2^{9.0}_{7.6}$	13^{18}_{10}	$3.0^{4.02}_{2.36}$
Global	13,353	$3.2^{5.3}_{2.3}$	$8.2^{9.1}_{7.6}$	13^{18}_{10}	$3.0^{4.02}_{2.36}$
		NGC 628			
C	393	$3.1^{9.6}_{1.6}$	$8.7^{11.1}_{7.6}$	17^{37}_{12}	$3.29^{5.25}_{2.36}$
SA	9,733	$1.7^{3.2}_{1.1}$	$8.2^{8.9}_{7.6}$	14^{21}_{10}	$3.13^{4.38}_{2.36}$
IA	16,068	$1.6^{3.1}_{1.1}$	$8.2^{8.8}_{7.7}$	14^{22}_{11}	$3.2^{4.5}_{2.4}$
Global	26,194	$1.7^{3.2}_{1.1}$	$8.2^{8.8}_{7.6}$	14^{22}_{11}	$3.16^{4.47}_{2.37}$
		NGC 1566			
C+B	627	$10.9^{34.5}_{5.4}$	$10.3^{16.0}_{8.15}$	$16^{29}_{10.5}$	$3.13^{4.53}_{2.25}$
SA	4,268	$7.5^{17.6}_{4.2}$	$9.4^{13.4}_{8.1}$	$16^{29}_{10.5}$	$3.0^{4.25}_{2.25}$
IA	15,711	$5.7^{11.5}_{3.6}$	$8.6^{9.5}_{8.0}$	14^{22}_{10}	$3.2^{4.59}_{2.37}$
Global	20,606	$6.1^{12.9}_{3.7}$	$8.7^{9.9}_{8.0}$	14^{22}_{10}	$3.13^{4.5}_{2.36}$
		NGC 4321			
C+B	2,446	$7.1^{16.6}_{3.6}$	$12.2^{19.3}_{9.4}$	14^{22}_{10}	$2.93^{4.02}_{2.25}$
SA	5,314	$4.6^{9.3}_{2.9}$	$9.9^{12.2}_{8.8}$	13^{19}_{10}	$3.0^{4.0}_{2.36}$
IA	8,885	$4.2^{8.1}_{2.7}$	$9.3^{10.6}_{8.5}$	13^{20}_{10}	$3.0^{4.25}_{2.36}$
Global	16,645	$4.6^{9.5}_{2.9}$	$9.7^{11.7}_{8.6}$	13^{20}_{10}	$3.0^{4.1}_{2.36}$

Table 4.4 – Characteristics of the cloud populations of each galaxy at their respective physical resolution (native sample). (1) Galactic environment: C(+B)= Centre(+Bar), SA=Spiral arms, IA=Inter-arm, or D=Disc in the case of NGC 4689. (2) Number of clouds per environment, $N_{\rm clouds}$. (3) Cloud mass, M. (4) Average gas surface density of clouds, $\Sigma_{\rm avg}$. (5) Medial axis length, $L_{\rm MA}$. (6) Moment aspect ratio, ${\rm AR}_{\rm MA}$. For columns (3)-(6), the median of the distribution is presented, with the 25$^{\rm th}$ and 75$^{\rm th}$ percentiles being the subscript and superscript, respectively.

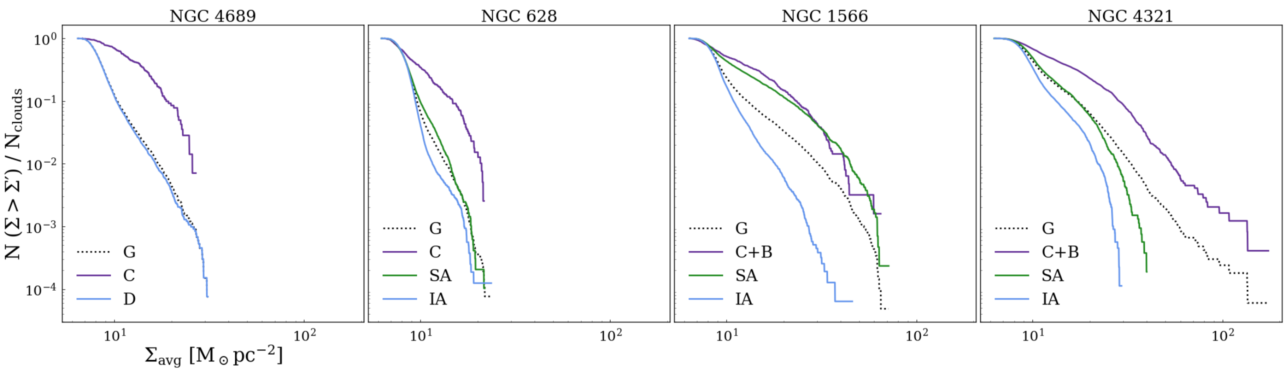

Figure 4.8 – Cumulative average cloud surface density distributions across the different environments within our sample of galaxies: NGC 4689, NGC 628, NGC 1566 and NGC 4321 (from left to right). The different environments are colour-coded, with the centre (C) in purple (C+B for NGC 1566 and NGC 4321), the spiral arms (SA) in green, the inter-arm regions (IA) in blue, and the global (G) distribution being the dotted black line. For NGC 4689, the blue denotes the disc (D). All distributions are normalised by the total number of clouds within each relevant environment, N_{clouds} (as listed in Table 4.4).

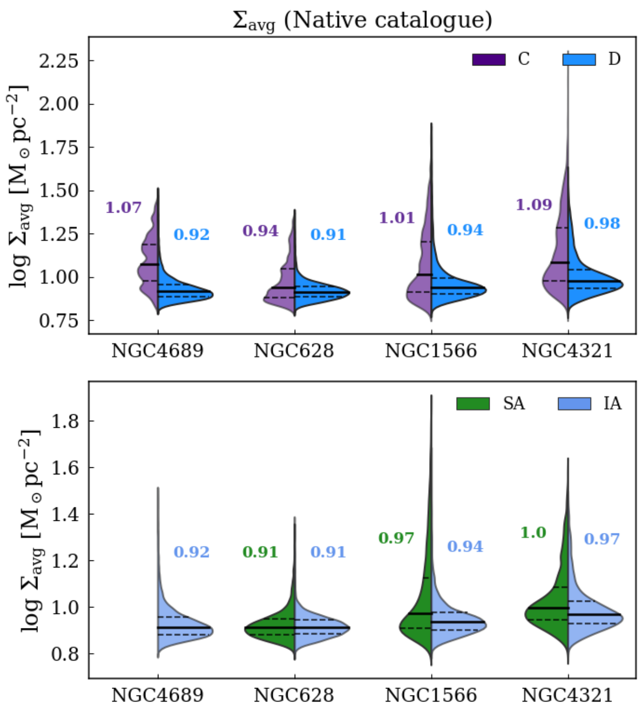

Figure 4.9 – Violin plots showing the contrast between the average cloud surface density (Σ_{avg}) distributions in different environments across the 4 galaxies (native resolution). The top row shows the difference between the centre (C, in purple) and the disc (D, in blue) populations, whilst the bottom row shows the arm population (SA, in green) against the inter-arm (IA, in light blue). For all distributions, the solid black line within the violin represents the median, whilst the dashed lines depict the interquartile range. Next to each distribution, the written label is the relevant median (in logarithmic scale), colour-coded by environment.

shows that cloud surface densities are consistently higher in the centres of galaxies versus the disc - a finding consistent with the literature (e.g. Sun et al., 2020b; Querejeta et al., 2021; Faustino Vieira et al., 2024). This is also seen with cloud masses. For both of the unbarred galaxies (NGC 4689 and NGC 628), although the centre and disc cumulative distributions extend to the same $\Sigma_{\rm avg}$ values, the amount of high-surface density clouds is much higher in the centre than in the disc environments. On the other hand, the centre of NGC 4321, which has a very large bar, extends past the arms and inter-arm into much higher surface densities. This results in a much more top-heavy distribution of $\Sigma_{\rm avg}$ for the centre of this galaxy relative to the disc (see Fig. 4.9).

Across the sample of spirals, there also seems to be some difference between cloud properties in the arm versus inter-arm. For the barred galaxies in the sample, there is an increase in $\Sigma_{\rm avg}$ towards the arms relative to the inter-arm (Fig. 4.9). This difference is more pronounced in NGC 1566 than in NGC 4321 (see also Fig. 4.8). For NGC 628, the difference between SA and IA is next to none, as can be seen from Fig. 4.8 and Fig. 4.9.

Figure 4.10 illustrates the $\Sigma_{\rm avg}$ distributions for the barred galaxies within their sub-divided environments, as per Querejeta et al. (2021). In NGC 1566, clouds appear to have similar $\Sigma_{\rm avg}$ (and mass) across the centre and bar, with an increase toward the bar ends (and a higher spread in the distribution). This increase in $\Sigma_{\rm avg}$ is also seen towards the innermost section of the spiral arms (within the radius of the bar, $\rm R_{bar}$) and towards the inter-bar. Outside $\rm R_{bar}$, the SA and IA distributions appear more bottom-heavy for this galaxy. In NGC 4321, the centre harbours higher surface density clouds, followed by a slight increase in the bar ends[10]. Although less pronounced than what was seen in NGC 1566, the inner spiral arms and inter-bar environments are also displaying higher $\Sigma_{\rm avg}$ in NGC 4321, whilst the environments at $> \rm R_{bar}$ again appear more bottom-heavy. This indeed suggests that the dynamics driven by bars are affecting the environments within its radius.

It is also possible to isolate the highest surface density objects of each galaxy, and investigate their preferred location within the galactic context. If there is a higher than expected concentration of high-$\Sigma_{\rm avg}$ clouds towards a given large-scale environment, it could hint at some physical process that benefits the formation and evolution of clouds in that region. Figure 4.11 showcases the positions of the clouds with highest surface density across the sample. For each galaxy, these clouds compose the top 5% of the $\Sigma_{\rm avg}$ distribution. This subsample constitutes 667 clouds in NGC 4689, 1309 in NGC 628, 1030 in NGC 1566 and 832 in NGC 4321. Visually, it appears that the flocculent NGC 4689 harbours most of its high-$\Sigma_{\rm avg}$ clouds at small galactocentric radii. As for the spiral galaxies, Fig. 4.11 clearly shows these clouds tracing the

[10]This behaviour remains unchanged if the clouds in NGC 4321 with more uncertain masses are not considered, as explained in Section 4.4.

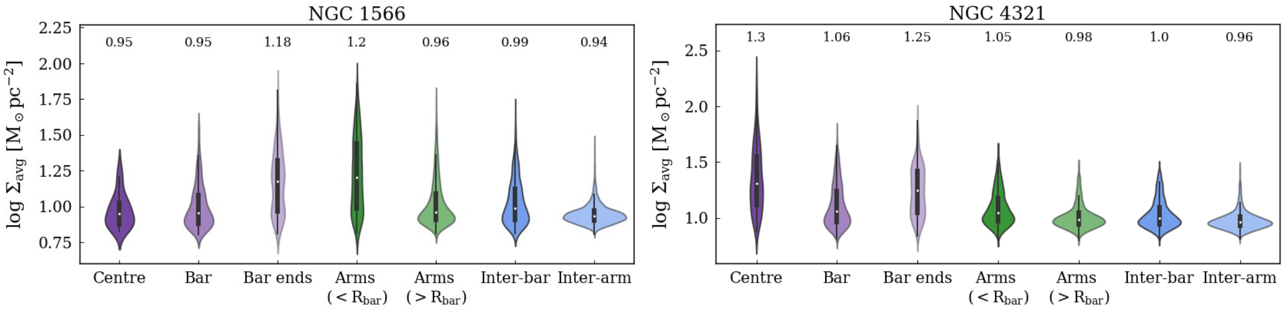

Figure 4.10 – Violin plots showing the average cloud surface density distributions for the barred galaxies in the sample: NGC 1566 (left) and NGC 4321 (right). The centre+bar, spiral arms and inter-arm total environments were subdivided into centre, bar, bar ends, arms within the bar radius (R_{bar}), arms outside of R_{bar}, inter-bar (inter-arm within R_{bar}) and inter-arm ($> R_{bar}$), as defined in Querejeta et al. (2021). For each violin plot, the black box depicts the interquartile range of the relevant distribution, with the white dot representing the median (which is also written in logarithmic form above each violin plot).

arms, with also a fair amount concentrated in the centres. NGC 1566, in particular, displays many high-Σ_{avg} objects along the arms, and very little in the inter-arm. The longer bar in NGC 4321 is heavily populated by high surface density clouds, as well as the starting points of the spiral arms. Interestingly, there is a hint of a radial trend for this galaxy, as there are barely any high-Σ_{avg} clouds past the radius of the bar.

It could be that the distribution of these high-Σ_{avg} across the large-scale environments is not significant, and just an effect of random sampling. To test that, a comparison is performed between the fraction of these clouds per environment and the fraction that is expected from the general all-galaxy distribution, through a Pearson χ^2 statistical analysis (see Eq. 3.2). This analysis is similar to that performed in Section 3.3.4. First, 10^6 random draws (without replacement) of N clouds are performed, N being the number of clouds corresponding to the top 5% of Σ_{avg} values for each galaxy. A χ^2 value is calculated for each draw, which allows us to build a cumulative distribution across the 10^6 iterations, thus giving an estimated likelihood (p_{rnd}) for a given χ^2 (see Fig. 4.12, which is representative of the entire sample). If the p_{rnd} associated to the observed χ^2 value is low, then the respective distribution is unlikely to arise from random sampling, and thus the relevant environment may have a role in promoting these specific types of clouds. There is no attempt to perform this categorical χ^2 test on NGC 4689, since for this galaxy there are only 2 categories (i.e. environments) with a huge discrepancy in population. This means that when performing random draws, it is highly likely to pull only clouds from the disc, which makes determining a χ^2 not realistic.

For all galaxies considered, high values of χ^2 were obtained, all with $p_{rnd} < 10^{-5}$. This is true both when considering the "total" large-scale environments (i.e. C, SA, IA) and when

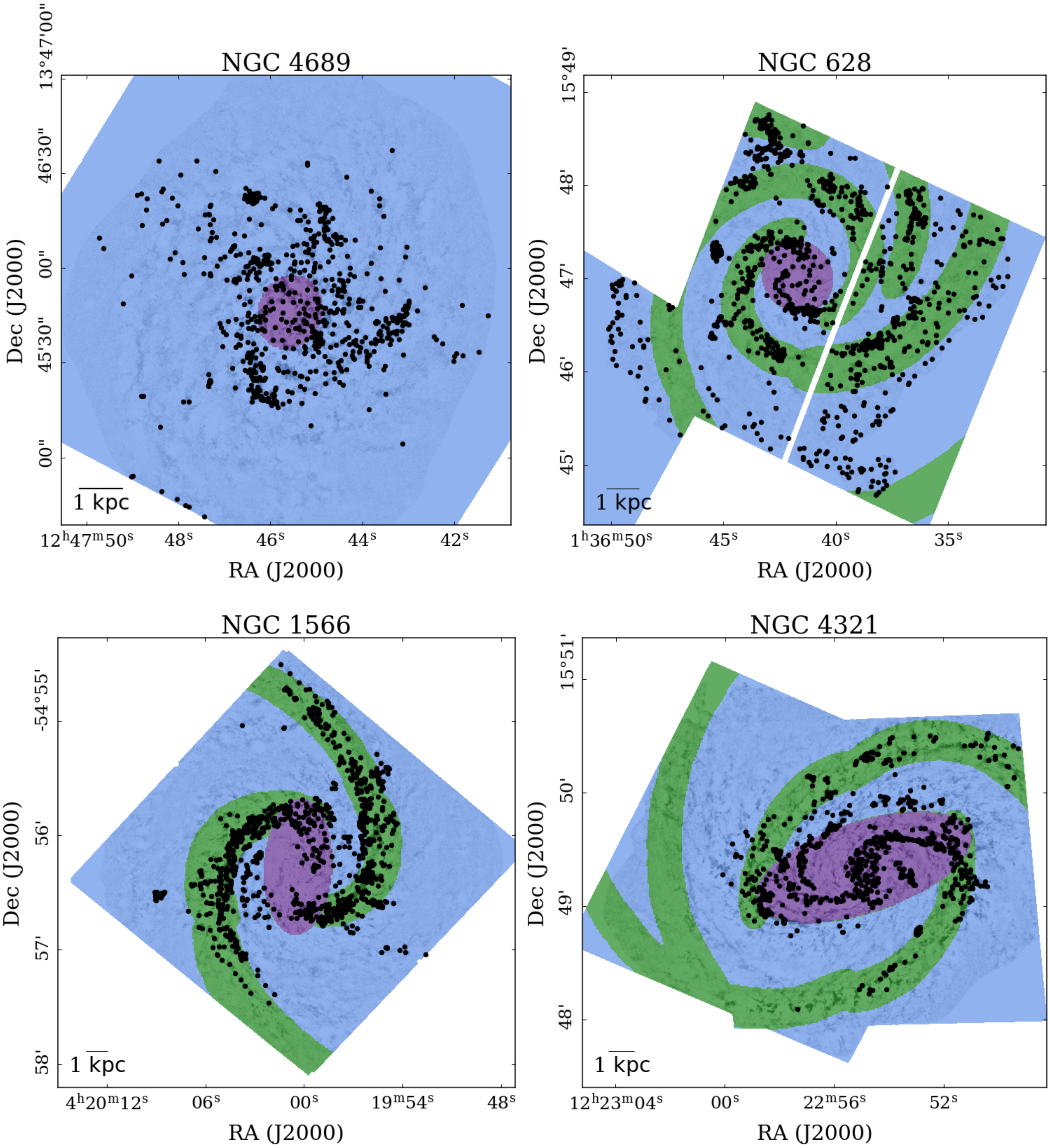

Figure 4.11 – Spatial distribution of the top 5% clouds in terms of average surface density (Σ_{avg}) across the sample, represented as black dots. For each galaxy, the background greyscale is the gas surface density map, and the environmental masks are in colour (purple for centre, green for spiral arms, and blue for inter-arm or disc in NGC 4689).

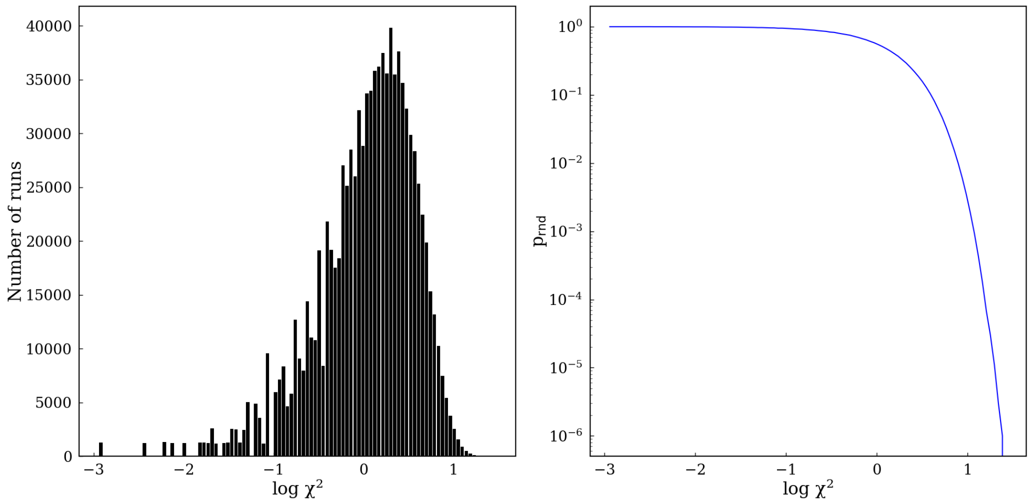

Figure 4.12 – Distribution of χ^2 values (in log-form) across 10^6 random draws of $N = 832$ clouds for NGC 4321 (*left*), with the cumulative distribution of said χ^2 values (*right*). The y-axis of the right panel effectively showcases the likelihood ($\mathrm{p_{rnd}}$) of obtaining a given χ^2 from random sampling.

performing the test across the sub-environments in the case of the barred galaxies (as in Fig. 4.10, per Querejeta et al. 2021). This test confirms that these clouds with high surface density are not randomly distributed, and suggests that some large-scale environments offer physical conditions which are more conducive to the formation of high surface density objects than others. Additionally, the fact that these high-density clouds are not located in the same environments across the sample of galaxies suggests that the specific galactic dynamics may also be playing a determining role in the formation of such objects.

As already mentioned, Figs. 4.10 and 4.11 also hint at some potential radial trends. Figure 4.17 illustrates the running radial medians of Σ_{avg} and cloud mass, M, for the present sample of galaxies. Following the methodology of Section 3.4.2, the surface density radial profiles are shown for the separate environments of each galaxy, to investigate any environmental trends. This was not repeated for cloud mass, as the trends between environments are similar to those observed with average surface density.

In the flocculent NGC 4689, average cloud surface densities (and masses) generally decrease with larger galactocentric distance, although there is an apparent spike in the transition between the centre and the disc. This is likely not a real physical feature, as implied by the larger errorbars seen towards those radii. Since the central bulge is not perfectly round (see Fig. 4.6), the concentric radial bins used here do not perfectly cover it, resulting in a reduced number of clouds from each environment in certain bins which in turn leads to higher uncertainty in this transition between centre and disc.

In NGC 628, there is a peak of average cloud surface densities where the centre meets the

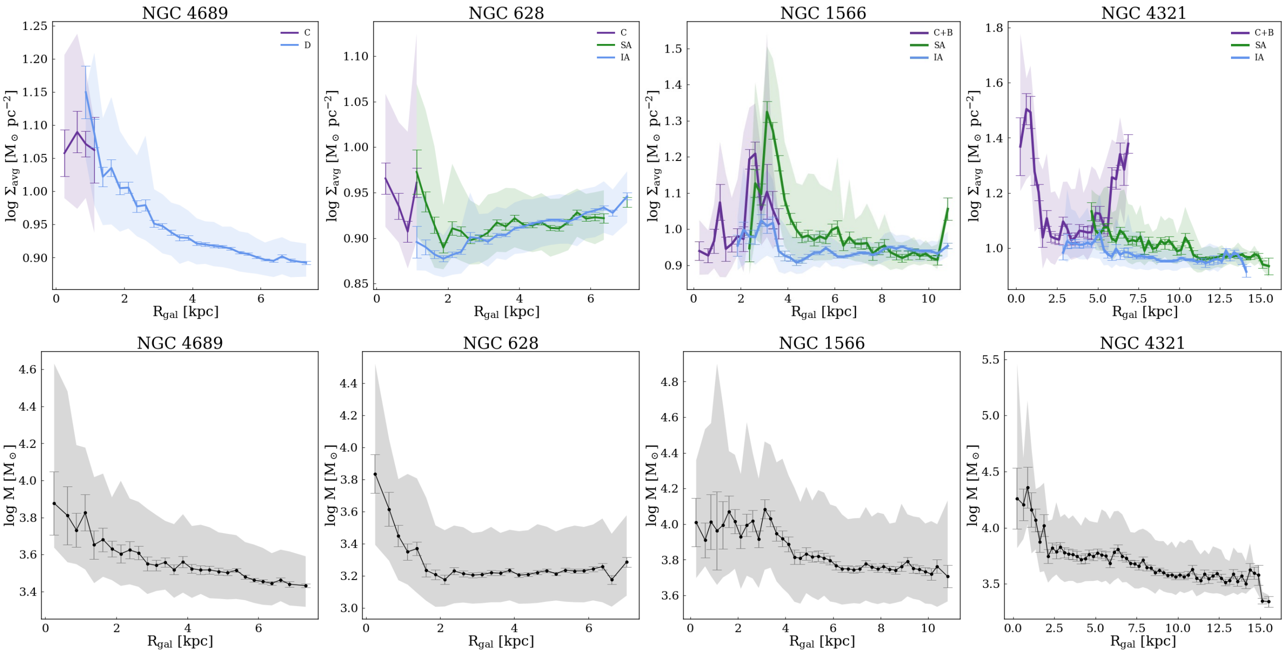

Figure 4.13 – *Top row*: Average cloud surface density ($\Sigma_{\rm avg}$) as a function of galactocentric distance for (from left to right) NGC 4689, NGC 628, NGC 1566 and NGC 4321. The different galactic environments are colour-coded as purple for the centre (+bar), green for the spiral arms, or blue for the inter-arm regions (disc in the case of NGC 4689). *Bottom row:* Cloud mass (M) as a function of galactocentric distance. For all panels, the solid line depicts the running median, whilst the shaded regions represent the interquartile range of the relevant distribution. The errorbars represent the standard error on the median given the bin count, N ($1.253\sigma\sqrt{N}$).

spiral arms, which is also seen as a concentration of points in Fig. 4.11. At short galactocentric radii ($R_{gal} \lesssim 2.5$ kpc), the clouds in the spiral arms show higher values of surface density compared to inter-arm clouds. Past this radius, the disc seems to behave in similar fashion, with minimal differences between the two environments, resulting in the very similar distributions seen in Fig. 4.9. It is important to note that although in Fig. 4.17 there seems to be a slight rise in Σ_{avg} in the disc towards larger R_{gal}, this trend is not likely to be significant, as the increase is of the order $\sim 0.02 - 0.03$ dex (well within the observed interquartile scatter), and the cloud statistics become more incomplete towards larger radii. The cloud mass radial profile shows a decrease up until $R_{gal} \sim 2$ kpc, after which it seems to flatten.

As was already suggested in Fig. 4.10, Fig. 4.17 shows that NGC 1566 has a peak of surface density at $R_{gal} = 2 - 4$ kpc (i.e. towards the end of the bar and start of spiral arms), while NGC 4321 shows an increase of average cloud surface density towards the very centre and end of the bar, with very little variation in the actual disc of the galaxy. This difference in radial profiles within the bars of these galaxies could suggest a difference in dynamics and gas flows driven by the bars. However, a kinematic follow-up is needed for any conclusions to be drawn (e.g. Querejeta et al., 2016). Both barred galaxies show a larger Σ_{avg} in the SA versus the IA up until a given radius (~ 8 kpc for NGC 1566 and ~ 11 kpc for NGC 4321), after which they become similar. This difference at small radii is much more pronounced in NGC 1566 than in NGC 4321, as was already seen with Figs. 4.8 and 4.9. Both barred galaxies showcase a mild decrease of Σ_{avg} with increasing R_{gal}.

4.5.2 Cloud size and morphology

There is no obvious trend of cloud size (as measured by L_{MA}) across the environments of NGC 1566 and NGC 4321 (see Fig. 4.14). On the other hand, both of the unbarred galaxies (NGC 4689 and NGC 628), show a slight tendency towards longer objects in the centre where the distributions are more top-heavy. Across the entire sample there is no discernible difference in cloud length between arm and inter-arm. In terms of aspect ratio or cloud elongation, it appears that all galaxies generally have elongated clouds with $AR_{MA} \sim 3$ (see Table 4.4), with no obvious environmental trend across the sample.

It is important to note however, that an aspect ratio metric is not the most conclusive. Although the medial axis approach does a better job at identifying truly elongated clouds than the moment-based aspect ratio (see Neralwar et al., 2022; Faustino Vieira et al., 2024), it will still confuse "straight", filamentary clouds with ring-like clouds, as they can have similar aspect ratios despite being vastly different morphologies. Filamentary clouds could be a sign of stretching due to shear (e.g. Koda et al., 2009), whilst ring-like "bubbles" are usually associated

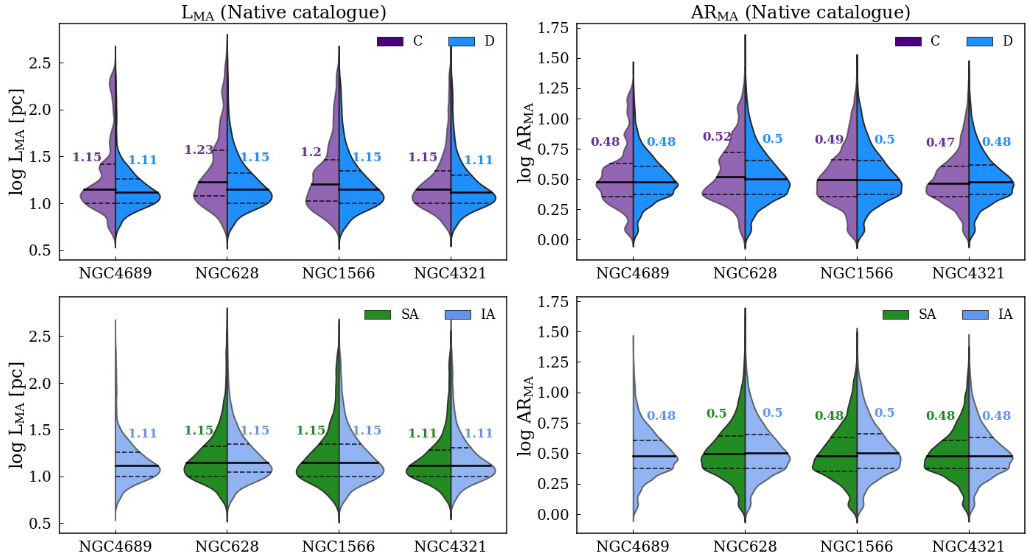

Figure 4.14 – Violin plots showing the contrast between the medial axis length (L_{MA}, *left*) and aspect ratio ($\mathrm{AR}_{\mathrm{MA}}$, *right*) distributions in different environments across the 4 galaxies (native resolution). The top row shows the difference between the centre (C, in purple) and the disc (D, in blue) populations, whilst the bottom row shows the arm population (SA, in green) against the inter-arm (IA, in light blue). For all distributions, the solid black line within the violin represents the median, whilst the dashed lines depict the interquartile range. Next to each distribution, the written label is the relevant median (in logarithmic scale), colour-coded by environment.

with stellar feedback (e.g. Barnes et al., 2023)[11]. Given that these shapes of clouds are likely driven by different physical processes, it is important to disentangle them.

Figure 4.15 displays the RJ-plots for all galaxies in the sample, as well as for each large-scale environment within them. It appears that the majority of clouds in the native resolution catalogues appear quasi-circular (i.e. either circular or ring-like). However, there is no obvious trend of RJ distribution across environments within each galaxy, as all the distributions look similar.

Clouds that could approximate large-scale filaments (LSFs) are shown in Fig. 4.16. These are clouds belonging to the elongated RJ classes (RJ=3 or 4), with $L_{\mathrm{MA}} > 100$ pc. There are 126 of such objects for NGC 4689, 265 for NGC 628, 309 for NGC 1566, and 272 for NGC 4321. From the figure, it appears that these LSFs are more "ordered" in NGC 1566 and NGC 4321, whilst in NGC 4689 and especially NGC 628 their orientation seems more random. In other words, in the barred targets, the LSFs in the inter-arm (i.e. akin to inter-arm "spurs"; e.g. La Vigne et al. 2006) appear to become more aligned with the arm as they approach it (i.e. the concave side, see also Duarte-Cabral & Dobbs, 2016, 2017). On the convex side of the arms (i.e. downstream),

[11]It is important to note, however, that these bubbles are not likely to be formed of one single cloud, but likely many arc-shaped objects.

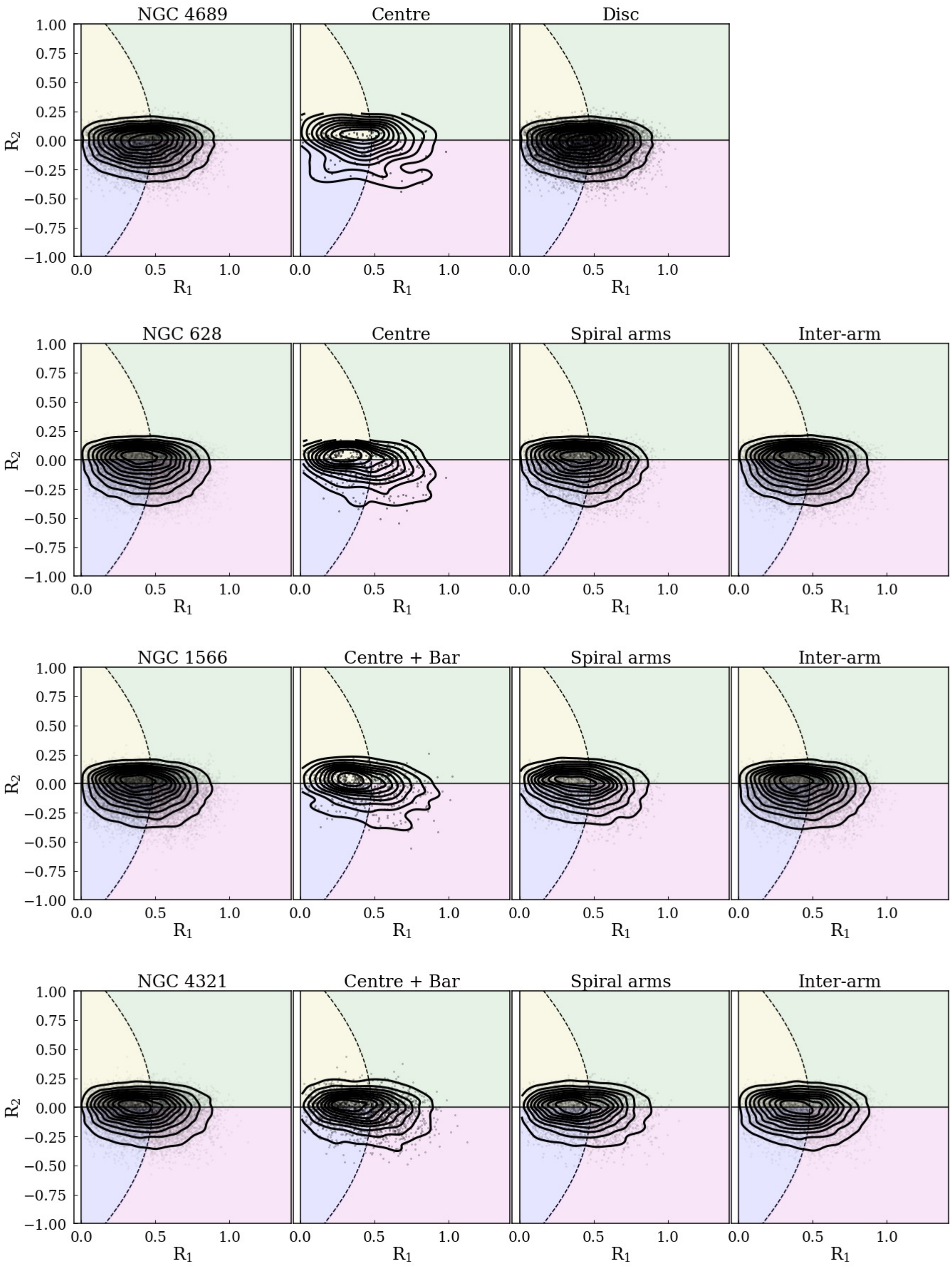

Figure 4.15 – RJ-plots (Jaffa et al., 2018; Clarke et al., 2022) for all galaxies in the sample and their respective environments (native resolution). Clouds are categorised into 4 morphological classes: circular (RJ=1, yellow), ring-like (RJ=2, purple), centrally overdense elongated (RJ=3, green) and centrally underdense elongated (RJ=4, pink). The black contours represent the 2D kernel density estimation (KDE) of the underlying distribution of clouds.

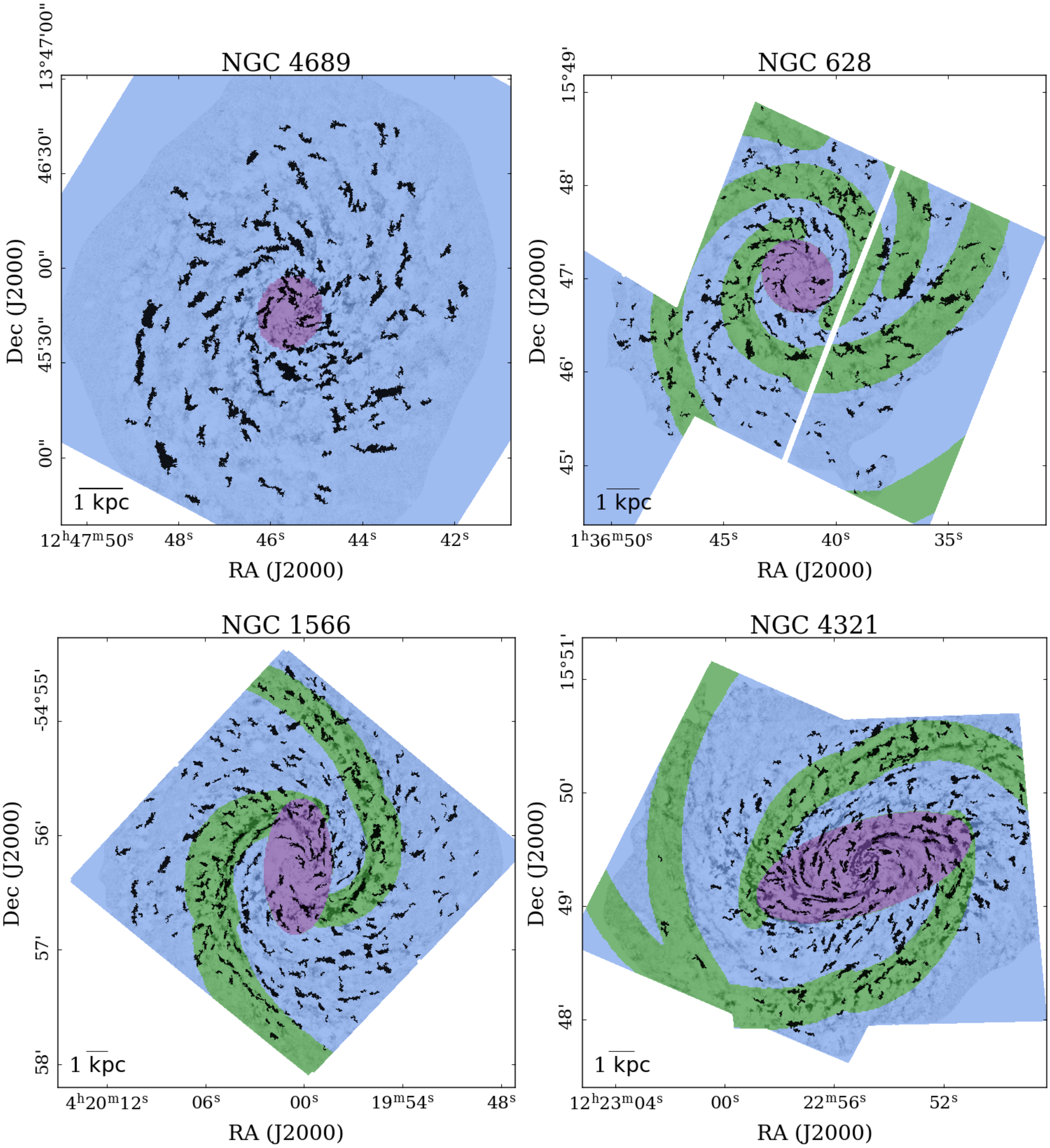

Figure 4.16 – Spatial distribution of "large-scale filaments" (LSFs), which are elongated (RJ=3 or 4) and simultaneously very long ($L_{\mathrm{MA}} > 100$ pc) clouds. For each galaxy, the background greyscale is the gas surface density map, and the environmental masks are in colour (purple for centre, green for spiral arms, and blue for inter-arm or disc in NGC 4689).

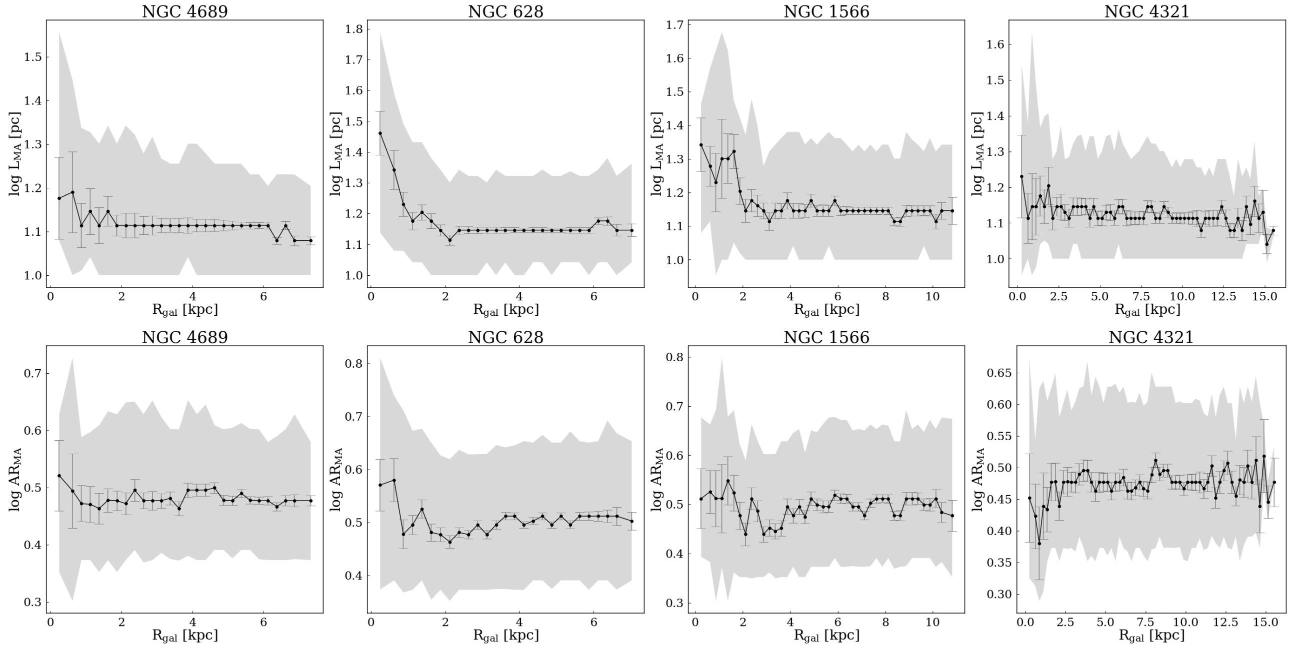

Figure 4.17 – *Top row*: Cloud size as measured by the medial axis length (L_{MA}) as a function of galactocentric distance. *Bottom row:* Cloud aspect ratio ($\mathrm{AR}_{\mathrm{MA}}$) as a function of galactocentric radius. For all panels, the solid line depicts the running median, whilst the shaded regions represent the interquartile range of the relevant distribution. The errorbars represent the standard error on the median given the bin count, N ($1.253\sigma\sqrt{N}$).

where the gas would be exiting the arm, these LSFs appear nearly perpendicular to the arm. This behaviour is particularly visible in NGC 1566. This could be a sign of a stronger influence of the spiral dynamics exerted on the ISM of these galaxies, given that this behaviour is not seen in NGC 628, which has visually fainter arms. Still, for more firm conclusions, these visual trends need to be confirmed by studying the relative orientation of these filaments with respect to the nearest arm in a more quantitative way.

As was done with the extremely high surface density clouds in the previous Section, the fraction of observed LSFs for each environment is compared to what is expected from the general all-galaxy distribution, to investigate if the observed environmental trends are significant. This is done through a Pearson χ^2 statistical analysis[12]. Large values of χ^2 were obtained across the sample, all with very low likelihoods ($\mathrm{p}_{\mathrm{rnd}} < 10^{-6}$) of being a by-product of random sampling. This implies that these LSFs have a statistically different distribution than what is expected from the overall cloud distribution. There is an increased concentration of LSFs in the centre and arms of NGC 628. NGC 1566 holds a considerable amount of LSFs in both its bar and along the arms. In NGC 4321, there is an increase of LSFs in the bar, but also towards the inter-bar and the arm regions within the bar radius, again implying that the bar is heavily affecting the

[12]Again, given the reduced number of environments in NGC 4689, this analysis is not performed for this galaxy (see Section 4.5.1).

Galaxy	N_{clouds}	M (10^3 M$_\odot$)	Σ_{avg} (M$_\odot$ pc^{-2})	L_{MA} (pc)	AR$_{\mathrm{MA}}$
(1)	(2)	(3)	(4)	(5)	(6)
NGC 4689	9,015	$4.3^{6.8}_{3.1}$	$8.4^{9.2}_{7.8}$	$16^{21}_{12.5}$	$3.53^{4.72}_{2.76}$
NGC 628	8,423	$4.7^{9.2}_{3.3}$	$8.5^{9.1}_{8.0}$	28^{41}_{21}	$5.3^{7.16}_{3.95}$
NGC 1566	20,606	$6.1^{12.9}_{3.7}$	$8.7^{9.9}_{8.0}$	14^{22}_{10}	$3.13^{4.5}_{2.36}$
NGC 4321	12,280	$6.2^{13.1}_{3.9}$	$9.9^{12.1}_{8.8}$	16^{24}_{12}	$3.37^{4.7}_{2.68}$
Centre+Bar	2,835	$9.8^{26.6}_{5.1}$	$11.7^{18.1}_{9.2}$	17^{30}_{12}	$3.36^{4.75}_{2.47}$
Disc	47,489	$5.3^{10.4}_{3.5}$	$8.8^{9.8}_{8.1}$	17^{26}_{12}	$3.58^{5.14}_{2.68}$
Spiral arms	11,314	$6.2^{13.8}_{3.8}$	$9.3^{11.5}_{8.3}$	18^{30}_{12}	$3.64^{5.3}_{2.65}$
Inter-arm	27,274	$5.5^{10.8}_{3.6}$	$8.8^{9.6}_{8.1}$	17^{27}_{12}	$3.55^{5.25}_{2.65}$

Table 4.5 – Characteristics of the homogenised cloud sample. (1) Galaxy name (or selected environment). (2) Number of clouds per environment, N_{clouds}. (3) Cloud mass, M. (4) Average gas surface density of clouds, Σ_{avg}. (5) Cloud length from the medial axis, L_{MA}. (6) Medial axis aspect ratio, AR$_{\mathrm{MA}}$. For columns (3)-(6), the median of the distribution is presented, with the 25$^{\mathrm{th}}$ and 75$^{\mathrm{th}}$ percentiles being the subscript and superscript, respectively. The centre+bar, disc (spiral arms + inter-arm), spiral arms and inter-arm populations (bottom 4 rows) show the relevant values for the total cloud sample within the denoted environments. The spiral arms and inter-arm populations (bottom 2 rows) do not include clouds from NGC 4689, since it is a flocculent.

ISM within its influence.

Figure 4.17 showcases the radial profiles of cloud size and aspect ratio for all galaxies in the sample. Despite a general increase in the innermost radial bins, cloud length seems to show no discernible trend with R$_{\mathrm{gal}}$ for all galaxies. There is also no discernible trend of aspect ratio towards any given galactocentric radius for the sample, apart from NGC 628 which tentatively shows higher AR$_{\mathrm{MA}}$ in its centre (see Fig. 4.14).

4.6 CLOUD TRENDS ACROSS GALAXIES

To draw any conclusions from the comparison of different galaxies, and the environments within them, it is important to make this comparison as fair as possible. In this Section, a homogenised or common resolution catalogue is built, which considers only the clouds from each galaxy's catalogue that would be well-resolved at the distance of the furthest target in the sample (i.e. NGC 1566). The resulting composition of the catalogue, as well as the statistics of the cloud properties studied here, are listed in Table 4.5. In this Section, any correlations between large-scale environments and the characteristics of the clouds are explored for the homogenised sample. In particular, special attention is paid to any differences between the centre (+ bar) versus disc clouds, as well as arm versus inter-arm.

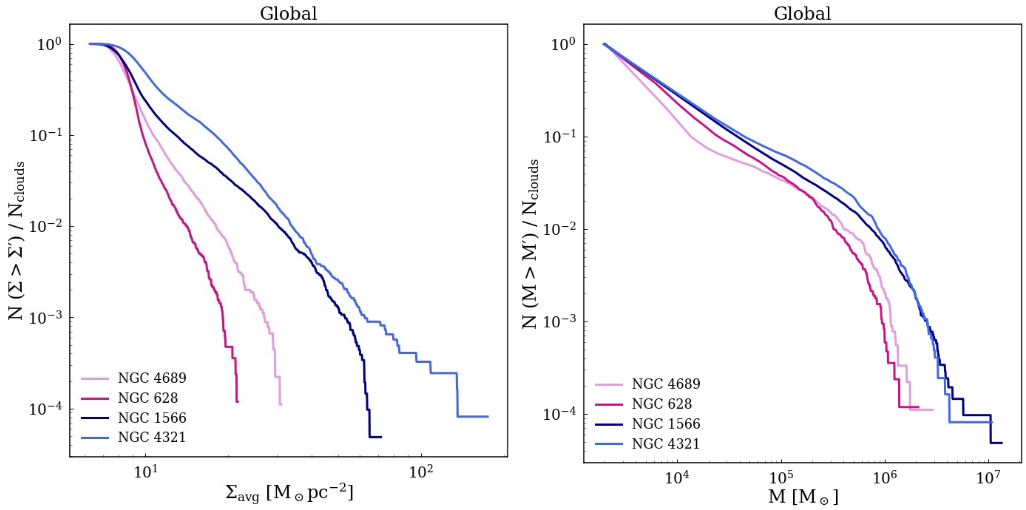

Figure 4.18 – Global cumulative distributions for the average cloud surface density ($\Sigma_{\rm avg}$, *left*) and cloud mass (M, *right*), across the homogenised sample (NGC 4689 in light pink, NGC 628 in dark pink, NGC 1566 in dark blue, and NGC 4321 in light blue). All distributions are normalised by the total number of clouds for that distribution, $N_{\rm clouds}$ (as listed in Table 4.5).

4.6.1 Cloud mass and surface density

Figure 4.18 showcases the cumulative distributions of both cloud surface density and mass for the homogenised sample. From the figure, we can see that the barred galaxies (NGC 1566 and NGC 4321) tend to have the most massive and higher surface density clouds of the sample. NGC 628 and NGC 4689 seem to have similar cloud mass distributions, although the distribution of $\Sigma_{\rm avg}$ for NGC 628 seems to fall short of the flocculent's. This suggests that the clouds in NGC 628 are on average larger in size, as is evidenced by Table 4.5 (further discussed in Section 4.6.2).

From Table 4.5, it is possible to see that the mass $\Sigma_{\rm avg}$ median values are higher in the centre than the disc. This is expected, given that each of the individual galaxies in the sample displayed this trend in the native resolution analysis (Section 4.5.1). Figure 4.19 also showcases the differences between the cloud distributions in the centre versus the disc. It is possible to see that the $\Sigma_{\rm avg}$ distribution for the centre has a much larger interquartile spread versus the disc, which is more compact and concentrated towards low-$\Sigma_{\rm avg}$ values. This is also observed with cloud mass, although less pronounced.

Like what was seen in the native resolution catalogues (Section 4.5.1), clouds in a spiral arm environment present marginally different properties to clouds in the inter-arm, although this contrast is not as large as what is seen between the centre and the disc. In fact, from Fig. 4.19, it seems that the bulk of both populations is quite similar, with differences arising in the tail-end of the distribution, where there are more high-$\Sigma_{\rm avg}$ clouds in the arms. Given that

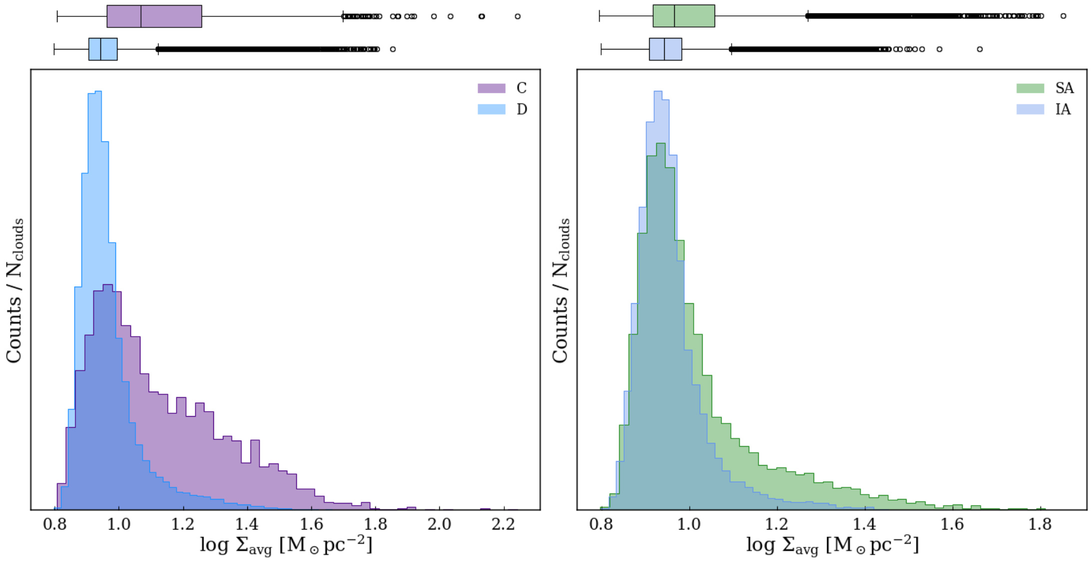

Figure 4.19 – Histograms of the average cloud surface density (Σ_{avg}) for the centre (C, purple) versus disc (D, blue) on the left panel, and arms (SA, green) versus inter-arm (IA, light blue) on the right panel. The y-axis holds the amount of clouds in each bin, normalised by the total number of clouds for the relevant environment (N_{clouds}). Above each panel are the respective boxplots of the distributions (following the same colour scheme). The coloured box illustrates the interquartile spread of the distribution (i.e. from 25th to 75th percentile), with the solid black line within the box being the median. The circles represent the outliers of the distribution. The right panel does not include clouds from the flocculent NGC 4689.

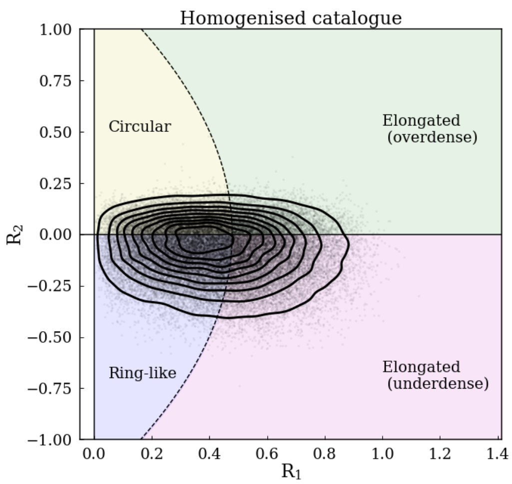

Figure 4.20 – RJ-plot for all clouds in the homogenised catalogue. The black contours represent the 2D kernel density estimation (KDE) of the underlying distribution of clouds.

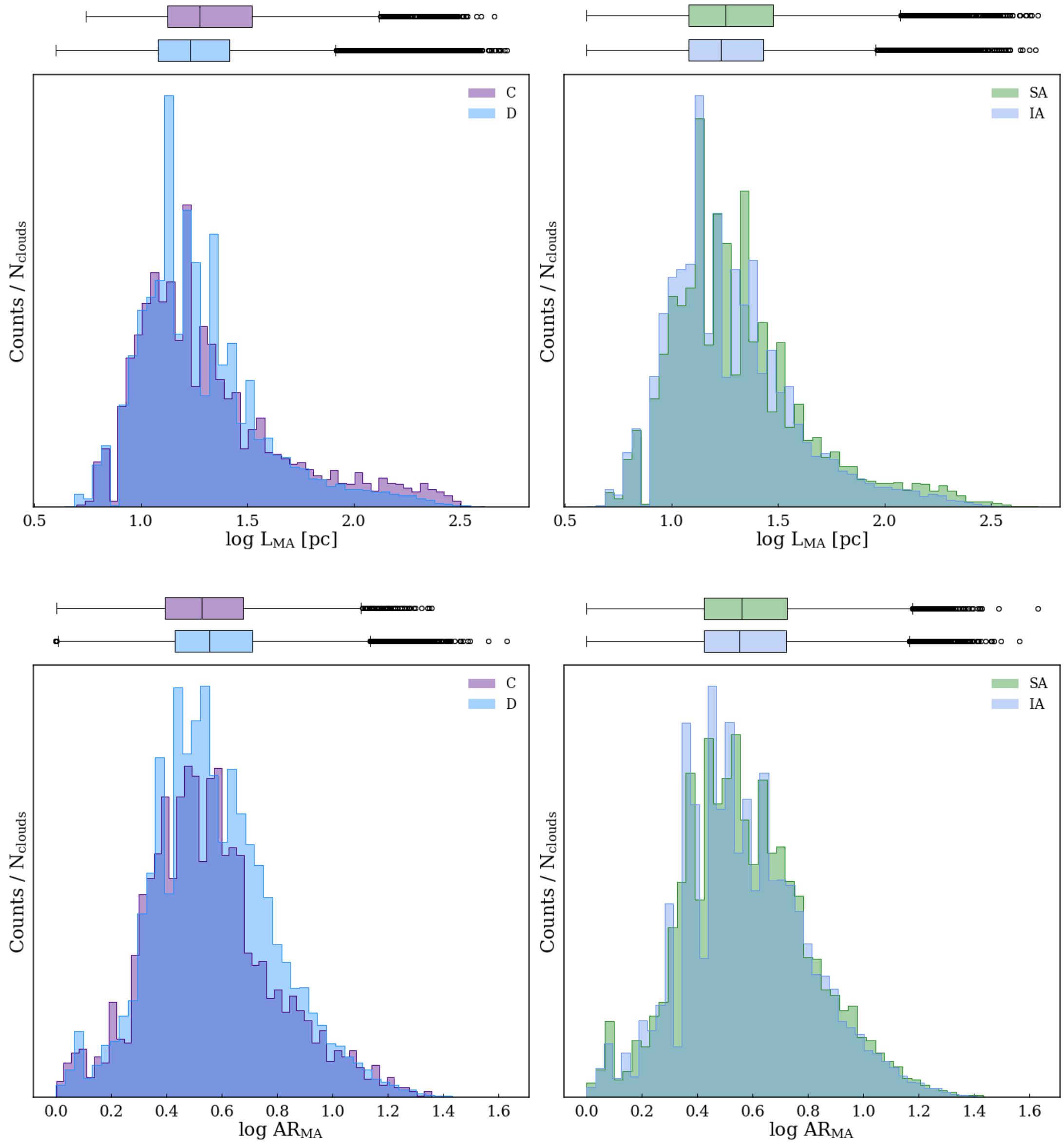

Figure 4.21 – Histograms of cloud length (L_{MA}, *top row*) and medial axis aspect ratio ($\mathrm{AR}_{\mathrm{MA}}$, *bottom row*). For both rows, the left panel displays the contrast between the centre (C, purple) and disc (D, blue), and the right panel the arms (SA, green) versus inter-arm (IA, light blue). For all panels, the y-axis holds the amount of clouds in each bin, normalised by the total number of clouds for the relevant environment (N_{clouds}). Above each panel are the respective boxplots of the depicted distributions (following the same colour scheme). The coloured box illustrates the interquartile spread of the distribution (i.e. from 25th to 75th percentile), with the solid black line within the box being the median. The circles represent the outliers of the distribution. The right panel (for both rows) does not include clouds from the flocculent NGC 4689.

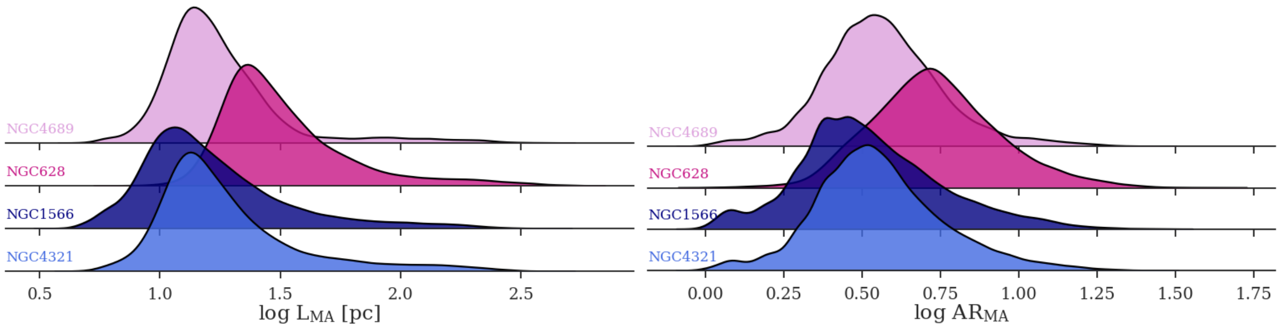

Figure 4.22 – Ridge plot showcasing the kernel density estimates (KDE) across the sample of galaxies (from top to bottom: NGC 4689, NGC 628, NGC 1566 and NGC 4321) for cloud length ($L_{\rm MA}$, *left*) and cloud aspect ratio ($\mathrm{AR}_{\rm MA}$, *right*). All KDEs are normalised by the relevant number of observations.

for the native catalogue (Section 4.5.1) NGC 1566 had the highest observed contrast between SA and IA distributions (in terms of mass and surface density), it is likely that this galaxy is driving this tail-end difference.

4.6.2 Cloud size and morphology

Figure 4.20 shows the RJ-plot for all clouds in the homogenised catalogue. Roughly 20% of clouds appear circular, 40% are ring-like, and the remaining 40% are elongated (11% centrally overdense and 29% centrally underdense). As was also seen in Section 4.5.2, clouds tend to be quasi-circular (either circular or ring-like) and there are no detected variations with galactic environment.

The distribution of cloud length and aspect ratio across the environments considered is displayed in Fig. 4.21. From the figure, it is possible to see that there is no significant difference between the arm and inter-arm distributions for either $L_{\rm MA}$ or $\mathrm{AR}_{\rm MA}$. Likewise, the centre and disc distributions of cloud length and aspect ratio are also very similar.

Figure 4.22 showcases the distribution of cloud length and aspect ratio across the galaxies in the homogenised sample. Despite some small variations, the distributions look fairly similar, with the exception of NGC 628, which is a clear outlier. In the homogenised sample, this galaxy has systematically longer clouds with also higher $\mathrm{AR}_{\rm MA}$. This is in contradiction with what was seen in the native resolution analysis (Section 4.5.2), where these properties did not seem to fluctuate much across the sample (see Fig. 4.14). This discrepancy points towards some biasing that must have taken place when performing the area cut to build the homogenised cloud catalogue.

In fact, as can be seen from Fig. 4.23, quite a significant portion of clouds in NGC 628 are

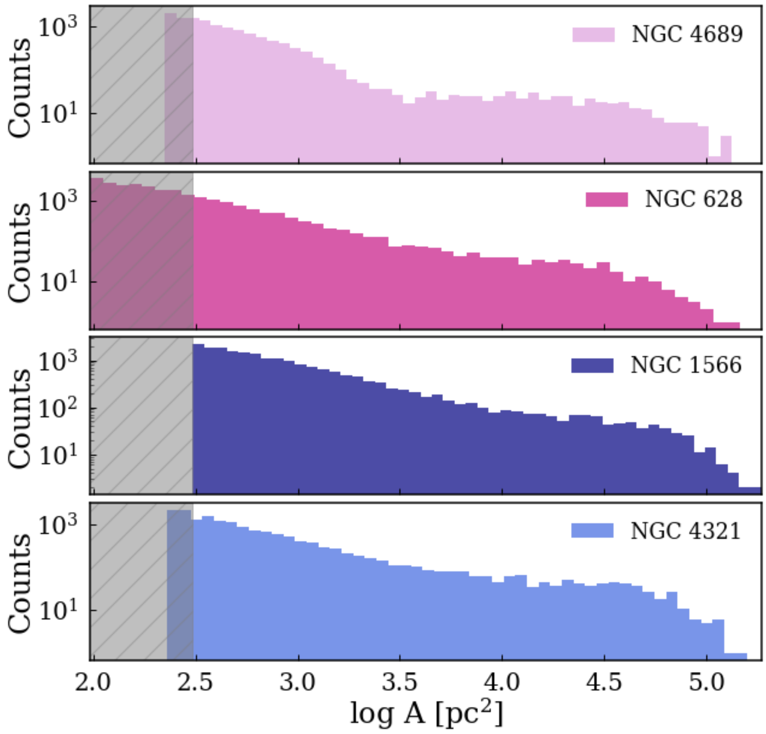

Figure 4.23 – Histogram of cloud area (A) for the native resolution catalogue of NGC 4689, NGC 628, NGC 1566 and NGC 4321 (from top to bottom). The grey shaded area represents the clouds that are neglected when making the area cut for the common resolution catalogue.

below the area cut performed when building the homogenised catalogue ($\sim$ 66%). This is unfairly biasing the statistics of properties such as length, aspect ratio and mass towards higher values, since most of the smaller (likely also small aspect ratio), lower-mass objects in this galaxy are ruled out from the common resolution catalogue (see Fig. 4.24). If the full sample was observed at the distance of NGC 1566 (the furthest away target), it could be that these small, low-mass objects would not be resolved, but it would also be likely that they would be smeared within the observing beam into larger associations which would be resolved. It is clear from Fig. 4.23 that this "selection" effect is worse for NGC 628, as it is the closest target, but it cannot be ruled out that this is also having an impact in the analysis of NGC 4689 and NGC 4321.

In conclusion, to properly compare cloud trends between galaxies, a simple cloud size cut is insufficient. It is difficult to disentangle observed trends that might arise from real, physical processes, from the implicit selection bias (see Hughes et al., 2013). Instead, a better approach is to replicate the gas surface density maps of the closest galaxies at the resolution of the most distant (i.e. NGC 1566), prior to the cloud extraction. Still, the analysis in this Section points towards little difference between arms and inter-arm, and some contrast between centres and discs for some cloud properties. Albeit with caveats due to the incorrect cloud size cut,

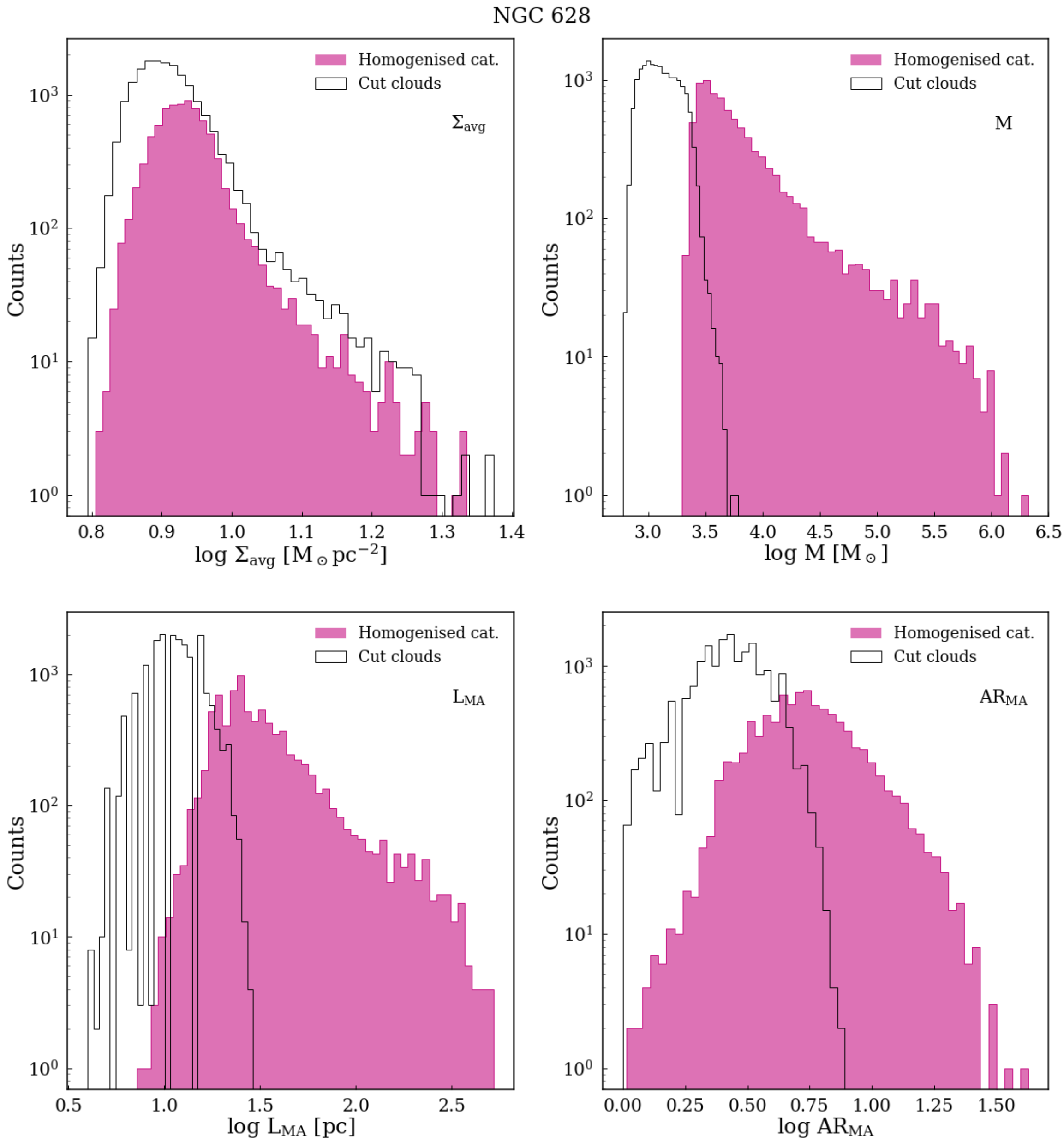

Figure 4.24 – Histograms of the average surface density ($\Sigma_{\rm avg}$, *top left*), mass (M, *top right*), length ($L_{\rm MA}$, *bottom left*) and aspect ratio ($\rm AR_{MA}$, *bottom right*) for the homogenised catalogue (in pink) versus the clouds that did not make the common resolution area cut (black outline).

this homogenised catalogue suggests that looking at cloud properties merely as a function of large-scale environment across galaxies is not the most informative, since you lose information on interesting galaxy-to-galaxy variations, which are showcased in the native resolution analysis (Section 4.5). Although small, the present sample of galaxies holds galactic environments that, even though are technically within the same classification, look visually distinct (e.g. the bars of NGC 1566 and NGC 4321), and that may also have distinct dynamics which could be affecting the ISM differently. Therefore, it may be more informative to not only look at environmental trends, but also look for any correlation with physical quantities such as pressure, shear and torques (e.g. Miyamoto et al., 2014; Sun et al., 2020a, 2022), to infer if any cloud property variations within each galaxy are linked to any specific environmental conditions.

4.7 FURTHER WORK

As seen in the previous Section, in order to analyse and compare galaxies with different physical resolutions, it is not sufficient to perform a simple area cut on the cloud catalogues, as this can introduce biases. This will be corrected by first homogenising the resolution of the extinction-derived gas surface density maps, similar to the procedure adopted by Rosolowsky et al. (2021). Therefore, the maps of NGC 4689, NGC 628, and NGC 4321 will be smoothed to the resolution of the NGC 1566 map (~ 9.4 pc, see Table 4.1). After that, the cloud extraction will be repeated. The result will be a new homogenised catalogue which will allow for a robust comparative analysis between galaxies (and environments). The analysis performed for the native resolution catalogues will then be replicated for the new homogenised catalogue, including studying clouds which approximate large-scale filaments (Section 4.5.2) and the highest surface density clouds (Section 4.5.1). This will include looking into whether these objects are particularly enhanced in a given galaxy in the sample, and whether this has any correlation with the galaxy's morphology. Additionally, a correlation test between RJ values and a given cloud's properties could tell us if certain types of clouds tend to have a particular morphology.

4.8 CONCLUSION

This Chapter presents the application of the extinction imaging technique, outlined in Chapter 2, to a wider sample of nearby disc galaxies. This sample consists of a flocculent (NGC 4689), and spirals with bars (NGC 1566, NGC 4321) and without (NGC 628). The goal of this work, much like in Chapter 3, is to investigate any links between ISM properties and large-scale environment, now with a more varied range of galaxy morphology. This Chapter also describes the improvements added to the technique to increase its robustness and effectiveness in retrieving extinction features. The findings are summarised below:

- There is a substantial difference in cloud masses and average surface densities between the centres and discs across the whole sample, with centres having consistently higher values. Within the disc, the bulk of the cloud populations in the arm and inter-arm appear quite similar in terms of mass and surface density, although the arm distributions extend towards higher values (particularly in NGC 1566).

- In the barred galaxies (NGC 1566 and NGC 4321), the average cloud surface density distributions for the arm and inter-arm regions are different inside and outside the radius of the bar, with higher values (and spread) inside R_{bar}. This trend is much more pronounced in NGC 4321, which has a more prominent bar.

- The radial profiles of cloud mass and average cloud surface density show some differences between the spiral arms and inter-arm populations at small R_{gal}, with both distributions becoming similar at larger R_{gal}. There also seem to be different radial behaviours for the bars in the sample, with NGC 4321 holding most of its mass in its very centre, whilst NGC 1566 does so more towards the ends of the bar and beginning of spiral arms, which could hint at different dynamics and gas flows driven by these bars.

- There is no significant trend of cloud length, size or aspect ratio with galactic environment across the native resolution catalogue. Furthermore, clouds in this work tend to be quasi-circular (i.e. either circular or ring-like), with no detected variations between environments. When looking at the very elongated and long (>100 pc) objects for each galaxy, they appear more "ordered" in NGC 1566 and NGC 4321, following the orientation of the more prominent spiral arms, than in NGC 4689 and NGC 628, where their orientation seems more random.

- The homogenised resolution catalogue, at first glance, re-iterates the findings from the native resolution analysis: there is a high contrast in cloud masses and surface densities between the centre and disc, with the arm and inter-arm populations only showing dissimilarities in the tail end of the distributions. There is also no observed change of cloud sizes or morphology across environments. However, the simple cloud area cut performed when building this catalogue is introducing some bias towards higher values, therefore requiring this comparative analysis to be repeated in a more robust manner. Still, this type of analysis where clouds of a given environment are all binned together potentially leads to loss of information on galaxy-to-galaxy variations, which may be the key in understanding what drives the properties of molecular clouds.

Chapter 5

CONCLUSION

"All adventures - especially into new territory - are scary."

SALLY RIDE

This Thesis presents an investigation into the distribution of the molecular gas in nearby spiral galaxies, with a focus on environmental trends. For that purpose, an imaging technique was developed, which utilises dust extinction (observed at optical wavelengths) in order to produce high-resolution maps of the dust (and gas) content of face-on, disc galaxies. It consists of determining the dust attenuation from the comparison of optical data to a smooth, reconstructed stellar light model on a pixel-by-pixel basis. There is also an additional calibration step with observations of cold dust emission in the far-infrared, to ensure mass estimates from dust extinction and emission are generally consistent with each other. This technique provides a different, high-resolution viewpoint on the star-forming gas, which is highly complementary not only to more traditional tracers (i.e. CO), but also to the new and exciting observations of the near/mid-infrared dust emission provided by JWST.

This dust extinction technique is first applied to M51 (NGC 5194) as a proof-of-concept (Chapter 2). Subsequently, a significant catalogue of resolved molecular clouds is extracted, which provided a foundation for an investigation into the properties of the ISM as a function of galactic environment and radius for this galaxy (Chapter 3). This analysis is then expanded to include a wider sample of nearby spiral galaxies, with various morphological features (Chapter 4).

The key result of this body of work is the creation of a technique with which we may image the dust (and gas) content of nearby galaxies at sub-arcsecond (∼parsec) resolution, using archival HST (and *Herschel*) data. From the resulting molecular cloud catalogues extracted from these high-resolution maps, it was found that the centres and discs of these nearby galaxies hold statistically different cloud populations. Clouds in centres are often higher mass and higher surface density than clouds in discs. Across the galaxies studied in this Thesis, it was also found that within discs, the bulk of the arm and inter-arm populations are very similar, with differences arising towards the higher masses/densities end, mostly at small galactocentric radii. Still, despite the small sample of galaxies analysed in this work, there are distinct trends of cloud properties within the same environment of different galaxies. This is not wholly unexpected, as large-scale structures such as spiral arms and bars present significant morphological variations from galaxy to galaxy, and thus will likely have different impacts on the ISM. Grouping clouds across different galaxies that qualitatively belong to the same environment may, therefore, not be the most informative. Instead, exploring if observed cloud properties are in any way linked to the physical conditions the ISM is actually experiencing (e.g. shear, inflows, pressure), rather than just as a function of galactic environment, may be a better approach.

Resolving parsec-scale clouds across the discs of nearby galaxies allows us to systematically study the effects of large-scale dynamics. During this work, I found that it is not particularly helpful to compare the actual values of quantities (e.g. medians of cloud mass) across studies, but rather the relationship between cloud populations holds much more information. In other words, it is more informative to ascertain whether the observed difference between clouds in different environments is similar between studies, rather than comparing actual values of a given cloud property. This is because the definition of a cloud in each study is heavily influenced by the chosen tracer, methodology differences, and cloud extraction algorithm, among other things.

Throughout this Thesis, it was very apparent that care is required when comparing findings of studies that employ different tracers or methodology. This is because not having the same *a priori* assumptions already introduces differences, which makes extrapolating any conclusions much more difficult. Particularly, it was found that assuming a different dust model (i.e. dust mass absorption coefficient) can by itself introduce significant discrepancies in results. This is especially true when comparing dust-based studies to CO-based ones, which often employ a standard, Milky Way CO-to-H_2 conversion factor.

5.1 FUTURE WORK

The research I have conducted thus far showcases that galactic environment and dynamics do in fact play an important role in shaping the ISM and setting cloud properties. The logical next

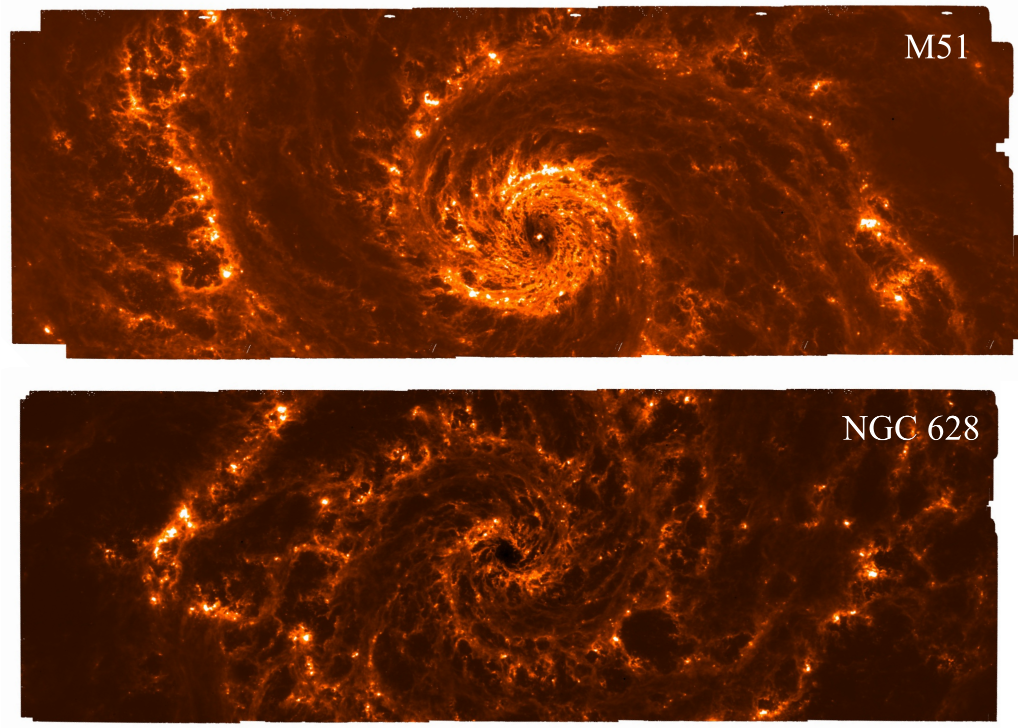

Figure 5.1 – JWST image of M51 (*top*) and NGC 628 (*bottom*) at the 7.7 µm (F770W) PAH (Polycyclic Aromatic Hydrocarbons) band. These observations were obtained by the JWST-FEAST (Feedback in Emerging extrAgalactic Star ClusTers) collaboration (A. Adamo, *in prep*).

step research-wise is to explore the role of star formation in this picture: does the environment play any critical role in the formation of stars and, once stars are formed, how does their feedback impact the ISM. One way of doing this would be by cross-matching this work's catalogue of resolved clouds with catalogues of embedded (or partially embedded) young stellar clusters (eYSCs) already available. The JWST-FEAST collaboration (Feedback in Emerging extrAgalactic Star ClusTers, PI Adamo), in particular, has published a catalogue of eYSCs for NGC 628 (Pedrini et al., 2024, Adamo, *in prep*), with on-going work to expand this to other nearby galaxies (including M51; Adamo, *in prep*). The characteristics of the eYSCs (i.e. mass, age, luminosity), as well as computed star formation rates/efficiencies (either from eYSC counts or extinction-corrected emission lines) can be correlated with the properties of the parent clouds in search for any specific trends, and for any variations with large-scale environment and galactocentric distance. Additionally, I plan to also extract "clouds" for several nearby galaxies from the 7.7 µm JWST band (see Fig. 5.1) - which traces polycylic aromatic hydrocarbons (PAHs) - and investigate if there are any significant environmental variations or differences from the cloud trends observed in this Thesis.

Furthermore, there is space to compare the HST extinction-derived dust maps to the emerging near/mid-infrared dust emission observations from JWST (see Fig. 5.1), given the similar spatial scales. Mid-infrared emission is thought to mostly arise from small dust grains which undergo stochastic heating (e.g. Draine & Li, 2007; Galliano et al., 2018), whilst the dust acting to attenuate optical light is composed of larger grains in thermal equilibrium with the interstellar radiation field (see Chapter 1.3.2.1). Comparing the two could be used to better understand the conditions affecting the different dust populations.

Another avenue of future work is to expand the current sample to more nearby galaxies. There is also room for further improvements on the extinction imaging technique, particularly on the handling of disc and bar inclinations. Additionally, there are plans to compare the findings of this Thesis to numerical simulations, particularly the work within the FFOGG collaboration (Following the Flow Of Gas in Galaxies; PI Duarte-Cabral), which has high-resolution, live-potential numerical models designed to match this work's sample of galaxies. Notably, we can use the environmental trends seen observationally to test the numerical predictions of the effect of different types of spiral pattern on molecular clouds (e.g. Pettitt et al., 2020).

5.2 CONCLUDING REMARKS

This Thesis presents a body of work focused on investigating the spatial distribution of the ISM as a function of large-scale galactic environment, with the use of a new, dust-based imaging technique. There is still much more to be done. Together with increasingly higher resolution maps from facilities like ALMA, the combination of the technique described here with the new exciting view JWST provides us of young star formation (and PAHs), is incredibly powerful and brings a fascinating multi-wavelength view of the star formation cycle within galaxies. Future facilities (e.g. SKA and ELT) will complement the wealth of information already available, and push the boundaries in terms of resolution and sensitivity, providing more pieces to the puzzle. In particular, for galaxies outside the Local Group, our understanding of the atomic phase of the ISM, as well as the use of dense gas tracers (e.g. HCN, N_2H^+), is currently mainly limited to integrated measurements over large areas, which may be improved with future facilities. Together with ground-breaking numerical and theoretical work, there is an exciting future ahead for the star formation community, both extragalactic and Galactic.

BIBLIOGRAPHY

Abdeen S., et al., 2022, *MNRAS*, 512, 366

Ali A. A., Dobbs C. L., Bending T. J. R., Buckner A. S. M., Pettitt A. R., 2023, *MNRAS*, 524, 555

Alves J., Lombardi M., Lada C. J., 2007, *A&A*, 462, L17

André P., et al., 2010, *A&A*, 518, L102

Andriesse C. D., 1978, *A&A*, 66, 169

Aniano G., et al., 2012, *ApJ*, 756, 138

Aniano G., et al., 2020, *ApJ*, 889, 150

Astropy Collaboration et al., 2013, *A&A*, 558, A33

Astropy Collaboration et al., 2018, *AJ*, 156, 123

Astropy Collaboration et al., 2022, *ApJ*, 935, 167

Bacmann A., André P., Puget J. L., Abergel A., Bontemps S., Ward-Thompson D., 2000, *A&A*, 361, 555

Ballesteros-Paredes J., Mac Low M.-M., 2002, *ApJ*, 570, 734

Ballesteros-Paredes J., Hartmann L. W., Vázquez-Semadeni E., Heitsch F., Zamora-Avilés M. A., 2011, *MNRAS*, 411, 65

Ballesteros-Paredes J., Román-Zúñiga C., Salomé Q., Zamora-Avilés M., Jiménez-Donaire M. J., 2019, *MNRAS*, 490, 2648

Barnard E. E., 1927, A photographic atlas of selected regions of the Milky Way. Carnegie Institute, Washington, DC

Barnes P. J., Muller E., Indermuehle B., O'Dougherty S. N., Lowe V., Cunningham M., Hernandez A. K., Fuller G. A., 2015, ApJ, 812, 6

Barnes P. J., Hernandez A. K., Muller E., Pitts R. L., 2018, *ApJ*, 866, 19

Barnes A. T., et al., 2023, *ApJ*, 944, L22

Barrera-Ballesteros J. K., et al., 2020, *MNRAS*, 492, 2651

Becklin E. E., Neugebauer G., 1967, *ApJ*, 147, 799

Bell T. A., Roueff E., Viti S., Williams D. A., 2006, *MNRAS*, 371, 1865

Bell T. A., Viti S., Williams D. A., 2007, *MNRAS*, 378, 983

Bergin E. A., Langer W. D., Goldsmith P. F., 1995, *ApJ*, 441, 222

Bertschinger E., 1998, *ARAA*, 36, 599

Bianchi S., 2013, *A&A*, 552, A89

Bigiel F., Leroy A., Walter F., Brinks E., de Blok W. J. G., Madore B., Thornley M. D., 2008, *AJ*, 136, 2846

Bigiel F., et al., 2011, *ApJ*, 730, L13

Binney J., Tremaine S., 1987, Galactic dynamics. Princeton University Press

Binney J., Tremaine S., 2008, Galactic Dynamics: Second Edition. Princeton University Press

Blitz L., 1993, in Levy E. H., Lunine J. I., eds, Protostars and Planets III. p. 125

Blitz L., Thaddeus P., 1980, *ApJ*, 241, 676

Bohlin R. C., Savage B. D., Drake J. F., 1978, *ApJ*, 224, 132

Bolatto A. D., Leroy A. K., Rosolowsky E., Walter F., Blitz L., 2008, *ApJ*, 686, 948

Bolatto A. D., Wolfire M., Leroy A. K., 2013, *ARAA*, 51, 207

Boquien M., Burgarella D., Roehlly Y., Buat V., Ciesla L., Corre D., Inoue A. K., Salas H., 2019, *A&A*, 622, A103

Boselli A., et al., 2012, *A&A*, 540, A54

Bradley L., et al., 2020, astropy/photutils: 1.0.1, doi:10.5281/zenodo.4049061, `https://doi.org/10.5281/zenodo.4049061` den Brok J. S., et al., 2022, A&A, 662, A89

Buta R. J., et al., 2015, *ApJS*, 217, 32

Calzetti D., 2001, *PASP*, 113, 1449

Calzetti D., 2013, Star Formation Rate Indicators. Proceedings of the XXIII Canary Islands Winter School of Astrophysics, doi:10.48550/arXiv.1208.2997

Calzetti D., Liu G., Koda J., 2012, *ApJ*, 752, 98

Calzetti D., et al., 2015, *AJ*, 149, 51

Calzetti D., et al., 2024, *ApJ*, 971, 118

Carruthers G. R., 1970, ApJ, 161, L81

Casey C. M., 2012, *MNRAS*, 425, 3094

Chevance M., et al., 2020, Space Sci. Rev., 216, 50

Chevance M., et al., 2022, *MNRAS*, 509, 272

Choi W., et al., 2023, *MNRAS*, 522, 4078

Ciardullo R., Feldmeier J. J., Jacoby G. H., Kuzio de Naray R., Laychak M. B., Durrell P. R., 2002, *ApJ*, 577, 31

Clark C. J. R., Schofield S. P., Gomez H. L., Davies J. I., 2016, *MNRAS*, 459, 1646

Clark C. J. R., et al., 2018, *A&A*, 609, A37

Clark C. J. R., et al., 2019, *MNRAS*, 489, 5256

Clarke S. D., Jaffa S. E., Whitworth A. P., 2022, *MNRAS*, 516, 2782

Colman T., et al., 2022, *MNRAS*, 514, 3670

Colombo D., et al., 2014a, *ApJ*, 784, 3

Colombo D., et al., 2014b, *ApJ*, 784, 4

Colombo D., Rosolowsky E., Ginsburg A., Duarte-Cabral A., Hughes A., 2015, *MNRAS*, 454, 2067

Colombo D., et al., 2019, *MNRAS*, 483, 4291

Colombo D., et al., 2021, *A&A*, 655, L2

Colombo D., et al., 2022, *A&A*, 658, A54

Conroy C., 2013, *ARAA*, 51, 393

Crain R. A., van de Voort F., 2023, *ARAA*, 61, 473

Crain R. A., et al., 2015, *MNRAS*, 450, 1937

Croxall K. V., Pogge R. W., Berg D. A., Skillman E. D., Moustakas J., 2015, *ApJ*, 808, 42

Crutcher R. M., 1999, *ApJ*, 520, 706

Crutcher R. M., Wandelt B., Heiles C., Falgarone E., Troland T. H., 2010, *ApJ*, 725, 466

Dabrowski I., 1984, Canadian Journal of Physics, 62, 1639

Dame T. M., Hartmann D., Thaddeus P., 2001, *ApJ*, 547, 792

Davies J. I., et al., 2017, *PASP*, 129, 044102

De Looze I., et al., 2014, *A&A*, 571, A69

De Looze I., et al., 2020, *MNRAS*, 496, 3668

Dobbs C. L., 2008, *MNRAS*, 391, 844

Dobbs C. L., Bonnell I. A., 2007, *MNRAS*, 374, 1115

Dobbs C. L., Pringle J. E., 2013, *MNRAS*, 432, 653

Dobbs C. L., Theis C., Pringle J. E., Bate M. R., 2010, *MNRAS*, 403, 625

Dobbs C. L., Burkert A., Pringle J. E., 2011, *MNRAS*, 417, 1318

Dobbs C. L., et al., 2014, in Beuther H., Klessen R. S., Dullemond C. P., Henning T., eds, Protostars and Planets VI. pp 3–26 (`arXiv:1312.3223`), doi:10.2458/azu_uapress_9780816531240-ch001

Draine B. T., 1978, *ApJS*, 36, 595

Draine B. T., 2003, *ARAA*, 41, 241

Draine B. T., Li A., 2007, *ApJ*, 657, 810

Draine B. T., et al., 2007, *ApJ*, 663, 866

Duarte-Cabral A., Dobbs C. L., 2016, *MNRAS*, 458, 3667

Duarte-Cabral A., Dobbs C. L., 2017, *MNRAS*, 470, 4261

Duarte-Cabral A., et al., 2021, *MNRAS*, 500, 3027

Eales S., et al., 2012, *ApJ*, 761, 168

Elia D., et al., 2013, *ApJ*, 772, 45

Elmegreen B. G., 1987, *ApJ*, 312, 626

Elmegreen B. G., 1994, *ApJ*, 425, L73

Elmegreen B. G., Elmegreen D. M., 1986, *ApJ*, 311, 554

Elmegreen B. G., Elmegreen D. M., 2019, *ApJS*, 245, 14

Elmegreen B. G., Elmegreen D. M., Seiden P. E., 1989, *ApJ*, 343, 602

Engargiola G., Plambeck R. L., Rosolowsky E., Blitz L., 2003, *ApJS*, 149, 343

Faustino Vieira H., Duarte-Cabral A., Davis T. A., Peretto N., Smith M. W. L., Querejeta M., Colombo D., Anderson M., 2023, *MNRAS*, 524, 161

Faustino Vieira H., Duarte-Cabral A., Davis T. A., Peretto N., Smith M. W. L., Querejeta M., Colombo D., Anderson M., 2024, *MNRAS*, 527, 3639

Feldmann R., Gnedin N. Y., Kravtsov A. V., 2011, *ApJ*, 732, 115

Foyle K., Rix H. W., Walter F., Leroy A. K., 2010, *ApJ*, 725, 534

Freedman W. L., et al., 2001, *ApJ*, 553, 47

Fujimoto M., 1968, *ApJ*, 152, 391

Galliano F., 2022, Habilitation Thesis, p. 1

Galliano F., Galametz M., Jones A. P., 2018, *ARAA*, 56, 673

Genel S., et al., 2014, *MNRAS*, 445, 175

Giannetti A., et al., 2017, *A&A*, 606, L12

Gong M., Ostriker E. C., Kim C.-G., Kim J.-G., 2020, *ApJ*, 903, 142

Grand R. J. J., et al., 2017, *MNRAS*, 467, 179

Gratier P., et al., 2010, *A&A*, 522, A3

Griffin M. J., et al., 2010, *A&A*, 518, L3

Gunawardhana M. L. P., et al., 2011, *MNRAS*, 415, 1647

Guth A. H., 1981, *Phys. Rev. D*, 23, 347

Guélin M., Zylka R., Mezger P. G., Haslam C. G. T., Kreysa E., 1995, *A&A*, 298, L29

Harris C. R., et al., 2020, *Nature*, 585, 357

Heath T. L., Archimedes 1897, The Sand-Reckoner of Archimedes. Cambridge University Press, https://sacred-texts.com/cla/archim/sand/sandreck.htm

Heath T. L., Aristarchus o. S., 1913, Aristarchus of Samos, the ancient Copernicus - a history of Greek astronomy to Aristarchus, together with Aristarchus's Treatise on the sizes and distances of the sun and moon. Oxford : Clarendon Press, http://archive.org/details/aristarchusofsam00heatuoft

Henry A. L., Quillen A. C., Gutermuth R., 2003, *AJ*, 126, 2831

Henshaw J. D., et al., 2016, *MNRAS*, 457, 2675

Herrington N. P., Dobbs C. L., Bending T. J. R., 2023, *MNRAS*, 521, 5712

Herschel W., 1785, Philosophical Transactions of the Royal Society of London, 75, 213–266

Herschel J. F. W., 1833, Philosophical Transactions of the Royal Society of London, 123, 359

Herzberg G., 1949, Nature, 163, 170

Heyer M. H., Brunt C. M., 2004, *ApJ*, 615, L45

Heyer M., Krawczyk C., Duval J., Jackson J. M., 2009, *ApJ*, 699, 1092

Hildebrand R. H., 1983, *Quarterly Journal of the Royal Astronomical Society*, 24, 267

Hollenbach D., Salpeter E. E., 1971, *ApJ*, 163, 155

Holmberg E., 1958, Meddelanden fran Lunds Astronomiska Observatorium Serie II, 136, 1

Holwerda B. W., et al., 2007, *AJ*, 134, 1655

Hubble E. P., 1925, Popular Astronomy, 33, 252

Hughes A., et al., 2013, *ApJ*, 779, 46

van de Hulst H. C., 1946, Recherches Astronomiques de l'Observatoire d'Utrecht, 11, 2.i

Hunter J. D., 2007, Computing in Science and Engineering, 9, 90

Israel F. P., Tilanus R. P. J., Baas F., 2006, *A&A*, 445, 907

Jacobs B. A., Rizzi L., Tully R. B., Shaya E. J., Makarov D. I., Makarova L., 2009, *AJ*, 138, 332

Jaffa S. E., Whitworth A. P., Clarke S. D., Howard A. D. P., 2018, *MNRAS*, 477, 1940

Jeans J. H., 1902, Philosophical Transactions of the Royal Society of London Series A, 199, 1

Jeffreson S. M. R., Kruijssen J. M. D., Keller B. W., Chevance M., Glover S. C. O., 2020, *MNRAS*, 498, 385

Jenkins E. B., 2009, *ApJ*, 700, 1299

Jeřábková T., Hasani Zonoozi A., Kroupa P., Beccari G., Yan Z., Vazdekis A., Zhang Z. Y., 2018, *A&A*, 620, A39

Jiménez-Donaire M. J., et al., 2019, *ApJ*, 880, 127

Jones A. P., Fanciullo L., Köhler M., Verstraete L., Guillet V., Bocchio M., Ysard N., 2013, *A&A*, 558, A62

Jones A. P., Köhler M., Ysard N., Bocchio M., Verstraete L., 2017, *A&A*, 602, A46

Kahre L., et al., 2018, *ApJ*, 855, 133

Kainulainen J., Juvela M., Alves J., 2007, *A&A*, 468, 581

Kauffmann J., Pillai T., 2010, *ApJ*, 723, L7

Kauffmann J., Bertoldi F., Bourke T. L., Evans N. J. I., Lee C. W., 2008, *A&A*, 487, 993

Kegel W. H., 1989, *A&A*, 225, 517

Kennicutt Robert C. J., 1998, *ARAA*, 36, 189

Kennicutt R. C., Evans N. J., 2012, *ARAA*, 50, 531

Kennicutt Robert C. J., et al., 2007, *ApJ*, 671, 333

Kessler S., Leroy A., Querejeta M., Murphy E., Rebolledo D., Sandstrom K., Schinnerer E., Wong T., 2020, *ApJ*, 892, 23

Kim S.-H., Martin P. G., Hendry P. D., 1994, *ApJ*, 422, 164

Kim J.-h., et al., 2014, *ApJS*, 210, 14

Kleinmann D. E., Low F. J., 1967, *ApJ*, 149, L1

Klessen R. S., Heitsch F., Mac Low M.-M., 2000, *ApJ*, 535, 887

Knapp G. R., Kerr F. J., Rose W. K., 1973, Astrophys. Lett., 14, 187

Koda J., et al., 2009, *ApJ*, 700, L132

Koda J., et al., 2023, *ApJ*, 949, 108

Könyves V., et al., 2015, *A&A*, 584, A91

Kormendy J., Kennicutt Robert C. J., 2004, *ARAA*, 42, 603

Kourkchi E., Tully R. B., 2017, *ApJ*, 843, 16

Kourkchi E., Courtois H. M., Graziani R., Hoffman Y., Pomarède D., Shaya E. J., Tully R. B., 2020, *AJ*, 159, 67

Kreckel K., et al., 2013, *ApJ*, 771, 62

Kreckel K., Blanc G. A., Schinnerer E., Groves B., Adamo A., Hughes A., Meidt S., 2016, *ApJ*, 827, 103

Krumholz M. R., McKee C. F., 2005, *ApJ*, 630, 250

La Vigne M. A., Vogel S. N., Ostriker E. C., 2006, *ApJ*, 650, 818

Lada C. J., Lada E. A., 2003, *ARAA*, 41, 57

Lada C. J., Alves J. F., Lombardi M., 2007, in Reipurth B., Jewitt D., Keil K., eds, Protostars and Planets V. p. 3

Lang P., et al., 2020, *ApJ*, 897, 122

Larson R. B., 1981, *MNRAS*, 194, 809

Larson R. B., 2003, Reports on Progress in Physics, 66, 1651

Leavitt H. S., Pickering E. C., 1912, Harvard College Observatory Circular, 173, 1

Lee J. C., et al., 2022, *ApJS*, 258, 10

Lee J. C., et al., 2023, *ApJ*, 944, L17

Leja J., Johnson B. D., Conroy C., van Dokkum P. G., Byler N., 2017, *ApJ*, 837, 170

Leroy A. K., Walter F., Brinks E., Bigiel F., de Blok W. J. G., Madore B., Thornley M. D., 2008, *AJ*, 136, 2782

Leroy A. K., et al., 2013, *AJ*, 146, 19

Leroy A. K., et al., 2017, *ApJ*, 846, 71

Leroy A. K., et al., 2021, *ApJS*, 257, 43

Li A., 2005, in Journal of Physics: Conference Series. p. 028

Lilly S. J., Le Fevre O., Hammer F., Crampton D., 1996, *ApJ*, 460, L1

Lin C. C., Shu F. H., 1964, *ApJ*, 140, 646

Liu G., Koda J., Calzetti D., Fukuhara M., Momose R., 2011, *ApJ*, 735, 63

Liu L., Bureau M., Blitz L., Davis T. A., Onishi K., Smith M., North E., Iguchi S., 2021, *MNRAS*, 505, 4048

Lombardi M., Alves J., Lada C. J., 2006, *A&A*, 454, 781

Lombardi M., Alves J., Lada C. J., 2010, *A&A*, 519, L7

Lord S. D., Young J. S., 1990, *ApJ*, 356, 135

Mac Low M.-M., 1999, *ApJ*, 524, 169

Machida M. N., Higuchi K., Okuzumi S., 2018, *MNRAS*, 473, 3080

Madau P., Dickinson M., 2014, *ARAA*, 52, 415

Marsh K. A., Whitworth A. P., Lomax O., 2015, *MNRAS*, 454, 4282

Masters K. L., et al., 2011, *MNRAS*, 411, 2026

Mathis J. S., Rumpl W., Nordsieck K. H., 1977, *ApJ*, 217, 425

McKee C. F., Ostriker E. C., 2007, *ARAA*, 45, 565

McKee C. F., Williams J. P., 1997, *ApJ*, 476, 144

Meidt S. E., Rand R. J., Merrifield M. R., Shetty R., Vogel S. N., 2008, *ApJ*, 688, 224

Meidt S. E., et al., 2013, *ApJ*, 779, 45

Meidt S. E., et al., 2015, *ApJ*, 806, 72

Mentuch Cooper E., et al., 2012, *ApJ*, 755, 165

Messa M., et al., 2018, *MNRAS*, 473, 996

Messa M., Dessauges-Zavadsky M., Adamo A., Richard J., Claeyssens A., 2024, *MNRAS*, 529, 2162

Miyamoto Y., Nakai N., Kuno N., 2014, *Pub. Astron. Soc. Japan*, 66, 36

Moore T. J. T., Urquhart J. S., Morgan L. K., Thompson M. A., 2012, *MNRAS*, 426, 701

Mouschovias T. C., 1976, *ApJ*, 207, 141

Mouschovias T. C., Spitzer L. J., 1976, *ApJ*, 210, 326

Muñoz-Mateos J. C., et al., 2009, *ApJ*, 701, 1965

Mutchler M., Beckwith S. V. W., Bond H. E., Christian C., Hamilton F., Hamilton M., Levay Z., Noll K., 2005, Hubble Space Telescope multi-color ACS mosaic of M51, the Whirlpool Galaxy

Naab T., Ostriker J. P., 2017, *ARAA*, 55, 59

Narayanan D., Krumholz M. R., Ostriker E. C., Hernquist L., 2012, *MNRAS*, 421, 3127

Neralwar K. R., et al., 2022, *A&A*, 663, A56

Nersesian A., et al., 2019, A&A, 624, A80

Nersesian A., et al., 2020, *A&A*, 643, A90

Noll S., Burgarella D., Giovannoli E., Buat V., Marcillac D., Muñoz-Mateos J. C., 2009, *A&A*, 507, 1793

Noon K., De Napoli K., 2022, First Knowledges Astronomy. First Knowledges, Thames and Hudson, Fisherman's Bend, Australia

Oka T., Hasegawa T., Sato F., Tsuboi M., Miyazaki A., Sugimoto M., 2001, *ApJ*, 562, 348

Ossenkopf V., Henning T., 1994, *A&A*, 291, 943

Padoan P., Jimenez R., Juvela M., Nordlund Å., 2004, *ApJ*, 604, L49

Pan H.-A., Kuno N., 2017, *ApJ*, 839, 133

Patra N. N., 2019, *MNRAS*, 484, 81

Pedrini A., et al., 2024, *ApJ*, 971, 32

Peretto N., Fuller G. A., 2009, *A&A*, 505, 405

Pessa I., et al., 2021, *A&A*, 650, A134

Pettitt A. R., Dobbs C. L., Baba J., Colombo D., Duarte-Cabral A., Egusa F., Habe A., 2020, *MNRAS*, 498, 1159

Pety J., et al., 2013, *ApJ*, 779, 43

Pilbratt G. L., et al., 2010, *A&A*, 518, L1

Pineda J. E., Caselli P., Goodman A. A., 2008, *ApJ*, 679, 481

Planck Collaboration et al., 2011, *A&A*, 536, A19

Planck Collaboration et al., 2014, *A&A*, 564, A45

Planck Collaboration et al., 2016, *A&A*, 594, A13

Poglitsch A., et al., 2010, *A&A*, 518, L2

Puget J. L., Abergel A., Bernard J. P., Boulanger F., Burton W. B., Desert F. X., Hartmann D., 1996, *A&A*, 308, L5

Querejeta M., et al., 2016, *A&A*, 588, A33

Querejeta M., et al., 2019, *A&A*, 625, A19

Querejeta M., et al., 2021, *A&A*, 656, A133

Querejeta M., et al., 2024, arXiv e-prints, p. arXiv:2405.05364

Ragan S. E., Henning T., Tackenberg J., Beuther H., Johnston K. G., Kainulainen J., Linz H., 2014, *A&A*, 568, A73

Ragan S. E., Moore T. J. T., Eden D. J., Hoare M. G., Elia D., Molinari S., 2016, *MNRAS*, 462, 3123

Rahman N., et al., 2012, *ApJ*, 745, 183

Regan M. W., 2000, *ApJ*, 541, 142

Renaud F., et al., 2015, *MNRAS*, 454, 3299

Renzini A., Peng Y.-j., 2015, *ApJ*, 801, L29

Rickard L. J., Palmer P., Morris M., Zuckerman B., Turner B. E., 1975, *ApJ*, 199, L75

Rieke G. H., et al., 2004, *ApJS*, 154, 25

Rigby A. J., et al., 2016, *MNRAS*, 456, 2885

Rigby A. J., et al., 2021, *MNRAS*, 502, 4576

Roberts W. W., 1969, *ApJ*, 158, 123

Roman-Duval J., et al., 2014, *ApJ*, 797, 86

Rosolowsky E., Blitz L., 2005, *ApJ*, 623, 826

Rosolowsky E. W., Pineda J. E., Kauffmann J., Goodman A. A., 2008, *ApJ*, 679, 1338

Rosolowsky E., et al., 2021, *MNRAS*, 502, 1218

Saintonge A., Catinella B., 2022, *ARAA*, 60, 319

Saintonge A., et al., 2011, *MNRAS*, 415, 32

Saintonge A., et al., 2017, *ApJS*, 233, 22

Sandstrom K. M., et al., 2013, *ApJ*, 777, 5

Scalo J., 1990, in Capuzzo-Dolcetta R., Chiosi C., di Fazio A., eds, Astrophysics and Space Science Library Vol. 162, Physical Processes in Fragmentation and Star Formation. pp 151–176, doi:10.1007/978-94-009-0605-1_12

Schinnerer E., Weiß A., Aalto S., Scoville N. Z., 2010, *ApJ*, 719, 1588

Schinnerer E., et al., 2013, *ApJ*, 779, 42

Schinnerer E., et al., 2017, *ApJ*, 836, 62

Schmidt M., 1959, *ApJ*, 129, 243

Schruba A., Leroy A. K., Walter F., Sandstrom K., Rosolowsky E., 2010, *ApJ*, 722, 1699

Schruba A., et al., 2011, *AJ*, 142, 37

Schuller F., et al., 2009, *A&A*, 504, 415

Schuller F., et al., 2021, *MNRAS*, 500, 3064

Schuster K. F., Kramer C., Hitschfeld M., Garcia-Burillo S., Mookerjea B., 2007, *A&A*, 461, 143

Scoville N. Z., Solomon P. M., 1975, *ApJ*, 199, L105

Seifried D., et al., 2017, *MNRAS*, 472, 4797

Seigar M. S., James P. A., 2002, *MNRAS*, 337, 1113

Shabani F., et al., 2018, *MNRAS*, 478, 3590

Sheth K., Vogel S. N., Regan M. W., Thornley M. D., Teuben P. J., 2005, *ApJ*, 632, 217

Sheth K., et al., 2008, *ApJ*, 675, 1141

Shetty R., Kelly B. C., Bigiel F., 2013, *MNRAS*, 430, 288

Silva-Villa E., Larsen S. S., 2012, *A&A*, 537, A145

Smith M. W. L., et al., 2012, *ApJ*, 756, 40

Smith M. W. L., et al., 2016, *MNRAS*, 462, 331

Sodroski T. J., et al., 1995, *ApJ*, 452, 262

Solomon P., Edmunds M., 1980, Giant Molecular Clouds in the Galaxy: 3rd Gregynog Astrophysics Workshop, University of Wales, Cardiff. August, 1977. Oxford: Pergamon Press

Solomon P. M., de Zafra R., 1975, *ApJ*, 199, L79

Solomon P. M., Scoville N. Z., Penzias A. A., Wilson R. W., Jefferts K. B., 1972, *ApJ*, 178, 125

Solomon P. M., Rivolo A. R., Barrett J., Yahil A., 1987, *ApJ*, 319, 730

Somerville R. S., Davé R., 2015, *ARAA*, 53, 51

Spitzer Lyman J., 1949, *ApJ*, 109, 337

Spitzer L., 1998, Physical Processes in the Interstellar Medium

Spitzer L. J., Jenkins E. B., 1975, *ARAA*, 13, 133

Spitzer L. J., Cochran W. D., Hirshfeld A., 1974, *ApJS*, 28, 373

Springel V., Hernquist L., 2003, *MNRAS*, 339, 289

Stamatellos D., Whitworth A. P., 2003, *A&A*, 407, 941

Stebbins J., Huffer C. M., Whitford A. E., 1939, *ApJ*, 90, 209

Stecher T. P., 1965, *ApJ*, 142, 1683

Steinicke W., 2012, Journal of Astronomical History and Heritage, 15, 19

Stone J. M., Ostriker E. C., Gammie C. F., 1998, *ApJ*, 508, L99

Strong A. W., Mattox J. R., 1996, *A&A*, 308, L21

Struve W., 1847, Etudes d'Astronomie Stellaire: Sur la voie lactée et sur la distance des étoiles fixes. Imprimerie de l'Académie Impériale des Sciences de St. Pétersbourg, doi:10.3931/E-RARA-68770, `https://www.e-rara.ch/zut/doi/10.3931/e-rara-68770`

Sun J., et al., 2020a, *ApJ*, 892, 148

Sun J., et al., 2020b, *ApJ*, 901, L8

Sun J., et al., 2022, *AJ*, 164, 43

Tacconi L. J., Genzel R., Sternberg A., 2020, *ARAA*, 58, 157

Thilker D. A., et al., 2023, *ApJ*, 944, L13

Thompson T. W. J., Howk J. C., Savage B. D., 2004, *AJ*, 128, 662

Toomre A., Toomre J., 1972, *ApJ*, 178, 623

Traficante A., et al., 2018, *MNRAS*, 477, 2220

Treß R. G., Smith R. J., Sormani M. C., Glover S. C. O., Klessen R. S., Mac Low M.-M., Clark P. C., 2020, *MNRAS*, 492, 2973

Treß R. G., Sormani M. C., Smith R. J., Glover S. C. O., Klessen R. S., Mac Low M.-M., Clark P., Duarte-Cabral A., 2021, *MNRAS*, 505, 5438

Trumpler R. J., 1930, *PASP*, 42, 214

Tuffs R. J., Popescu C. C., Völk H. J., Kylafis N. D., Dopita M. A., 2004, *A&A*, 419, 821

Tully R. B., 1974, *ApJS*, 27, 449

Urquhart J. S., et al., 2021, *MNRAS*, 500, 3050

de Vaucouleurs G., de Vaucouleurs A., Corwin H. G. J., Buta R. J., Paturel G., Fouque P., 1991, Third Reference Catalogue of Bright Galaxies

Vázquez-Semadeni E., Ballesteros-Paredes J., Rodríguez L. F., 1997, *ApJ*, 474, 292

Vázquez-Semadeni E., Gómez G. C., Jappsen A. K., Ballesteros-Paredes J., González R. F., Klessen R. S., 2007, *ApJ*, 657, 870

Vázquez-Semadeni E., Gómez G. C., Jappsen A. K., Ballesteros-Paredes J., Klessen R. S., 2009, *ApJ*, 707, 1023

Vázquez-Semadeni E., Palau A., Ballesteros-Paredes J., Gómez G. C., Zamora-Avilés M., 2019, *MNRAS*, 490, 3061

Virtanen P., et al., 2020, Nature Methods, 17, 261

Visser R., van Dishoeck E. F., Black J. H., 2009, *A&A*, 503, 323

Vogel S. N., Boulanger F., Ball R., 1987, *ApJ*, 321, L145

Vogel S. N., Kulkarni S. R., Scoville N. Z., 1988, *Nature*, 334, 402

Wakelam V., et al., 2017, Molecular Astrophysics, 9, 1

Waskom M., 2021, The Journal of Open Source Software, 6, 3021

Watkins E. J., et al., 2023, *ApJ*, 944, L24

Wechsler R. H., Tinker J. L., 2018, *ARAA*, 56, 435

Whittet D. C. B., 2022, Dust in the Galactic Environment (Third Edition). 2514-3433, IOP Publishing, doi:10.1088/2514-3433/ac7204, `https://dx.doi.org/10.1088/2514-3433/ac7204`

Wiebe D. V., et al., 2009, *ApJ*, 707, 1809

Willett K. W., et al., 2013, *MNRAS*, 435, 2835

Wilson R. W., Jefferts K. B., Penzias A. A., 1970, *ApJ*, 161, L43

Wilson C. D., Scoville N., Freedman W. L., Madore B. F., Sanders D. B., 1988, *ApJ*, 333, 611

Wolfire M. G., Hollenbach D., McKee C. F., 2010, *ApJ*, 716, 1191

Wong T., Blitz L., 2002, *ApJ*, 569, 157

Wright T., 1750, An Original Theory or New Hypothesis of the Universe. London

Young J. S., Scoville N. Z., 1991, *ARAA*, 29, 581

Young J. S., Kenney J. D., Tacconi L., Claussen M. J., Huang Y. L., Tacconi-Garman L., Xie S., Schloerb F. P., 1986, *ApJ*, 311, L17

Ysard N., et al., 2012, *A&A*, 542, A21

Yu S.-Y., Ho L. C., Wang J., 2021, *ApJ*, 917, 88

Zhang X., Buta R. J., 2012, arXiv e-prints, p. arXiv:1203.5334

Zuckerman B., Evans N. J. I., 1974, *ApJ*, 192, L149

Zweibel E. G., 2015, in Lazarian A., de Gouveia Dal Pino E. M., Melioli C., eds, Astrophysics and Space Science Library Vol. 407, Magnetic Fields in Diffuse Media. p. 285, doi:10.1007/978-3-662-44625-6_11